Physical and Numerical Analysis of Long Wave Modeling for Tsunamis and Tides

Edward Payson Myers III

B.Sc., Washington University, 1992
M.Sc., Oregon Graduate Institute of Science & Technology, 1994

A dissertation submitted to the faculty of the
Oregon Graduate Institute of Science & Technology
in partial fulfillment of the
requirements for the degree
Doctor of Philosophy
in
Environmental Science and Engineering

November 1998

The dissertation "Physical and Numerical Analysis of Long Wave Modeling for Tsunamis and Tides" by Edward Payson Myers III has been examined and approved by the following committee:

António M. Baptista, Ph.D., Thesis Advisor
Professor

William Fish, Ph.D.
Adjunct Associate Professor

Robert L. Doneker, Ph.D.
Assistant Professor

George R. Priest, Ph.D.
Department of Geology and Mineral Industries

To my parents, Edward and Shirley,

and my sister, Brynn

ACKNOWLEDGMENTS

I would like to express my gratitude to my advisor, António Baptista, for his guidance and encouragement throughout my graduate education at OGI. His assiduous work ethic has indelibly inspired his students to take pride in all their life endeavors. I am very grateful to my committee members, Dr. William Fish, Dr. Robert L. Doneker, and Dr. George R. Priest, for their suggestions, comments, and conversations which have been invaluable to this thesis.

This thesis is dedicated to my family and relatives, the support from which has continually improved my focus and integrity. Thanks to all the students in the department for their friendship and support over the past several years. I would also like to express my appreciation for the dedication of the professors in the department, whose genuine focus on providing quality education has made the learning process enjoyable.

I thank Rick Luettich and Joannes Westerink for providing the base code for ADCRIC and Roy Walters for providing the base code for TIDE2D. I would like to acknowledge the support from the Department of Defense Army Research Office Grant DAALO3-92-G-0065, Office of Naval Research Grant N00014-96-1-0893, Department of Geology and Mineral Industries Contracts 6175001 and 411001, NEHRP Award 1434-HQ-96-GR-02712, and Oregon Sea Grant 2-5706-01.

TABLE OF CONTENTS

LIST OF FIGURES

ABSTRACT

Physical and Numerical Analysis of Long Wave Modeling for Tsunamis and Tides

Edward Payson Myers III

Oregon Graduate Institute of Science & Technology

Supervising Professor: António M. Baptista

Numerical models are increasingly being used as tools in the analysis of ocean, coastal, and estuarine dynamics. This thesis examines finite element modeling of two types of long waves, tsunamis and tides, and scrutinizes the numerical representation of the physics governing their propagation.

The Eastern North Pacific Ocean is the domain used to evaluate the ability of numerical models to reproduce regional tidal observations. Inversion techniques identified the amplitudes and phases of tidal constituents along the open boundary based upon tide gauge observations. The goal of this study was not only to minimize RMS errors between the model and the observations, but to also accurately depict the physics as the waves propagate through the domain. This regional model of tides was further examined by contrasting results with global models, and by using regional model results as input to a local modeling study of the Columbia River.

Eliminating errors from tsunami models is more difficult than for tidal modeling, primarily because initial conditions for tsunamis, the movement of the ocean floor during the earthquake, are difficult to verify. Two approaches to overcoming this uncertainty were examined. First, more effective representations of plate movement in the subduction zone were used to compute probable deformations for future Cascadia subduction zone (CSZ) events. Computations for the CSZ allowed us to numerically simulate potential wave dynamics off the northwest coast of the United States resulting from future CSZ

earthquakes. With proper parameterization, such computations also may be used for any tsunami event. Results of the CSZ simulations were used by the Oregon Department of Geology and Mineral Industries and the National Oceanic and Atmospheric Administration to provide state and local governments with tools to design effective hazard mitigation strategies. The second approach to eliminating errors in tsunami simulations was to identify and quantify the effects of factors that can alter the quality of the results. Such factors include tide and tsunami interactions, selection of model parameters, grid refinement, truncation errors, and energy errors. Methods were formulated to control and minimize these errors and to better preserve energy in the simulations.

CHAPTER 1

Introduction

1.1 Context

This thesis examines the ability of numerical models to reproduce the physics of two types of long waves: tsunamis and tides. The goal was not to produce a model of tides everywhere in the world, nor to provide simulations of all recent tsunamis. Rather, a specific region was selected for the tidal modeling, and a few selected tsunami events were simulated. The focus is therefore placed on examining the use of the numerical model as a tool, the lessons of which can help to understand better ways of utilizing such tools. Numerical modeling of long waves is not at the stage where scientists can unequivocally say that the physics is always well reproduced, and it is instructive to dissect numerical results in more detail to identify limitations and improve results.

Both tsunamis and tides historically have been classified as long waves, but their strikingly disparate geneses lead to differences in wave and energy characteristics. Tides are the oceans' continuous response to the gravitational forces acting between earth and celestial bodies. Tsunamis are instantaneous events caused primarily by movement of the ocean floor during subduction earthquakes. The ocean floor deformation generates an instantaneous wave that usually consists of an initial crest and trough resulting from uplift and subsidence along the seabed below. The initial tsunami wave has a wavelength less than those associated with tides, and its free movement thereafter leads to waves which carry concentrated energy at higher frequencies. Thus, the tides tend to have energy dispersed over the entire ocean and undulate at known frequencies lower than those of tsunamis. A schematic energy spectrum is shown in Figure 1.1 and portrays the wave period differences between the tides and tsunamis. Note also that tsunamis occupy a nebulous region between the classic long wave tides and short waves (swells, wind waves, capillary waves).

There are various reasons why numerical models of tides and tsunamis still produce significant errors from what is observed. The phrase "significant errors" also has different meanings for each type of wave. For tsunamis, quantification of errors is difficult owing to poor definition of the ocean floor deformation. This lack of accuracy for the initial conditions of the model makes error quantification a difficult task. Because tsunamis are more loosely defined as long waves, there is also a greater likelihood of incurring errors based upon using long wave assumptions in the models. Both tsunami and tide modeling suffer a variety of common error sources, including bathymetric representation, shoreline depiction, model parameterization (friction, diffusion, weighting factors), and numerical sources of contamination (time step, grid spacing, ill-conditioned matrices). As alluded to, errors in tidal simulations are much less than those of tsunami simulations, considering that the astronomical forcings are more clearly defined.

The motivations behind the need to examine tide and tsunami modeling are discussed in more detail in the next section. While the objectives for each study are often unique to a certain modeling application, a broader picture of how the lessons from a wide array of experiments interweave and fit together will emerge. Such a vantage will permit more efficient use of such models in the future and better approaches to solving the problems faced by scientists, planners, and citizens who would like to utilize such tools. The layout of the structure for subsequent chapters in this thesis is presented after the individual discussions of the tide and tsunami modeling approaches.

1.2 Numerical Modeling of Tides

Tidal patterns have long been monitored by civilizations throughout history. Examples range from the Romans compiling relationships between the sea and the moon to theories about these relationships by Galileo, Descartes, and Kepler (Pugh, 1987). The evolution of methods for recording tidal elevations at specific locations has included tide poles, stilling-well gauges, pressure recorders, reflection time gauges, deep-sea pressure recorders, and satellite altimetry. Harmonic analysis of such tidal measurements (Godin, 1972, Foreman, 1977) permits the ability to produce accurate forecasts of tidal behavior at the point of measurement. Prediction of tides at specific sites, however, does not yield any information about the nature of the tides in between such sites. While interpolation can be used to provide a rough estimate of tidal patterns in between locations, the most reliable approach is to try to reproduce the physics of how the waves propagate spatially.

Modeling the spatial variability of tidal processes provides needed information in studies of oceanography, geodesy, geophysics, and space technology. Tidal propagation is increasingly being used in modeling physical processes occurring in estuaries as well. Such processes include residence time analyses (Oliveira and Baptista, 1997), residual currents (Sommerfield and Baptista, 1998), coastal erosion (Komar, 1992), and river interactions with tidal currents (Jay and Flinchem, 1997). Advances in our understanding of tidally dependent physical processes are in turn linked to tangible applications such as water quality analysis, coastal engineering, commercial navigation, military tactics, marine biology, and hazard mitigation. Society's increased reliance and interaction with the world's waterways demands that our understanding of the oceans' physics be effectively utilized as a tool in management decisions.

Numerical models serve as the primary tool for integrating physical equations with geographic domains and applications. Hydrodynamic numerical models attempt to simulate the balance of forces and conservation of mass affecting a body of water. The physical equations used are generally based upon some variation of the Navier-Stokes equations for incompressible fluids. Ideally, the three-dimensional form of these equations would be used by the model. However, the equations used by a numerical model must first be discretized for a given domain using finite element, finite difference, or finite volume techniques. The discretized forms of these equations are then computed at specified locations interconnected through a grid structure. The number of discrete grid points required to adequately reproduce the physics imbedded in the three-dimensional equations is, for most applications, too onerous for today's computers.

Numerical schemes therefore generally rely on a modified form of the Navier-Stokes equations. For tides, most models rely on the depth-averaged shallow water equations. Shallow water theory (Kinnmark, 1986) assumes that the wavelength is much larger than the depth through which the wave is travelling. Under this assumption, dimensional analysis can be used to eliminate negligible terms from the three-dimensional equations. Depth-averaging leads to a set of equations that can directly be solved for water surface elevations and depth-averaged velocities, thus avoiding the need to solve for variations in the vertical structure of velocities. The depth-averaged shallow water equations are thus valid when the wavelength to depth ratio is very large, when the vertical structure of velocities can be neglected, and when vertical density variations are not expected to affect the flow significantly. For the purposes of modeling tidal propagation in open waters, these assumptions are valid and the model is categorized as a barotropic model. In situations where accelerations from density gradients are important (i.e. estuarine studies), baroclinic models such as QUODDY (Ip and Lynch, 1995) serve as more appropriate tools. Similarly, in cases where resolution of the three-dimensional structure of velocities is necessary, models such as ADCIRC (Luettich et al., 1991) permit internal mode calculations of equations over vertical profiles.

Which equations, and thus which models, to use for a particular application depend upon the region of interest and the relevant physical processes. Tides are generally represented in a model in one of two ways. A force derived from the tidal potential (Doodson, 1921) can be directly included in the balance of forces depicted in the momentum equations. The other approach is to impose, through the use of an elevation-specified Dirichlet boundary, a selected tidal forcing along the open ocean boundary of a given domain. Inclusion of the tidal potential as the sole tidal forcing is generally only used in global tide models. Regional tide models (i.e. large portions of an ocean or sea) tend to utilize both the tidal potential terms and a specified tidal forcing along the ocean boundary. Finally, local modeling studies rely solely on the ocean boundary tidal forcing. Since local models are designed to examine more complex physical processes characteristic of smaller space scales, use of baroclinic or internal mode models may be the more appropriate selection. Regional and global models are not significantly affected by such smaller scale processes, and barotropic modeling is therefore a more effective way of reproducing the physical propagation of tides in these larger domains.

Local, regional, and global hydrodynamic modeling studies individually yield insight on system dynamics that the others cannot always provide. Pieced together, these varying modeling applications can provide a comprehensive view of tidal effects as waves propagate through the deep oceans, continental slopes, shelf regions, coastal waters, and estuaries. Global tide models have contributed by examining the spatial patterns of tidal constituents throughout the world's open oceans. Schwiderski (1980a-c) pioneered much of the early global tide modeling efforts by showing that global tide charting could achieve an elevation accuracy of 10 cm at open ocean tide gauges. Various techniques have been utilized to map open ocean tidal patterns since then.

Le Provost (1994) used a nonlinear shallow water equation model to simulate global tides through inclusion of the tidal potential. As data has become readily available from satellite altimetry missions such as TOPEX/POSEIDON, empirical methods of interpolating tidal patterns (Desai and Wahr, 1995, Ray et al., 1994) have also proved to be effective tools. Rather than relying solely on pure hydrodynamic modeling or on data interpolation, a new class of models has emerged that attempt to assimilate data or empirical solutions into a hydrodynamic model (Egbert et al., 1994, Matsumoto et al., 1995). Finally, adjustments to these models using new altimetry data or algorithms has led to more accurate global tide solutions (Sanchez and Pavlis, 1995, Eanes and Bettadpur, 1994, Andersen, 1995). While all of these global tide models are capable of reproducing observations well in the open oceans, they are not designed to accurately represent processes in coastal regions. The reason stems from the computational requirements of trying to discretize all the world's oceans in one model. Such discretization often results in model grid spacings of 0.5-1.0°, the coarseness of which is not capable of adequately representing coastal features or processes.

Local models, on the other hand, are designed to simulate processes characteristic of coastal and estuarine systems. While there are numerous such studies, the CORIE project (Baptista et al., 1998) provides a representative look at the objectives and analyses examined by such a model. CORIE integrates real-time data collection with two and three-dimensional models to characterize and predict the physics in the lower Columbia River estuary. The relevant forces in this system include tidal propagation, river flow, density gradients, and wind stress. In addition, significant inundation occurs in tidal flats throughout the estuary, and short waves play a non-negligible role in the dynamics of the system. All of these features are interwoven such that their contribution and interactions must be accounted for in the characterization of the system's physical attributes. Local modeling approaches such as this must clearly identify and incorporate a much wider range of processes than global modeling of tides.

Despite the wide range in spatial scales between local models and global models, tidal boundary conditions for the former are often provided by results of the latter. This discrepancy is one of the incentives for developing regional tide models. The spatial scales attainable through grid refinement in a regional model are larger than those of local models but much less than those of global models. The focus of most regional models is placed on how the physics in the deep oceans is translated to what is observed in coastal waters. For tides, energy redistributions along the continental slope and shelf will determine the eventual nonlinear generation of overtides and compound tides in coastal regions. While the grid resolution in global tide models often satisfies the dimensionless wavelength criteria (enough grid points per wavelength) for the relevant tidal constituents, it is generally not adequate for representing the underlying bathymetric features along the continental slope, shelf, and coastal waters. Since the bathymetry will in turn influence the propagation of the tidal waves, such influences will not be portrayed in most global models. Thus, a regional model can facilitate better reproduction of the physical changes occurring as the tides approach the shoreline.

Since regional modeling applications must be able to handle varying degrees of spatial scales, it is generally convenient to use finite element grids and models. Examples of finite element regional tide models include applications in the Arctic Ocean (Lyard, 1997) and the Gulf of Mexico (Westerink et al., 1992). Besides being able to provide more detailed input to local modeling studies, some regional studies have also been used to improve global tide models in those regions. For the purposes of this thesis, regional modeling of tides was considered an ideal experiment for examining the ability of reproducing complex tidal patterns with a numerical model. The eastern north Pacific Ocean is selected as the regional domain. Composed of deep abyssal regions, seamounts, trenches, continental slopes, shelves, islands, coastal waters, and river inlets, this region provides many interesting bathymetric and topographic challenges for a model to handle. The model's ability to capture the changing physical processes as the tides move into shallower areas can also be tested in this region by providing its results to the CORIE local modeling study. As this thesis also examines numerical modeling of tsunamis, the tide modeling results will further be closely examined as to how they may be used in evaluating tide and tsunami interactions during such events as the 1964 Alaska tsunami.

1.3 Numerical Modeling of Tsunamis

Tsunamis are generally formed by the vertical motion of the ocean floor during a subduction earthquake. Subduction zones are locked interfaces between two seismic plates, one of which is dipping underneath the other at a certain angle. The two plates become locked over time due to accumulated stresses along the subduction interface, and the floor of the ocean buckles in response. When these stresses become too burdensome, the stored energy is released in a subduction earthquake as the underlying plate thrusts further underneath the overlying plate. Simultaneously, the floor of the ocean attempts to spring back to its zero-stress form before the buckling commenced. This movement (Figure 1.2) generally leads to a region of uplift juxtaposed with a similar region of subsidence. The underlying plate is usually an oceanic plate, whereas the overlying plate is most often the plate containing a land mass. This configuration leads to the zone of subsidence being located closer to (or on) land and the zone of uplift on the seaward side.

The deformation occurs over such a short amount of time during the earthquake that the movement of the ocean above is essentially instantaneous. Thus, the initial tsunami waveform along the ocean's surface is equivalent to the deformation below. The initial wave profile subsequently splits in two, sending one wave towards the ocean and the other towards land. Depending on how far both of these waves must travel before reaching land, a train of waves may develop from each by dispersing some of the initial wave energy into higher frequency components. Strong bathymetric gradients in the path of the tsunami can cause reflection and refraction of waves propagating into shallower water. Similarly, after waves reflect off the coastline, they will refract as they travel back into deeper water. At some depth, these reflected waves can refract so much that they bend back towards the coastline. The tangential line at which this occurs is called a caustic, and this phenomenon is responsible for trapping much of the tsunami energy in coastal waters until frictional dissipation and dispersion can eventually retard the tsunami's energy. Refraction, reflection, and resonance all contribute to redistribution of tsunami energy to higher frequencies and the long periods of time tsunamis can remain in coastal waters. Camfield (1990) provides a comprehensive summary of such propagation characteristics of tsunamis.

A numerical model of a tsunami must therefore rely on knowledge of the ocean floor deformation for initial conditions. For the depth-averaged shallow water equations, the continuity equation is usually altered to incorporate vertical movement of the ocean floor,

$$\frac{\partial \eta}{\partial t} - \frac{\partial \beta}{\partial t} + \frac{\partial UH}{\partial x} + \frac{\partial VH}{\partial y} = 0 \tag{1}$$

where η is the wave elevation, β is the bottom deformation, (U, V) are the depth-averaged velocities, and H is the total water depth. Use of a small enough time step (on the order of one second) enables the bottom motion to behave instantaneously. Since the latter two velocity gradient terms in (1) will be very close to zero in the first few seconds, the wave elevation term will equal the bottom deformation term. Thus, the initial wave will be equivalent to the imposed bottom deformation. Unfortunately, this bottom deformation along the ocean floor is difficult to verify. The only observations of vertical crustal movement along the ocean floor derive from changes between bathymetric surveys before and after the earthquake. However, depth changes still leave an uncertainty of about 3 meters due to measurement techniques and the time interval between surveys. Considering that most deformation during an earthquake is less than this uncertainty, such measurements cannot provide accurate depictions of the vertical crustal movement. Observations of deformation on land can provide some useful information. Vertical datum changes at tide gauges and benchmarks can be calculated to an accuracy of 10 cm or less. Vertical changes can also be less accurately estimated from barnacle and vegetation growth patterns, coastline marker differences, and leveling surveys performed before and after the earthquake. Such land observations of vertical movement have been reported for recent events, including the 1964 Alaska earthquake (Holdahl and Sauber, 1994) and the 1993 Hokkaido Nansei-Oki earthquake (Kumaki et al., 1993). While such data should be used to help guide calculations of deformation patterns on land, its use in assessing deformation patterns along the ocean floor is limited owing to the fact that most of the deformation occurs off land.

In order to calculate an offshore deformation pattern to be used by a tsunami model, fault dislocation models have been developed to compute crustal movement during an earthquake. Okada (Okada, 1985, Okada, 1992) has presented closed analytical equations for computing displacements due to shear and tensile faulting mechanisms. Okada's rectangular source model is widely used in generating initial conditions for tsunami modeling applications (Myers and Baptista, 1995, Whitmore, 1993). An array of seismic and fault parameters are utilized as input to dislocation models. Figure 1.3 displays how the subduction zone is represented in such a model and which parameters are provided as input. The locked zone between the two plates is assumed to be rectangular and slanted at a constant dip angle to a specified depth. The strike direction provides the horizontal orientation of the subduction zone, and the amount of slip (U) specifies the amount and direction of movement between the two plates during the subduction earthquake. Instead of relying on a rectangular source, Flück et al. (1997) integrate Okada's point source formulas to permit for spatial variation of the dip angle, depth, width, length, and slip. For any deformation model, though, the quality of the computed displacements will depend on the reliability of these seismic and fault parameters, whether they are spatially varying or constant.

These input parameters for dislocation models are computed by seismological research institutions such as the USGS after an earthquake has occurred. Unfortunately, there is usually significant ambiguity with regards to solutions of these parameters. Myers and Baptista (1995) investigated 11 proposed scenarios of parameters for the July 12, 1993 Hokkaido Nansei-Oki earthquake, each of which produced very different deformation patterns when passed through Okada's rectangular source dislocation model. Subsequently, the numerically modeled waves for each of these scenarios produced a wide range of wave elevation results throughout the Sea of Japan domain. This problem is not unique to this event, and determining which, if any, of the scenarios is correct is difficult to verify from land observations.

Inversion techniques have been proposed as a way in which to better define the seismic source. Instead of computing a seismic source, simulating a tsunami based on that source, and comparing model results with observations, inverse theory evaluates how observations can help determine the most probable seismic source. Generally, the amount of slip between the two plates is used as an unknown value, and values are assumed for the other parameters in the dislocation model. Tide gauge recordings of the tsunami waves are used as the known data values. An optimal amount of slip is then formulated which, when used by the hydrodynamic model as initial conditions, procures a wave propagation consistent with observations at the tide gauges. Inverse theory has been used in calculations of deformation for several events, including tsunamis in Japan (Satake, 1989, Satake, 1993, Takahashi et al. 1995) and Alaska (Johnson et al., 1996, Johnson and Satake, 1993, Johnson and Satake, 1994).

There are several underlying assumptions in using inverse theory with tsunami observations, however, that still leave considerable uncertainty in the seismic source. First, aside from the amount of slip, values for parameters used in the dislocation model are still being assumed. There is still the same ambiguity in deciding what values to assume for these parameters. Second, the inversion erroneously assumes that errors in the hydrodynamic model are small. Significant errors can be generated from a model's spatial and temporal discretization, the representation of bathymetry and topography, tide-tsunami interactions, numerical diffusion, friction parameterization, and shallow water theory assumptions. For tsunami simulations such model errors can be very large, as discussed in Chapters 4 and 5. The inversion embeds such errors into the seismic source. The errors can be large enough such that the final pattern of deformation contains more uncertainties than using the reported amounts of slip provided by seismological agencies after an event.

It is reasonable to conclude, therefore, that tsunami modeling is still an experiment for which the initial conditions are difficult to ascertain. This does not mean that such modeling applications cannot provide useful information. Rather, it beckons the modeler to identify, quantify, and minimize errors in the calculations of deformation and in the hydrodynamic modeling. While this thesis does not examine reasons for ambiguity in reported seismic parameters for earthquakes, Chapter 3 utilizes new methods for calculating the three-dimensional geometry of the subduction zone and the slip vectors within its locked zone. Such approaches better represent the subduction zone processes, which in turn should help minimize errors in calculations of the deformation. Chapters 4 and 5 evaluate sources and sensitivities of errors in the hydrodynamic modeling of tsunamis. By minimizing such errors, numerical modeling solutions can converge on solutions that better depict the true physics governing these events.

As with the regional modeling of tides, a finite element model using the shallow water equations is utilized to simulate tsunamis in this thesis. Many options are available for choosing a numerical modeling technique and a corresponding system of equations. Finite difference methods (FDMs) are a popular alternative to the finite element method (FEM) for regional modeling of tsunamis. For FDMs, terms in the partial differential equations are expanded in Taylor series form, the discretization of which can be solved on a spatially structured grid. FEMs divide the spatial domain into an unstructured grid of triangular elements. Weighted residuals from the governing equations are then defined over each element, the contributions of which are assembled into a global weighted residual statement. Thus, the FEM forces residuals to zero in a global sense, utilizing contributions from each of the triangular elements. FDMs and FEMs generally use either the shallow water equations or the Boussinesq equations. The Boussinesq equations are similar to the shallow water equations, except that the vertical structure of the vertical velocity is not neglected. Thus, higher order terms are represented, permitting for higher frequency components of the wave propagation to be reproduced. Both sets of equations have advantages and disadvantages, and the debate as to which set of equations to use (Murty and Kowalik, 1993) is still inconclusive. However, the errors discussed in later chapters are larger than differences between Boussinesq and shallow water models, thus making such errors a higher priority than the choice of equations. Walters and Takagi (1996) and Imamura (1996) summarize finite element and finite difference tsunami applications, respectively.

Although FEMs and FDMs are usually used in regional tsunami modeling applications, other modeling approaches are available for two-dimensional applications. One of these is the boundary element method (BEM), which is used to solve Laplace's velocity potential equation in conjunction with time integration of the free surface boundary equation (Grilli, 1996). BEM applications are two-dimensional in the vertical and one of the horizontal directions. Marker and cell (MAC) methods have also been used to simulate tsunamis in this two-dimensional setting (Raad, 1996). The vorticity equation is used to represent the conservation of mass, and the Navier-Stokes equations are used to balance the forces in finite difference cells throughout the domain. Pressure is applied to a surface that is tracked using massless markers.

BEM and MAC approaches can be extended to three dimensions, yet as mentioned before, such discretization is not computationally feasible in accurately depicting the physics in tsunami applications. This is a key factor in deciding which model and equations to use for this thesis. Tsunamis are strongly affected by reflection and refraction in the two horizontal dimensions for hours after the initial earthquake. Attempting to represent tsunami events utilizing only one horizontal direction is unreliable. Since three-dimensional tsunami applications are still computationally infeasible, FDM and FEM regional modeling applications remain the most viable tools. This thesis uses finite element models, for the FEM permits for variable grid spacing to be used throughout the spatial domain. As will be shown, grid spacing is a critical component in accurately depicting tsunami waves across a range of frequencies. Some areas of the grid will require more refinement than others, and the FEM allows for the most efficient placement of grid points to account for such differences.

With a finite element approach considered to be the most adept at simulating tsunami events, Chapters 3-5 of this thesis are structured so as to evaluate the model's ability to represent the dynamics of these waves. There are several objectives involved in such an analysis, including the following:

- Effectively use a finite element model to simulate tsunamis which are most likely to be generated from an active subduction zone. The Cascadia subduction zone (CSZ) off the coast of Oregon, Washington, and Vancouver Island presents a useful scenario for examining the utility of finite element simulations of potential tsunamis. Geologic evidence (Atwater et al., 1995) suggests that the CSZ ruptures approximately every 200-600 years and that many of these past events have generated large-scale tsunamis. Dendrochronological evidence has shown that the last CSZ event occurred in the year 1700. Therefore, the threat of future tsunamis poses a significant hazard to coastal communities in these areas. New approaches for estimating the deformation that would result from a future event need to be evaluated. The results of such simulations (wave elevations, velocities, uncertainties) should be made available to communities in a manner which procures effective hazard mitigation efforts.

- Evaluate the factors which most significantly influence modeling efforts of well-documented tsunamis in recent history. While it remains difficult to verify initial conditions for such applications, examinations of the extent of influence from a variety of factors can be determined. By identifying the sensitivity of a model to such a wide range of parameters, the model problem is better defined and systematic approaches to ameliorating the solution can be made. The July 12, 1993 Hokkaido Nansei-Oki and 1964 Alaska tsunamis are selected as test cases, because they are two of the best documented events in recent history.

- Examine in detail the numerical errors that can adversely affect tsunami simulation results. By identifying the most influential factors from above, these can be explored in detail by dissecting the numerical algorithm to search for generating mechanisms of errors. Truncation errors from the discretized shallow water equations and energy errors serve as the tools used in the numerical dissection. Detailed examination of numerical errors can in turn yield insight as to how those errors can be attenuated.

1.4 Organization

This thesis consists of five chapters and an appendix. Chapter 2 presents a regional tide model of the eastern north Pacific Ocean. Inversion techniques are used to determine tidal patterns in a domain stretching from the Aleutian Islands to central California. The sensitivity of the inversion to selected parameters is examined first through the use of a frequency domain model. A final inversion is subsequently performed using a time domain model which depicts better the physical processes in this system. Results are contrasted with global tide models and used as boundary conditions to a local modeling study in the Columbia River.

Chapter 3 focuses on the Cascadia subduction zone and the ability to provide tangible simulations of potential future tsunamis. The deformation for plausible earthquakes is formulated by using new approaches involving geodetic, geologic, and geothermal data. Effects of the simulated tsunamis from California to Vancouver Island are investigated to identify energy focusing mechanisms and patterns of wave elevations and velocities over an eight hour period. The influence of grid refinement on the numerical simulations is introduced, and will be discussed in more detail in subsequent chapters. The coastal communities of Seaside and Newport, Oregon are selected to examine local tsunami inundation effects in detail. Results are presented so as to allow proper management decisions regarding local hazard mitigation.

Chapter 4 examines the sensitivity of a numerical model to a variety of factors. Such factors include the grid refinement, tide and tsunami interactions, the generalized wave continuity equation weighting factor, the time step, friction parameterization, the diffusion coefficient, and the depth near the shoreline. The 1993 Hokkaido Nansei-Oki and 1964 Alaska tsunamis are used to exemplify the lessons which can be learned by evaluating these influencing factors in detail. Energy loss in tsunami simulations is also introduced as a primary culprit in the underprediction of wave amplitudes and misrepresentation of higher frequency components of the waves.

Chapter 5 investigates some of the sources of errors in tsunami simulations from a numerical perspective. Discrepancies between the numerical solution of the shallow water equations and the conservation of energy equation are quantified. Energy error expressions are formulated both globally and for individual grid nodes, the results of which are related to parameters discussed in Chapter 4. Truncation errors from the nonlinear shallow water equations are also derived and contrasted with these same parameters. The energy errors are shown to be more dominant than other errors, and techniques for optimizing parameters such as the grid spacing are composed.

1.5 References

Andersen, O.B., 1995. Global Ocean Tides From ERS1 and TOPEX/POSEIDON Altimetry, *Journal of Geophysical Research*, 100(C12), 25249-25259.

Atwater, B.F., A.R. Nelson, J.J. Clague, G.A. Carver, D.K. Yamaguchi, P.T. Bobrowsky, J. Bourgeois, M.E. Darienzo, W.C. Grant, E. Hemphill-Haley, H.M. Kelsey, G.C. Jacoby, S.P. Nishenko, S.P. Palmer, C.D. Peterson and M.A. Reinhart, 1995. Summary of Coastal Geologic Evidence for Past Great Earthquakes at the Cascadia Subduction Zone, *Earthquake Spectra*, 11(1), 1-18.

Baptista, A.M., M. Wilkin, P. Pearson, P. Turner, C. McCandlish, P. Barrett, S. Das, W. Sommerfield, M. Qi, N. Nangia, D. Jay, D. Long, C. Pu, J. Hunt, Z. Yang, E. Myers, J. Darland and A. Farrenkopf, 1998. Towards a Multi-Purpose Forecast System for the Columbia River Estuary, submitted to *Ocean Community Conference*, Marine Technology Society, Baltimore, MD.

Camfield, F.E., 1990. *Tsunami*, Handbook of Coastal and Ocean Engineering, Volume 1 Wave Phenomena and Coastal Structures, Gulf Publishing Company, Houston, TX, 591-633.

Desai, S.D. and J.M. Wahr, 1995. Empirical Ocean Tide Models Estimated From TOPEX/POSEIDON Altimetry, *Journal of Geophysical Research*, 100(C12), 25205-25338.

Doodson, A.T., 1921. The Harmonic Development of the Tide-Generating Potential, *Proceedings of the Royal Society of London*, Ser. A 100, 306-328.

Eanes, R.J. and S.V. Bettadpur, 1994. Ocean Tides From Two Years of TOPEX/POSEIDON Altimetry (abstract), *EOS Transactions, AGU*, 75(44), 61.

Egbert, G.D., A.F. Bennett and M.G.G. Foreman, 1994. TOPEX/POSEIDON Tides Estimated Using a Global Inverse Model, *Journal of Geophysical Research*, 99(C12), 24821-24852.

Flück, P., R.D. Hyndman and K. Wang, 1997. Three-Dimensional Dislocation Model for Great Earthquakes of the Cascadia Subduction Zone, *Journal of Geophysical Research*, 102(B9), 20539-20550.

Foreman, M.G.G., 1977. *Manual for Tidal Heights Analysis and Prediction*, Pacific Marine Science Report 77-10, Institute of Ocean Sciences, Victoria, B.C.

Godin, G., 1972. *The Analysis of Tides*, University of Toronto Press, Toronto, CA.

Grilli, S., 1996. Fully Nonlinear Potential Flow Models Used for Long Wave Runup Prediction, *Long-Wave Runup Models*, World Scientific, Singapore, 116-180.

Holdahl, S.R. and J. Sauber, 1994. Coseismic Slip in the 1964 Prince William Sound Earthquake: A New Geodetic Inversion, *Pure and Applied Geophysics*, 142(1), 55-82.

Hyndman, R.D. and K. Wang, 1993. Thermal Constraints on the Zone of Major Thrust Earthquake Failure: The Cascadia Subduction Zone, *Journal of Geophysical Research*, 98(B2), 2039-2060.

Imamura, F., 1996. Review of Tsunami Simulation with a Finite Difference Method, *Long-Wave Runup Models*, World Scientific, Singapore, 25-42.

Ip, J.T.C. and D.R. Lynch, 1995. Comprehensive Coastal Circulation Simulation Using Finite Elements, Nonlinear Prognostic Time-Stepping Model, *QUODDY3 User's Manual*, Dartmouth College, Report Number NML95-1.

Jay, D.A. and E.P. Flinchem, 1997. Interaction of Fluctuating River Flow with a Barotropic Tide: A Demonstration of Wavelet Tidal Analysis Methods, *Journal of Geophysical Research*, 102(C3), 5705-5720.

Johnson, J.M. and K. Satake, 1993. Source Parameters of the 1957 Aleutian Earthquake from Tsunami Waveforms, *Geophysical Research Letters*, 20(14), 1487-1490.

Johnson, J.M. and K. Satake, 1994. Rupture Extent of the 1938 Alaskan Earthquake as Inferred from Tsunami Waveforms, *Geophysical Research Letters*, 21(8), 733-736.

Johnson, J.M., K. Satake, S.R. Holdahl and J. Sauber, 1996. The 1964 Prince William Sound Earthquake: Joint Inversion of Tsunami and Geodetic Data, *Journal of Geophysical Research*, 101(B1), 523-532.

Kinnmark, I., 1986. *The Shallow Water Wave Equations: Formulation, Analysis and Application*, Springer-Verlag, Berlin.

Komar, P.D., 1992. Ocean Processes and Hazards Along the Oregon Coast, *Coastal Natural Hazards: Science, Engineering, and Public Policy*, Oregon Sea Grant ORESU-B-92-001, 38-73.

Kumaki, Y., J. Kisanuki, T. Ohtani, Y. Ono and S. Kajikawa, 1993. Vertical Seismic Crustal Movement of the 1993 Hokkaido Nansei-Oki Earthquake Based on Coastal Landform Changes in the Okushiri Island, West of Hokkaido, Japan, *Meeting of the Seismological Society of Japan*, A63, 63 (in Japanese).

LeBlond, P.H. and L.A. Mysak, 1978. *Waves in the Ocean*, Elsevier Scientific Publishing Company, Amsterdam.

LeProvost, C., M.L. Genco, F. Lyard, P. Vincent and P. Canceil, 1994. Spectroscopy of the World Ocean Tides from a Finite-Element Hydrodynamic Model, *Journal of Geophysical Research*, 99(C12), 24777-24797.

Luettich, R.A., J.J. Westerink and N.W. Scheffner, 1991. *An Advanced Three-Dimensional Circulation Model for Shelves, Coasts, and Estuaries*, Dept. of the Army, U.S. Army Corps of Engineers, Washington, D.C.

Lyard, F.H., 1997. The Tides in the Arctic Ocean from a Finite Element Model, *Journal of Geophysical Research*, 102(C7), 15611-15638.

Matsumoto, K., M. Ooe, T. Sato and J. Segawa, J., 1995. Ocean Tide Model Obtained From TOPEX/POSEIDON Altimetry Data, *Journal of Geophyical Research*, 100(C12), 25319-25330.

Murty, T.S. and Z. Zowalik, 1993. Use of Boussinesq Versus Shallow Water Equations in Tsunami Calculations, *Marine Geodesy*, 16(2), 149-151.

Myers, E.P. and A.M. Baptista, 1995. Finite Element Modeling of the July 12, 1993 Hokkaido Nansei-Oki Tsunami, *Pure and Applied Geophysics*, 144(3/4), 769-801.

Okada, Y., 1985. Surface Deformation Due to Shear and Tensile Faults in a Half-Space, *Bulletin of the Seismological Society of America*, 75(4), 1135-1154.

Okada, Y., 1992. Internal Deformation Due to Shear and Tensile Faults in a Half-Space, *Bulletin of the Seismological Society of America*, 82(2), 1018-1040.

Oliveira, A.P. and A.M. Baptista, 1997. Diagnostic Modeling of Residence Times in Estuaries, *Water Resources Research*, 33(8), 1935-1946.

Pugh, D.T., 1987. *Tides, Surges and Mean Sea Level*, John Wiley & Sons Ltd., Chichester.

Raad, P., 1996. Modeling Tsunamis with Marker and Cell Methods, *Long-Wave Runup Models*, World Scientific, Singapore, 181-203.

Ray, R.D., B.V. Sanchez and D.E. Cartwright, 1994. Some Extensions to the Response Method of Tidal Analysis Applied to TOPEX/POSEIDON Altimetry (abstract), *EOS Transactions, AGU*, 75(16), 108.

Sanchez, B.V. and N.K. Pavlis, 1995. Estimation of Main Tidal Constituents From TOPEX Altimetry Using a Proudman Function Expansion, *Journal of Geophysical Research*, 100(C12), 25229-25248.

Satake, K., 1989. Inversion of Tsunami Waveforms for the Estimation of Heterogeneous Fault Motion of Large Submarine Earthquakes: The 1968 Tokachi-oki and 1983 Japan Sea Earthquakes, *Journal of Geophysical Research*, 94(B5), 5627-5636.

Satake, K., 1993. Depth Distribution of Coseismic Slip Along the Nankai Trough, Japan, From Joint Inversion of Geodetic and Tsunami Data, *Journal of Geophysical Research*, 98(B3), 4553-4565.

Schwiderski, E.W., 1980a. On Charting Global Ocean Tides, *Reviews of Geophysics and Space Physics*, 18(1), 243-268.

Schwiderski, E.W., 1980b. Ocean Tides I, A Global Ocean Tidal Equations, *Marine Geodesy*, 3, 161-217.

Schwiderski, E.W., 1980c. Ocean Tides II, A Hydrodynamic Interpolation Model, *Marine Geodesy*, 3, 219-255.

Sommerfield, W.N. and A.M. Baptista, 1998. Variability of Residual Properties in the Columbia River Estuary, (in preparation for *Water Resources Research*).

Takahashi, To., Ta. Takahashi, N. Shuto, F. Imamura and M. Ortiz, 1995. Source Models for the 1993 Hokkaido Nansei-Oki Earthquake Tsunami, *Pure and Applied Geophysics*, 144(3/4), 747-767.

Walters, R. and T. Takagi, 1996. Review of Finite Element Methods for Tsunami Simulations, *Long-Wave Runup Models*, World Scientific, Singapore, 43-87.

Westerink, J.J., R.A. Luettich, A.M. Baptista, N.W. Scheffner and P. Farrar, 1992. Tide and Storm Surge Predictions Using a Finite Element Model, *ASCE Journal of Hydraulic Engineering*, 118(10), 1373-1390.

Whitmore, P.M., 1993. Expected Tsunami Amplitudes and Currents Along the North American Coast for Cascadia Subduction Zone Earthquakes, *Natural Hazards*, 8(1), 59-73.

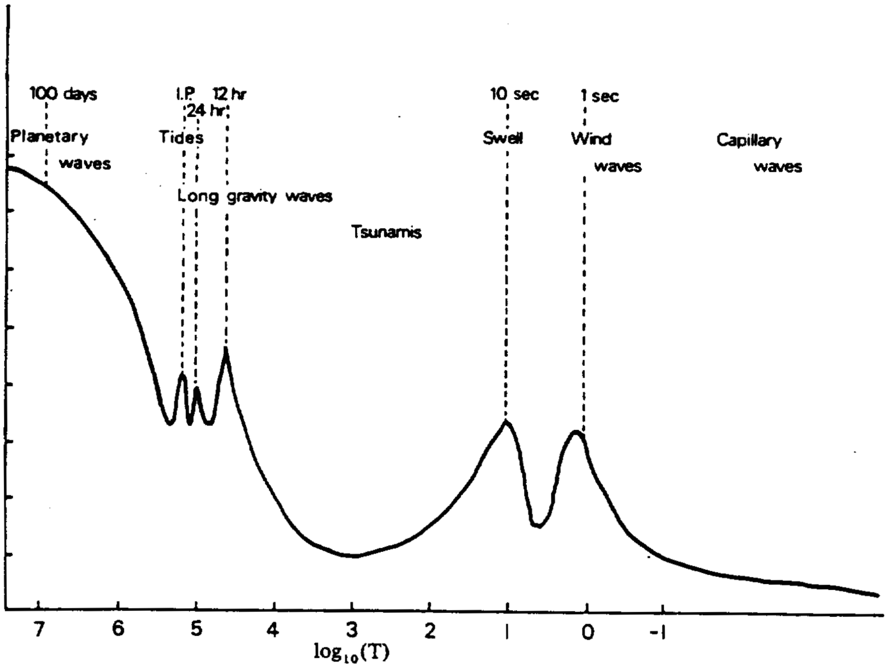

Figure 1.1 Energy spectrum of ocean waves (extracted from LeBlond and Mysak, 1978 with permission from the authors).

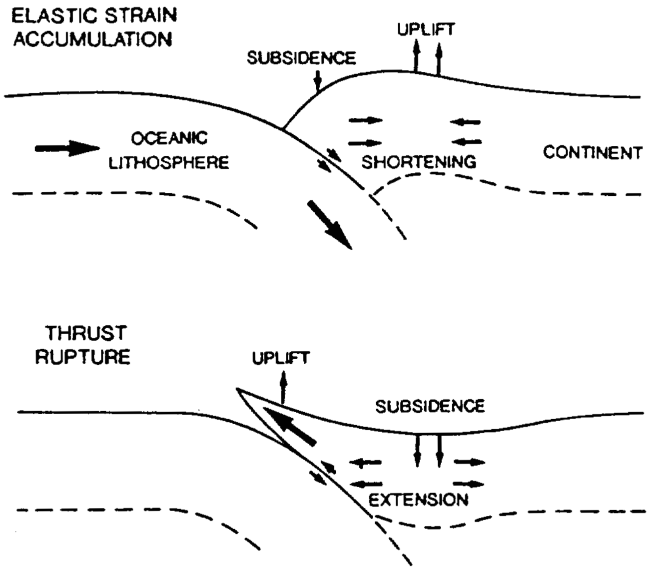

Figure 1.2 Plate subduction and deformation cycles (extracted from Hyndman and Wang, 1993 with permission from the Journal of Geophysical Research).

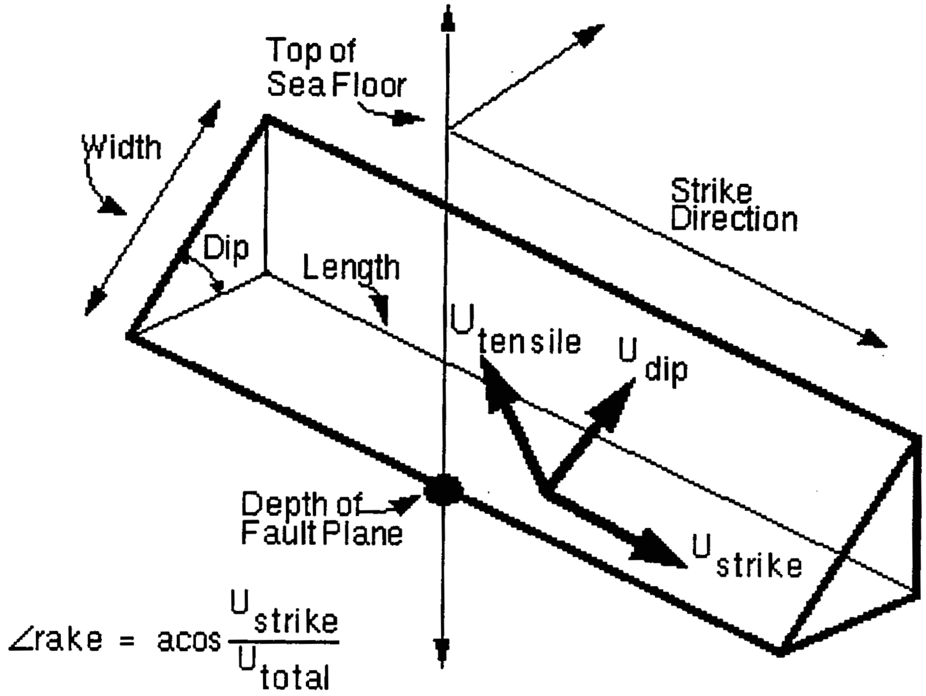

Figure 1.3 Representation of the subduction zone in fault dislocation models.

CHAPTER 2

Inversion for Tides in the Eastern North Pacific Ocean

2.1 Introduction

Modeling of ocean tides provides an ideal experiment for exploring the ability to manifest the physics of the oceans through the use of numerical models. The periodic nature of tides consists of a set of known residual gravitational forces of the sun and moon acting upon the earth, and the hydrodynamic equations which govern the manner in which incompressible fluids respond to Newton's laws are well recognized. Translating this information into a numerical model requires discretization of the oceanic domain such that the bathymetry and coastlines are realistic and conform to certain numerical constraints, quantifying the effects of friction and diffusion, determining boundary conditions representative of the spatially varying periodicity of the tides, and solving the discretized (in space and time) form of the hydrodynamic equations.

This paper presents the results of a regional tide modeling study of the Eastern North Pacific Ocean (Figure 2.1). Bathymetry for this region consists of deep abyssal plain features, the continental slope and shelf, and littoral zones. The deep waters are often interrupted by seamounts including the Gilbert, Patton, Gulf of Alaska, Kodiak, Hodgkins, and Dellwood seamounts. Amplitudes for the astronomic tides generally increase in a northeasterly direction and tend to propagate in a counter-clockwise direction with respect to the coastline. The O_1 and K_1 constituents have amphidromes located roughly near the middle of the Pacific Ocean (not within the domain considered here), and the M_2 and S_2 have amphidromes near the southeast portion of the region shown in Figure 2.1. More local amphidromes may exist as well, such as the M_2 amphidrome located near the southeast corner of Vancouver Island (Foreman et al., 1995). In order to understand the need for this regional modeling study of tides, it is instructive to review past modeling studies of large-scale tide patterns.

Numerical models have increasingly been used ever since Schwiderski (1980a-c) quantitatively demonstrated the ability to model global ocean tides to within a 10 cm root mean square (RMS) error limit in the open ocean. Schwiderski used a $1° \, x \, 1°$ finite difference grid for which errors were most likely introduced by the representation of the bathymetry and coastlines. Nevertheless, Schwiderski's representation of energy redistribution along the continental slope and shelf through the inclusion of interpolated empirical data in the hydrodynamic equations helped facilitate accurate model predictions at pelagic tide gauges.

More recently, satellite altimeter data have become accessible through the Geosat, ERS 1, and TOPEX/POSEIDON missions. Cartwright and Ray (1990) developed a model of global diurnal and semidiurnal tidal constituents using empirical analysis of the Geosat Exact Repeat Mission altimetric data. RMS differences between this model and that developed by Schwiderski are as large as 15 cm, depending upon the location. Molines et al. (1994) showed that for open ocean tide gauge positions, the Cartwright and Ray model has an average RMS difference of about 6 cm. They also show that for the Pacific Ocean, both models are approximately equivalent in terms of RMS differences.

While Schwiderski used a numerical model and Cartwright and Ray used analysis of altimetric data to map the world's tides, a new class of global models has emerged which utilize both of these approaches. Le Provost et al. (1994) developed a finite element model which employs an inversion technique to optimize solutions with respect to tide gauge data and data assimilation to improve ocean tide results. Zahel (1995) used a least-squares technique to optimize the combination of data assimilation with finite difference model results. Egbert et al. (1994) directly inverted the TOPEX/POSEIDON data in a least squares manner with respect to the governing hydrodynamic equations. Numerical models taking advantage of inversion techniques with assimilated data have been able to improve the ability to reproduce tidal patterns and observations at open ocean tide gauges.

Global tide models are weakest nearshore, due to the difficulty of discretizing a very large domain and of representing the generation of nonlinear constituents in coastal environments. This translates into a weaker depiction of the continental slope and littoral zone processes due to errors in representing the bathymetry and coastline. Since much of the energy redistribution between various frequencies is occurring as the tides are propagating from the deeper water into coastal environments along the continental slope, global tide models are not the most appropriate tools to portray tidal processes in these zones. Further, since most local modeling studies are generally constrained to littoral regions, an effective tool is needed to link processes occurring in the open ocean and those occurring in more local environments. Regional tide models such as Baptista et al. (1989) and Westerink et al. (1992) have proven effective at bridging this gap between pelagic and littoral regions. A similar regional model is presented here for the eastern north Pacific Ocean.

Two finite element hydrodynamic models were utilized in this regional inversion study. Both are based on unstructrured grids, enabling variable resolution and thus potentially facilitating the transition between a coarser representation of the deeper ocean and a finer representation of nearshore environments. A description of these models and their governing equations is provided in the next section. The inverse tidal method is also reviewed to demonstrate the manner in which open boundary conditions are determined. Results from the inversion with a frequency domain model are then presented, with the emphasis of these results being placed on the sensitivity of the inversion process to selected parameters. The knowledge gained from these tests is then used in a final inversion for tidal constituents with a time domain model. These modeling results are contrasted with observations and with the results of selected global tide models. Spatial patterns of amplitudes and phases are also presented for the final inversion results and for how these results differ from global tide models.

2.2 The Numerical Models

Two finite element models (TIDE2D, Walters 1987; ADCIRC, Luettich et al., 1991) of the depth-averaged shallow water equations are used to simulate tides in this study. The shallow water equations are derived by integrating the Navier-Stokes equations vertically from the free surface to the bottom of the water column. The key assumptions in using this set of equations are that the depth scale is much less than the horizontal scales and that pressure is hydrostatic (thus neglecting accelerations associated with the vertical velocity). Both of these assumptions are valid for tidal simulations. The shallow water equations are written as follows,

$$\frac{\partial \eta}{\partial t} + \nabla \bullet [u(H + \eta)] = 0 \qquad (1)$$

$$\frac{\partial u}{\partial t} + u \bullet \nabla u + f \times u + g \bullet \nabla \eta + \tau_b = 0 \qquad (2)$$

where η is the elevation, u is the depth-averaged velocity, H is the water column depth, f is the coriolis vector, g is the gravitational acceleration, and τ_b is the bottom friction.

TIDE2D is formulated in the frequency domain whereby the elevation and depth-averaged velocity are expressed as a summation of a time-independent constant (subscript 0) and a periodic component (subscript n):

$$\eta(x, y, t) = \eta_0(x, y) + \frac{1}{2} \sum_{n=-N}^{N} \eta_n(x, y) \exp(-i\omega_n t) \qquad (3)$$

$$u(x, y, t) = u_0(x, y) + \frac{1}{2} \sum_{n=-N}^{N} u_n(x, y) \exp(-i\omega_n t) \qquad (4)$$

where ω_n is the n^{th} tidal frequency. Substitution of (3) and (4) into the shallow water equations eliminates the time dependence (t) and leads to the following,

$$-i\omega_n \eta_n + \nabla \bullet \left\{ \left[\frac{gH}{q_n^2 + f^2} \right] [q_n(\nabla \eta_n - T_n) - f \times (\nabla \eta_n - T_n)] \right\} - \nabla \bullet W_n = 0 \qquad (5)$$

$$(-i\omega_n + \tau)u_n + f \times u_n + g\nabla \eta_n = gT_n \qquad (6)$$

where $q_n = -i\omega_n + \tau$, τ is the time-independent friction component, W_n is the nonlinear wave drift term from the continuity equation, and gT_n represents the nonlinear advection and bottom friction terms from the momentum equations. The latter two terms are expressed as follows,

$$W_n = -\frac{1}{2}\sum_{i,j} \eta_i u_j \tag{7}$$

$$T_n = -\frac{1}{2g}\sum_{i,j} u_i \bullet \nabla u_j - \frac{\tau_b'}{g} + \frac{\tau_b''}{g} \tag{8}$$

The bottom friction contribution to the momentum equations can be expressed as (expanded to the right in a Taylor series),

$$\tau_b = \frac{\left(c_f\sqrt{u \bullet u}\right)u}{H+\eta} = \left(\frac{1}{H}\right)\left(1 - \frac{\eta}{H} + \ldots\right)\left(\tau u + \tau_b' + \tau_b'' + \ldots\right) \tag{9}$$

where c_f is a dimensionless friction coefficient, $\tau = \frac{c_f \lambda}{H}$, and λ is defined as,

$$\lambda = \frac{1}{2}\left[\sum_j u_j \bullet u_{-j} + 4u_0^2\right]^{1/2} \tag{10}$$

Finally, the secondary and tertiary expanded friction terms are given by,

$$\tau_b' = \frac{c_f}{8H\lambda}\sum_{ijm,i\neq j}\left(u_i \bullet u_j\right)u_m \tag{11}$$

$$\tau_b'' = \frac{-c_f}{128H\lambda^3}\sum_{ijpqm,i\neq j,p\neq -q}\left(u_i \bullet u_j\right)\left(u_p \bullet u_q\right)u_m \tag{12}$$

The bottom friction coefficient may be approximated using either a Manning or a Chezy formulation. Equations (5) and (6) are approximated using a Galerkin finite element treatment where η (using the continuity equation) and u (using the momentum equations) are solved for in an iterative convergent manner.

ADCIRC differs from TIDE2D in that it is a time domain model of the depth-averaged shallow water equations rather than a frequency domain model. ADCIRC has the capability of representing the process of inundation (Luettich and Westerink, 1995a-b), a feature not available in TIDE2D. TIDE2D also does not permit spatially varying coriolis factors or the inclusion of tidal potential forcings, both of which are accounted for in ADCIRC. TIDE2D was used in the sensitivity tests because it is less computationally demanding and can therefore be used to test a wide range of sensitivities to selected parameters. Because ADCIRC is able to better represent the physics, though, it is used for the final inversion results. While TIDE2D relies on the primitive continuity equation to represent mass preservation, ADCIRC uses a generalized wave continuity equation (GWCE) in its place. The GWCE is formulated by adding the time derivative of the continuity equation, the primitive continuity equation weighted by a factor, and the spatial gradient of the conservative momentum equations. The GWCE is used to solve for surface elevations, while the nonconservative form of the momentum equations are used to solve for depth-averaged velocities. These equations are shown below:

$$\begin{gathered}
\frac{\partial^2\eta}{\partial t^2}+G\frac{\partial\eta}{\partial t}-\frac{\partial^2\gamma}{\partial t^2}-G\frac{\partial\gamma}{\partial t}+\\
\frac{\partial}{\partial x}\left\{u\frac{\partial\eta}{\partial t}-uH\frac{\partial u}{\partial x}-vH\frac{\partial u}{\partial y}+fvH-H\frac{\partial}{\partial x}\left[\frac{p_s}{\rho_0}+g(\eta-\alpha\Psi)\right]\right\}+\\
\frac{\partial}{\partial x}\left\{-E_h\frac{\partial^2\eta}{\partial x\partial t}+\frac{\tau_{sx}}{\rho_0}-(\tau-G)uH\right\}+\\
\frac{\partial}{\partial y}\left\{v\frac{\partial\eta}{\partial t}-uH\frac{\partial v}{\partial x}-vH\frac{\partial v}{\partial y}-fuH-H\frac{\partial}{\partial y}\left[\frac{p_s}{\rho_0}+g(\eta-\alpha\Psi)\right]\right\}+\\
\frac{\partial}{\partial y}\left\{-E_h\frac{\partial^2\eta}{\partial y\partial t}+\frac{\tau_{sy}}{\rho_0}-(\tau-G)vH\right\}=0
\end{gathered}\tag{13}$$

$$\begin{gathered}
M\equiv\frac{\partial\bar{u}}{\partial t}+\bar{u}\bullet\nabla\bar{u}+\vec{f}\times\bar{u}+\tau\bar{u}+\nabla\left[\frac{p_s}{\rho_0}+g(\eta-\alpha\Psi)\right]+\\
\frac{E_h}{H}\left[\frac{\partial^2 uH}{\partial x^2}+\frac{\partial^2 vH}{\partial y^2}\right]+\frac{\tau_{sx}}{\rho_0 H}=0
\end{gathered}\tag{14}$$

where η is the free surface elevation, (u, v) are the depth-averaged velocities, H is the total water column, G is a weighting factor, γ is the bottom deformation (positive for uplift), f is the Coriolis factor, α is the effective Earth elasticity factor, Ψ is the Newtonian equilibrium tide potential, E_h is the horizontal eddy diffusion coefficient, $\tau_{s\bar{x}}$ is the applied free surface stress, τ is the bottom friction, c_f is the bottom friction coefficient, p_s is the atmospheric pressure at the free surface, ρ_0 is the reference density of water, and g is the acceleration due to gravity. A Manning formulation is used to represent bottom friction.

TIDE2D and ADCIRC are used to simulate tides for given boundary conditions. A free-slip condition is imposed at land boundary interfaces, while amplitudes and phases are enforced as a Dirichlet condition at the open ocean. Open ocean boundary conditions may be determined in several manners. If the boundary points are contained within the domain of another reliable tidal model, the boundary conditions may be interpolated from the larger model. If the boundary points happen to coincide with actual tide gauge locations, then harmonic data from those gauges may be used as boundary conditions. Finally, tidal data from the interior of the domain may be used through inverse theory to determine amplitudes and phases at the boundary.

Inverse theory is used here to determine boundary forcings for the constituents of interest. The inverse tidal method (ITM), developed by Nunez (1990), uses a least-squares fitting technique to match tidal observations with numerical simulations. Amplitudes and phases of the tidal constituents along the boundary are treated as unknowns, and harmonic analysis of elevations at interior tide gauges represent known values for a particular tidal system. It is desirable to have the number of known values be greater or equal to the number of unknowns. Therefore, the number of tide gauges should be at least equal to the number of constituents. ITM uses singular value decomposition for the case where the number of knowns is greater than the number of unknowns.

The inversion begins with an initial guess in which a set of assumed amplitudes and phases are used as boundary conditions in a fully nonlinear simulation. For selected tide gauges, the differences between the model's results from the nonlinear guess and the tide gauge observation will represent the known value, y_i, or

$$y_i = (\text{nonlinear guess})_i - (\text{known observational data})_i \tag{15}$$

The inversion then tries to represent these known values at each of the i stations as a weighted combination of transfer functions. A transfer function is a linear tidal simulation using a pre-determined boundary condition. The simulation is linear because its results are used in the singular value decomposition, a linear process in itself. The choice of transfer functions should be unique enough such that their linear combination is able to reproduce differences between observed tide gauge data and a nonlinear simulation guess. If $\varphi_j(t_i)$ is the transfer function response at station i, then the difference between the weighted combinations of transfer functions and the known value is represented as:

$$\Delta_i = \sum_{j=1}^{N} c_j \varphi_j - y_i \tag{16}$$

The objective of the inversion is to minimize, in a least squares sense, these differences:

$$\frac{\partial^2 \Delta}{\partial c_k} = 0, \quad k = 1, N \tag{17}$$

where

$$\Delta = \left(\sum_{i=1}^{M} \left(\sum_{j=1}^{N} c_j \varphi_j(t_i) - y_i \right)^2 \right)^{1/2} \tag{18}$$

M is the number of stations and N is the number of transfer functions. The weights, c_j, are the unknowns in this system of equations. Once these weights are solved for, the initial guess boundary conditions are corrected by adding on these same weights multiplied by the transfer functions along the boundary. This new boundary condition is then used to create a new initial guess simulation. The inversion will converge on the best solution as the corrections approach zero.

2.3 Setup of the Domain

Two finite element grids were used throughout the course of this study. The first grid (Figure 2.2) used in the sensitivity tests with TIDE2D consists of 11,167 nodes and 16,990 elements and has an open ocean boundary which extends in a straight line from the Aleutian Islands to central California. The final inversion results are simulated with ADCIRC on the second grid (Figure 2.3). The open boundary in this grid has a north-south component running along the 165°W meridian and an east-west leg along the 35°N parallel. Added refinement (45780 nodes, 81979 elements) permits a better depiction of the bathymetry, and thus of the physics. One of the advantages of using a finite element grid and model is that more refinement can be placed in shallower areas, to account for the smaller wavelengths associated with the bathymetric change, compound tides, and overtides.

The grids cover a domain consisting of abyssal regions, the continental slope, and the continental shelf, thus permitting an accurate representation of the transition in wave behavior as the tides approach the coastline. Many of the coastal channels and rivers are represented in this grid, although the bathymetry in such local thoroughfares is not well depicted. Several different bathymetric databases were utilized in determining nodal depths. These included marine gravity anomaly data from satellite altimetry (Sandwell and Smith, 1997) digitized NOAA/NOS hydrographic charts, NOAA/NOS raw bathymetric data, and NOS/EEZ data. Tidal data from 305 tide gauges in this region (Figure 2.1) were collected into a database either for use in the inversion or for comparison with results. Most of these tide gauges are located in coastal regions, but there are also several bottom pressure recorders distributed in the pelagic regions.

2.4 Parameter Sensitivity of the Inversion

Inversion for tidal boundary conditions is sensitive to a myriad of factors. Some of these factors are unique to the inverse tidal method, including the choice of transfer functions and tide gauges to be utilized by the inversion. Since the inversion is essentially a least-squares minimization problem, it is important to note that there are innumerable combinations of tide gauge data and transfer functions which could potentially lead to a wide range of solutions. Evaluating the performance of the inversion under varying conditions can help in converging upon a sound strategy for inverting for the final boundary conditions.

The selection of transfer functions is a critical first step for applying inverse methods in the solution for open boundary conditions. These building blocks of the boundary condition must be able to represent the spatial variability of tidal forcing. Each transfer function consists of a set of amplitudes and phases that are imposed at the boundary in a linear simulation using TIDE2D. For each frequency, the inverse tidal method will seek the least-squares linear combination of transfer function results which matches the tide gauge data at certain selected locations. For the purposes of this sensitivity test, the gauges used for the inversion (nine were used) are all located in generally open ocean regions so as to avoid coastal effects and much of the compound and overtide generation from the astronomic frequencies.

The first tidal inversion attempted to use thirteen transfer functions in determining boundary conditions for the O_1, K_1, M_2, and S_2 tidal constituents. While only these four constituents were targeted in the inversion, the hydrodynamic simulations were designed to allow generation of the M_4, MS_4, M_6, $2MS_6$, and MO_3 constituents as well. The transfer functions consisted of either linearly varying or constant amplitude or phase (i.e. in various combinations) profiles over the entire open ocean boundary of the first grid as well as over quarter segments of the boundary, as shown in Figure 2.4. Results from this inversion were unsuccessful, as exemplified in a plot of isolines of amplitude and phase in Figure 2.5 for the M_2 tidal frequency. Also shown in Figure 2.5 are time histories of elevation errors between the model results and observations at the tide gauges which were used in the inversion. The inversion is constraining the elevation errors to reasonable values, but the isolines of amplitude and phase clearly show that the regional tidal patterns are in disarray.

The inversion with these 13 transfer functions appears to be attempting to force the numerous functions to fit the data, losing a realistic representation of the physics in the process. To test this idea, a simpler set of transfer functions was used for the next inversion (with the same grid and selection of tide gauges). This time, three transfer functions were used: 1) constant amplitude and constant phase, 2) constant amplitude and negative linearly varying phase, and 3) constant amplitude and positive linearly varying phase. These transfer functions are shown as the first three functions in Figure 2.4. Each varied over the entire open ocean boundary, and because the elevations are represented as a complex number that is a function of both amplitude and phase, this combination of transfer functions should be capable of representing the varying nature of both amplitudes and phases along the boundary. The results from this inversion are shown in Figure 2.6, and as may be seen, regional M_2 patterns are more realistic. Therefore, reducing the complexity of the inversion by utilizing a simpler set of linear transfer functions permitted a better reproduction of tidal patterns.

The nine tide gauges used in the above transfer function sensitivity tests are located in relatively open ocean waters in order to avoid coastal interference with the tides as well as to capture as much of the astronomic tide signal as possible. To test whether or not inclusion of coastal tide gauges in the inversion adversely or advantageously affects the final results, two new inversions were constructed. These new inversion tests use the same set of three transfer functions discussed above. The only difference is the selection of tide gauges used for the inversion. The first of these new inversions is designed to use the previously used nine tide gauges as well as an additional nine gauges which are each located alongshore in coastal areas. The second inversion attempts to utilize all tide gauges located within the interior of the grid domain, a total of 270 tide gauges.

Figures 2.7 and 2.8 show the isolines of M_2 amplitude and phase, including time histories of elevation errors at selected tide gauges for these two inversion tests. The elevation errors are seen to increase with the added coastal tide gauges used in the inversion. The errors using all 270 stations (Figure 2.8) are larger than those from the inversion with 18 tide gauges (Figure 2.7), which are in turn worse than the inversion with the original nine gauges (Figure 2.6). The inversion with all of the tide gauges was so inaccurate that the M_2 coamplitude lines show an amphidrome to erroneously form along the northern portion of the boundary. There are a couple of explanations for the inefficacy of the inversion with more coastal tide gauges. First, as the number of knowns (i.e. tide gauge data) becomes much greater than the number of unknowns (amplitudes and phases for the constituents), the condition number in the singular value decomposition worsens and makes an accurate solution less feasible. Second, many of the local features at a coastal tide gauge are often not incorporated in a regional grid at this scale. Thus, it is recommended that the number of tide gauges used in the inversion should be similar to the number of frequencies being inverted for, and only those gauges which are known to be unobstructed by local features not accounted for in the grid should be used.

While the selection of transfer functions and tide gauges is specific to the inversion, there are other modeling factors that will affect the quality of the results. These include the representation of the bathymetry, the selection of coordinate transformations, and the choice of model input parameters. Model input parameters include the amount of friction along the seafloor, the diffusion coefficients, and the GWCE weighting factor (for ADCRIC). The bathymetry for the grids was collected from as many reliable sources as possible. However, there may be errors associated with merging data which have been collected in different manners and at different times. In addition, bathymetry is generally referenced to a local MLLW at the time of the data collection, yet corrections between this MLLW and MSL for a variety of bathymetry databases are often difficult to ascertain. Coordinate transformations are critical for regional modeling applications. Most transformations rely on the definition of a center point for the region of interest. Choosing too large or too small a center point latitude may lead to poor spatial approximations and resultant errors in the solution. Sensitivity tests were performed and showed that a center point of 141°W and 44.25°N in a Carte Parallelogrammatique Projection (Pearson, 1990) proved effective at capturing the spatial scales of interest for this region. A Manning friction coefficient of 0.0263 $s \cdot m^{-1/3}$ was used, based upon sensitivity tests performed by Baptista et al. (1989). No diffusion was added in the simulations, in order to avoid overly damping the solution. Finally, a GWCE weighting factor was selected based upon selection criteria presented in Kolar et al. (1994).

2.5 Final Inversion Results

The final inversion results are generated using the information gained from the above sensitivity tests. The finite element model, ADCIRC, is used to model the hydrodynamics in this final inversion. Calculations are now carried out on the second finite element grid, shown in Figure 2.3. This grid extends further into the deep ocean and also has added refinement to reproduce both bathymetric changes and physical processes to a higher degree. As mentioned, the use of ADCIRC permits the inclusion of the tidal potential forcing, variable coriolis effects, and the ability to facilitate inundation. Because ADCIRC is a time domain model, results at the end of each run are harmonically analyzed for amplitudes and phases of the pertinent frequencies. The open ocean boundary is forced with the O_1, K_1, Q_1, P_1, K_2, N_2, M_2, and S_2 tidal constituents. The simulations are fully nonlinear and therefore permit for the generation of all possible overtides and compound tides.

Since the open ocean boundary now consists of two straight line segments, a set of three slightly different linear functions are used (Figure 2.9). The first has the amplitude and phase linearly increasing with latitude along the 165°W meridian, the second has them linearly increasing with longitude along the 35°N parallel, and the third has linear variations along both segments yet in opposite directions as the first two functions. The maximum values of 1.0 for these transfer functions are actually multiplied first by a factor of 20% for the amplitudes and 0.3% for the phases of each of the forcing frequencies. The boundary amplitudes and phases are subsequently multiplied by amplitudes and phases extracted from the TPXO.3 global tide model (Egbert et al., 1994). The theory here is to commence the inversion with the initial conditions of this global tide model, and to design the transfer functions so as to allow efficient changes to those boundary conditions to be calculated.

The transfer functions were thus calculated using these three boundary conditions in separate linear simulations. Differences between nonlinear simulation results and tide gauge observations will therefore be approximated by a least-squares fit of a weighted combination of these transfer function results at the tide gauges. The tide gauges selected for comparative purposes in this inversion are displayed in Figure 2.10. Several of these locations are the same as those used in the final sensitivity tests. The new locations are ones for which data was not available at the time of the sensitivity tests, but whose addition was considered to ameliorate the solution. In all, two of the tide gauges are located in unobstructed coastal waters, two are in the vicinity of continental slopes, and the rest are situated in pelagic regions. While the selected tide gauges and the transfer functions for this final inversion are slightly different than the final conditions derived from the sensitivity tests, the strategy of their setup is essentially equivalent.

The next step in the inversion is to conduct a nonlinear ADCIRC simulation with an assumed set of boundary conditions. The result of this simulation will be compared with observations at the selected tide gauges, and differences between the two will be computed. A weighted combination of the transfer functions will then be fitted in a least-squares sense to these differences. These weights may then be applied to the values of the transfer functions along the open ocean boundary, and a new set of boundary conditions for the next nonlinear simulation are derived. The process is repeated until the nonlinear simulations have converged upon a solution.

The boundary conditions assumed for the first nonlinear simulation are extracted from TPXO.3. As previously mentioned, the transfer functions have been constructed so as to permit quick convergence to changes from this global model solution. Such changes from the global model will most likely be associated with the increased grid resolution in this regional model inversion, although it is also possible that differences in modeling approaches could be imbedded within such changes as well.

Four inversions were performed before the results were considered to have converged upon their final solution. Changes in boundary conditions from each inversion are displayed in Figure 2.11 for the frequencies forced along the open ocean boundary. The changes represent the amplitude difference between the new amplitudes from this inversion and the old amplitudes from the previous inversion (or initial run for the first inversion). Thus, by the third and fourth inversions the changes for each frequency were minimal, indicating solution convergence. The sum of all these changes for each constituent represent the total change in the boundary amplitude from the original TPXO.3 boundary conditions. As may be seen, the K_1 constituent shows the largest discrepancies with a maximum amplitude difference of 19 cm. Differences for the M_2 and S_2 were on the order of several centimeters, while those of the O_1, K_2, and N_2 were approximately one centimeter. Changes for the P_1 and Q_1 frequencies were negligible. The phases for each of the constituents along the boundary displayed a similar convergence.

The spatial variability of the final amplitudes and phases for each of the boundary forcing frequencies is displayed in Figures 2.12a-h. These patterns were determined from harmonic analysis of the last ADCIRC simulation, forced with the boundary conditions determined through the inversion. Amplitudes for each constituent generally increase in the northeast direction, while phases generally show the tides to be rotating in a counterclockwise swath. Some of the constituents, particularly the diurnals, show the remnants of small accumulations of numerical noise in the northwest corner of the domain. This occurs as a result of the tides sweeping counterclockwise to that corner and not efficiently exiting the grid in shallow waters. These accumulations were monitored so as to ensure that they did not affect regions along the boundary or outside of a small radius in that corner. The spatial tide patterns also revealed significant amplitude increases for most constituents in Alaska's Cook Inlet and along the Hecate Strait behind the Queen Charlotte Islands. Convergence of phases for the K_2 and S_2 frequencies identifies amphidromes in close proximity to the boundary in the southeastern portion of the domain. Phase patterns for the other constituents also provide an indication as to where other amphidromes reside in the Pacific Ocean. The ability of the inversion to handle amphidromes close to the boundary for the K_2 and S_2 attests to the versatility of this inverse tidal method.

The spatial patterns shown in Figures 2.12a-h were next compared with those of TPXO.3, the differences of which are portrayed in Figures 2.13a-h. The K_1 exhibited the most significant differences throughout the open oceans, while the P_1, Q_1, and K_2 had more negligible differences. The M_2 and S_2 constituents showed more definitive increases along the Oregon and Washington coastlines. For most of the constituents, the inversion results lead to larger amplitudes in the open oceans than those of TPXO.3 (positive amplitude differences). Significant amplitude differences are also seen in coastal areas for most frequencies, most likely attributable to the difficulty of representing coastal processes in the global TPXO.3 solution. Such coastal differences are even more prominent in Cook Inlet and Hecate Strait.

Root mean square (RMS) errors between model results and tide gauge observations provide a measure of the accuracy and performance of a model. The RMS is computed as:

$$\mathrm{RMS} = \left\{ \frac{1}{N} \sum_{i=1}^{N} \left[(\eta_i - \tilde{\eta}_i) - \left(\frac{1}{N} \sum_{j=1}^{N} (\eta_j - \tilde{\eta}_j) \right) \right]^2 \right\}^{1/2} \tag{19}$$

where N is the number of points in the elevation time series, η is the elevation observation, and $\tilde{\eta}$ is the modeled elevation. Figure 2.14 displays RMS errors for three models. The errors were computed at all tide gauges located within the interior of the grid and are shown as a function of each tide gauge's latitude. The first model shown are the final inversion results, the second is the initial ADCIRC simulation using boundary conditions from TPXO.3, and the third represents the actual TPXO.3 results. Most RMS errors at these stations are less than 20 cm, while many stations actually keep the errors below 10 cm. The larger errors at higher latitudes are generally at stations located in complex coastal geometries, such as in waters behind the Alexander Archipelago (islands north of the Queen Charlotte Islands) and along British Columbia's inlets. The lower graph in Figure 2.14 shows differences between the inversion results and the other two models. Positive values indicate smaller errors using the inversion results. The inversion shows better performance than the initial ADCIRC simulation using TPXO.3 boundary conditions. Interestingly, though, the results are more ambiguous for comparisons with the TPXO.3 solution. Glancing over all of these latter differences shows a general improvement with the inversion results, yet there are ambiguous values between 40° and 51° latitude. Spatial representations of these RMS errors for the inversion results are also shown in Figure 2.15a, while differences between the inversion results and the TPXO.3 ADCIRC simulation are displayed in Figure 2.15b and differences between the inversion results and the TPXO.3 global solution are displayed in Figure 2.15c.

To evaluate the performance of the models in more detail at the tide gauges, 15 stations were selected for further analysis. These stations, shown in Figure 2.16, were selected so as to cover a wide range of spatial locations throughout the domain. The locations are also located in varying regions of bathymetry including deep ocean, continental slope, and coastal areas. Figures 2.17a-o display amplitude and phase errors at each of these stations for the inversion results, the ADCIRC simulation with TPXO.3 boundary conditions, the TPXO.3 global model, as well as five more global tide models. These other models consist of the modified enhanced Schwiderski (1980a-c), GSFC Ray-Sanchez-Cartwright (1994) RSC94, Eanes-Bettadpur (1994) CSR3.0, OSU Egbert et al. (1994) TPX0.2, and Grenoble Le Provost et al. (1994) FES95.2 models. Not all of the models have these eight constituents represented, and not all of the tide stations have data available for all of the constituents.

Some of the amplitude and phase errors at various stations tend to show similar behavior among all the different models. For example, the model amplitudes at station 7 all seem to underpredict the tide gauge observations, and almost all of the phases at station 14 have the same error sign. These types of errors perhaps indicate a common feature that is not being represented in the models correctly. Such features may include bathymetry, coastline geometry, or a physical process not correctly being generated in a certain region of the domain. Some of the models individually have trouble reproducing certain constituents. Examples include the K_2 phase errors of CSR3.0, the N_2 phase errors of the TPXO.3 ADCIRC simulation, and the M_2 amplitude errors of FES95.2 at stations 11-13. Results for the most dominant tide in the eastern north Pacific Ocean, the M_2, show variable performance at the different stations. The M_2 amplitude errors are generally constrained within 5 cm, and M_2 phase errors are usually kept under 5 degrees. Figure 2.18 shows RMS errors over a month at these tide stations. Most of the RMS errors are below 10 cm, with some as low as 1 cm. Station 15 showed large errors, most likely associated with difficulties in representing local features at this coastal site.

Since one of the purposes of this regional model is to provide a tool which effectively links tidal processes occurring in the deep ocean with those occurring in coastal environments, a local modeling experiment was set up in the Columbia River. The Columbia River, displayed in Figure 2.19, is situated between the states of Oregon and Washington. The modeling results and data for the Columbia River that are presented here are derived from the CORIE project. CORIE is a nowcast-forecast system for the Columbia River that integrates real-time monitoring with numerical modeling (Baptista et al., 1998) to characterize and predict hydrodynamic processes in the river.

Four ADCIRC simulations were designed for the domain shown in Figure 2.19. Each simulation used a different set of boundary conditions. The first set of boundary conditions were interpolated from the inversion results, the second from the TPXO.3 ADCIRC simulation, the third from the final TIDE2D results in the sensitivity tests, and the fourth from the original TPXO.3 global tide model. RMS errors from these simulations were computed at the eight tide stations shown in Figure 2.19. These errors are shown in Figure 2.20 and exemplify the ability of the inversion results to generally provide improved boundary conditions to a local domain such as the Columbia River. RMS errors were below 20 cm at all stations using the inversion results, which generally outperformed the other models at most stations.

2.6 Summary and Discussion

The regional inversion for tides presented here is designed to provide an effective link between tidal circulation in coastal and abyssal waters. Inversion techniques were used to determine open ocean boundary conditions from observations at selected tide gauges throughout the domain. The sensitivity of the inversion process to the selection of transfer functions, tide gauges, and model parameters was utilized to select final parameters for the model. It was shown that a simple set of linear transfer functions was able to best facilitate physically realistic and accurate model solutions. The selection of tide gauges used in the inversion was optimal when the number of knowns was approximately equal to the number of unknowns in the inversion matrix. Ensuring that such features as bathymetry and coastline geometry were well represented around each tide gauge proved essential to accurate inversion results.

The final inversion results were generated using a time domain hydrodynamic model that allowed for inundation, variable coriolis forcing, and the tidal potential forcing. The TPXO.3 global tide model was utilized as a starting point in the inversion. Four inversions were performed before the solution was considered to have converged upon a final set of differences from the starting point solution. The K_1 constituent provided the most significant changes seen in the inversion, with amplitude differences up to 19 cm along the open ocean boundary. Amplitude differences for other constituents ranged from negligible values to several centimeters. Spatial patterns of amplitudes and phases in the final inversion results identified strong modeled tides in Cook Inlet and Hecate Strait. They also revealed the ability of the inversion technique to represent amphidromes for the K_2 and S_2 constituents that were in close proximity to the open boundary.

RMS errors at individual tide gauges were constrained to reasonable levels. Errors at deep ocean locations were generally below 5-10 cm, while those in more coastal locations were usually below 20 cm. Some stations showed errors among many models to all have the same sign, a feature most likely indicative of a common inadequacy in each of the models. In general, the inversion results showed similar performance as global tide models at tide gauges that were located in relatively open waters.

While the inversion for tides in this regional model showed similar accuracy as global models in the open ocean, the primary strength of such a regional model was expounded in its use in a local modeling study of the Columbia River. RMS error improvements in this local study ranged from a few centimeters to approximately ten centimeters over what was attainable using global modeling input. Thus, the inversion is seen to produce accurate results both in open ocean regions and as input to local modeling studies within the Eastern North Pacific Ocean domain.

2.7 References

Baptista, A.M., J.J. Westerink and P.J. Turner, 1989. Tides in the English Channel and Southern North Sea. A Frequency Domain Analysis Using Model TEA-NL, *Advances in Water Resources*, 12(4), 166-183.

Baptista, A.M., M. Wilkin, P. Pearson, P. Turner, C. McCandlish, P. Barrett, S. Das, W. Sommerfield, M. Qi, N. Nangia, D. Jay, D. Long, C. Pu, J. Hunt, Z. Yang, E. Myers, J. Darland and A. Farrenkopf, 1998. Towards a Multi-Purpose Forecast System for the Columbia River Estuary, submitted to *Ocean Community Conference*, Marine Technology Society, Baltimore, MD.

Cartwright, D.E. and R.D. Ray, 1990. Oceanic Tides from Geosat Altimetry, *Journal of Geophysical Research*, 95(C3), 3069-3090.

Eanes, R.J. and S.V. Bettadpur, 1994. Ocean Tides from Two Years of TOPEX/POSEIDON Altimetry (abstract), *EOS Transactions*, AGU, 75 (44), 61.

Egbert, G.D., A.F. Bennett and M.G.G. Foreman, 1994. TOPEX/POSEIDON Tides Estimated Using a Global Inverse Model, *Journal of Geophysical Research*, 99(C12), 24821-24852.

Foreman, M.G.G., R.A. Walters, R.F. Henry, C.P. Keller and A.G. Dolling, 1995. A Tidal Model for Eastern Juan de Fuca Strait and the Southern Strait of Georgia, *Journal of Geophysical Research*, 100(C1), 721-740.

Kolar, R.L., J.J. Westerink, M.E. Cantekin and C.A. Blain, 1994. Aspects of Nonlinear Simulations Using Shallow Water Models Based on the Wave Continuity Equation, *Computers and Fluids*, 23(3), 523-538.

Le Provost, C., M.L. Genco, F. Lyard, P. Vincent and P. Canceil, 1994. Spectroscopy of the World Ocean Tides from a Finite Element Hydrodynamic Model, *Journal of Geophysical Research*, 99(C12), 24777-24797.

Luettich, R.A., J.J. Westerink and N.W. Scheffner, 1991. *ADCIRC: An Advanced Three-Dimensional Circulation Model for Shelves, Coasts, and Estuaries*, Dept. of the Army, U.S. Army Corps of Engineers, Washington, D.C.

Luettich, R.A. and J.J. Westerink, 1995a. *An Assessment of Flooding and Drying Techniques for Use in the ADCIRC Hydrodynamic Model: Implementation and*

Performance in One-Dimensional Flows, Dept. of the Army, U.S. Army Corps of Engineers, Vicksburg, MS.

Luettich, R.A. and J.J. Westerink, 1995b. *Implementation and Testing of Elemental Flooding and Drying in the ADCIRC Hydrodynamic Model*, Dept. of the Army, U.S. Army Corps of Engineers, Vicksburg, MS.

Molines, J.M., C. Le Provost, F. Lyard, R.D. Ray, C.K. Shum and R.J. Eanes, 1994. Tidal Corrections in the TOPEX/POSEIDON Geophysical Data Records, *Journal of Geophysical Research*, 99(C12), 24749-24760.

Nunez, R., 1990. *Prediction of Tidal Propagation and Circulation in Chilean Inland Seas Using a Frequency-Domain Mode*, Master of Science Thesis, Oregon State University.

Pearson, F., 1990. *Map Projections: Theory and Applications*, CRC Press, Boca Raton, FL.

Ray, R.D., B.V. Sanchez and D.E. Cartwright, 1994. Some Extensions to the Response Method of Tidal Analysis Applied to TOPEX/POSEIDON Altimetry (abstract), *EOS Transactions AGU*, 75 (16), 108.

Sandwell, D.T. and W.H.F. Smith, 1997. Marine Gravity Anomaly from Geosat and ERS 1 Satellite Altimetry, *Journal of Geophysical Research*, 102(B5), 10039.

Schwiderski, E.W., 1980a. On Charting Global Ocean Tides, *Reviews of Geophysics and Space Physics*, 18(1), 243-268.

Schwiderski, E.W., 1980b. Ocean Tides, I, A Global Ocean Tidal Equations, *Marine Geodesy*, 3, 161-217.

Schwiderski, E.W., 1980c. Ocean Tides, II, A Hydrodynamic Interpolation Model, *Marine Geodesy*, 3, 219-255.

Walters, R., 1987. A Model for Tides and Currents in the English Channel and Southern North Sea, *Advances in Water Resources*, 10(3), 138-148.

Westerink, J.J., R.A. Luettich, A.M. Baptista, N.W. Scheffner and P. Farrar, 1992. Tide and Storm Surge Predictions Using Finite Element Model, *Journal of Hydraulic Engineering*, 118(10), 1373-1390.

Zahel, W., 1995. Assimilating Ocean Tide Determined Data into Global Tide Models, *Journal of Marine Systems*, 6(1/2), 3-13.

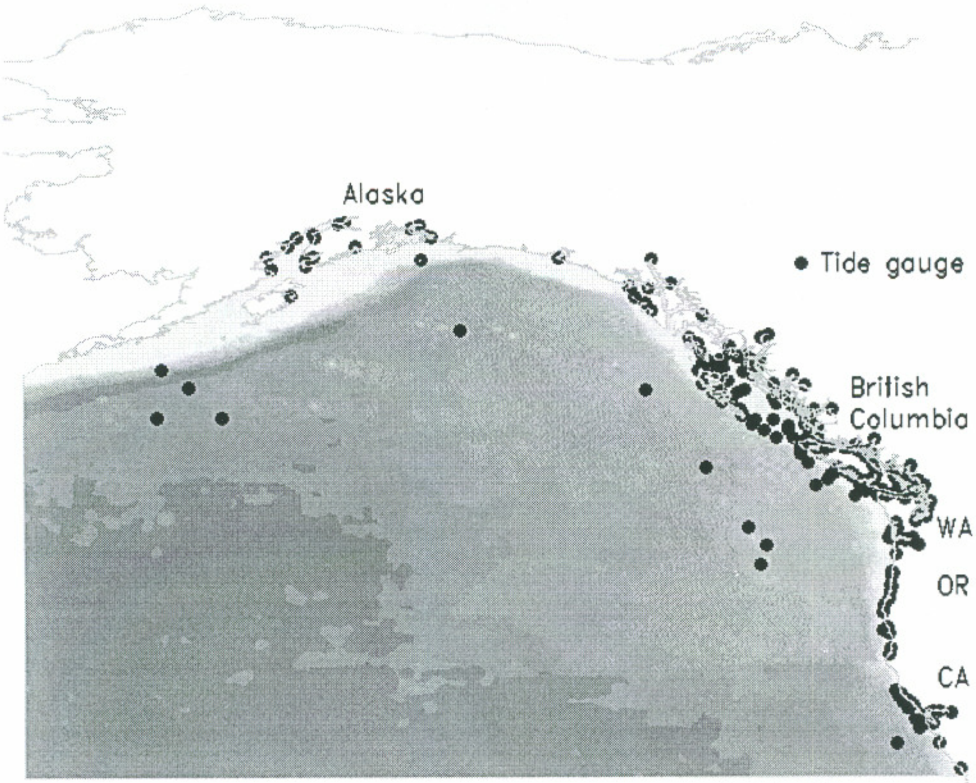

Figure 2.1 Eastern north Pacific Ocean domain and available tide gauges.

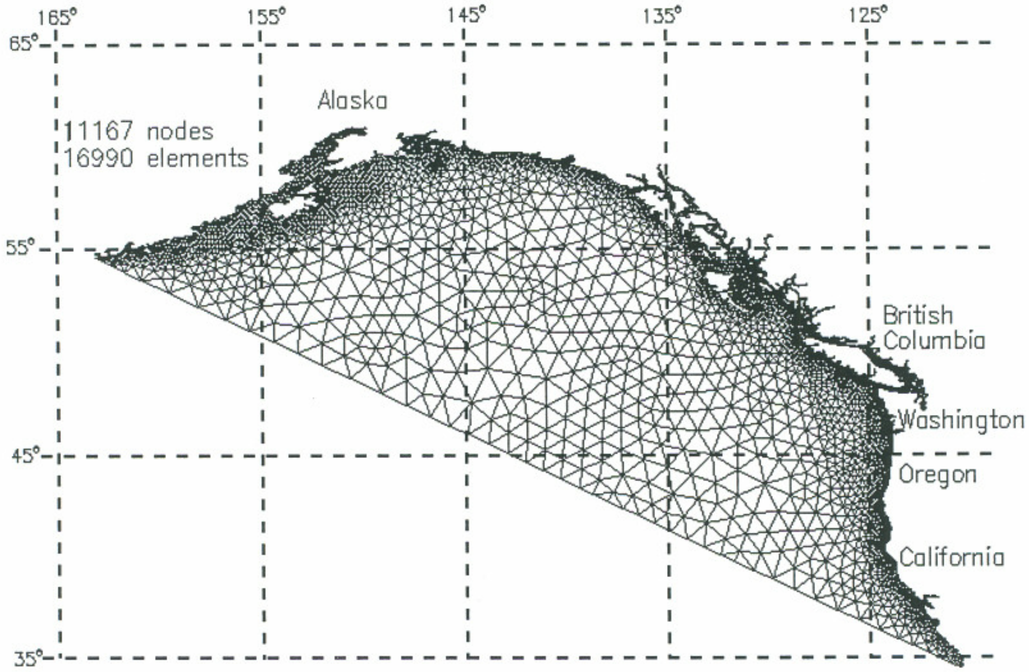

Figure 2.2 Finite element grid used for sensitivity tests with TIDE2D.

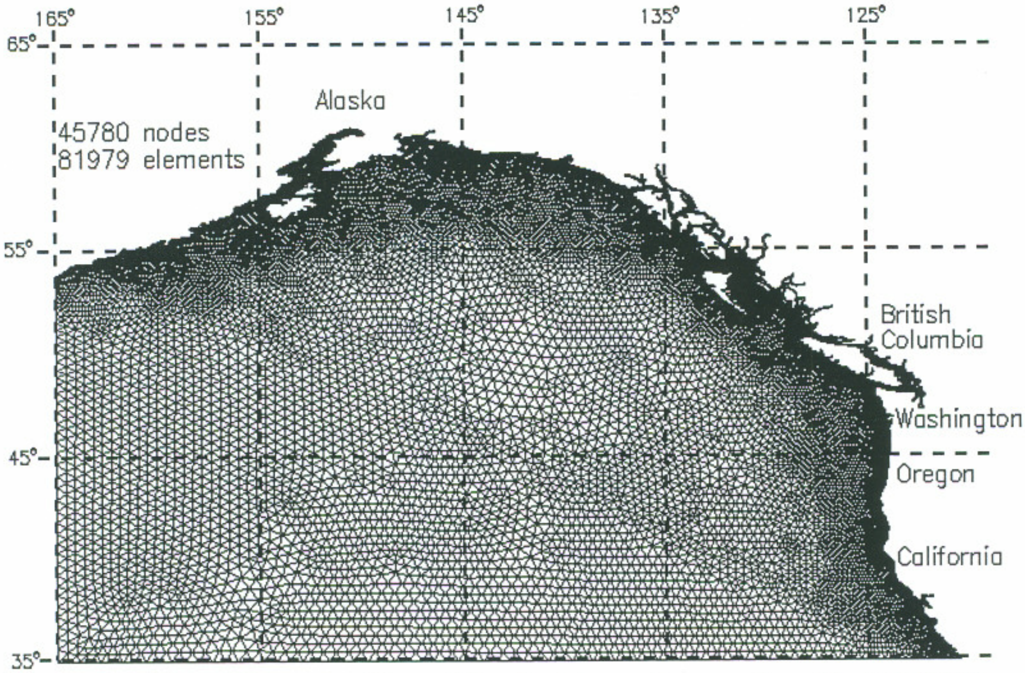

Figure 2.3 Finite element grid used for final inversion results with ADCIRC.

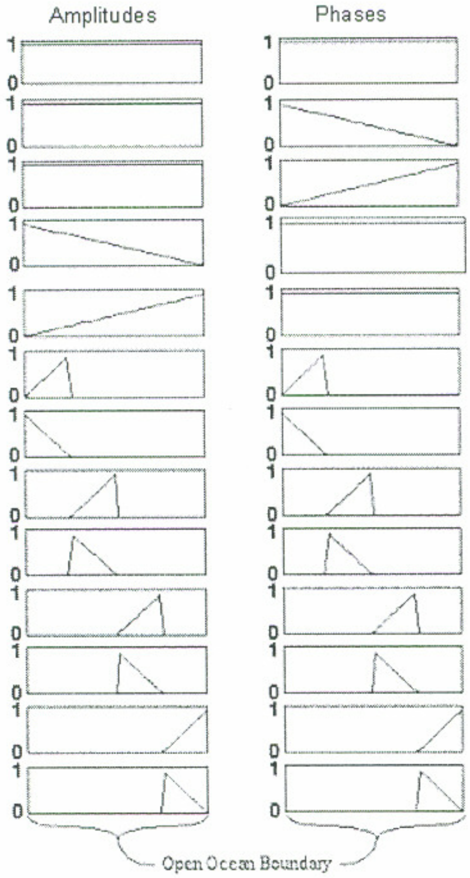

Figure 2.4 Transfer functions used in the sensitivity tests.

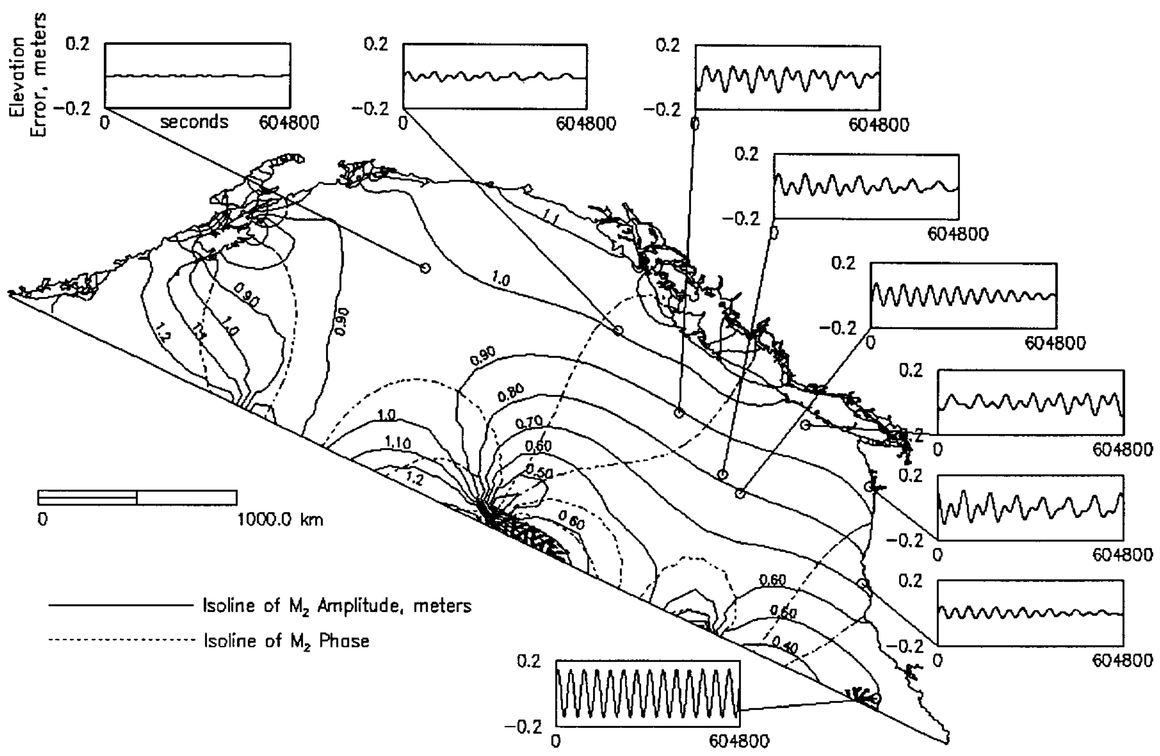

Figure 2.5 Inversion results using 13 transfer functions.

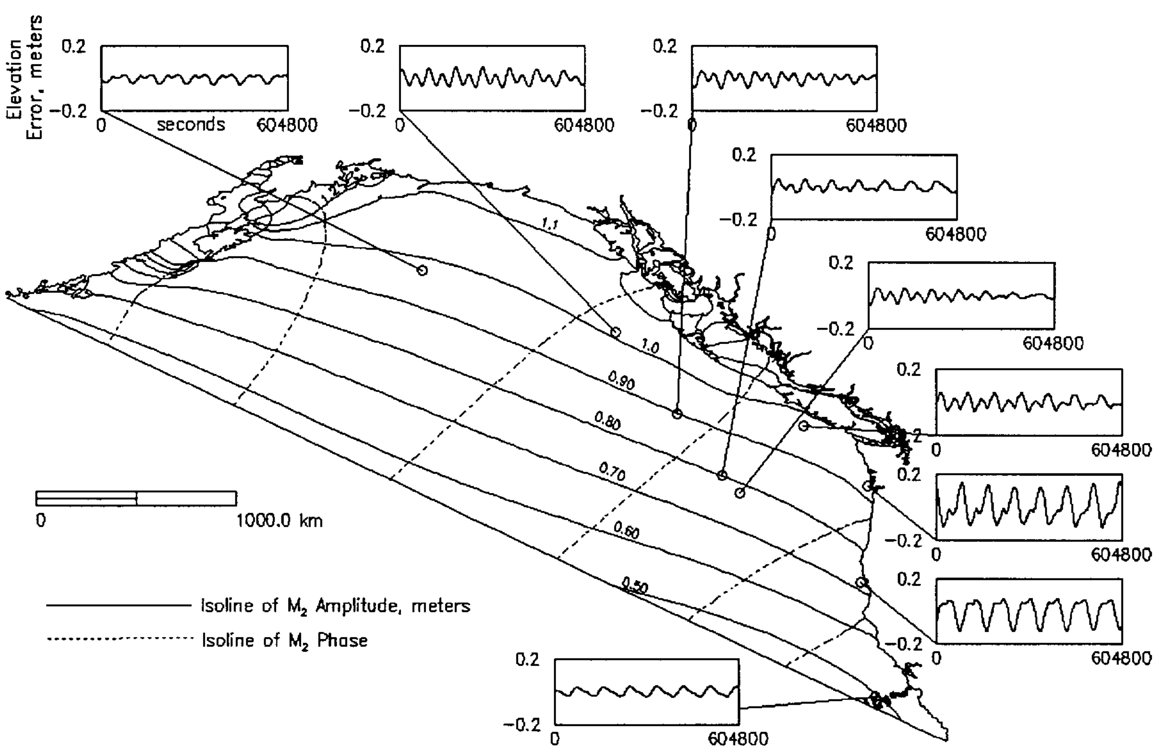

Figure 2.6 Inversion results using three transfer functions.

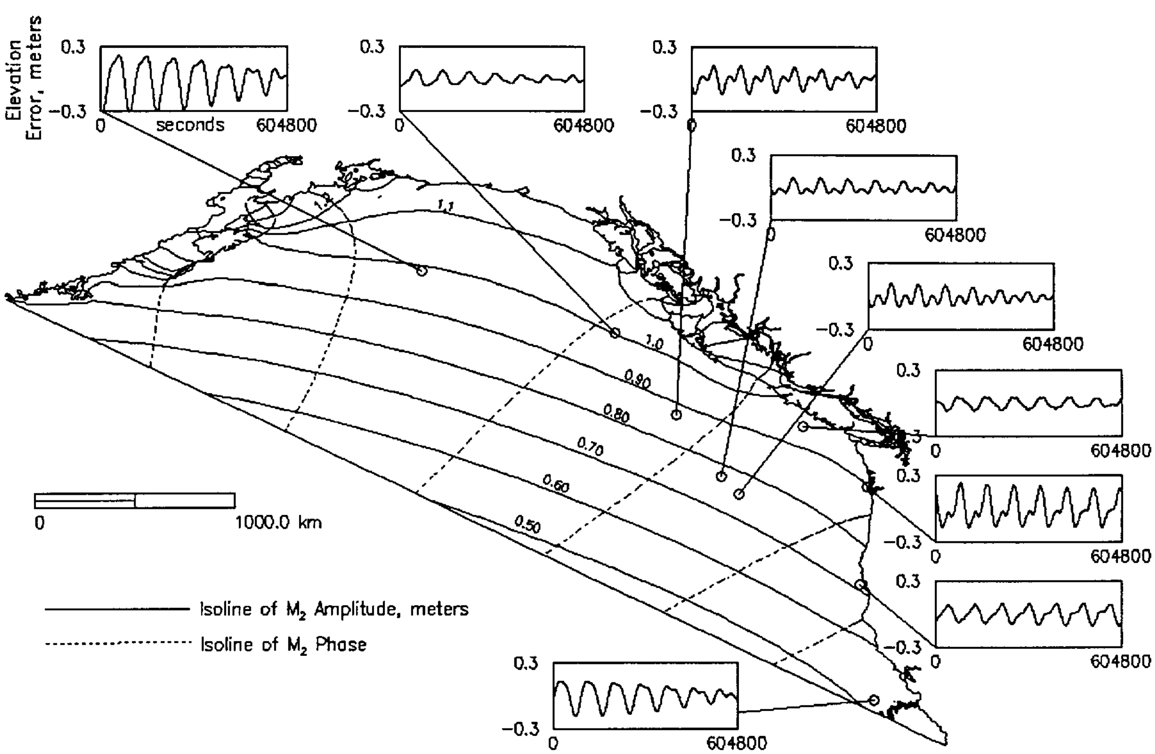

Figure 2.7 Inversion results using 18 tide gauges.

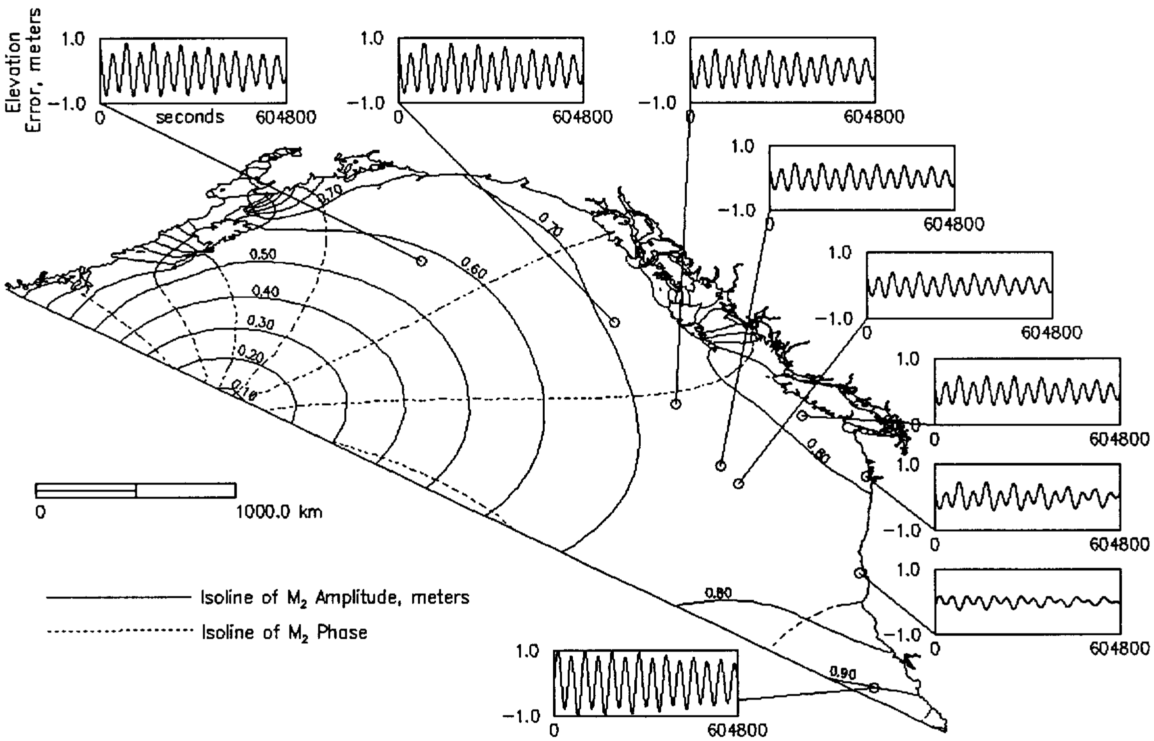

Figure 2.8 Inversion results using 270 tide gauges.

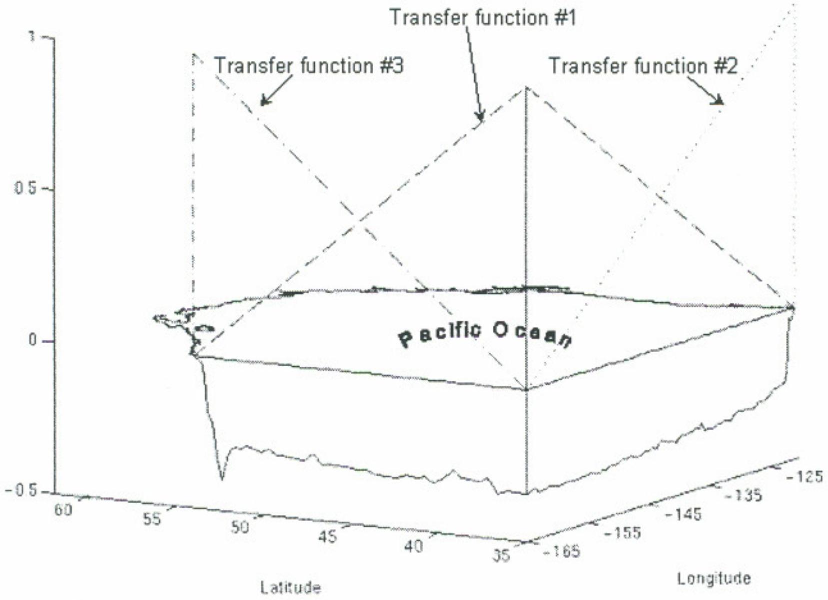

Figure 2.9 Transfer functions used in the final inversion with ADCIRC.

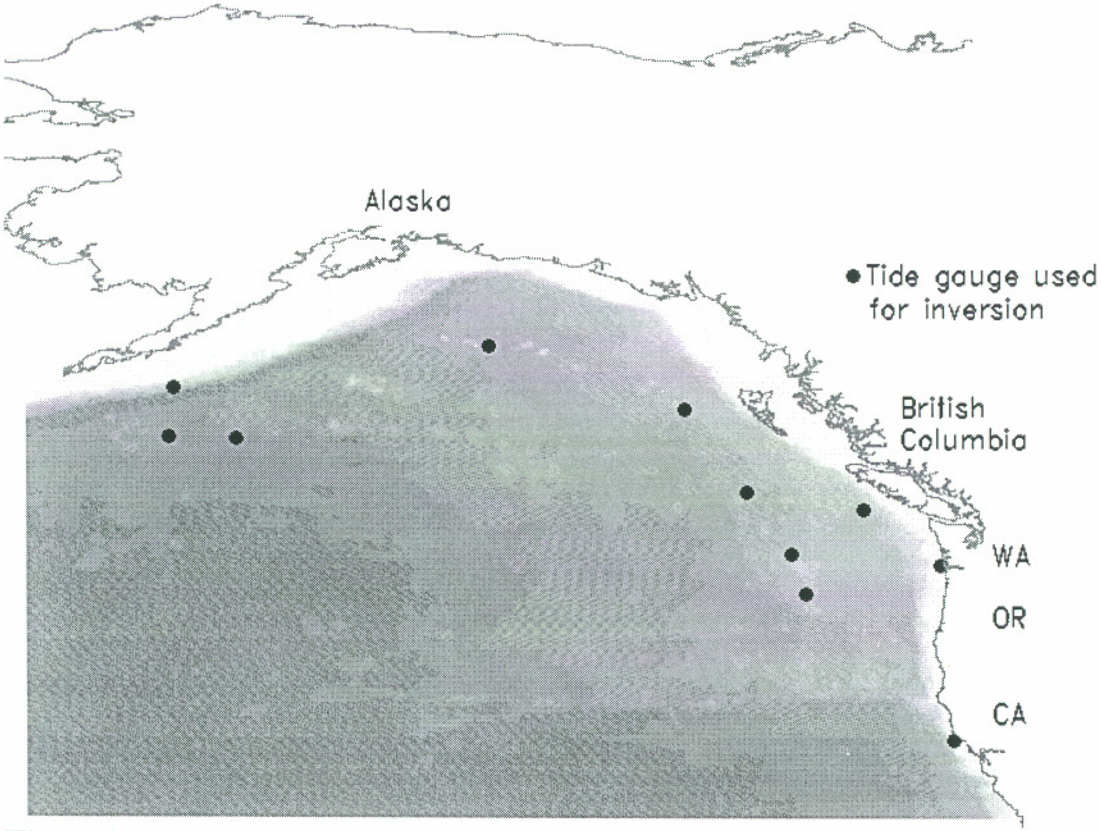

Figure 2.10 Tide gauges used in the final inversion with ADCIRC.

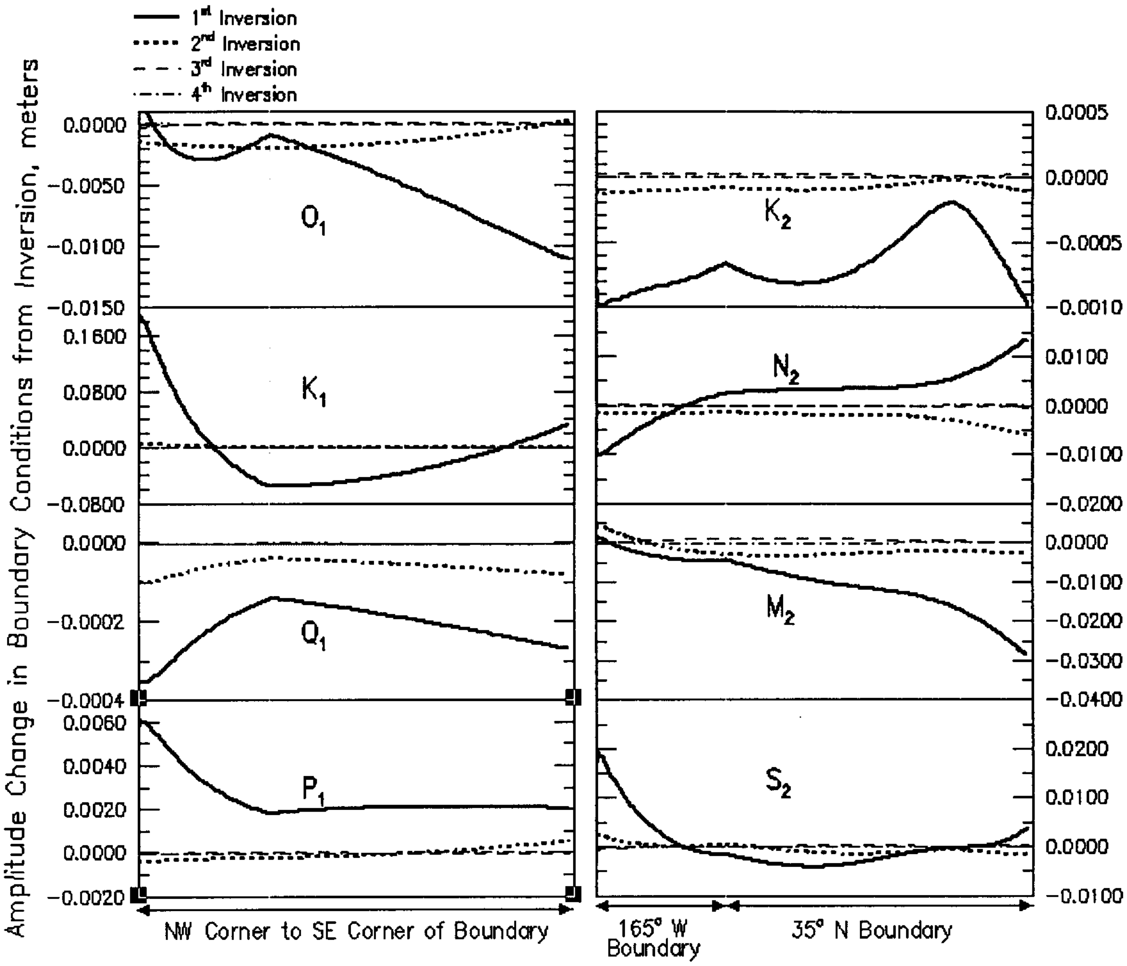

Figure 2.11 Amplitude changes attained with each successive inversion along the open ocean boundary.

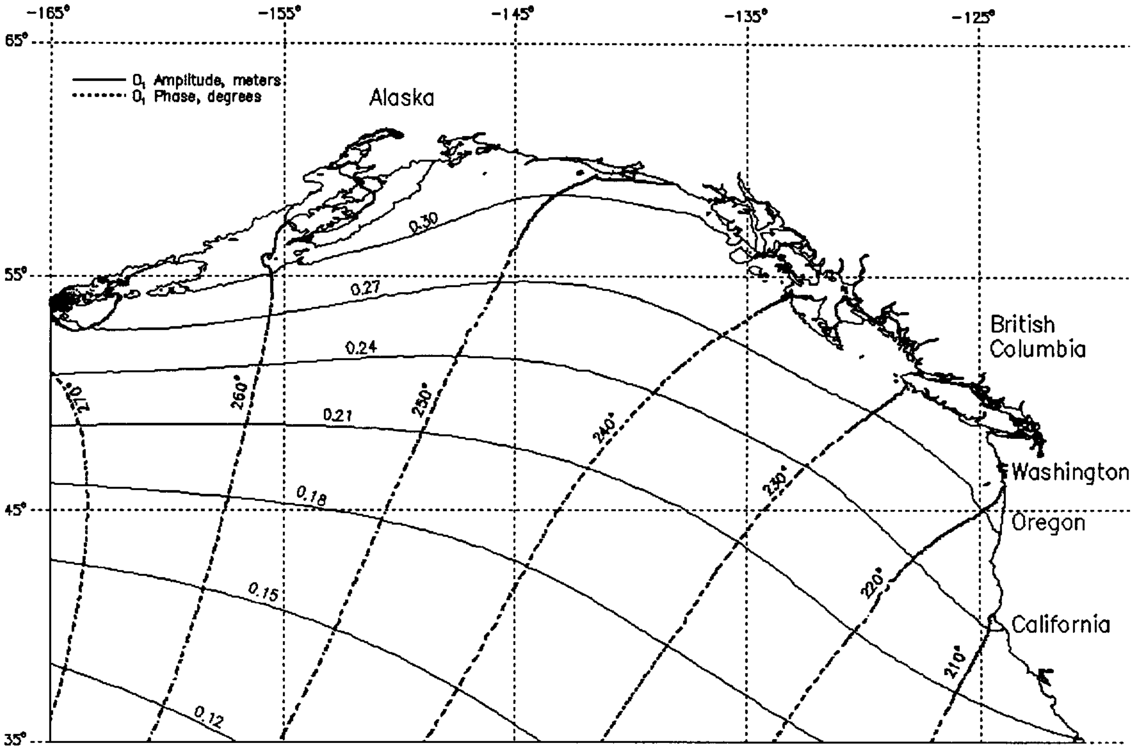

Figure 2.12a O_1 isolines of amplitude and phase from the inversion.

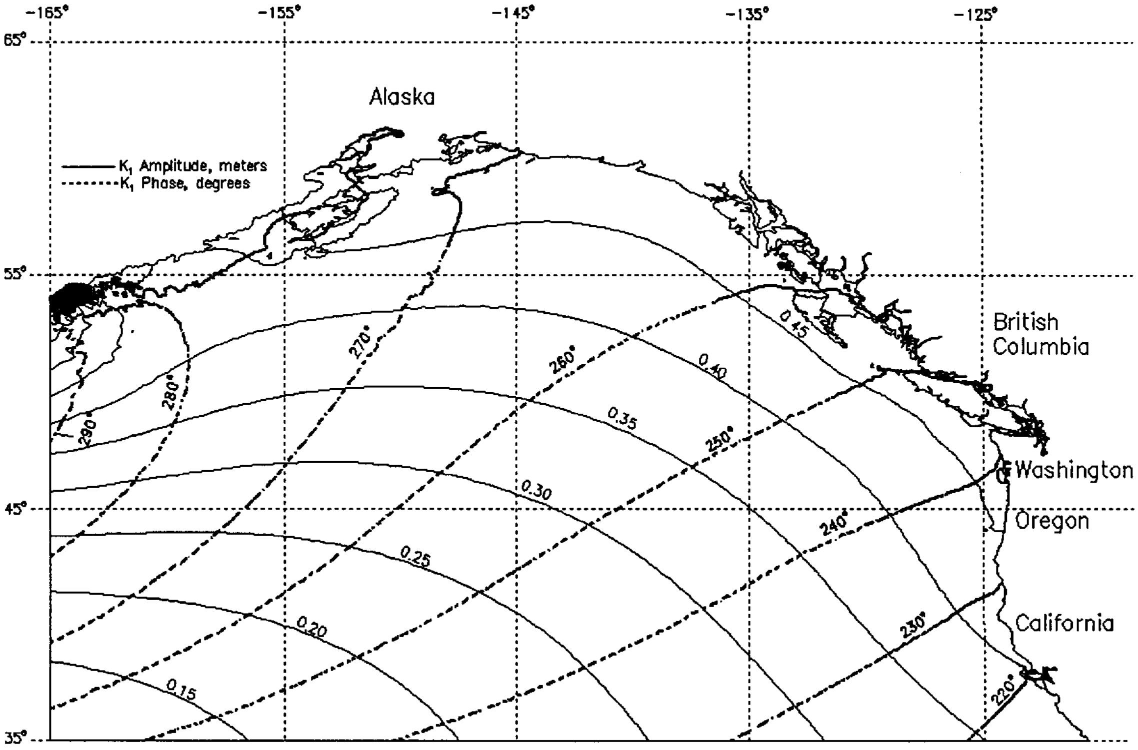

Figure 2.12b K_1 isolines of amplitude and phase from the inversion.

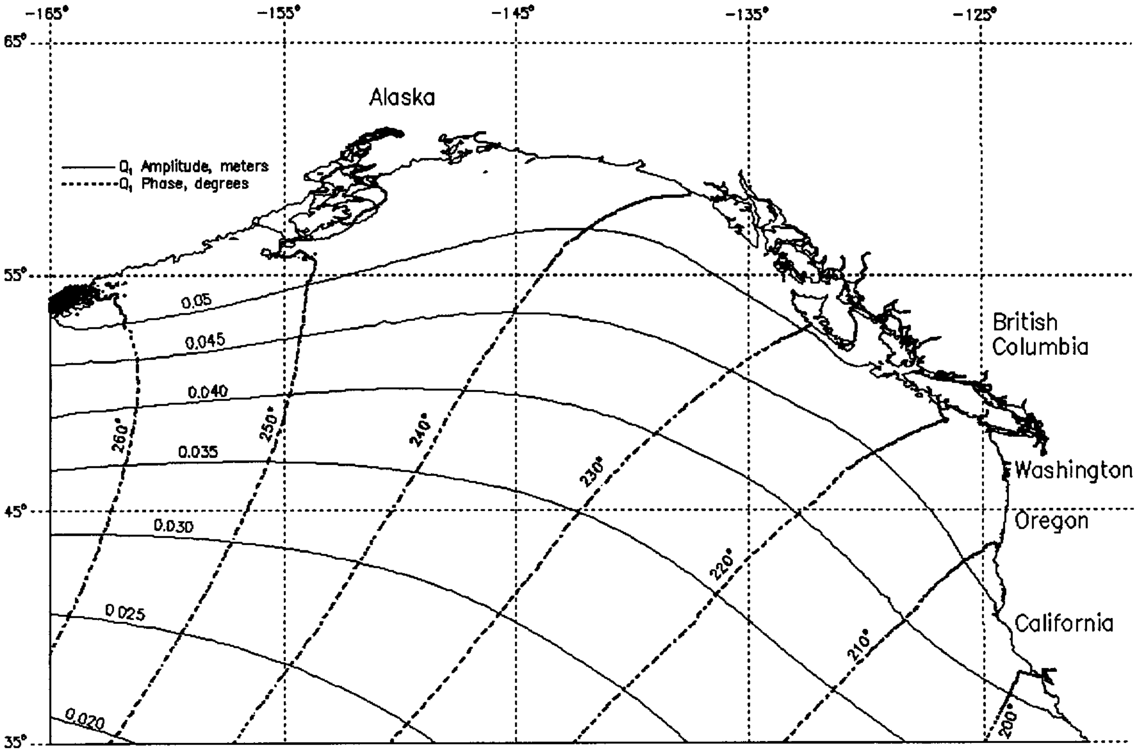

Figure 2.12c Q_1 isolines of amplitude and phase from the inversion.

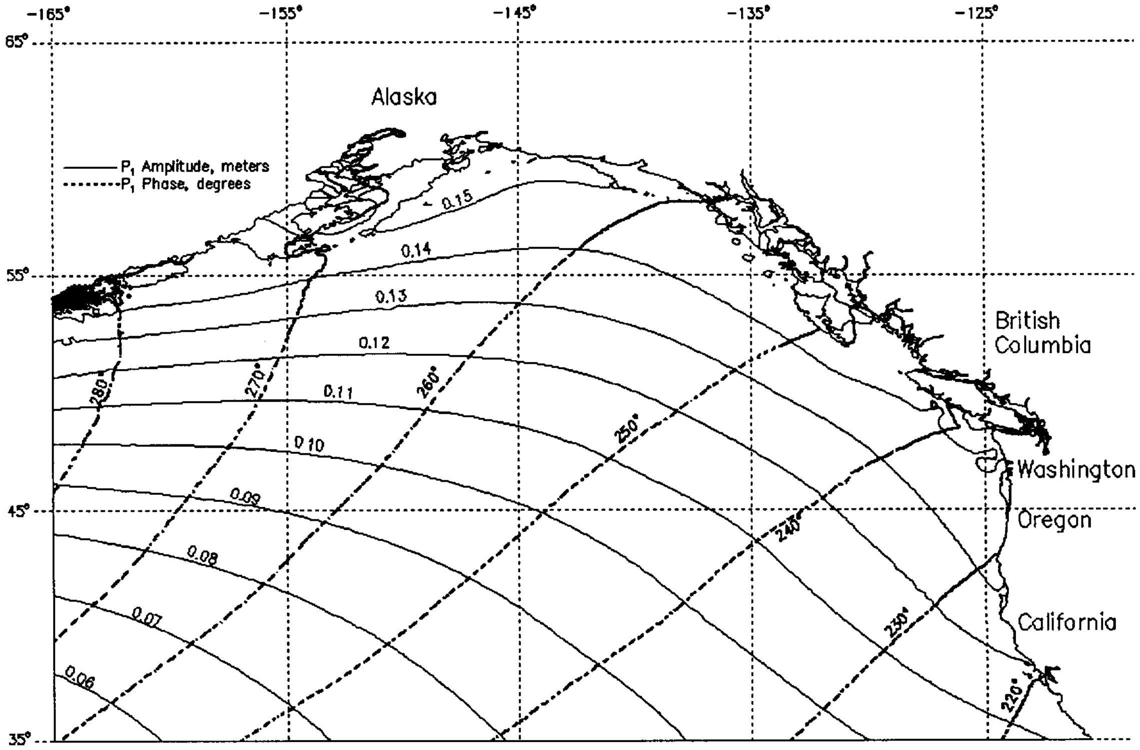

Figure 2.12d P_1 isolines of amplitude and phase from the inversion.

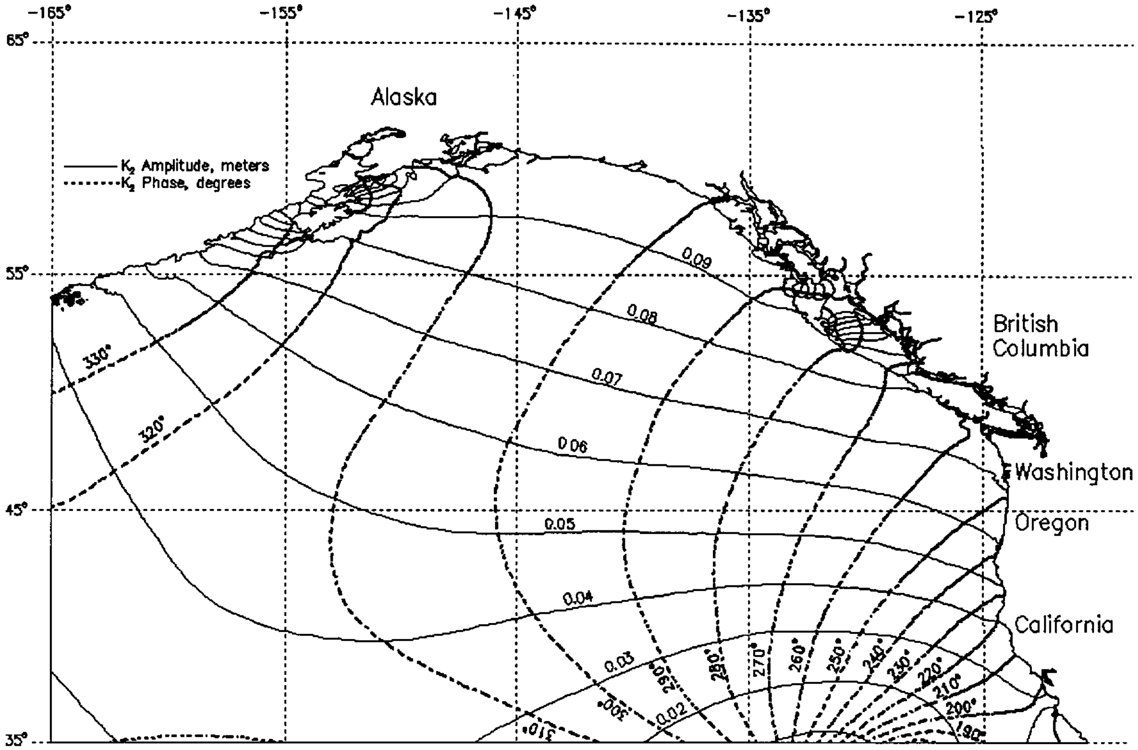

Figure 2.12e K_2 isolines of amplitude and phase from the inversion.

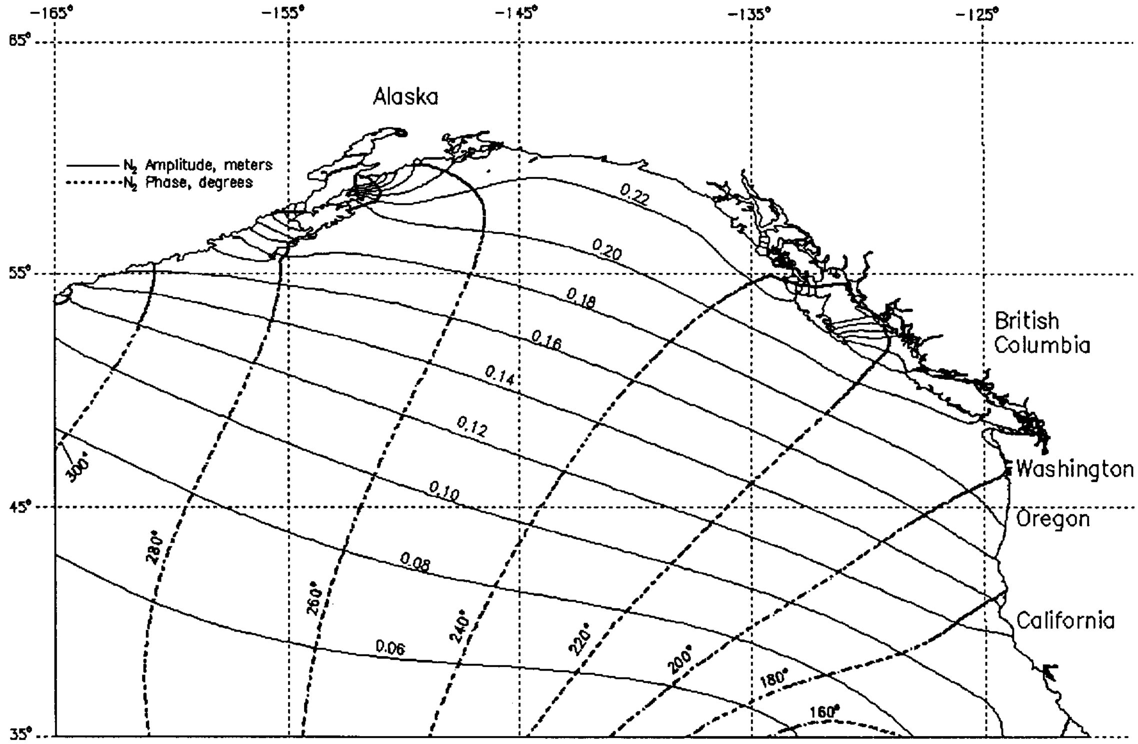

Figure 2.12f N_2 isolines of amplitude and phase from the inversion.

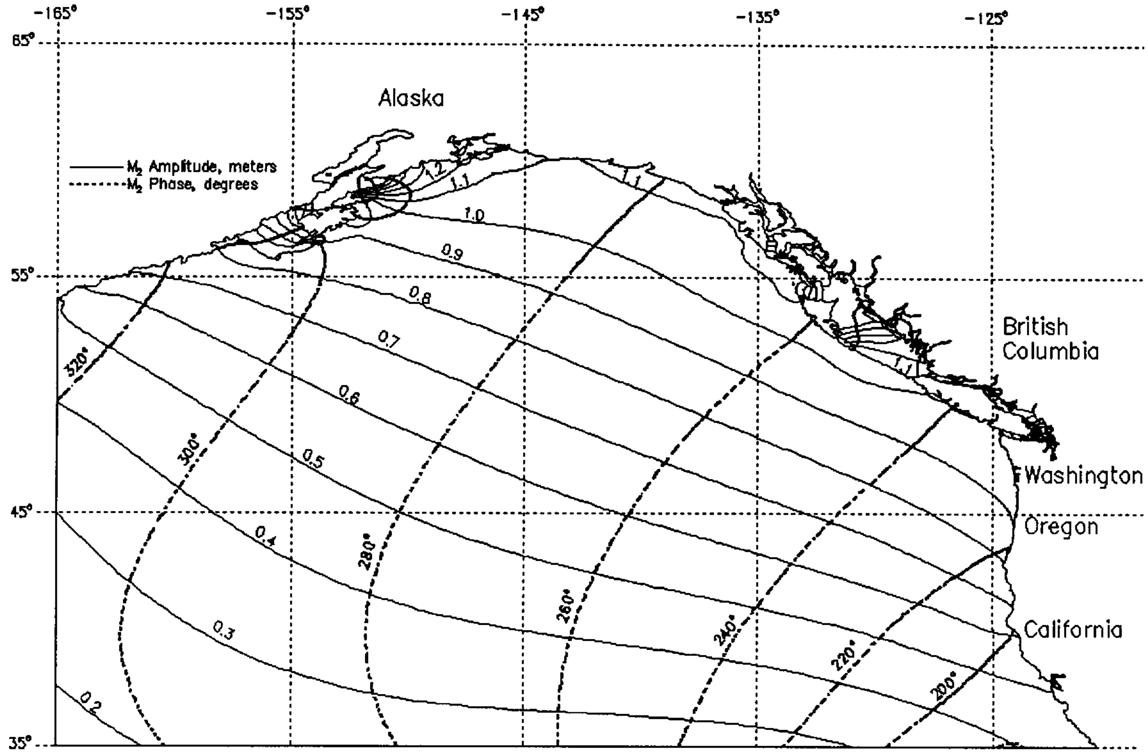

Figure 2.12g M_2 isolines of amplitude and phase from the inversion.

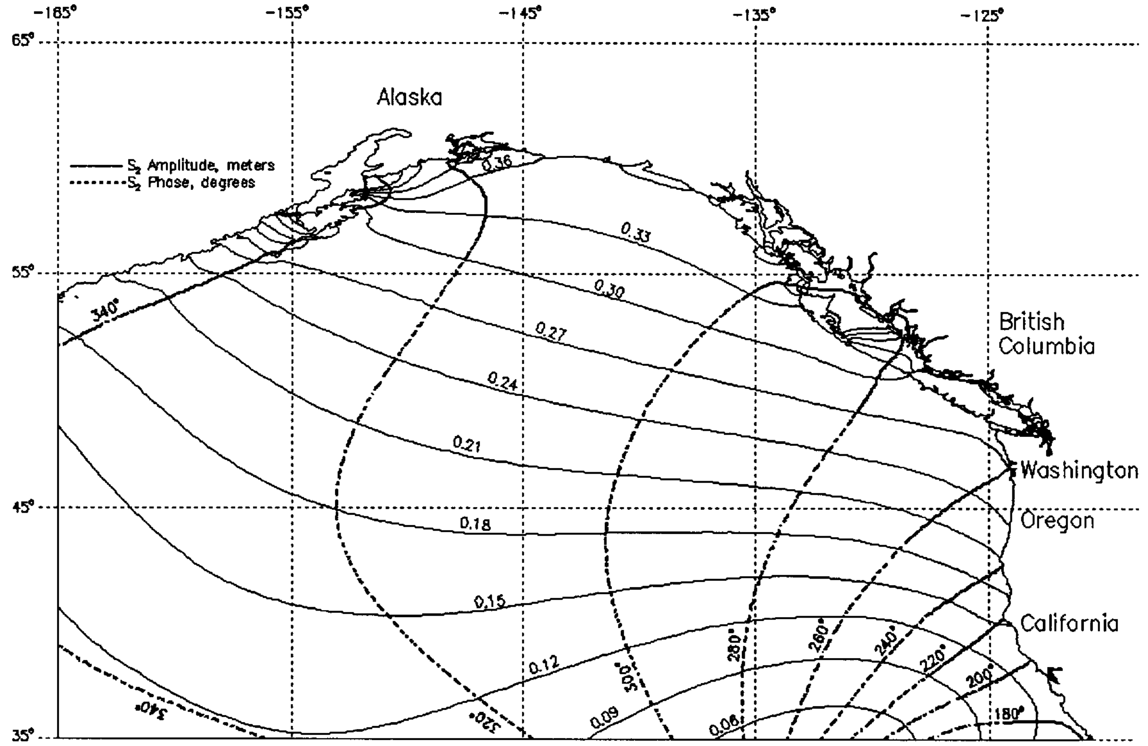

Figure 2.12h S_2 isolines of amplitude and phase from the inversion.

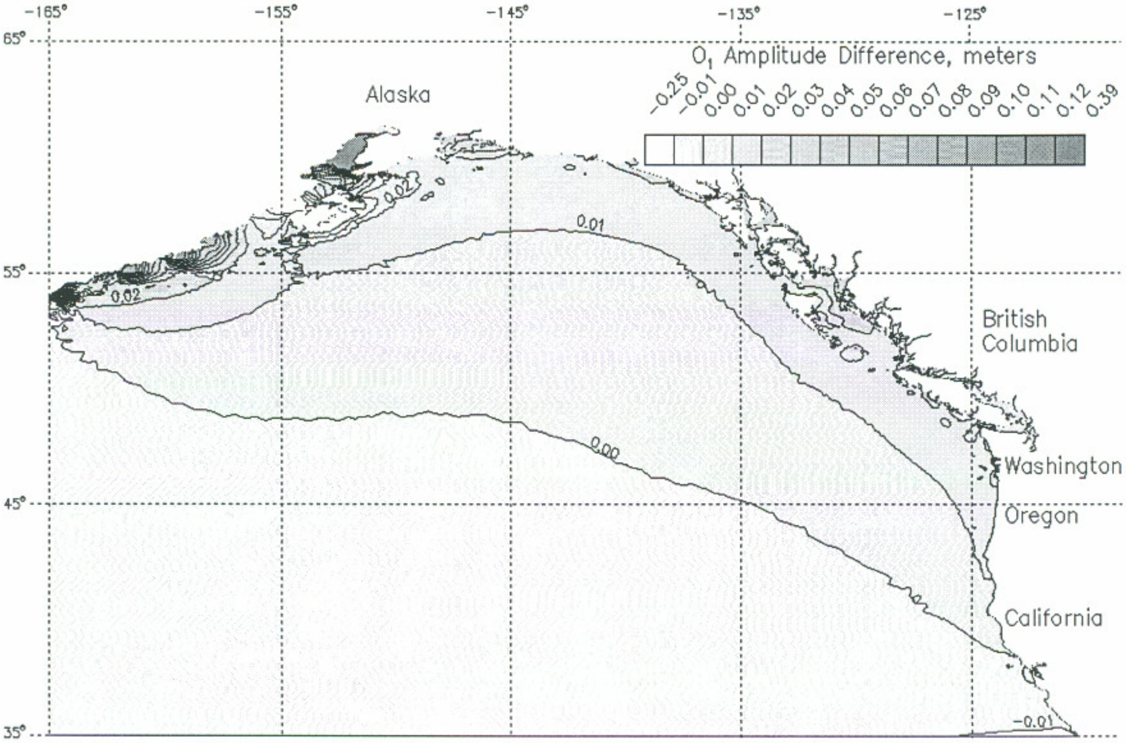

Figure 2.13a O$_1$ amplitude differences between the inversion results and TPXO.3.

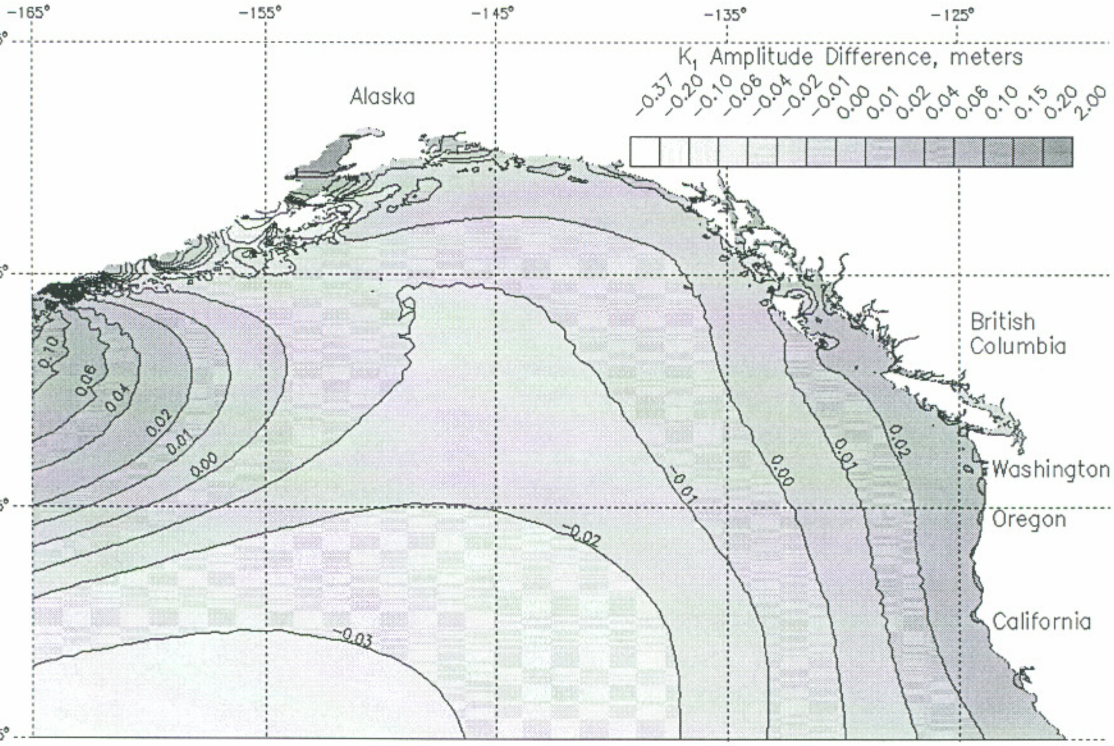

Figure 2.13b K$_1$ amplitude differences between the inversion results and TPXO.3.

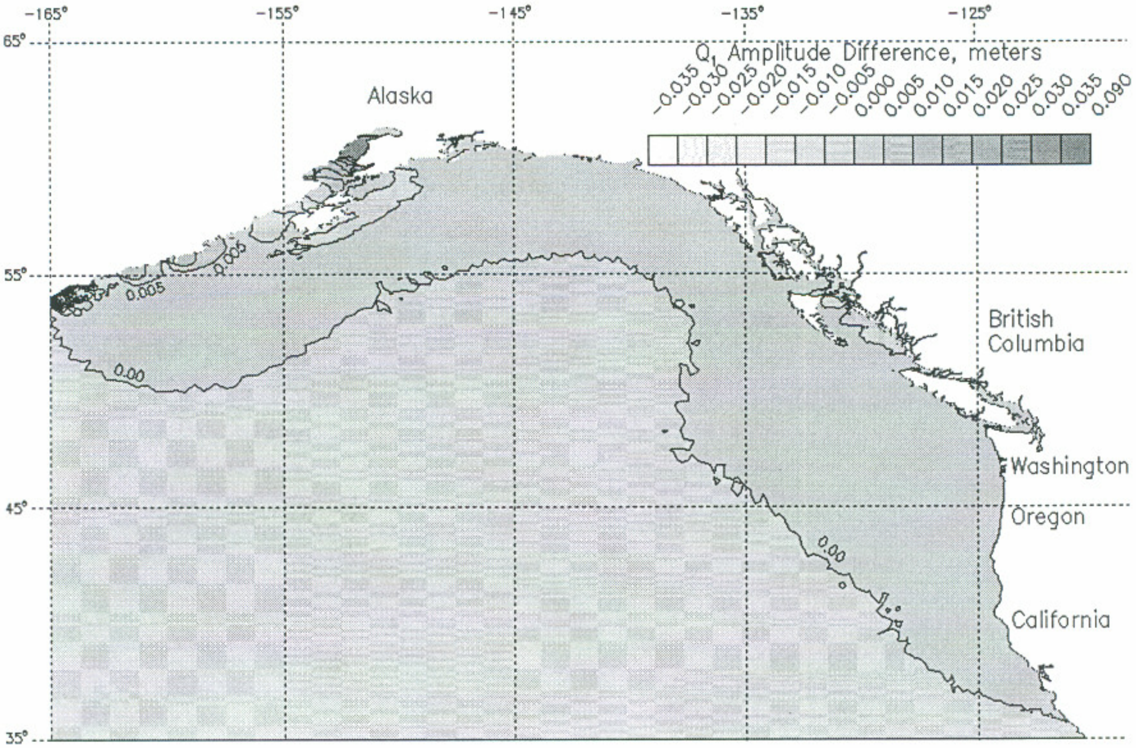

Figure 2.13c Q_1 amplitude differences between the inversion results and TPXO.3.

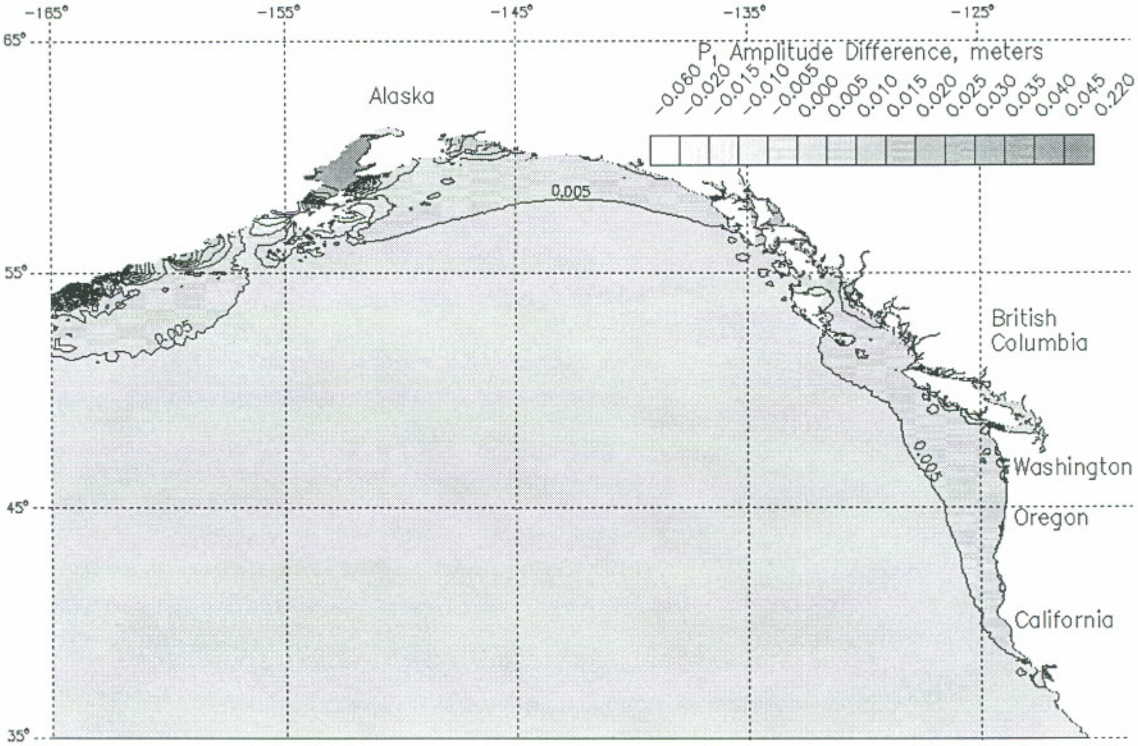

Figure 2.13d P_1 amplitude differences between the inversion results and TPXO.3.

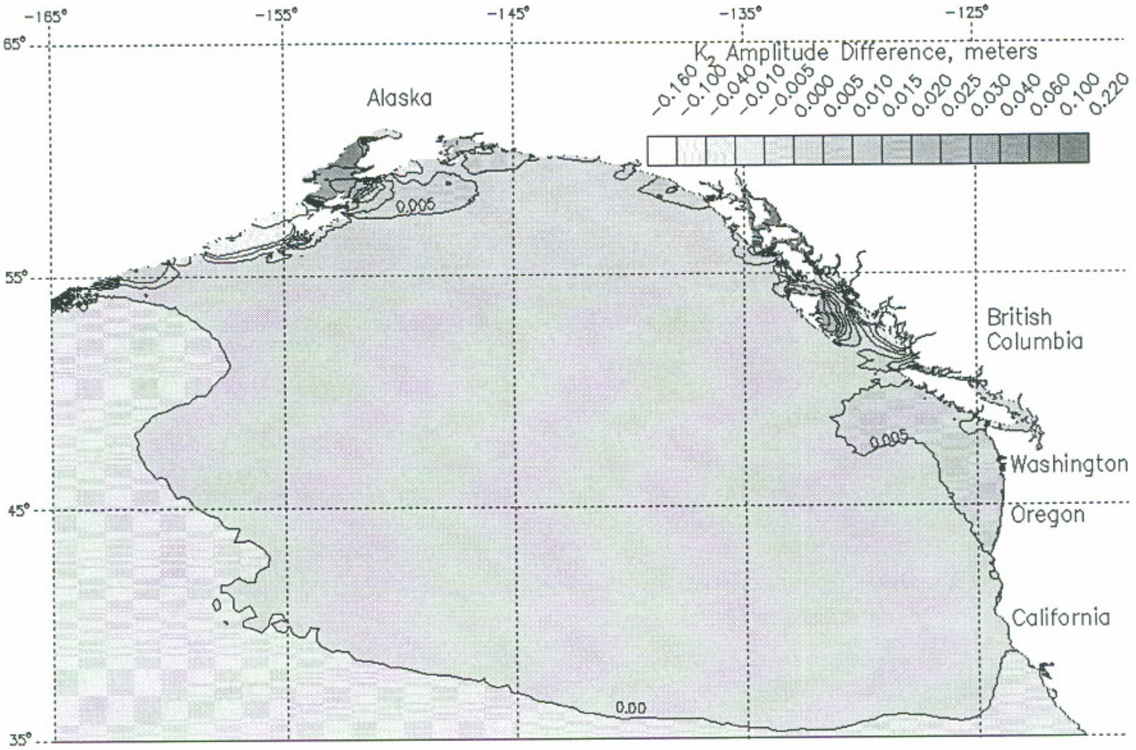

Figure 2.13e K_2 amplitude differences between the inversion results and TPXO.3.

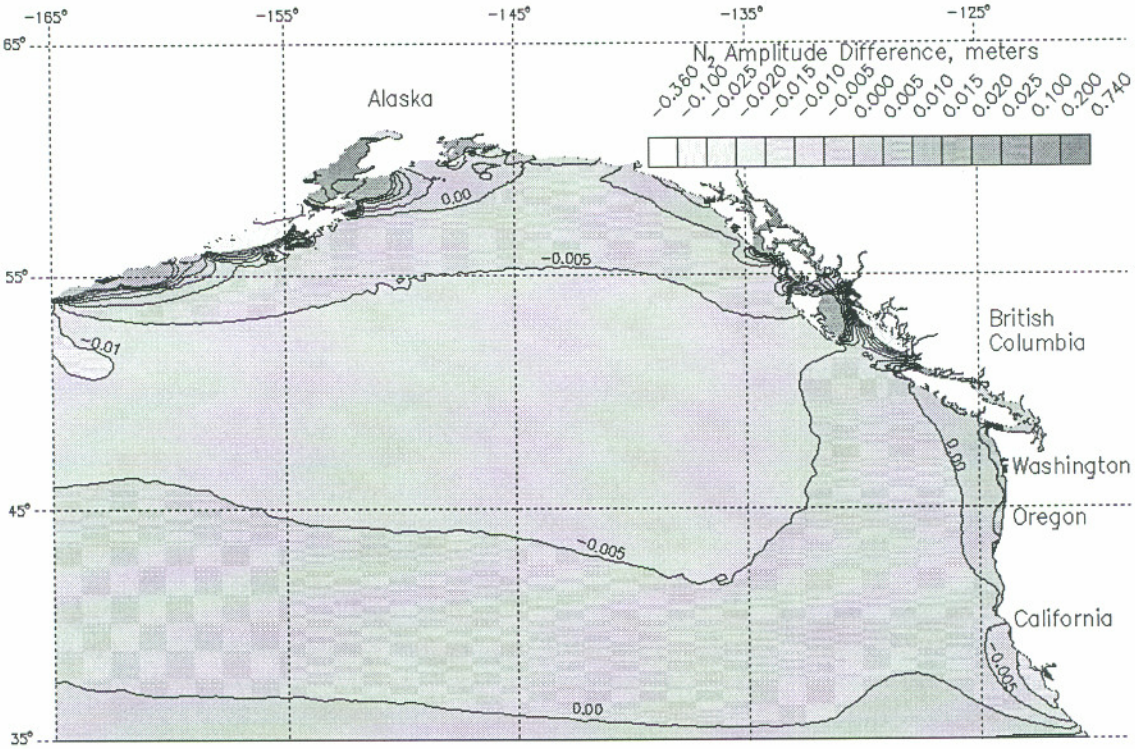

Figure 2.13f N_2 amplitude differences between the inversion results and TPXO.3.

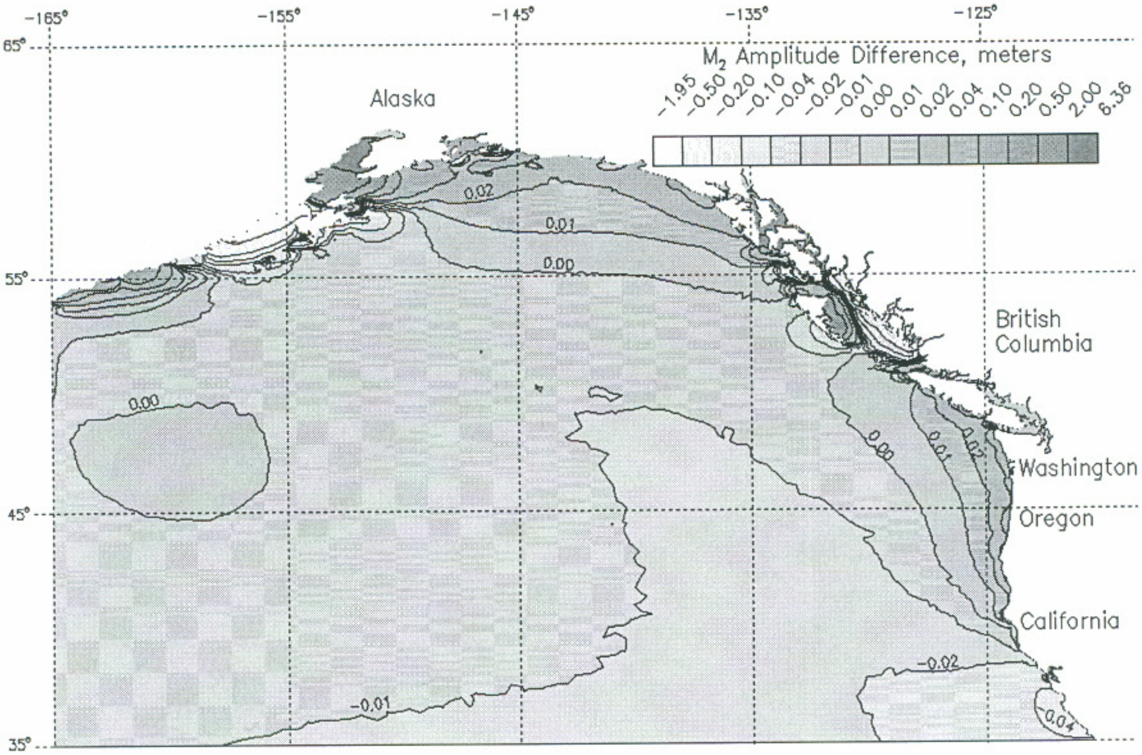

Figure 2.13g M_2 amplitude differences between the inversion results and TPXO.3.

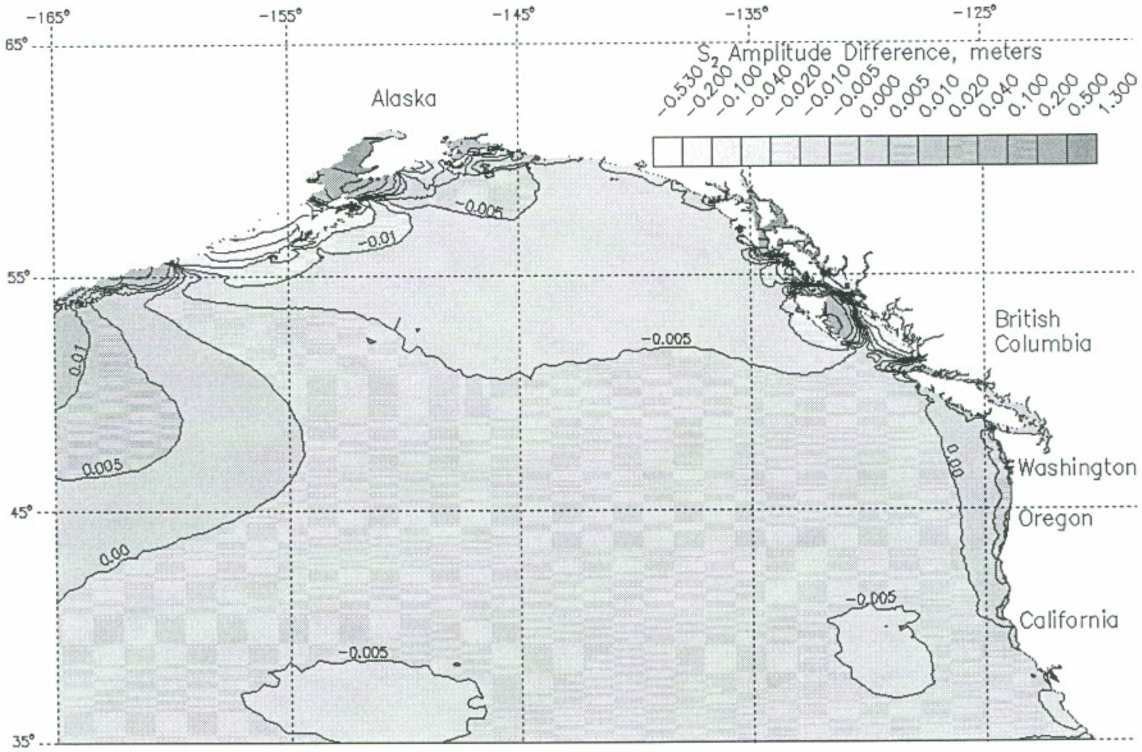

Figure 2.13h S_2 amplitude differences between the inversion results and TPXO.3.

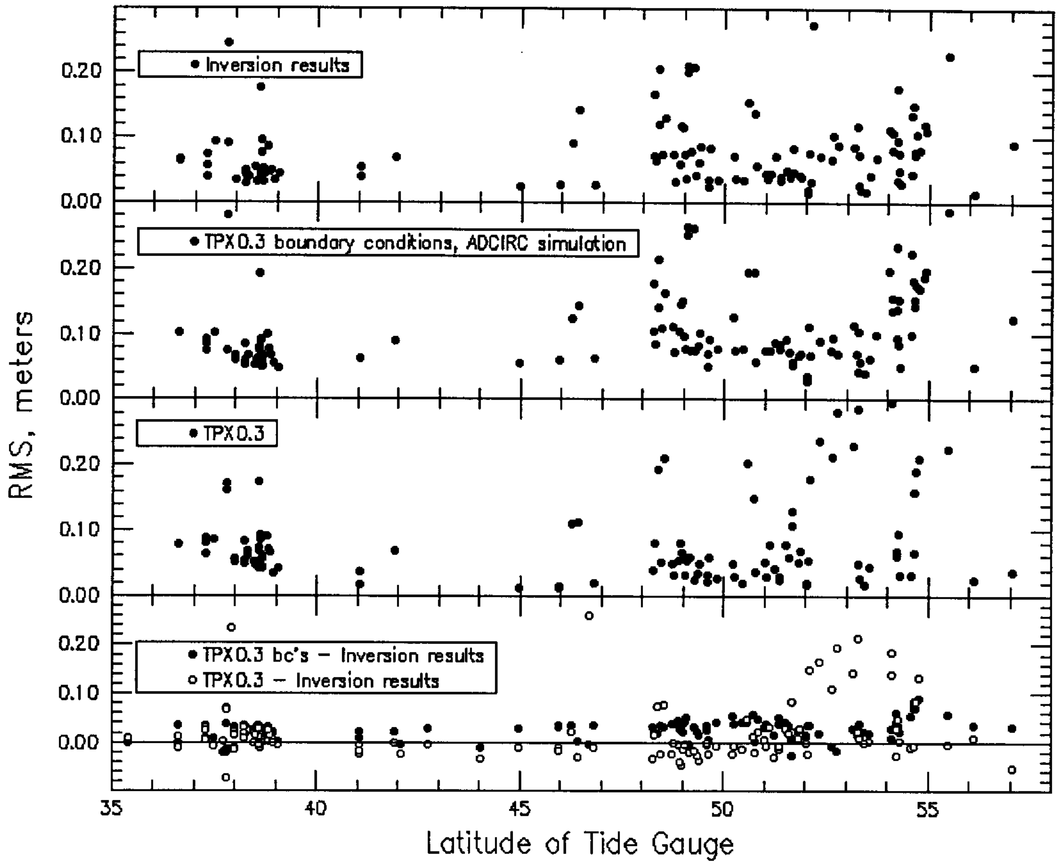

Figure 2.14 RMS errors for the inversion, the TPXO.3 ADCIRC simulation, and TPXO.3.

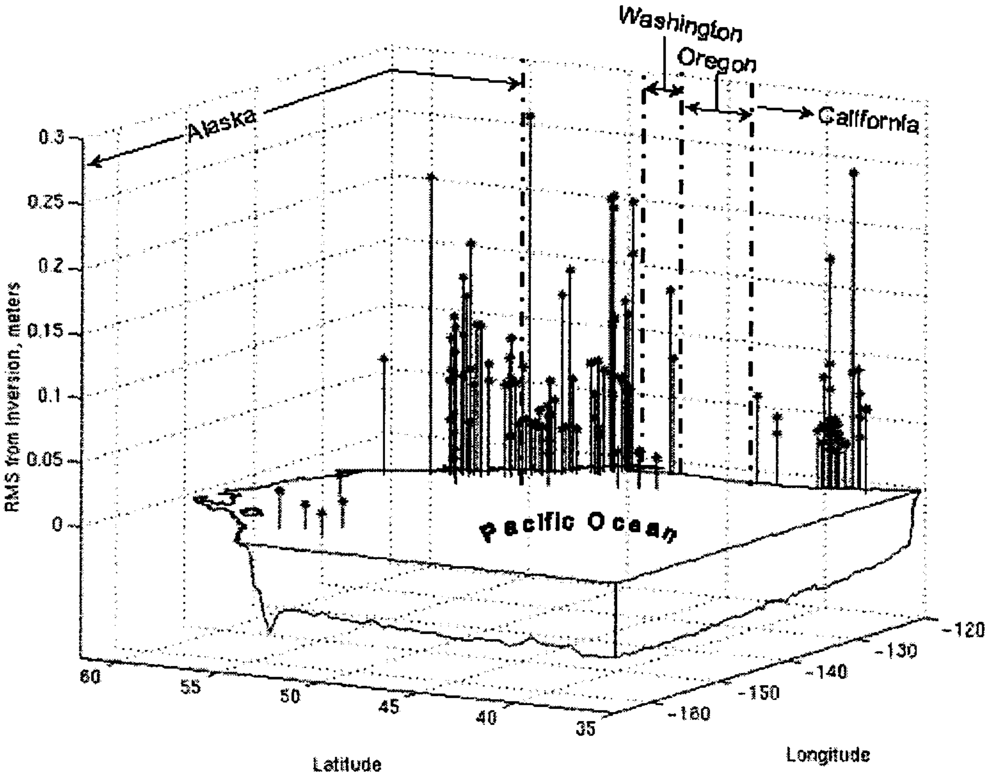

Figure 2.15a RMS errors from the inversion.

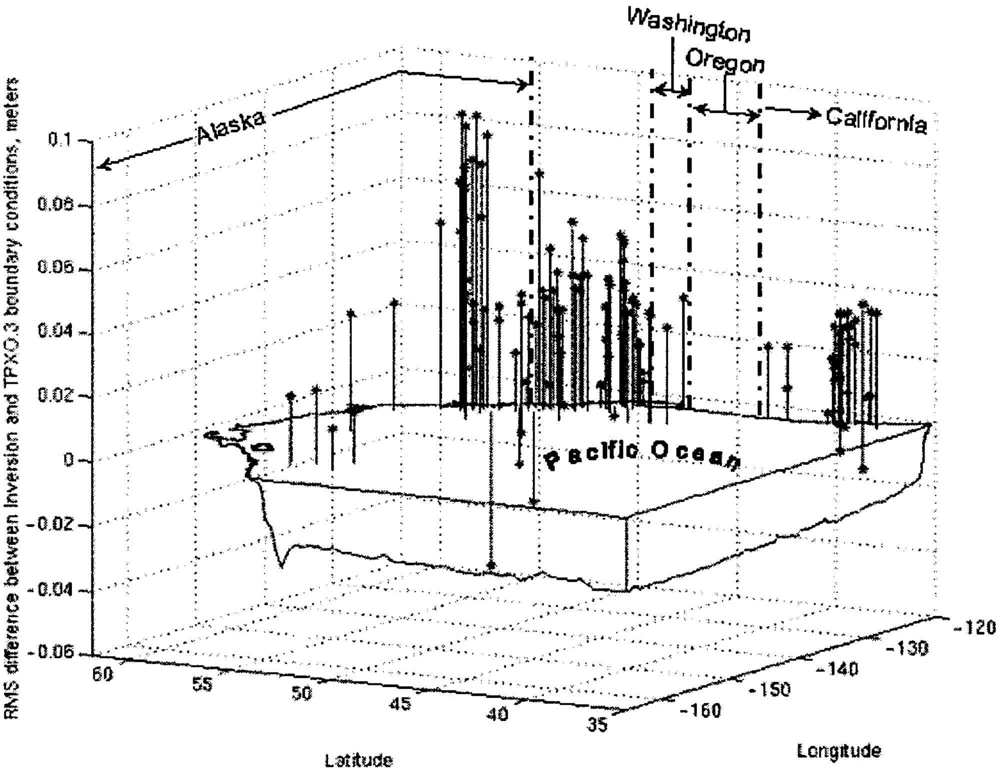

Figure 2.15b Differences in RMS errors between the inversion results and the TPXO.3 ADCIRC simulation.

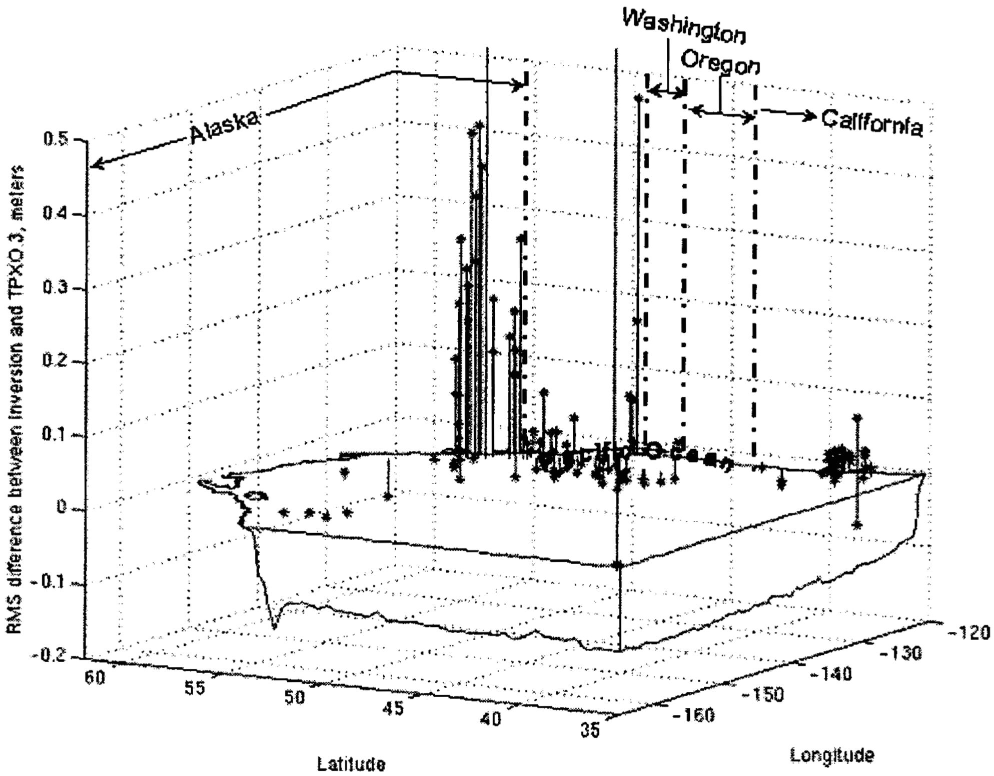

Figure 2.15c Differences in RMS errors between the inversion results and TPXO.3.

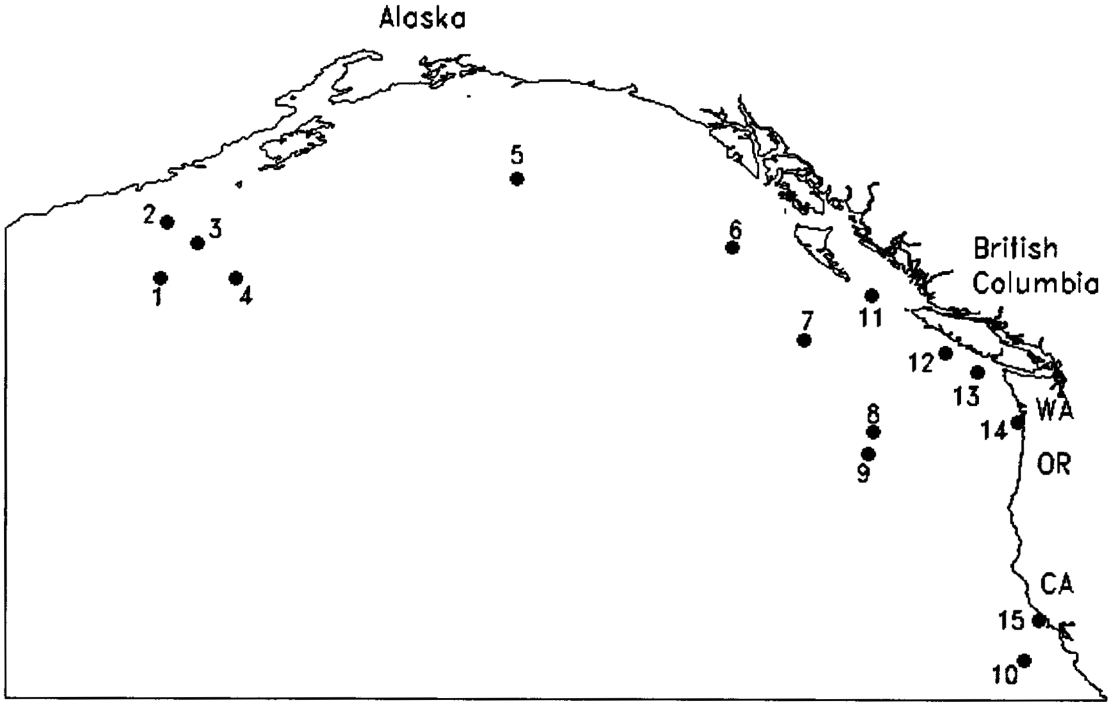

Figure 2.16 Tide gauges for results analysis.

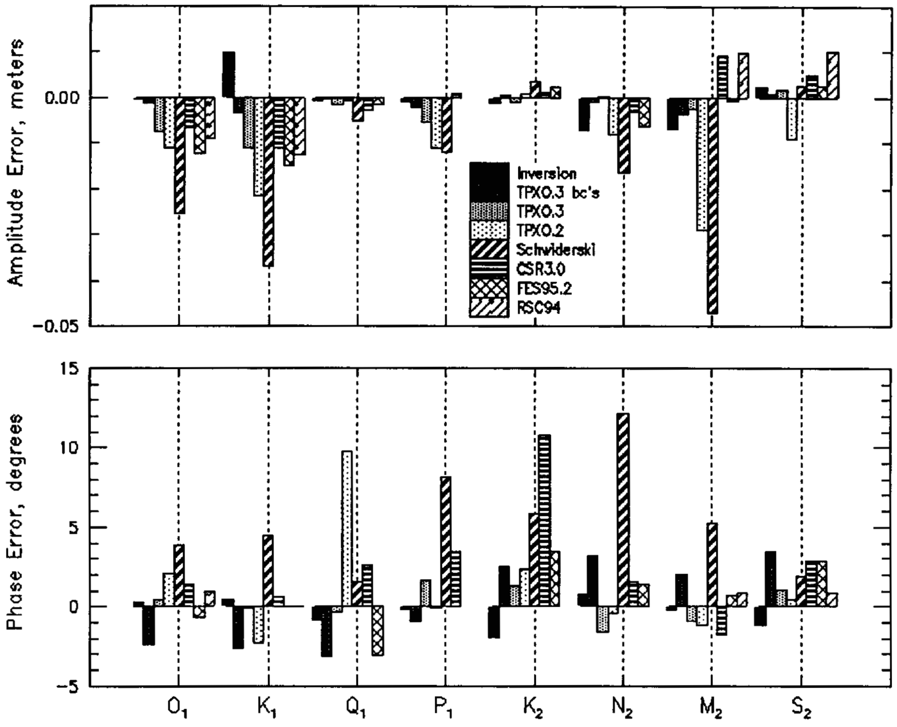

Figure 2.17a Amplitude and phase errors at tide station 1.

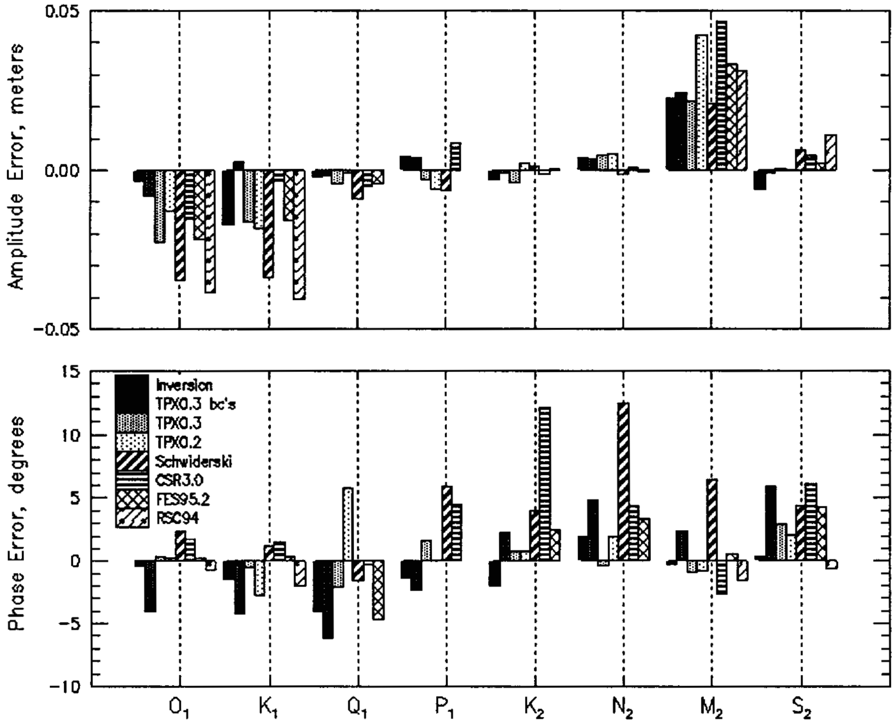

Figure 2.17b Amplitude and phase errors at tide station 2.

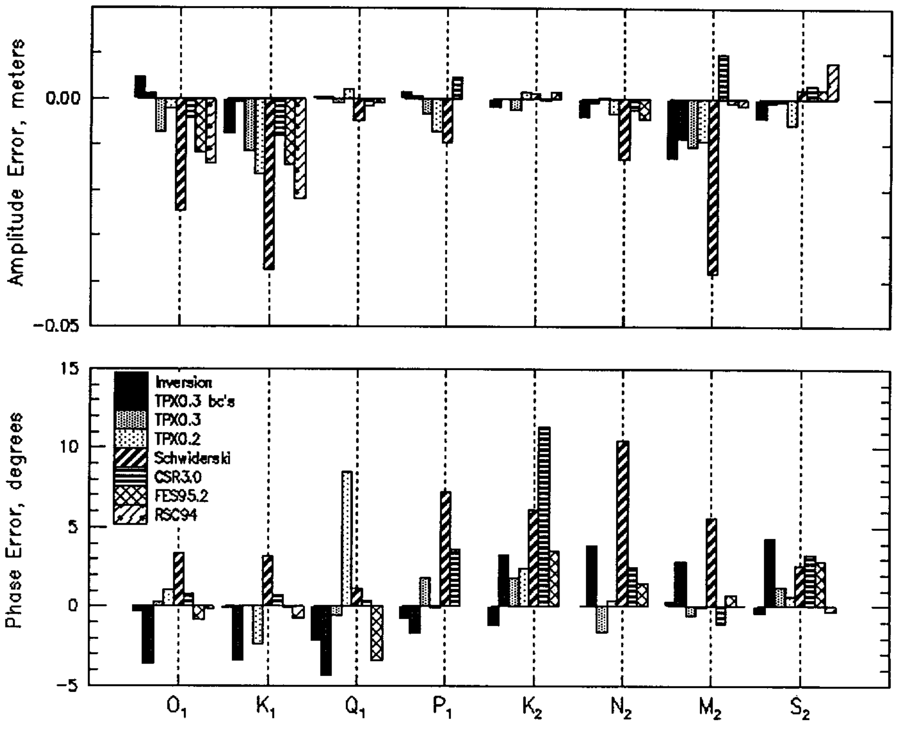

Figure 2.17c Amplitude and phase errors at tide station 3.

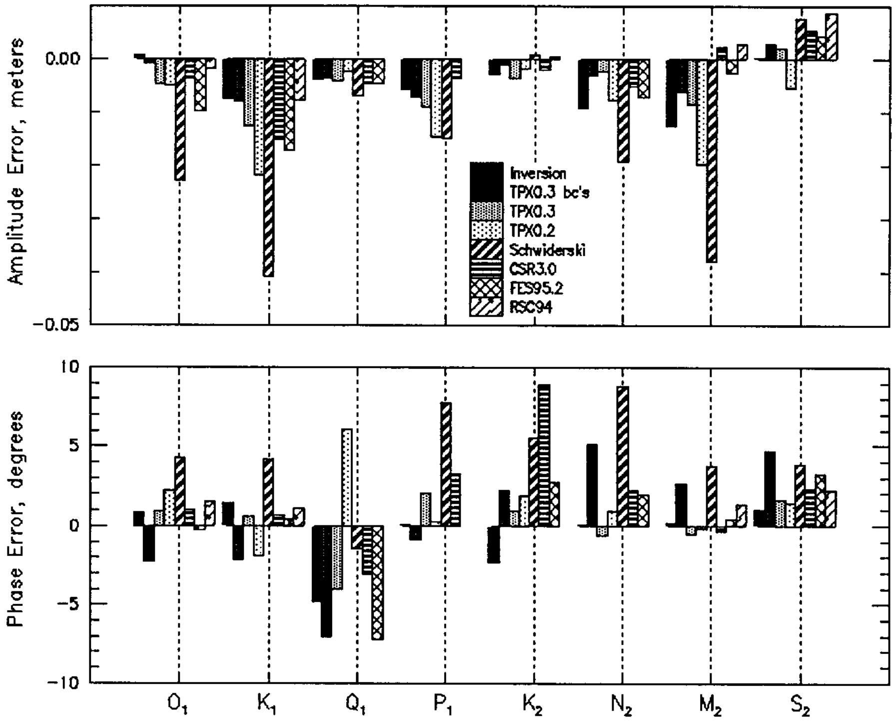

Figure 2.17d Amplitude and phase errors at tide station 4.

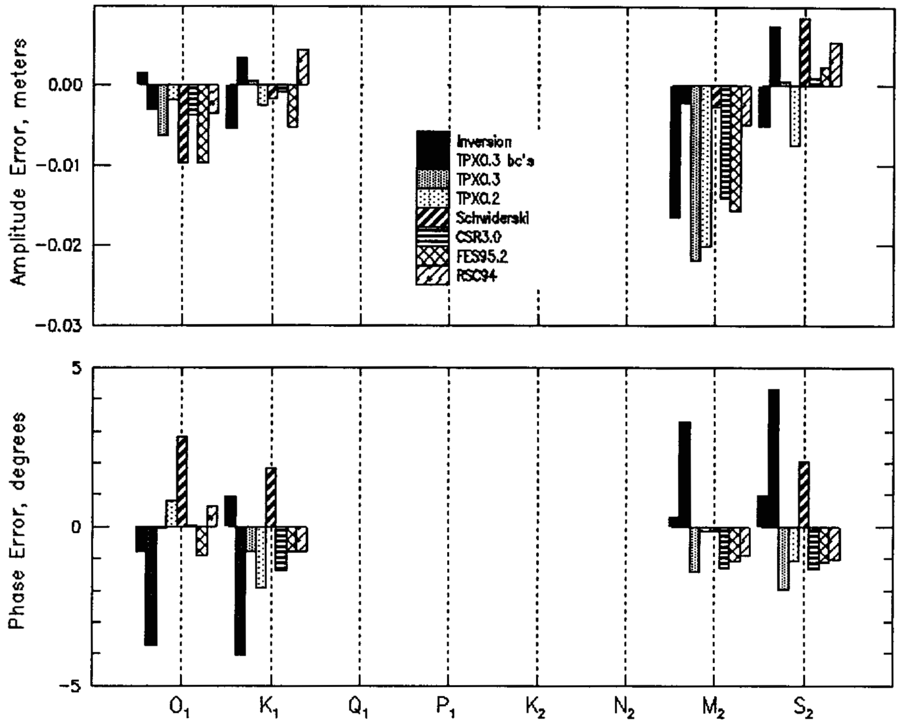

Figure 2.17e Amplitude and phase errors at tide station 5.

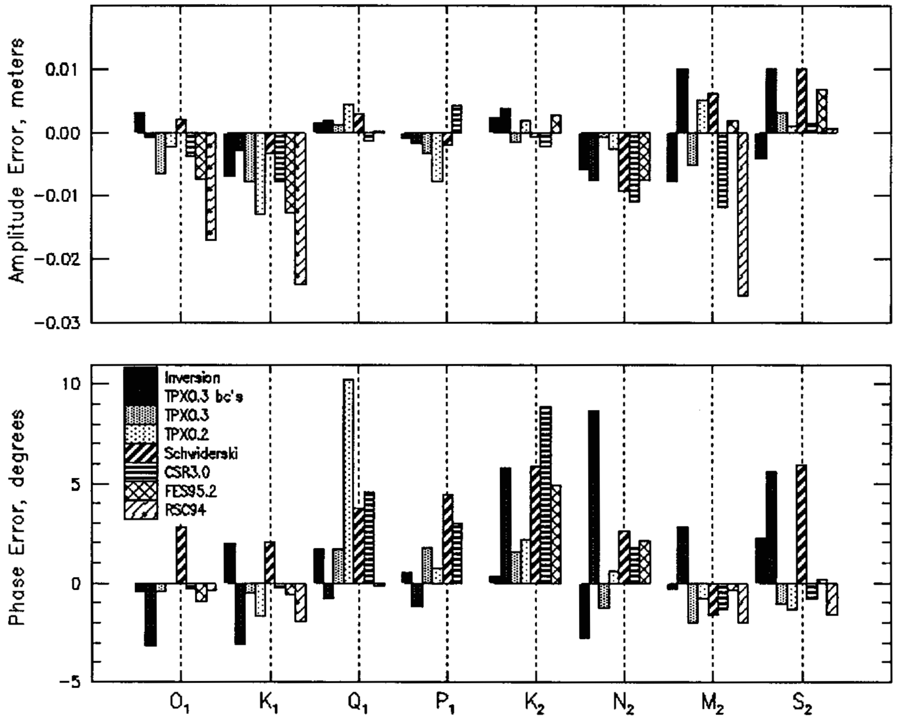

Figure 2.17f Amplitude and phase errors at tide station 6.

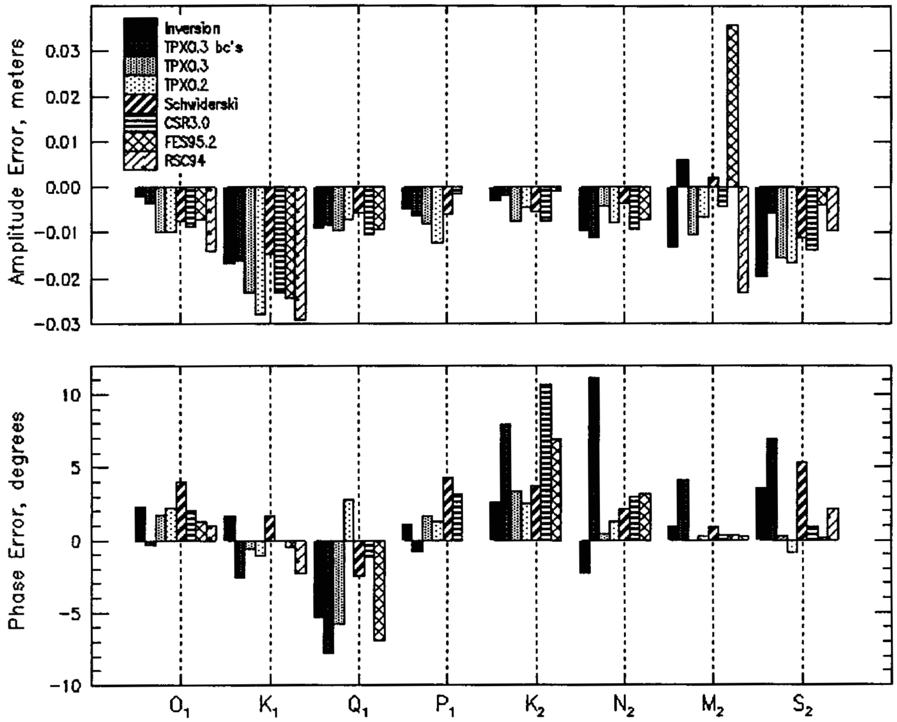

Figure 2.17g Amplitude and phase errors at tide station 7.

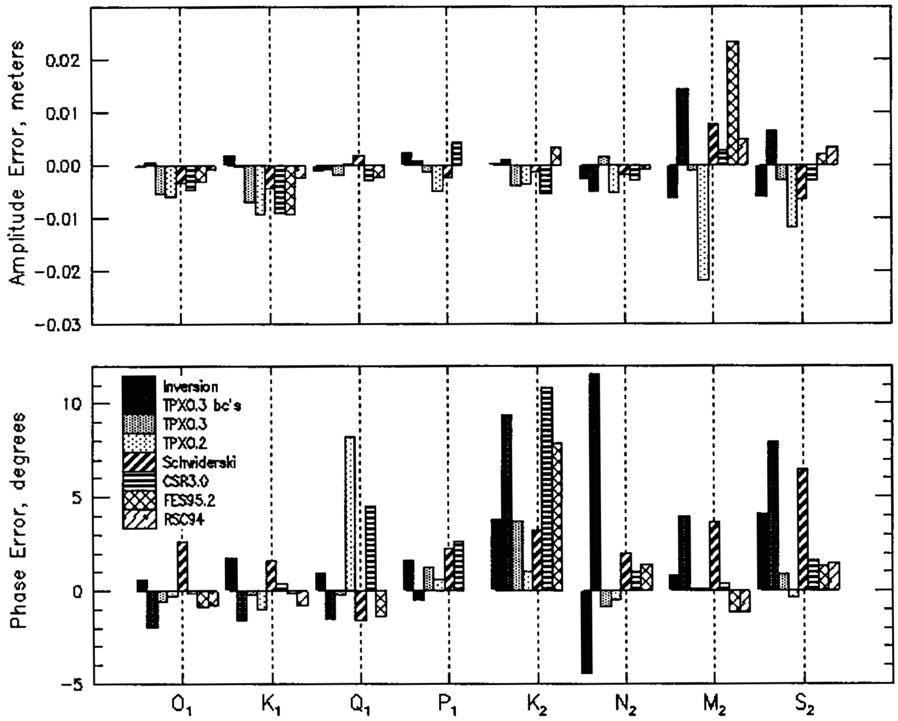

Figure 2.17h Amplitude and phase errors at tide station 8.

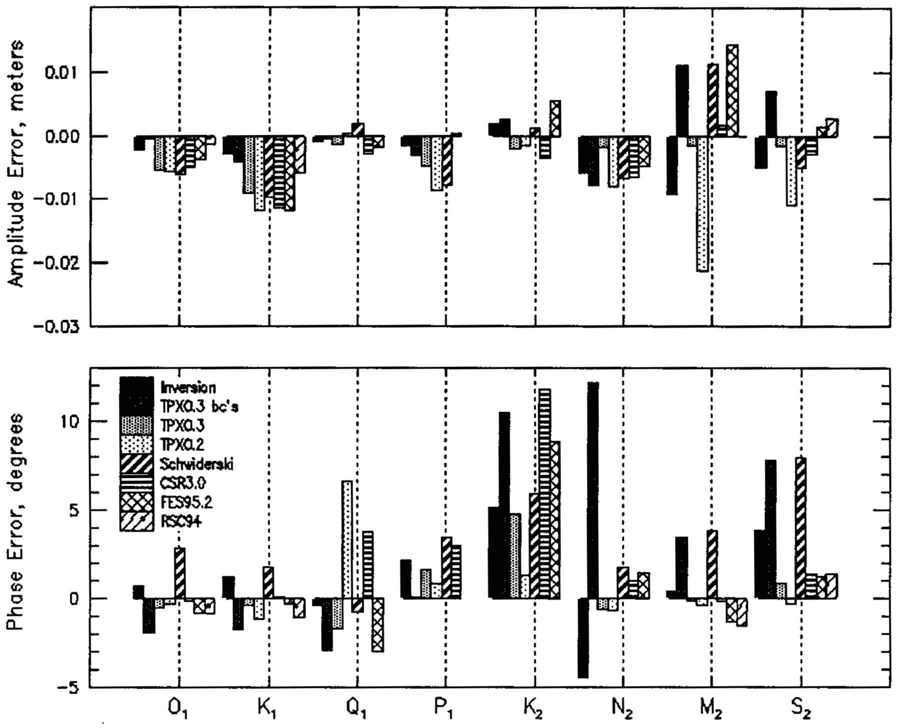

Figure 2.17i Amplitude and phase errors at tide station 9.

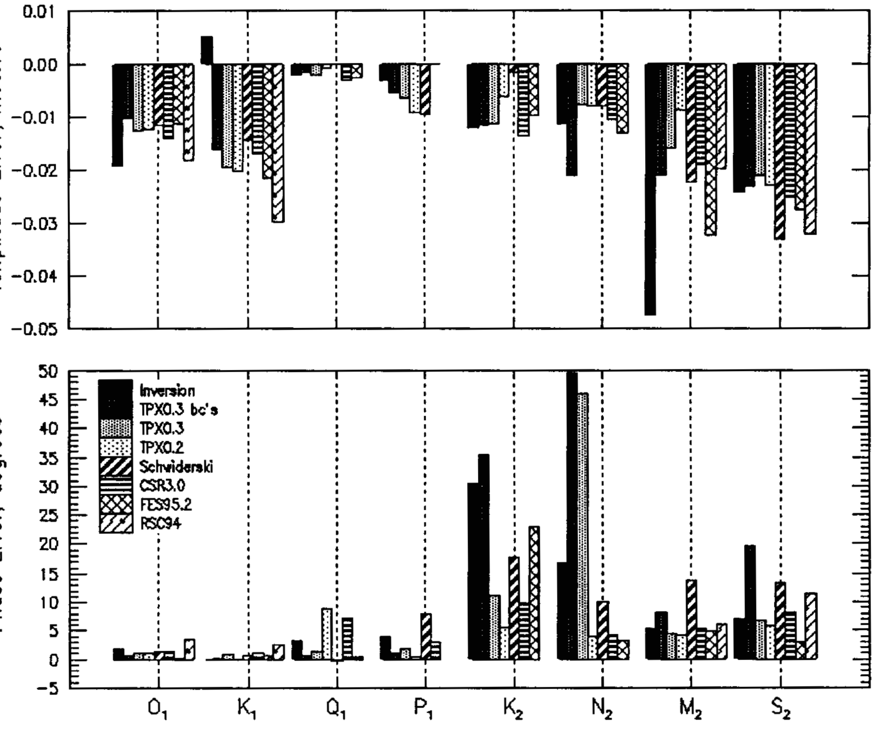

Figure 2.17j Amplitude and phase errors at tide station 10.

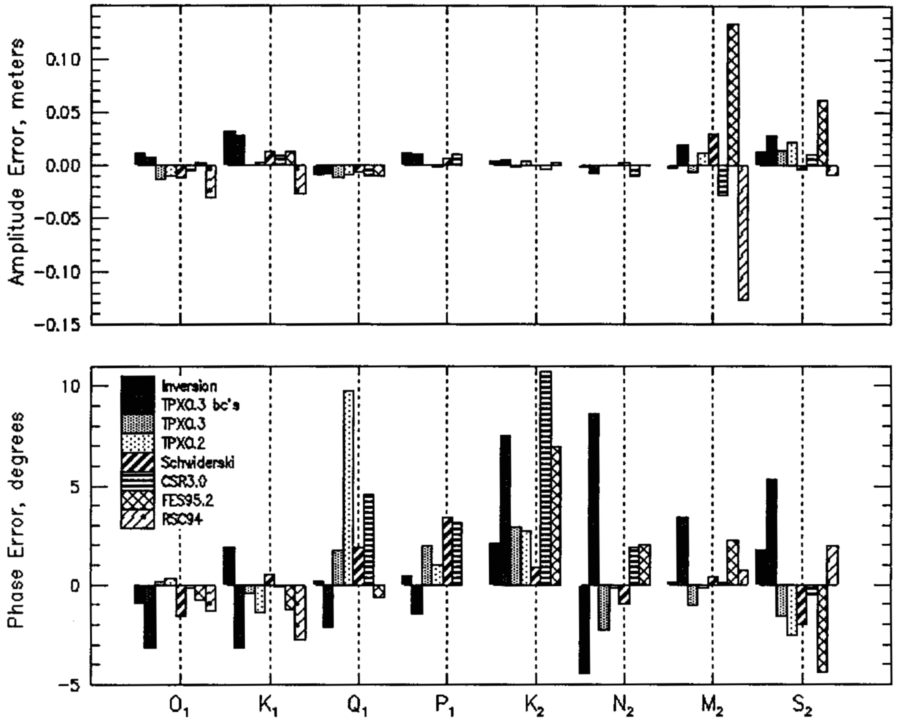

Figure 2.17k Amplitude and phase errors at tide station 11.

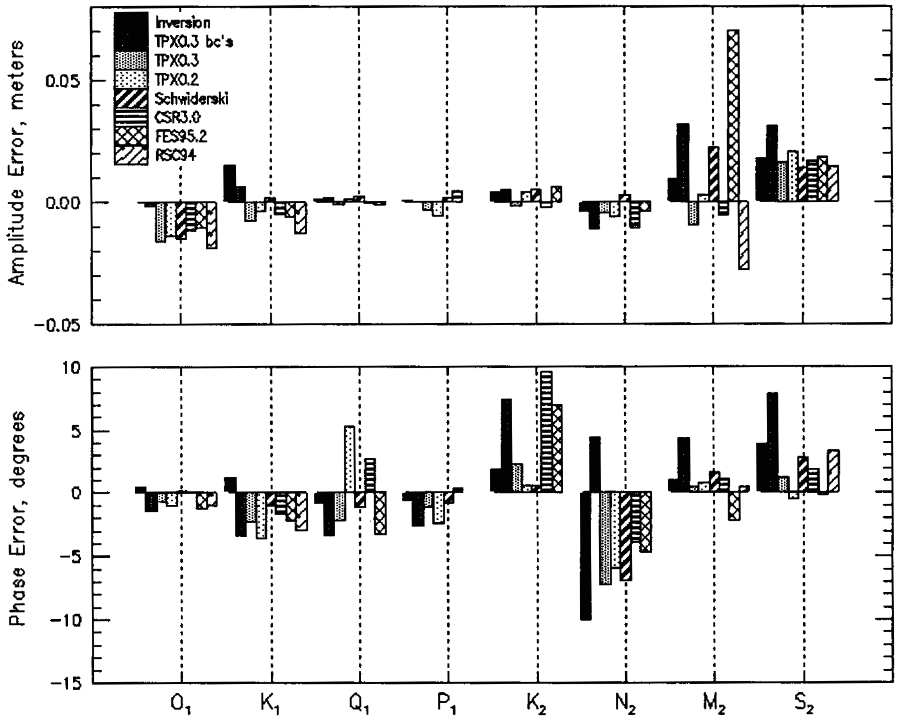

Figure 2.17l Amplitude and phase errors at tide station 12.

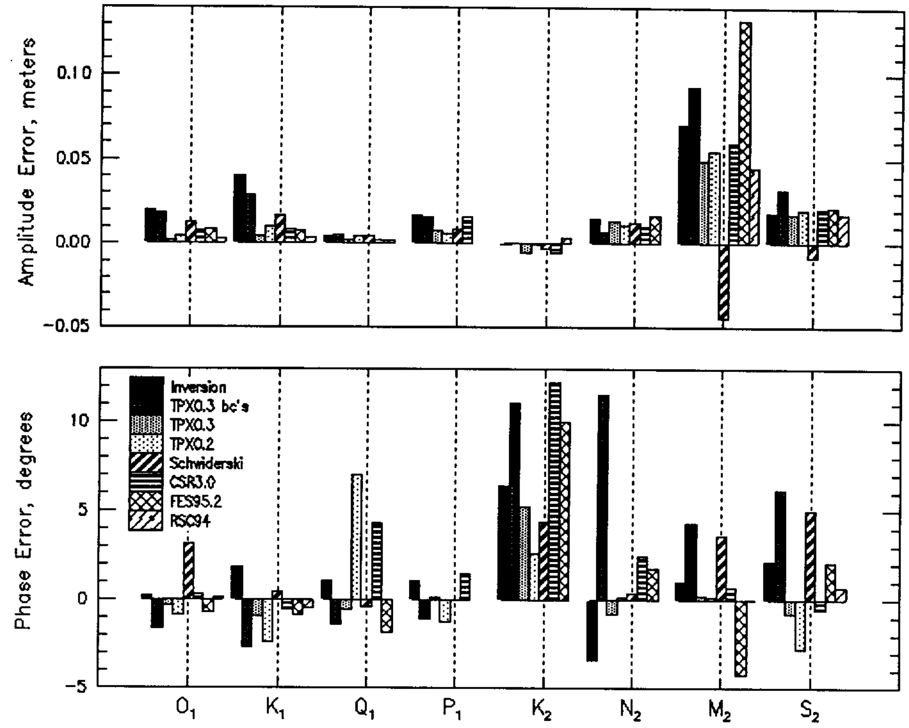

Figure 2.17m Amplitude and phase errors at tide station 13.

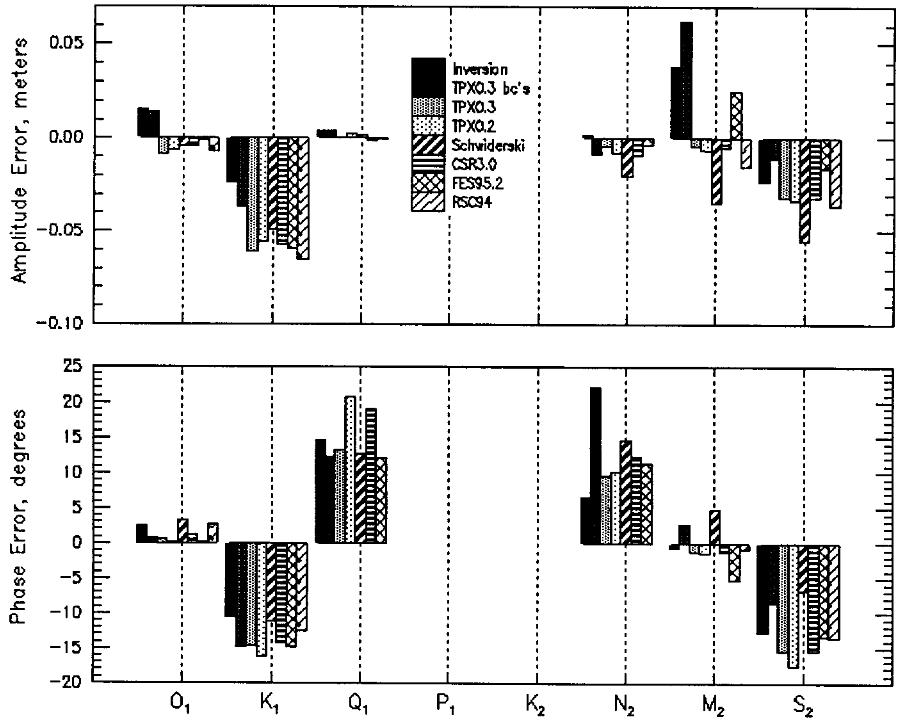

Figure 2.17n Amplitude and phase errors at tide station 14.

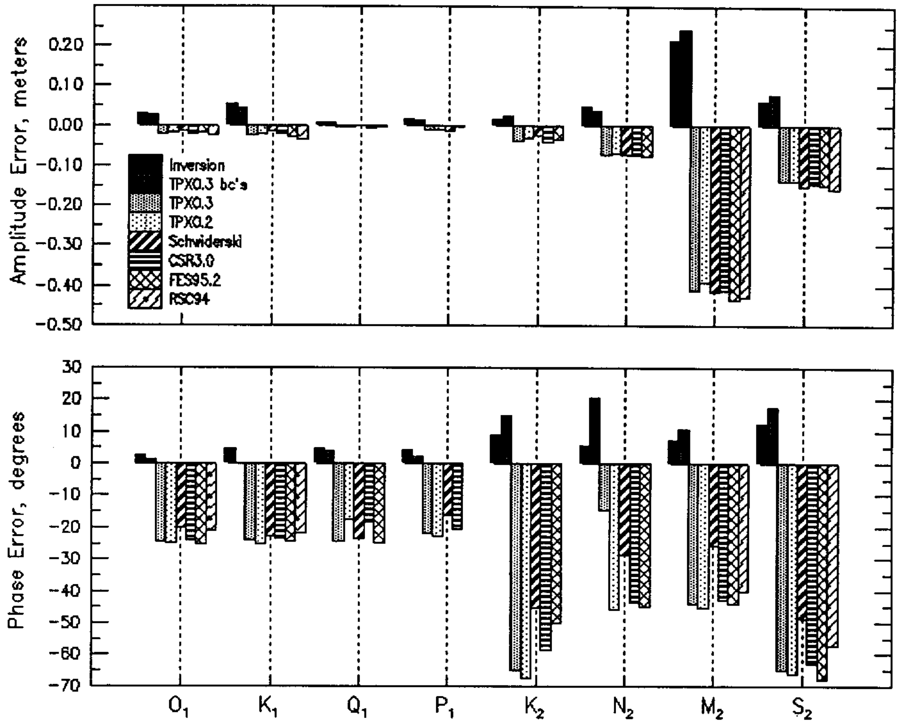

Figure 2.17o Amplitude and phase errors at tide station 15.

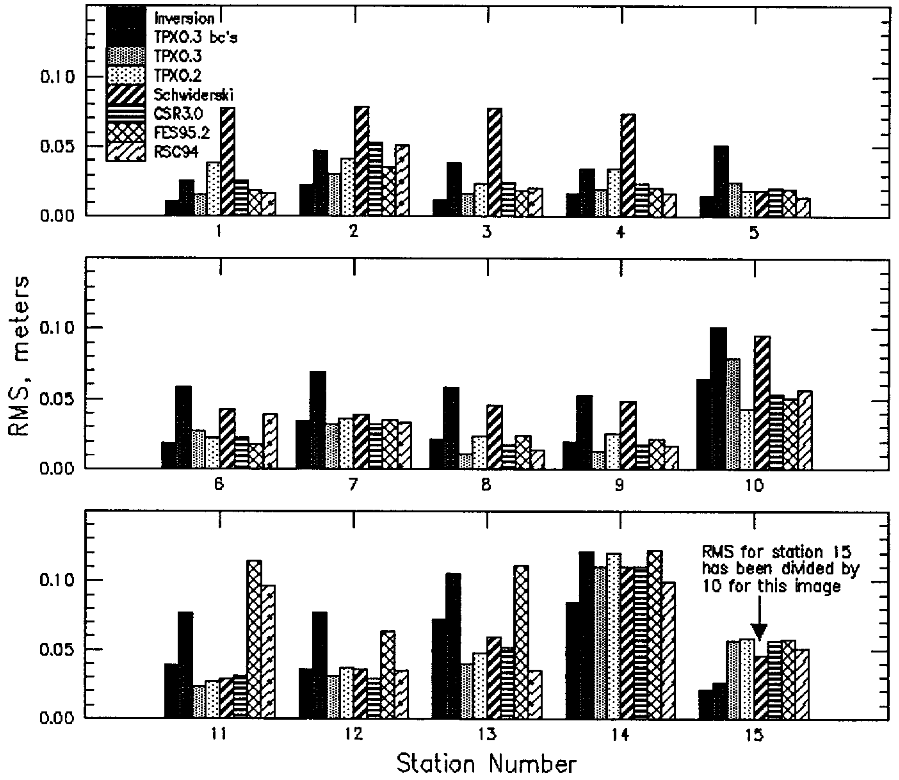

Figure 2.18 RMS errors at tide stations.

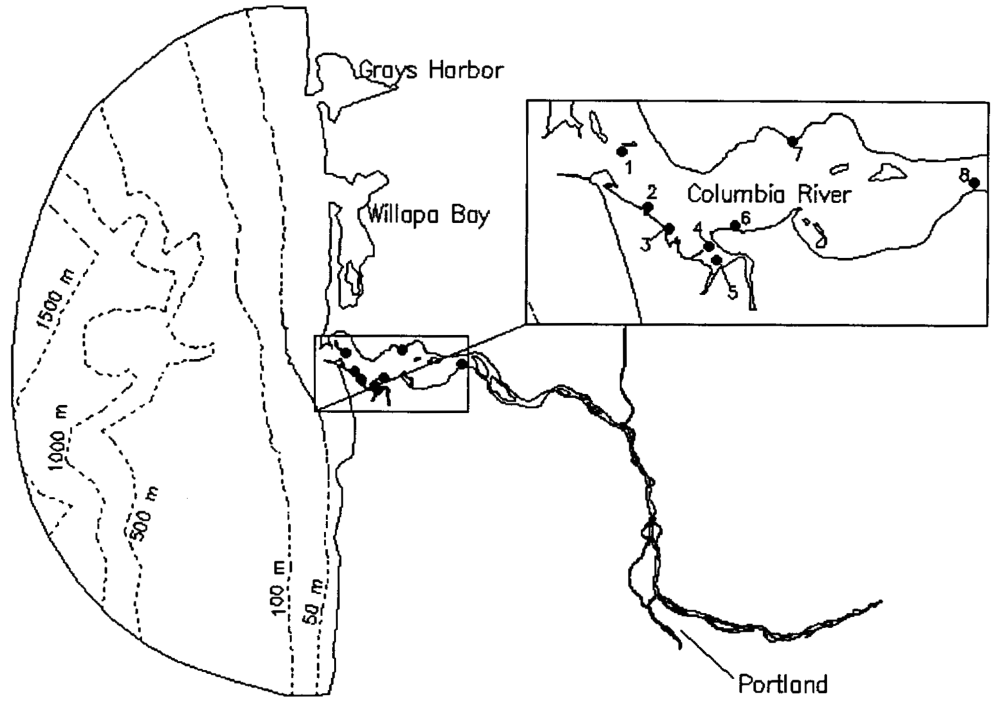

Figure 2.19 Columbia River modeling domain and available tide gauges.

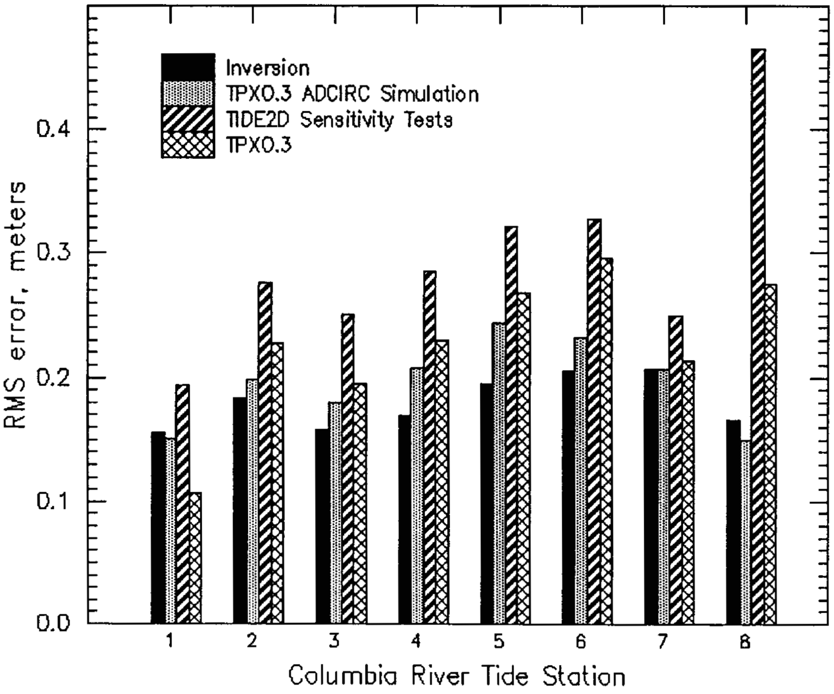

Figure 2.20 RMS errors from simulations in the Columbia River.

CHAPTER 3

Finite Element Modeling of Potential Cascadia Subduction Zone Tsunamis

3.1 Introduction

The primary challenge in evaluating future tsunami hazards is to estimate how future subduction zone earthquakes will occur. Even though no two earthquakes are ever the same, our only clues to what may occur in the future come from what we know happened in the past. We know the northwest coast of the United States has experienced large Cascadia subduction zone (Figure 3.1) earthquakes approximately every 200-600 years, and that the last such event occurred about 300 years ago. The evidence supporting this is summarized by Atwater et al. (1995).

Using available geophysical and geological data from the Cascadia subduction zone, this modeling study aims to reproduce deformations from these earthquakes and to simulate their ensuing tsunamis as an indicator of future hazards for Oregon and Washington coastal communities. The modeled tsunamis will first be analyzed from a regional perspective. While the spatial location, amplitudes, and shapes of the deformations are different among the considered seismic scenarios, the generated tsunami waves will all have to travel through much of the same bathymetry to reach the coast. Thus, the regional bathymetry will be a guiding factor in the ultimate fate of all of the tsunami scenarios. Evaluating the results from a regional vantage will identify the importance of such regional features on elevation, velocity, and wave frequency patterns throughout the domain.

While regional perspectives permit identification of energy focusing mechanisms as the tsunami approaches the coastline, local perspectives are equally important in analyzing what happens to the waves as they interact with the coastline. For example, the 1992 Nicaragua tsunami wave runup observations made by Baptista et al. (1993) indicate that some localities and embayments were subjected to very heterogeneous runup observation differences (on the order of five meters). Local coastline geometry, bathymetry, topography, and resonance conditions can affect the behavior of the waves as they interact between the coast and the continental shelf. To investigate such local phenomena, the finite element grid resolution needs be adequate enough to handle the rapidly changing nature of velocities and elevations in these regions. Such resolution is implemented in the areas of Seaside, OR and Newport, OR, and the modeling results are evaluated in detail for these communities.

The physical interpretation of both the regional and local results will provide clues to the determining factors in the fate of tsunami waves. The numerical interpretation, likewise, is a critical component in helping to assess the usefulness of numerical models in evaluating and mitigating tsunami hazards. The identification of the limits of a numerical model and how those limits can be minimized will in turn allow the physical mechanisms to be better represented and the mitigation to be more effective. It is the mitigation, after all, which is the end result of a study such as this. For example, the state of Oregon is utilizing these results in accordance with State Senate Bill 379 to estimate potential inundation patterns resulting from Cascadia tsunamis. To combine deformation estimates, hydrodynamic models for the tsunamis, and physical interpretation of results for the purpose of hazard mitigation, each component is scrutinized in the remaining sections.

3.2 Initial Conditions: Deformation

Finite element simulations of tsunamis are dependent upon the sea floor deformation resulting from the subduction earthquake. This deformation maps itself through the water column and is therefore treated as an initial condition in the hydrodynamic modeling of the tsunami. Wave and velocity patterns are thus highly dependent upon the assumed deformation along the ocean floor. This deformation must be computed through the use of dislocation models such as those presented by Okada (1985) and Mansinha and Smylie (1971). Dislocation models use fault parameters such as the length, width, dip angle, strike direction, rake angle, and slip to compute the deformation in an elastic half-space. Deformation patterns for most tsunami modeling applications have historically been computed by either assuming some characteristic shape (Hebenstreit and Murty 1989, Ng et al. 1990) or by using a dislocation model that assumes a rectangular fault locked over its entire area prior to rupture (Myers and Baptista 1995, Whitmore 1993). The magnitudes of tsunami waves generated using the latter approach, as compared with tide gauge responses, demonstrate that the deformations appear to be the right order of magnitude. However, there is significant ambiguity incorporated in the assumptions of the fault parameters as well as the location of the locked zone.

A better approach is to incorporate the wide range of three-dimensional heterogeneity of the fault zone into the dislocation model, and to allow transition zones where the slip will be less than that occurring in the fully locked zone. Flück et al. (1997) permit such an approach by not relying on the typical rectangular source formulas for computing deformation in an elastic half-space. Instead, the subduction is represented by the integration of many point sources throughout the subduction zone. Okada (1985) provides the necessary formulas for computing the deformation from either a point source or a rectangular source. Using the algorithm and program provided by Flück et al. (1997), it is feasible to computationally break the fault up into a grid of triangular elements. The nodes of these elements contain information about the horizontal and vertical positions of the fault at that point. Over each triangle, the slip and direction of convergence are specified, which permits varying amounts of slip to be distributed in different regions of the fault zone.

Geist and Yoshioka (1996) followed a similar approach to modeling the deformation by using a three-dimensional elastic finite element model. In that study, rupture along five different types of faults was considered for the Cascadia subduction zone. These included interplate thrust (rupture along the locked zone), décollement (rupture updip of the locked zone), landward and seaward vergent thrust faults (rupture along abrupt branches from the décollement to the surface), and prominent thrust fault rupture near the edge of the continental shelf. The seaward vergent faulting mechanism is theorized (Fukao, 1979) to be characteristic of tsunami earthquakes (earthquakes which generate unusually large tsunamis as compared to the seismic moment). Geist and Yoshioka then use the resulting deformation from each of these faulting mechanisms to simulate possible tsunami impacts from each scenario, assuming different seismic parameters. These simulations are one-dimensional in space, and do not include inundation (although inundation is approximated using various runup laws). The tsunami simulations in that study are not intended to be intensive, but rather illustrative of differences in wave impacts associated with different seismic sources.

The modeling of the deformation proposed here is similar to that of Geist and Yoshioka, in terms of utilizing an elastic three-dimensional source model. The fault scenarios to be considered, though, are somewhat different. Because many of the seaward and landward vergent thrust faults have not been seismically imaged for the entire Cascadia subduction zone (Geist and Yoshioka considered a smaller portion of the zone) and significant controversy still exists regarding the generating mechanism of tsunami earthquakes, these types of faults are not considered here. The most probable generating mechanisms for tsunamigenic earthquakes in the Cascadia margin appear to be interplate and décollement thrust type faults. Therefore, these two mechanisms are evaluated in the contexts shown in Figure 3.2. Three scenarios are evaluated, each of which varies with respect to how the slip is distributed over the seaward transition, locked, and landward transition zones. The first scenario assumes that the locked zone actually extends all the way up to the surface of the sea floor (scenario A). The second assumes that there is a seaward transition zone in which the slip varies linearly (scenario B). The third assumes that there is a seaward transition zone, but that no slip is occurring in this zone (scenario C). Each slip scenario assumes that a landward transition zone exists downdip of the locked zone in which the slip decreases linearly.

Two different cases will be considered, with each case consisting of the three slip scenarios mentioned above. The cases differ only in the placement of the 350° and 450° isotherms. The 350° isotherm is believed to represent the downdip extent of the locked zone due to the onset of quartz plasticity, and the 450° isotherm is theorized to represent the downdip limit of the stable sliding transition zone associated with the onset of feldspar plasticity (Hyndman and Wang, 1993). The first case (case 1, combined with the above slip scenarios: 1A, 1B, and 1C) assumes the positions of these two isotherms from Hyndman and Wang's (1995) finite element model of the thermal regime. The second case (case 2, combined with the above slip scenarios: 2A, 2B, 2C) positions these two isotherms based on paleoseismic evidence. While Hyndman and Wang's isotherms are well constrained north of the Columbia River by geophysical data, poorer constraints south of this point lead to greater uncertainties, particularly in terms of comparisons with estimates of the deformation from paleoseismic data. Priest (1995) concluded that south of the Columbia River, it would be more appropriate to use limits for the landward transition zone which are different from the 350° and 450° isotherms of Hyndman and Wang. Priest derived such limits based upon paleoseismic data and previous deformation models in the Cascadia Subduction Zone. Thus, the second case considered will use Priest's limits for the landward transition zone south of the Columbia River. It should be reiterated that both cases consider three different scenarios that differ in the way slip is distributed in the seaward transition zone, the locked zone, and the landward transition zone. The isotherms for both cases are shown in Figure 3.3 along with the positions of the surface of the fault zone and the seaward transition zone that were provided by Goldfinger (1996).

In addition to these six deformation models, several shorter segment breaks will be considered. In 1995, Geomatrix Consultants performed a probabilistic acceleration map for the state of Oregon which included probability estimates of the type and recurrence interval of Cascadia subduction zone earthquakes. This study concluded that a rupture length of 450 km was most probable. Despite the fact that recognized geologic evidence indicates recurrence intervals longer than 300 years, the probability study concluded that for a 450 km rupture length, a 225 year recurrence interval should be assumed. Using locations of local marine terraces and faults, Priest et al. (1997) concluded that 450 km rupture scenarios should be bounded (either above or below) by the 44.8° latitude near Depoe Bay, Oregon. Segment scenarios based on the case 2 isotherms will be considered both to the north and to the south of this latitude, extending 450 km in length (2CN and 2CS).

The depths of the Cascadia subduction zone fault were provided by Flück et al. (1997). The dip angles of the fault zone are calculated using these fault depths in the dislocation model. The magnitude and direction of slip for each node in the deformation grid were computed using convergence rates between the plates (program provided by Kanamori, 1996). Utilizing the North America-Juan de Fuca Euler vector computed by DeMets et al. (1990), slip magnitudes and directions were computed assuming a 450 year interval between earthquakes. The 2CN and 2CS scenarios, however, assumed a 225 year interval.

Patterns of deformation for each scenario are shown in Figures 3.4a-h. The width of the deformation region in each case is larger in Washington, particularly northern Washington. Notice also that scenarios without a seaward transition zone (1A, 1C, 2A, 2C, 2CN, 2CS) exhibit a pronounced spike of uplift on the seaward side. This is due to the fact that deformation models tend to conserve the volume of deformation. Thus at the seaward end of the locked zone, the model cannot assume the plates move any further along the fault dip and the primary direction for the ground to move is upward. This creates a spike of deformation, which may or may not completely be physical. How realistic this is depends on how inelastic the deformation is at the edge of the locked zone.

Cross sections of deformation at the latitude of Newport, OR are shown in Figure 3.5a for all of the scenarios considered. A similar graph of cross sections at the latitude of Seaside, OR is presented in Figure 3.5b. Scenarios 1A and 2A (fully locked to the surface) have large peaks of uplift near the deformation front. Case 2 has more volume of uplift for the three slip scenarios than Case 1, and the region of subsidence for Case 2 is located further towards the land than Case 1. The 2CN and 2CS scenarios are essentially one-half of the 2C deformation for the pertinent latitudes (2CN for Seaside and 2CS for Newport). Note also that, due to the assumptions in the slip distribution among the A, B, and C scenarios, the maximum uplift occurs at different distances away from the coastline for each scenario.

3.3 Description of the Model: Governing Equations and Inundation Algorithm

In this study, the finite element model ADCIRC (Luettich et al., 1991) is used to propagate waves in the open ocean until they reach the coastline, at which point inundation is allowed to occur. A recent extension of ADCIRC to allow for inundation and added matrix solver options (Luettich and Westerink, 1995a-b) ensures that the state-of-the-art in finite element modeling is used here. The use of a finite element method for the hydrodynamic modeling allows the discretization to vary depending upon the bathymetric domain and numerical criteria. The coastline and topographic features may also be better approximated, and the seismic source is more accurately depicted in an unstructured grid. The seismic source was imposed in ADCIRC by adjusting the kinematic boundary condition to allow the ocean floor to dynamically move over three time steps. This is essentially equivalent to mapping the bottom deformation into the water column directly.

ADCIRC uses a generalized wave continuity formulation to supplant the primitive continuity equation, a technique that has proven to avoid the spurious $2\Delta x$ oscillations of early finite element applications. The modified generalized wave continuity equation (GWCE) is derived as a summation of the time derivative of the continuity equation, the primitive continuity equation weighted by a factor, and the spatial gradient of the momentum equations expressed in conservative form. The GWCE is used to solve for elevations, and velocities are determined from the non-conservative form of the momentum equations. The final forms of the GWCE and momentum equations are written as:

$$\begin{gathered}
\frac{\partial^2\eta}{\partial t^2}+G\frac{\partial\eta}{\partial t}-\frac{\partial^2\gamma}{\partial t^2}-G\frac{\partial\gamma}{\partial t}+\\
\frac{\partial}{\partial x}\left\{u\frac{\partial\eta}{\partial t}-uH\frac{\partial u}{\partial x}-vH\frac{\partial u}{\partial y}+fvH-H\frac{\partial}{\partial x}\left[\frac{p_s}{\rho_0}+g(\eta-\alpha\Psi)\right]\right\}+\\
\frac{\partial}{\partial x}\left\{-E_h\frac{\partial^2\eta}{\partial x\partial t}+\frac{\tau_{sx}}{\rho_0}-(\tau-G)uH\right\}+\\
\frac{\partial}{\partial y}\left\{v\frac{\partial\eta}{\partial t}-uH\frac{\partial v}{\partial x}-vH\frac{\partial v}{\partial y}-fuH-H\frac{\partial}{\partial y}\left[\frac{p_s}{\rho_0}+g(\eta-\alpha\Psi)\right]\right\}+\\
\frac{\partial}{\partial y}\left\{-E_h\frac{\partial^2\eta}{\partial y\partial t}+\frac{\tau_{sy}}{\rho_0}-(\tau-G)vH\right\}=0
\end{gathered}\tag{1}$$

$$\begin{gathered}
M\equiv\frac{\partial\vec{u}}{\partial t}+\vec{u}\bullet\nabla\vec{u}+\vec{f}\times\vec{u}+\tau\vec{u}+\nabla\left[\frac{p_s}{\rho_0}+g(\eta-\alpha\Psi)\right]+\\
\frac{E_h}{H}\left[\frac{\partial^2 uH}{\partial x^2}+\frac{\partial^2 vH}{\partial y^2}\right]+\frac{\tau_{sx}}{\rho_0 H}=0
\end{gathered}\tag{2}$$

where η is the free surface elevation, (u, v) are the depth-averaged velocities, H is the total water column, G is a weighting factor, γ is the bottom deformation (positive for uplift), $\vec{f}$ is the coriolis vector, α is the effective Earth elasticity factor, Ψ is the Newtonian equilibrium tide potential, E_h is the horizontal eddy diffusion coefficient, $\tau_{s\bar{x}}$ is the applied free surface stress, τ is the bottom friction, c_f is the bottom friction coefficient, p_s is the atmospheric pressure at the free surface, ρ_0 is the reference density of water, and g is the acceleration due to gravity. A Manning formulation is used to represent bottom friction. Further details about the derivation of equations (1) and (2) are provided by Myers and Baptista (1995).

Dirichlet boundary conditions may be imposed in one of three manners: 1) elevations may be specified in the GWCE, 2) velocities may be enforced in the momentum equations, or 3) normal velocities may be set equal to zero to represent a no-slip condition. Transmissive boundaries have been added to ADCIRC using the first of these methods. A Lagrangian technique is used whereby the elevation at a boundary node is specified by backtracking a distance ct $\left(c=\sqrt{gH}\right)$ in a direction determined by the nodal velocities $\theta = \text{atan}(v/u)$ and interpolating the elevation from the previous time step at this location.

Inundation is handled inside ADCIRC through the use of an element based wetting and drying implementation (Luettich and Westerink, 1995a-b). Elements are turned on if they are considered wet and turned off if they are considered dry. Nodes are classified at each step as either being wet, dry, or interface nodes. Dry nodes are connected only to dry elements, interface nodes are connected to both wet and dry elements, and wet nodes are only connected to wet elements. Dry nodes are constrained to have a minimal water level and zero velocity, interface nodes have an imposed no slip condition, and wet nodes are not constrained in any manner.

Elements are allowed to dry if the water level at a node falls below a specified minimum value. If the node has recently become wet, though, the user may control the number of time steps before the node is permitted to dry (for stability purposes). Wetting of interface nodes may occur if the water level gradient favors motion toward all dry nodes connected to that interface node.

3.4 Modeling Results

3.4.1 Grid Setup

The semi-automatic grid generator, ACE/gredit (Turner and Baptista, 1991), permits interactive development of finite element grids. Such a flexible tool is critical in assembling a grid, as the manner in which elements are interconnected will influence the amount of numerical error introduced during a simulation. Some common rules in the grid construction include: 1) ensuring that the grid spacing abides by the Courant number $\left(\Delta t\sqrt{gH}/\Delta x \leq 1\right)$, 2) there should be at least 40 nodes per wavelength of interest, 3) the number of elements surrounding one node should be less than eight, 4) the skewness (maximum length of any side of an element divided by the equivalent diameter) should be kept as small as possible, and 5) there should be an even transition between larger and smaller elements. In addition, elements on land that may be inundated need to be much smaller (than wet elements) in order to facilitate a better representation of the wetting and drying process.

Using these criteria, two different grids for tsunami simulations were used in this study. Grid 1 is displayed in Figure 3.6a and extends from the Aleutian Islands to central California. Grid 2 is displayed in Figure 3.6b and extends between northern Washington and northern California. Both Grid 1 and Grid 2 have the same level of refinement in the Seaside and Newport regions. These two communities were selected to evaluate the local behavior of the waves in the estuaries and as the waves inundated the land. Figures 3.7a and 3.7b portray the differences between the two grids near Seaside and Newport, respectively. The grids are virtually the same near these two communities, but Grid 2 has more refinement along the rest of the coastline and in deeper waters. If the Grid 1 resolution is insufficient to propagate all the frequencies of the tsunami, then such insufficiencies should surface as differences between the results on the two grids. Figures 3.8a and 3.8b show enlargements of Seaside and Newport, respectively. A map scale is also included in these figures for spatial reference. The smallest elements are on the order 5-10 meters wide and are generally situated in areas where the velocities are expected to be large, such as in the entrances to the estuaries.

Bathymetry and topography were interpolated onto the finite element grids. The sources of these databases include NOAA/NOS hydrographic surveys, digitized NOAA charts, local bathymetric surveys (Goldfinger, 1996), USGS topographic data, and digital elevation models.

3.4.2 Regional Modeling Results

Results will first be evaluated from a regional perspective, thus permitting a preliminary vantage of what mechanisms affect the propagation of the waves before they reach the shoreline. It should first be mentioned that the Cascadia simulations do not include the influence of tides. The results shown here, rather, were generated assuming that mean higher high water (MHHW) exists throughout the duration of the simulation. MHHW is assumed for safety purposes, because it is instructive to evaluate the impact of the tsunami at maximum water levels. This research was performed before Myers and Baptista (1998a), a study that evaluates the nonlinear interactions between tides and tsunamis. The various safety factors used throughout the entire process needed to create inundation maps for the state of Oregon most likely compensated for this nonlinear tide-tsunami effect, yet it should be kept in mind that future mapping should account for such influences.

Bathymetry is the primary feature that will affect the manner in which the tsunami waves are propagated to the coastline. Figure 3.9 displays some of the bathymetric features for the domain of interest. First, a comparison should be made between this figure and Figure 3.3. The latter figure shows that the subduction zone extends further away from the coast in the higher latitudes. The exception to this is off the coast of Vancouver Island, but in general the deformation occurs in deeper waters the further north one is located. The implication of this is that waves initially generated in larger depths have more of an opportunity to amplify as they propagate towards the coast. This is due to the fact that waves increase in amplitude and decrease in wavelength as they travel into shallower water. Thus, the first incoming waves generated off the coast of northern Oregon and Washington will most likely be larger than those generated off the coast of southern Oregon.

Since the rake angle of the fault zone leads to deformations that are oriented almost north to south, the initial waves will be travelling in an approximate west-east manner. The heterogeneities in north-south transects of the bathymetry, therefore, will play an important role in the convergence or divergence of wave energy into certain regions. For example, Figure 3.9 shows some of the canyons, banks, and valleys throughout the domain that will affect the wave propagation. The shallow banks off the central coast of Oregon, for example, will slow down and amplify the waves passing over them. To the north and south of these banks, the waves will be traveling faster, thus creating a focusing effect of the entire wave front as it is bent towards the Alsea and

Yaquina bay vicinities. Such prominent effects are also present in northern Oregon and Washington, primarily due to canyons protruding into shallower waters.

Modeling results will now be evaluated in the context of regional wave patterns throughout the domain. Results from seven different simulations are presented, each of which uses a different source scenario for the initial conditions (1A, 1C, 2A, 2B, 2C, 2CN, and 2CS). 1B is not simulated because comparisons of 2B to 2A and 2C are sufficient to infer results from 1A and 1C simulations. In order to differentiate between these seven simulations, it is useful to evaluate the maximum coastal wave heights that are generated over the duration of each simulation. Figure 3.10a shows these maximum coastal wave elevations for the seven simulations that were made on Grid 1. Two of the scenarios (1A and 1C) were also simulated using Grid 2, the results of which are included in Figure 3.10a. Recall that Grid 1 and Grid 2 essentially have the same refinement in Newport and Seaside, but Grid 2 has more refinement along the rest of the coastline and through most of the domain.

On grid 1, scenario 1A generally has larger wave heights than 2A, and similarly 1C has larger wave heights than 2C. Most of the differences between "1" and "2" scenarios occur south of Willapa Bay down to California. This area south of Willapa Bay is where the landward transition zone was moved eastward in order to create the "2" cases. Due to this shift of the landward transition zone, the "1" scenarios have more volume of deformation occurring along the ocean floor as well as more subsidence occurring along the ocean floor. The increased volume obviously leads to more displacement of water in the initial waves that in turn could lead to higher runups at the coastline. The more subsidence occurring along the ocean floor for the "1" scenarios could also lead to higher runups, as Tadepalli and Synolakis (1994) have shown that leading depression waves generally lead to larger wave runups onto land.

Scenarios 1A and 1C give fairly similar results for Oregon and California. This is an interesting result, considering the cross sections of deformation shown in Figures 3.5a and 3.5b for Newport and Seaside. The shape and position of the 1A and 1C deformation uplifts are different enough to expect different wave heights along the coastline.

However, the subsidence for each case is almost identical, and perhaps more importantly, the volume of uplift is almost identical. Above Oregon, 1C shows higher coastal wave elevations than 1A, due to the fact that there is generally more volumetric uplift occurring along the ocean floor in these areas. Results among the 2A, 2B, and 2C scenarios are fairly similar from California through central Oregon (for the same reason that 1A and 1C were similar in Oregon and California). Above central Oregon, the 2A, 2B, and 2C scenarios begin to differ in the volume of uplift occurring: 2C has more volumetric displacement than 2B which has more displacement than 2A. The resulting wave heights are commensurate with this.

Scenarios 2CS and 2CN yield values that are about one half the values of the other scenarios, owing to about half as much deformation. This is due to the fact that 2CN and 2CS assumed only a 225 year interval between earthquakes, as compared to the 450 year interval for the other scenarios. The 2CN simulation resulted in larger wave heights in the northern part of the domain and smaller wave heights in the southern part. The southern wave heights from 2CN resulted from the trapping and propagation of waves along the shelf and coastline. As would be expected, the 2CS simulation yielded higher wave heights in the south than 2CN, but also led to significant waves in the northern part of the domain. Thus it appears that with segmented deformation scenarios, waves have more of a propensity to move north along the coast than they do to move south.

From a numerical modeling perspective, the most interesting results in Figure 3.10a derive from the differences between simulations made on Grid 1 versus those made on Grid 2. For both 1A and 1C, the Grid 2 simulations led to higher coastal wave elevations. The 1A differences were largest in the southern part of the domain and along the central and northern Oregon coastline. Differences in the 1C simulations were more evenly distributed throughout the entire domain, although larger wave height increases did occur in California and Washington. Clearly, though, energy is being lost in the Grid 1 simulations. This may be due to phenomena such as numerical diffusion, truncation errors, or assumptions in the shallow water equations. The energy may be lost in Grid 1 as the waves reach the coastline and/or as the waves propagate towards the coastline. Myers and Baptista (1998b) dissect the potential sources of such energy loss in tsunami simulations by evaluating nodal energy errors and truncation errors. The importance of these differences is far-reaching for regional tsunami modeling. Both Grid 1 and Grid 2 are approaching 100,000 nodes in the finite element grid. Such grids could not be used a few years ago and are currently pushing the limits of today's state-of-the-art computers.

Figure 3.10b shows the maximum coastal velocity magnitudes for the same simulations. A running average filter was applied to smooth the magnitudes for better viewing. The interpretation of these results is commensurate with that of the elevations. One difference of importance, though, lies in the velocity magnitudes in Newport and Seaside, Oregon. The reason that the velocities are higher in these two vicinities is most likely associated with the added grid refinement there. The added grid refinement therefore allows the kinetic energy to be better preserved. This is further emphasized by the general differences between Grid 1 and Grid 2 velocity results. Figure 3.11 shows some of the actual differences between the two grids. For each element in each grid, the average depth was calculated and plotted against the equivalent diameter (a measure of the grid spacing) for that element. This figure clearly shows the level of increased refinement attained in Grid 2.

The effect of the bathymetry upon elevations and velocities is more clearly viewed by examining isolines throughout the entire domain. Figures 3.12a-g display the isolines of maximum elevation for each of the scenarios. Each figure shows isolines for the same elevation values, for comparative purposes. The isolines for each scenario clearly show where the initial waves were generated, as indicated by the darker regions near the deformation front. More interesting, though, are the visible bathymetric conduits through which the tsunami energy is channeled. For the full segment scenarios, regions of higher elevation connecting the deformation front to the coastline can be seen along the shallow banks off of central Oregon (Stonewall, Perpetua banks) and to the north and south of the most prominent canyons (Astoria and Grays canyons). While the maximum coastal elevations are more clearly seen in Figure 3.10a, it is interesting to note that scenarios 2A, 2B, and 2C show increased wave elevations around Crescent City, CA and Humboldt Bay, CA. The increases in these areas may be associated with geometry effects from the coastline, yet the "1" scenarios do not show as much increased energy in those regions. The 2CN and 2CS half segment scenarios show some of these same conduits. They also show that the 2CS simulation affects the northern part of the coastline (i.e. north of the 2CS segment) more than the 2CN simulation affects the southern part (i.e. south of the 2CN segment).

While this paper concentrates on the tsunami effects along the west coast of the United States, Figures 3.12a-g also emphasize the need to examine the tsunami impact along Vancouver Island's coast. The deformation occurring off the coast of Vancouver Island is generally larger than other places, and therefore the generated waves contain more energy. While much of the affected Vancouver Island coastline is contained within the Pacific Rim National Park and thus uninhabited, many of the inlets could channel and potentially amplify the waves into ports such as Port Alberni and Port Renfrew. More grid resolution would need to be added to such areas to determine such effects.

Figures 3.13a-g show equivalent isoline plots for velocity magnitudes. The increased velocities along the shallow banks are particularly noticeable. The full segment scenarios also demonstrate the higher velocities that occur off the coasts of Washington and Vancouver Island. The geometry of the coastline in northern California is such that velocities and elevations appear to be enhanced as the tsunami waves meander along the shoreline and continental shelf.

The effect of regional features such as bathymetry should be seen in the changes in the frequency components of the tsunami waves. Figures 3.14a-b show isolines of the first and second dominant periods, respectively, for the 1A-Grid 2 simulation. These results were obtained by passing the elevation time series at every node through a power spectrum filter and then plotting the first and second most dominant periods. These isolines of dominant periods have three significant implications. First, the bathymetric influence on frequency modulation is clearly evident for the Stonewall/Perpetua banks, the extended shallow bank off the coast of northern Oregon, and the shallow bank centered off the coast of Grays Harbor. Second, since the bathymetry off the coast of northern California is not too unusual, it appears that the coastline geometry of this region is such that the behavior of the waves is noticeably changed as exemplified by the period, elevation, and velocity patterns. Third, the period changes in the above mentioned regions is non-intuitive from the vantage of the waves first arriving from the west. The dominant periods increase during this initial passage of the waves, as shown by the darker colors. As the waves continue east towards the shore, the dominant periods eventually decrease as would be expected. The question thus arises as to why the dominant periods increase as the waves first pass through these areas. Since the increase in periods is also seen along much of the coastline, it is possible that higher frequency information is being lost as the waves travel through certain bathymetric gradients. Such aliasing of energy from high frequency components to low frequency components may be occurring due to such influences as numerical diffusion, truncation errors, and/or energy errors.

As mentioned, the results presented in this study assumed an added water level commensurate with mean higher high water. Figure 3.15 shows the maximum coastal wave elevations for a simulation that was performed with simultaneous imposition of tides and the tsunami. The graph on the right in this figure exemplifies the significance of tide and tsunami interactions. The imposition of the tsunami was arbitrarily chosen to start at some point in the tidal cycle. For this particular tsunami generation time within the tidal cycle, the maximum tsunami elevations in the south seem to generally be damped due to interaction with the trough of the tidal components. However, the timing for this scenario is such that maximum elevations in northern Oregon occur as a result of positive interference between the tide and tsunami waves, thus resulting in larger than expected wave heights. This figure alludes to the importance of tide and tsunami interactions, and future inundation maps should attempt to capture this effect as best possible.

3.4.3 Local Modeling Results

While viewing the results in a regional format aids in interpreting the regional mechanisms that affect the large-scale propagation of the waves, it is also critical to evaluate the fate of the waves as they interact at a more local scale. One of the preliminary ways of viewing results locally is to examine the time history of elevations and velocities at specific points along the coastline. Figures 3.16a-u display the elevation time histories for points located in approximately five to ten meters depth of water near selected cities and entrances to bays. The stations are arranged in a south to north order. Notice the nature of the first waves from each scenario. All of the "1" scenarios commence with an initial trough. Thus, an observer along the shoreline would see the water initially receding and potentially drying some of the seabed. This initial trough is associated with the ocean floor subsidence that is located west of the region of uplift. The "2" scenarios also lead to such a receding of water in the trough of the wave, but only for stations located approximately north of Florence, OR. The majority of subsidence south of this point occurs on land, and uplift is primarily occurring along the ocean floor. Thus, south of Florence, the "2" scenarios show an initial rise in water associated with the incoming positive-elevation wave. This is important, considering the research of Tadepalli and Synolakis (1994) on increased runups associated with leading depression waves.

Figures 3.16a-u also demonstrate that the maximum wave elevations in each time series generally increase with latitude. This is primarily associated with the fact that the deformation generally occurs further away from the coast in the northern regions. As mentioned earlier, initial waves generated in deeper waters have more of an opportunity to amplify as they move into the shallower waters. Higher wave elevations along central and northern Oregon are also associated with whether the offshore bathymetric contours tend to focus the wave energy towards that region or not. The 1A and 1C simulations yield similar wave histories, although there is more of a phase difference between the two that varies proportionally with latitude. Similarly the 2A, 2B, and 2C simulations provide similar results at most locations, and there is a phase difference between these wave histories that also varies proportionally with latitude. The 2C waves, in general, have larger amplitudes than 2A, and the 2B elevation time histories are usually situated between the 1A and 2A results. The 2CN and 2CS wave elevations are about one-half the 2C elevations in the northern and southern parts of the domain, respectively.

Figures 3.17a-u display the velocity magnitude time histories at the same locations. The interpretations of these results are similar to those for the elevations. However, the velocities are particularly stronger in areas that have entrances leading back to bays or estuaries. Examples include Yaquina Bay, the Columbia River, Willapa Bay, and Grays Harbor. As more grid refinement is added to these entrances, the computed velocities are generally higher. The Columbia River appears to be a region in which much of the potential energy is converted to kinetic energy, thus dissipating the wave elevations while amplifying the velocities.

The effect of the added grid refinement in Grid 2 is dramatically seen again in Figures 3.16 and 3.17 in the graphs on the right. It should be noted that the 1C simulation on Grid 2 only ran for 90 minutes, as evidenced in Figures 3.16a-u and 3.17a-u. The increases in elevations and velocities on Grid 2 are generally more prominent in the southern sites, yet there are exceptions such as the increased velocities in Grays Harbor. The increases in elevations and velocities on Grid 2 can be as large as twice the values computed on Grid 1. The higher frequency components of the waves also are better preserved, thus validating the notion that the Grid 1 resolution caused higher frequencies to be aliased to lower frequencies. Myers and Baptista (1998a, 1998b) further investigate the importance of grid refinement on frequency aliasing, truncation errors, and energy errors.

The elevation and velocity time histories provide a temporal view of what is occurring at specific points, but to gain a spatial awareness of the wave behavior throughout a local area it is instructive to look at isolines of maximum elevations and velocities. Figures 3.18a-i and 3.19a-i display the isolines of maximum elevation observed throughout each simulation for the Newport and Seaside areas, respectively. The coastline is shown in each figure, which is useful in the context of viewing which land areas were inundated throughout each simulation. Figures 3.18a-i show that the

Newport area is susceptible to inundation in four main regions: 1) a valley extending from the open coastline just at the southern end of South Beach state park, 2) the region extending into the north end of South Beach state park from that part of the channel just west of the entrance breakwaters, 3) the bulbed peninsula next to the marina just west of the Highway 101 bridge, and 4) just to the north and south of the Yaquina Bay entrance breakwaters. All of the simulations show inundation occurring to some extent along the shoreline of this fourth region. The 1C simulation shows the most inundation in the first and second regions, whereas the 1A is the only simulation with significant inundation in the third region. The "2" simulations only appear to inundate the second and fourth regions. Some of the simulations also show inundation occurring along the land just north of the channel near some of the waterfront businesses. Following a path from the bay entrance to the back of the bay, the maximum wave elevations in Figures 3.18a-i show a decreasing trend, indicating that the potential energy is being damped and perhaps converted into kinetic energy. Note also that much of the portion of Newport north of the channel is not inundated, due to the higher elevations of the land (topography).

Figures 3.19a-i show the isolines of maximum elevation for the Seaside area. This area is much more susceptible to inundation than Newport, owing to the generally low topography of the region. The "1" scenarios inundate most of the town of Seaside and the valley south of Seaside. The town of Gearhart, just north of the Neawanna River, is inundated through much of the low areas, although there appear to be more potential evacuation routes than Seaside. Much of Seaside is located between the Necanicum River and the coastline and between the Neawanna River and Necanicum River. The "1" scenarios show much of this area to be inundated, although there may be a few spots that could potentially serve as last-option evacuation points (these areas are being resurveyed to ensure that the topography is adequately high at those points). The 1C simulation on Grid 2 indicates the most impact, with essentially all of Seaside experiencing inundation. There are some differences between the 1A and 1C simulations made on the two grids as well. The 1C simulation on Grid 2 showed more inundation than the Grid 1 simulation, most likely owing to the increased grid resolution offshore of Seaside (since the grids are equivalent in Seaside). The 1A simulation on Grid 2 also showed more inundation than the 1A results on Grid 1. In addition, the former simulation also shows a series of "wavefronts" of maximum elevation in between the coastline and the Necanicum River. These occur near a small rise in the topography that may have caused the disturbance. The "2" scenarios show less inundation than the "1" scenarios in the Seaside area. The inundation patterns in Gearhart are similar to the "2" scenarios, although not as extreme. In Seaside, much of the 2A, 2B, and 2C scenarios of inundation occurs near the Necanicum and Neawanna rivers, although there are some conduits in each case through which the waves inundated between the coast and the Necanicum River. The 2CN simulation shows inundation occurring primarily close to the coastline, with some inundation also occurring near Gearhart.

Figures 3.20a-i display the isolines of maximum velocity magnitudes for each of the simulations in the Newport region. The areas of inundation can be seen in these figures, but the more interesting aspect is how the velocities behave in the channels and ocean. Most of the simulations show a consistent pattern of velocity behavior near the breakwaters at the entrance of Yaquina Bay. The isolines of maximum elevation showed a decreasing trend in values as the waves passed through these breakwaters, yet the velocity magnitudes show an increase in values through this passageway. Thus, much of the potential energy is converted to kinetic energy in this entrance area. The isolines at the entrance also show a tapering off towards the south, representative of the large velocities occurring as the waves recede away from the bay. The velocities in each of the simulations remain fairly intense through the main channels, with magnitudes generally ranging between three and ten meters per second.

Figures 3.21a-i show the maximum velocity isolines for Seaside. Velocities are enhanced near the entrance to the Necanicum estuary, although they do not show the same channeling effect that the Yaquina Bay entrance velocities displayed. The maximum velocity magnitudes occurred in between the coastline and the Necanicum River and between the Necanicum and Neawanna rivers. This has critical implications for evacuation and hazard mitigation plans, since these areas are populated by many businesses and residences. These increased velocities seem to occur as the waves are overtopping small hills that are oriented north to south. The 1A, Grid 2 maximum velocities also show the "wavefront" patterns that were seen in the maximum elevation isolines for that simulation. The 1C, grid 2 simulation yields the more intense velocities over the entire region, while the "2" simulation velocities are smaller compared to the "1" simulations. As with the elevation isolines, the maximum velocities are different enough between the same simulations made on the two different grids to suggest that the evolution of the waves before arriving at Seaside are affected by the differences in grid resolution.

Figures 3.20 and 3.21 provide a feel for the intensity of the velocities in Newport and Seaside, yet Figures 3.22a-c and 3.23a-b portray both the direction and magnitude of the maximum velocities for the 1A scenario on Grid 2. Figure 3.22 shows a peculiar physical phenomenon in that there is a visible cutoff line in the ocean, west of which the maximum velocities are pointing westward and east of which they are pointing towards the coast. This line is evident all along the coastline, and may be helpful in determining whether a boat should try to head towards the ocean or toward the back of a bay. Figure 3.22b shows the maximum velocity vectors through the main channels leading to the north breakwaters in Yaquina Bay. These velocities are mostly between 5 and 10 m/s and are aligned in directions toward the back portions of the bay. Figure 3.22c displays the same vectors near the mouth of Yaquina Bay. The maximum velocities near the western end of the breakwaters occur during the receding of water out in the ocean. The maximum velocities in the inundated north end of South Beach state park also occurred primarily during the receding of the inundated region. Some of the stronger velocities occur as the waves are overtopping the land just north of the northern breakwater. It should be noted that the velocity patterns near the entrances to bays that have breakwaters could be different if those breakwaters collapse during the shaking of the earthquake (Visher, 1998).

Figures 3.23a-b show the maximum velocity vectors for the 1A, Grid 2 scenario in Seaside. The velocities in the inundated areas are more relevant for Seaside, since most of the region is flooded during the tsunami. The northern part of Seaside shows varying directions of maximum velocities between the shoreline and the Necanicum River. For the central and southern parts of Seaside, there appears to be a line between the shore and the Necanicum to the east of which the maximum velocities occur during the flooding of the waves and to the west of which the receding waves result in the largest velocities.

Another useful tool from a mitigation vantage is to view the arrival times of the first inundating waves. Figures 3.24a-i show the arrival times of the waves for each of the scenarios in Newport. Most of the scenarios show that much of the inundation in the Newport area occurs during the first 30 or 40 minutes, thus primarily associated with the initial waves. Only the 1A, Grid 1 simulation shows some areas (the northern fringes of the channel and the peninsula next to the marina) to not be inundated until several hours into the simulation. The tsunami arrival times in Seaside are shown in Figures 3.25a-i for all scenarios. The "1" and "2" scenarios show different behavior in terms of tsunami arrival times. The waves in the "1" scenarios show that much of the inundation comes from the initial waves overtopping the land from the shoreline. Therefore, the "1" arrival times show an increasing pattern from west to east. The northern fringes of Gearhart in these scenarios witness the waves arriving an hour or so after the earthquake. The "2" scenarios show most inundation occurring as the waves propagate through the estuary and into the Necanicum and Neawanna rivers. Much of the inundation in these scenarios is therefore along areas of land next to these waterways. There is also significant shoreline inundation that does show a few conduits of inundation back to the Necanicum River. However, the 2C simulation does display similar behavior as the "1" simulations in that the inundation is more associated with the initial waves overtopping the land regions from the shoreline.

While most of the hazard mitigation for tsunamis is related to land inundation and surges through estuaries and bays, there is also the issue of the best course of action boats should take during a tsunami. Depending on a boat's location in the ocean, the best course of action may be to head further out to sea in some cases. One way in which to evaluate the fate of a boat during a tsunami is to follow the path of a particle as it is moved around during the tsunami. The entrances to the Columbia River and Yaquina Bay were selected for this analysis, based on the increased boat traffic in these areas. Figures 3.26a-b show the initial positions of the particles (i.e. boats) as dark circles. The path of each particle during the 1A, Grid 2 simulation is followed and shown as the line extending from each initial position. The time between the initial position and the final position is four hours. In Figure 3.26a, numbers are shown to display the final position of the first four particles located closest to the mouth of the Columbia River. It can be seen that these first four particles are transported between 2 and 10 km towards the river. The other particles located further from the river end up within 2 km of their initial positions, but travel well over 2 km in the back and forth motion throughout the event. The transport of particles near Newport, shown in Figure 3.26b, shows that the first two particles closest to Newport are transported several kilometers and undergo significantly more motion than the other particles. The other particles generally do not deviate more than one kilometer from their initial positions. It should be kept in mind that these simulations do not account for tides, the inclusion of which could significantly affect these positions.

3.5 Conclusions

Communities in close proximity to the Cascadia subduction zone face the task of designing hazard mitigation plans for near-field tsunamis. Modeling past Cascadia events under the constraints of current geologic and geophysical data provides the best indicator as to what could potentially occur in future events. The seismic source scenarios used in this study were based upon a careful selection of deformation modeling techniques and utilization of geophysical, geologic, and thermal information in an effort to minimize uncertainties associated with the initial conditions to the hydrodynamic model.

Simulations of potential Cascadia tsunamis, using the initial conditions from the deformation scenarios, were evaluated from both regional and local perspectives. The regional simulations indicated the importance of bathymetry, coastline geometry, and the varying depths of water in which the deformation is occurring. All of these factors can affect the propagation behavior of the wave as it approaches the shoreline and interacts with the coastline. For example, the Stonewall and Perpetua banks off the coast of central Oregon were shown to affect the focusing of waves, exemplified by increased maximum elevations, increased maximum velocities, and changes in the frequencies of the waves. The offshore canyons and banks in northern Oregon and Washington were also shown to incite similar wave behavior. The placement and width of the deformation zone also affects what types of waves will be generated in which areas. For example, off the coast of Washington, the deformation is generally occurring in deeper water, and the width of the locked zone is larger. Therefore, the waves in the north should be larger and have longer wavelengths.

From a local perspective, a city's topography, shoreline geometry, and estuary configuration can each play a critical role in determining the wave behavior as it interacts with the coastline. The local modeling results at the two sites considered in this study, Newport and Seaside, showed a stark contrast in how the waves behaved in areas of such different topographies. Seaside, which is much lower in topography than Newport, was highly susceptible to inundation through the entire region. Newport, on the other hand, was primarily at risk in the lower regions south of Yaquina Bay. Because the channels leading back to the bay are more maintained and defined than the channels in Seaside, the velocities in the Newport waterways were more significant. The behavior of the waves and the evaluation of inundation risk in each of the simulations was evaluated in several contexts including maximum wave elevations, maximum velocities, maximum velocity vectors, time histories of flow, dominant frequencies, arrival times of the inundating waves, and particle tracking. Each of these tools helps in the assessment of the physical mechanisms of the waves and the likely impact of future tsunamis.

Assessment of the hazards along the coast should bear in mind that although numerical models are tools formulated from governing equations of physics, there are inherent uncertainties tied in to the modeling process that should be adequately identified and, when possible, quantified in its usage. These uncertainties can be classified as seismic source, hydrodynamic model, or data uncertainties. The seismic source uncertainties are the most problematic due to the inability to adequately validate whether the deformation models are reproducing the true deformations of any past subduction events. This leaves far too much freedom in selecting a source. In most cases of modeling the deformation for past events, the computed seismic source is the one which is optimized to produce numerically modeled tsunamis that are the most similar to the tide gauge recordings of the waves. But if there are uncertainties in the hydrodynamic numerical model, then those errors will be embedded into the seismic source, and ultimately there is no adequate way to verify that source. The approach taken in this study was to derive a source using an advanced deformation model with as much available geophysical data as input, and to not rely on the use of a hydrodynamic model in determining the source. We were thus trying to constrain the errors in the deformation model as much as possible, without embedding any other (i.e. hydrodynamic model) errors into the source.

These other errors are present, as exemplified by the differences in results on the two grids used in this study. Such uncertainties in the hydrodynamic model can be associated with energy preservation, underlying assumptions in the shallow water equations, numerical diffusion, and truncation errors. Each of these errors is dependent upon other factors such as grid refinement and parameter selection, as discussed in more detail in Myers and Baptista (1998a-b). Errors may also be present in the models due to data uncertainties. For example, the model's representation of the bathymetry and topography will always carry uncertainties in how well the geoid shape is reproduced. Many of these uncertainties can be minimized by increasing the grid refinement. However, this study used grids that had $8\text{-}10x10^4$ nodes, thus requiring the use of time steps on the order of a tenth of a second. Therefore, simulations on such grids are computationally intensive, and any further refinement needs to be carefully placed. These issues are further discussed in Myers and Baptista (1998a, 1998b) in an effort to quantify the performance of tsunami simulations.

3.6 References

Atwater, B.F., A.R. Nelson, J.J. Clague, G.A. Carver, D.K. Yamaguchi, P.T. Bobrowsky, J. Bourgeois, M.E. Darienzo, W.C. Grant, E. Hemphill-Haley, H.M. Kelsey, G.C. Jacoby, S.P. Nishenko, S.P. Palmer, C.D. Peterson and M.A. Reinhart, 1995. Summary of Coastal Geologic Evidence for Past Great Earthquakes at the Cascadia Subduction Zone, *Earthquake Spectra*, 11(1), 1-18.

Baptista, A.M., G.R. Priest and T.S. Murty, 1993. Field Survey of the 1992 Nicaragua Tsunami, *Marine Geodesy*, 16(2), 169-203.

Committee on the Alaska Earthquake of the Division of Earth Sciences National Research Council, 1972. *The Great Alaska Earthquake of 1964*, Oceanography and Coastal Engineering, National Academy of Sciences, Washington, D.C.

DeMets, C., R.G. Gordon, D.F. Argus and S. Stein, 1990. Current Plate Motions, *Geophysical Journal International*, 101(2), 425-478.

Flück, P., R.D. Hyndman and K. Wang, 1997. Three-Dimensional Dislocation Model for Great Earthquakes of the Cascadia Subduction Zone, *Journal of Geophysical Research*, 102(B9), 20539-20550.

Fukao, Y., 1979. Tsunami Earthquakes and Subduction Processes Near Deep-Sea Trenches, *Journal of Geophysical Research*, 84(B5), 2303-2314.

Geist, E. and S. Yoshioka, 1996. Source Parameters Controlling the Generation and Propagation of Potential Local Tsunamis along the Cascadia Margin, *Natural Hazards*, 13(2), 151-177.

Goldfinger, C., 1996. Personal communication, Oregon State University.

Hebenstreit, G.T. and T.S. Murty, 1989. Tsunami Amplitudes from Local Earthquakes in the Pacific Northwest Region of North America Part 1: The Outer Coast, *Marine Geodesy*, 13(2), 101-146.

Holdahl, S.R. and J. Sauber, 1994. Coseismic Slip in the 1964 Prince William Sound Earthquake: A New Geodetic Inversion, *Pure and Applied Geophysics*, 142(1), 55-82.

Horning, T., 1997. Personal communication, Seaside, Oregon.

Hyndman, R.D. and K. Wang, 1993. Thermal Constraints on the Zone of Major Thrust Earthquake Failure: The Cascadia Subduction Zone, *Journal of Geophysical Research*, 98(B2), 2039-2060.

Hyndman, R.D. and K. Wang, 1995. The Rupture Zone of Cascadia Great Earthquakes from Current Deformation and the Thermal Regime, *Journal of Geophysical Research*, 100(B11), 22133-22154.

Kanamori, H., 1996. Personal communication, California Institute of Technology.

Lander, J.L. and P.A. Lockridge, 1989. *United States Tsunamis*, National Geophysical Data Center, Publication 41-2.

Lander, J.L., P.A. Lockridge and M.J. Kozuch, 1993. *Tsunamis Affecting the West Coast of the United States*, National Geophysical Data Center, Documentation No. 29.

Luettich, R.A. and J.J. Westerink, 1995a. *An Assessment of Flooding and Drying Techniques for Use in the ADCIRC Hydrodynamic Model: Implementation and Performance in One-Dimensional Flows*, Dept. of the Army, U.S. Army Corps of Engineers, Vicksburg, MS.

Luettich, R.A. and J.J. Westerink, 1995b. *Implementation and Testing of Elemental Flooding and Drying in the ADCIRC Hydrodynamic Model*, Dept. of the Army, U.S. Army Corps of Engineers, Vicksburg, MS.

Luettich, R.A., J.J. Westerink and N.W. Scheffner, 1991. *An Advanced Three-dimensional Circulation Model for Shelves, Coasts, and Estuaries*, Dept. of the Army, U.S. Army Corps of Engineers, Washington, D.C.

Mansinha, L. and D.E. Smylie, 1971. The Displacement Fields of Inclined Faults, *Bulletin of the Seismological Society of America*, 61(5), 1433-1440.

Myers, E.P. and A.M. Baptista, 1995. Finite Element Modeling of the July 12, 1993 Hokkaido Nansei-Oki Tsunami, *Pure and Applied Geophysics*, 144 (3/4), 769-801.

Myers, E.P. and A.M. Baptista, 1998a. Modeling of Past Tsunamis: One Model's Lessons from the 1993 Hokkaido Nansei-Oki and 1964 Alaska Tsunamis, (submitted to *Natural Hazards*).

Myers, E.P. and A.M. Baptista, 1998b. Numerical Considerations in Finite Element Simulations of Tsunamis, (submitted to *International Journal for Numerical Methods in Fluids*).

Ng, M.K.-F., P.H. LeBlond and T.S. Murty, 1990. Simulation of Tsunamis from Great Earthquakes on the Cascadia Subduction Zone, *Science*, 250, 1248-1251.

Nunez, R., 1990. *Prediction of Tidal Propagation and Circulation in Chilean Inland Seas Using a Frequency-Domain Mode*, Master of Science Thesis, Oregon State University.

Okada, Y., 1985. Surface Deformation due to Shear and Tensile Faults in a Half-Space, *Bulletin of the Seismological Society of America*, 75(4), 1135-1154.

Priest, G.R., 1995. *Explanation of Mapping Methods and Use of the Tsunami Hazard Maps of the Oregon Coast*, State of Oregon, Department of Geology and Mineral Industries, Open-File Report O-95-67, 95 p.

Priest, G.R., E.P. Myers, A.M. Baptista, P. Flück, K. Wang and C. Goldfinger, 1998. Fault Dislocation Scenarios for a Tsunami Hazard Analysis of the Cascadia Subduction Zone (in preparation).

Tadepalli, S. and C.E. Synolakis, 1994. The Run-up of N-waves on Sloping Beaches, *Proceedings of the Royal Society of London A*, 445(1923), 99-112.

Turner, P.J. and A.M. Baptista, 1991. *ACE/gredit Users Manual: Software for Semi-automatic Generation of Two-Dimensional Finite Element Grids*, CCALMR Software Report SDS2(91-2), Oregon Graduate Institute of Science & Technology, Portland, OR.

Visher, P., 1998. Personal communication, Cannon Beach, Oregon.

Whitmore, P.M., 1993. Expected Tsunami Amplitudes and Currents Along the North American Coast for Cascadia Subduction Zone Earthquakes, *Natural Hazards*, 8(1), 59-73.

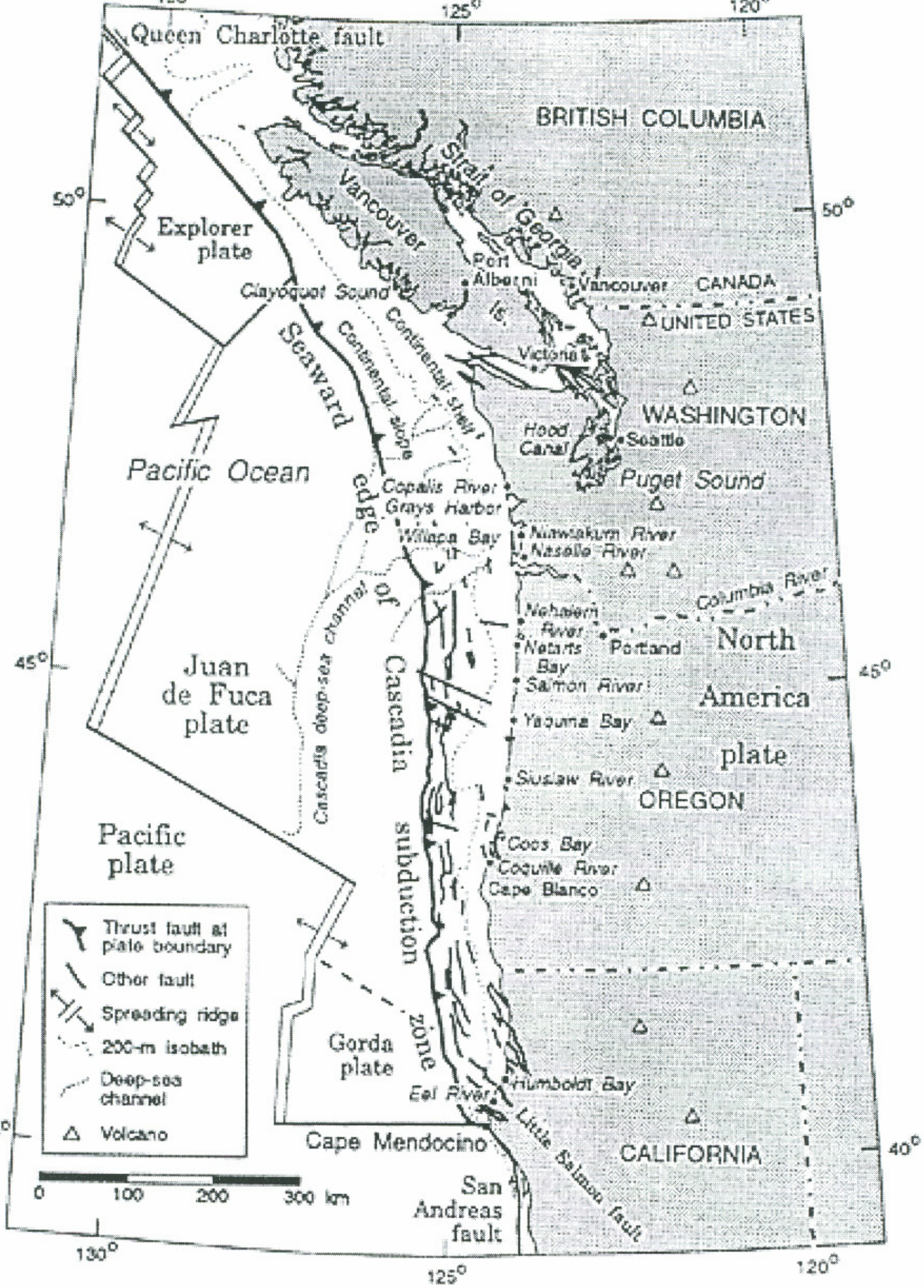

Figure 3.1 Cascadia Subduction Zone (extracted from Atwater et al., 1995 with permission from the Earthquake Engineering Research Institute).

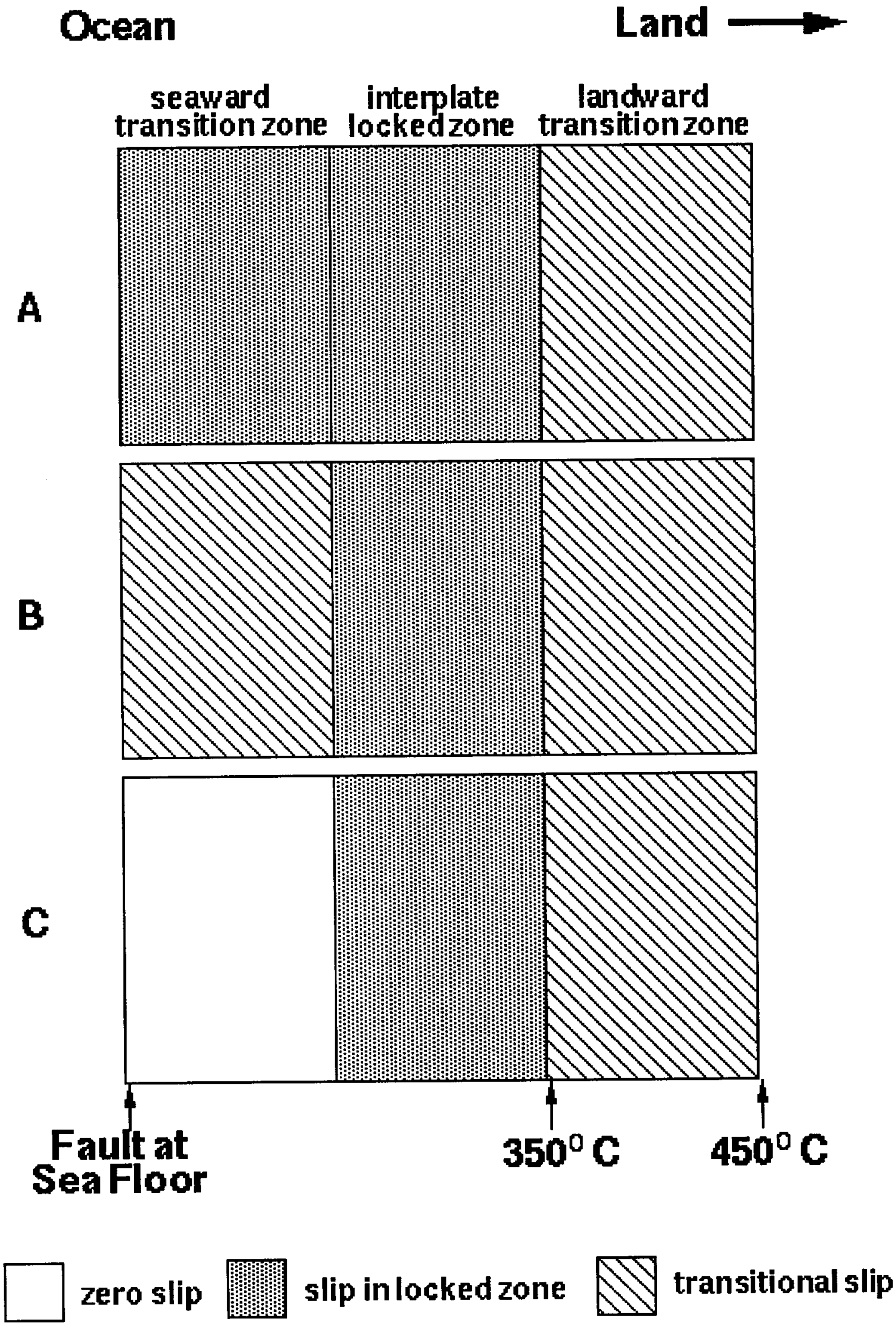

Figure 3.2 Distribution of slip for the three scenarios.

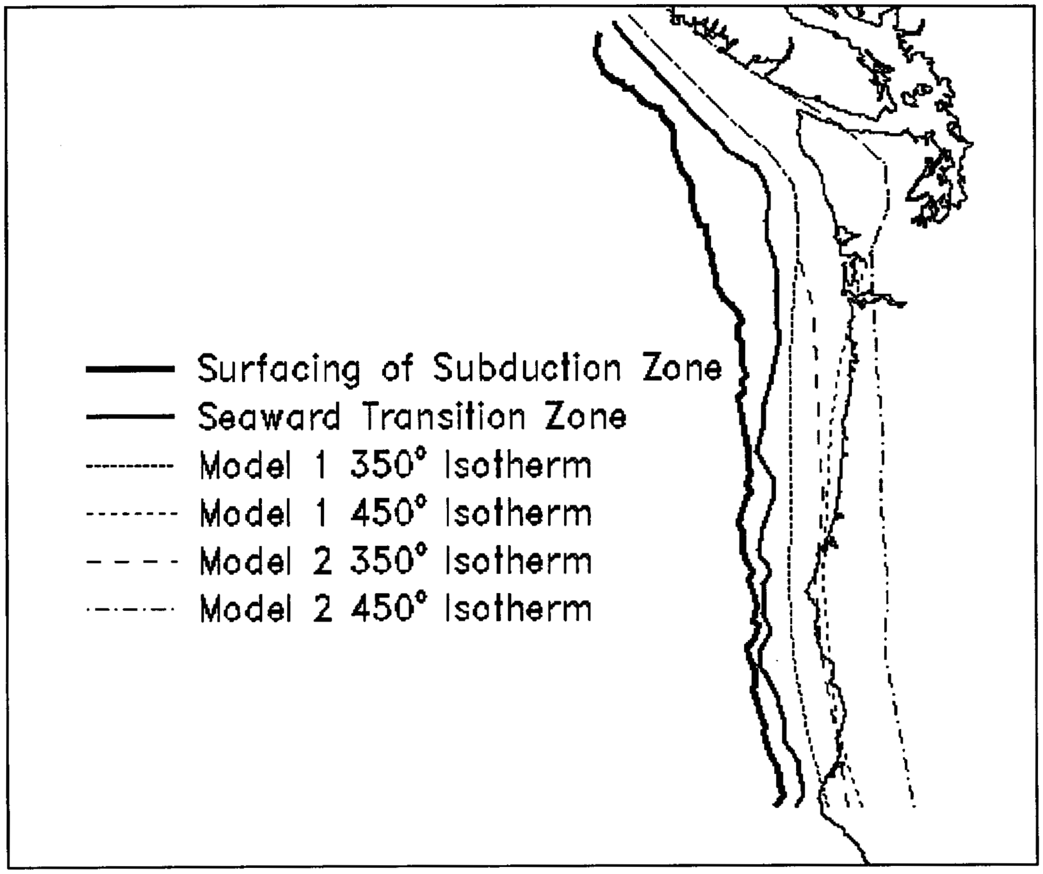

Figure 3.3 Positions of slip distribution zones.

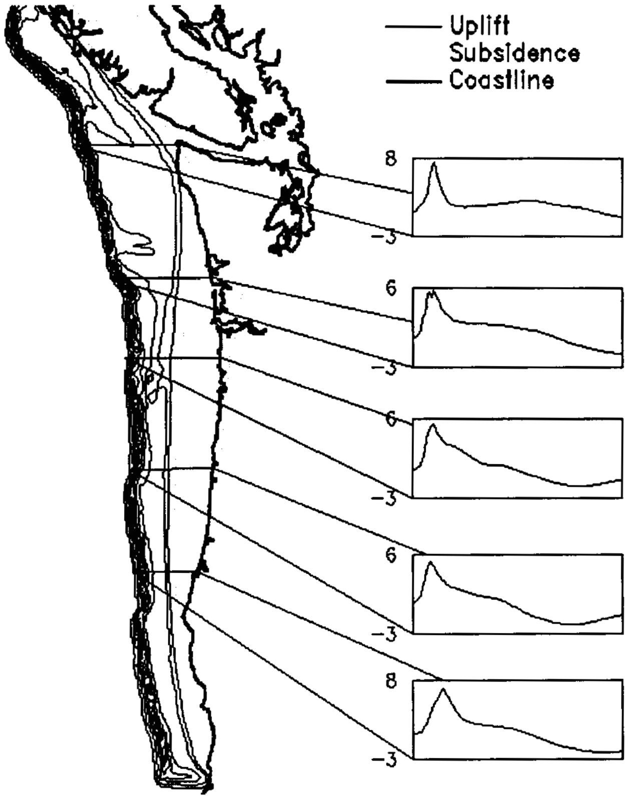

Figure 3.4a Deformation for scenario 1A.

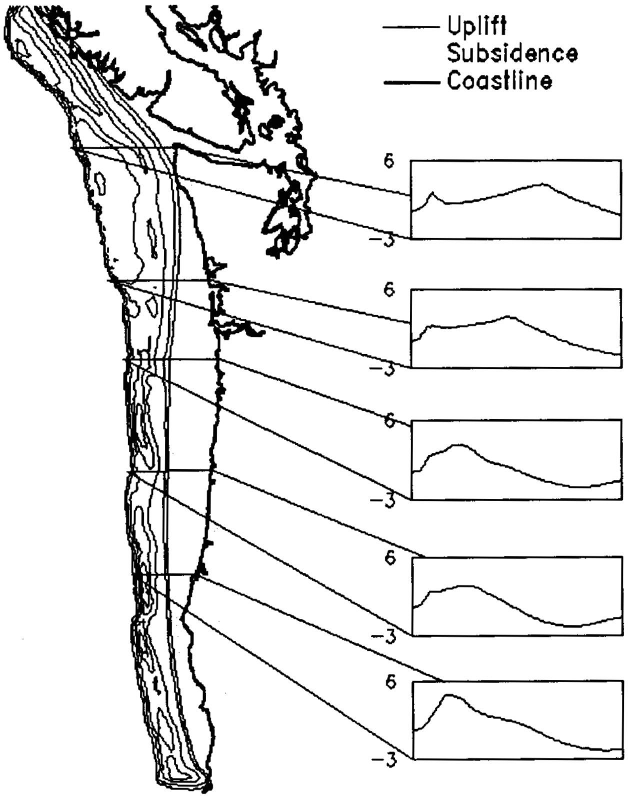

Figure 3.4b Deformation for scenario 1B.

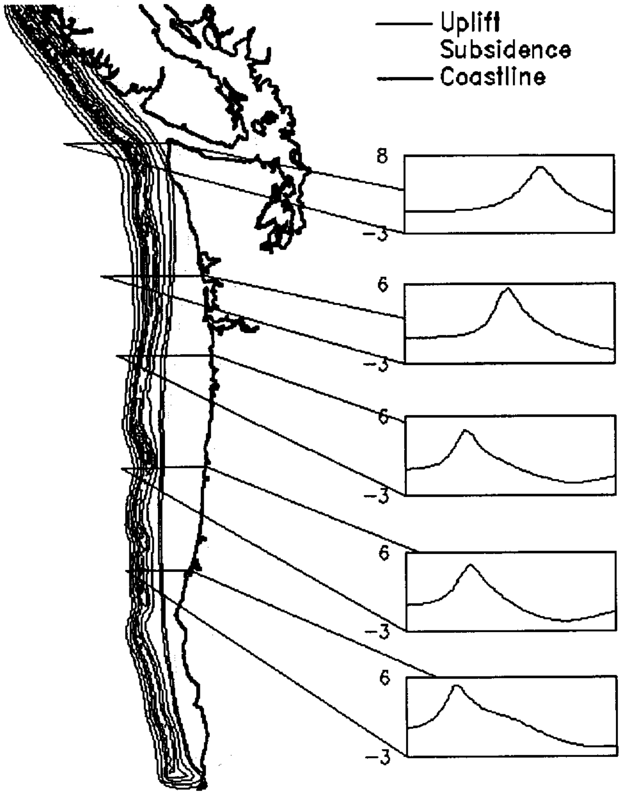

Figure 3.4c Deformation for scenario 1C.

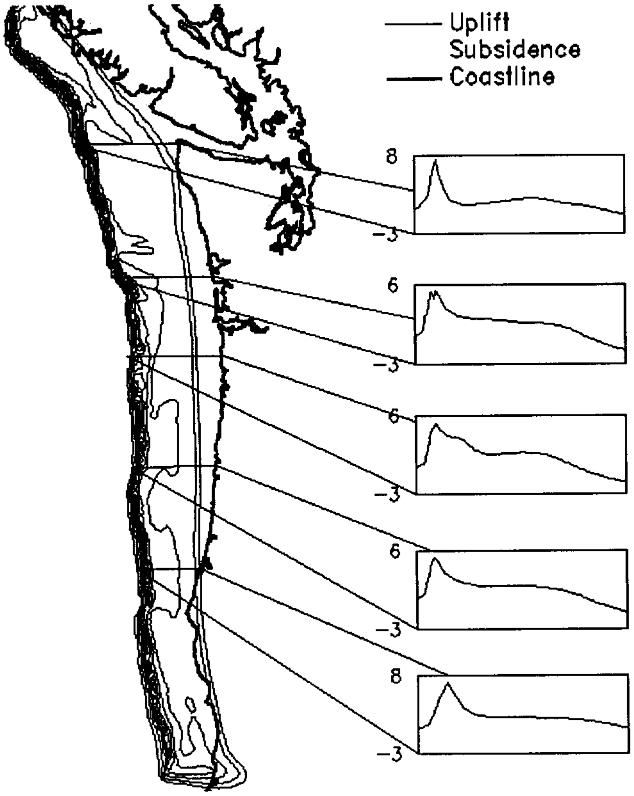

Figure 3.4d Deformation for scenario 2A.

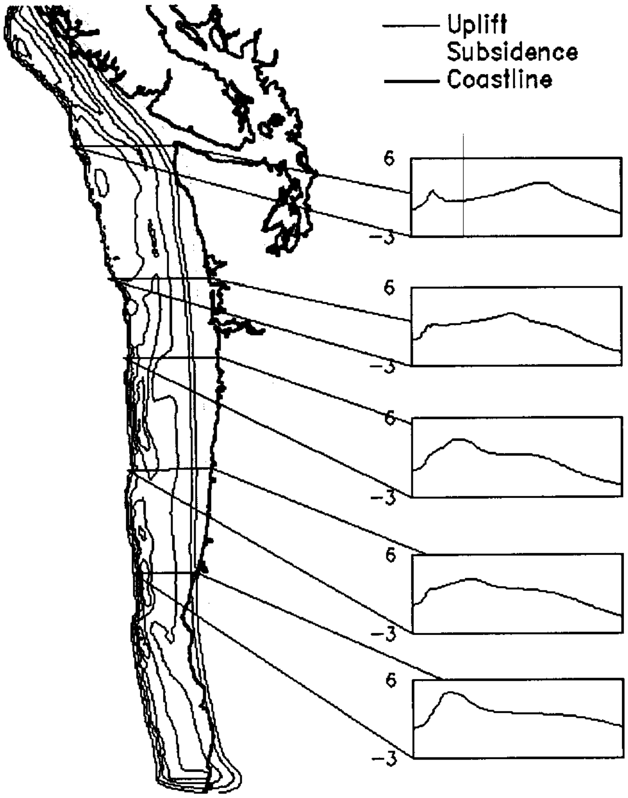

Figure 3.4e Deformation for scenario 2B.

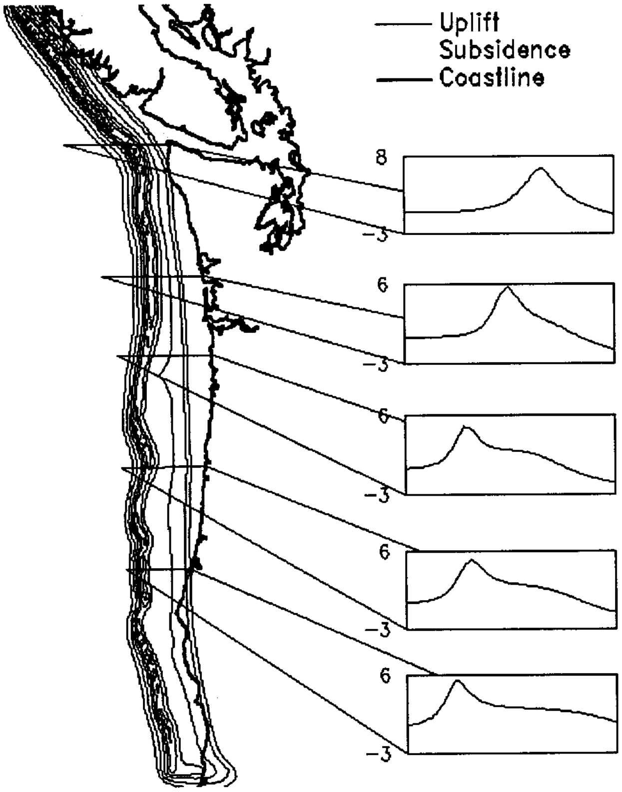

Figure 3.4f Deformation for scenario 2C.

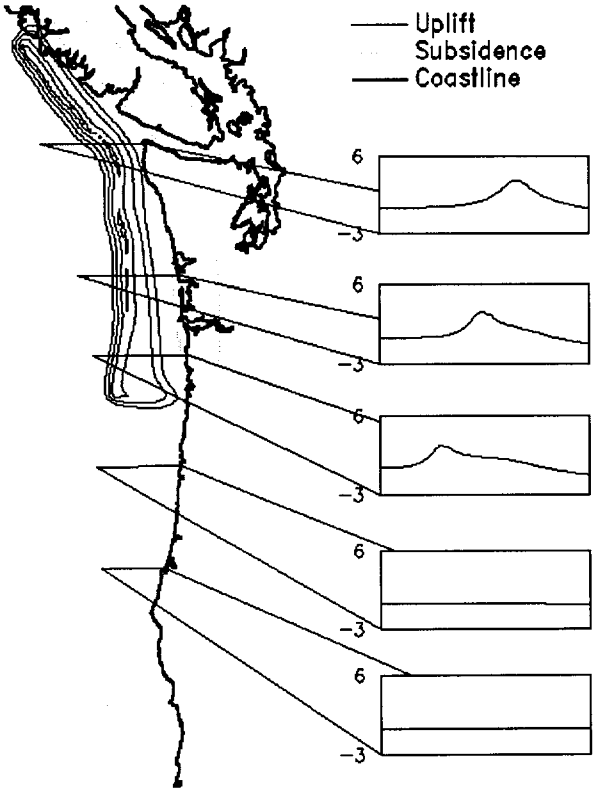

Figure 3.4g Deformation for scenario 2CN.

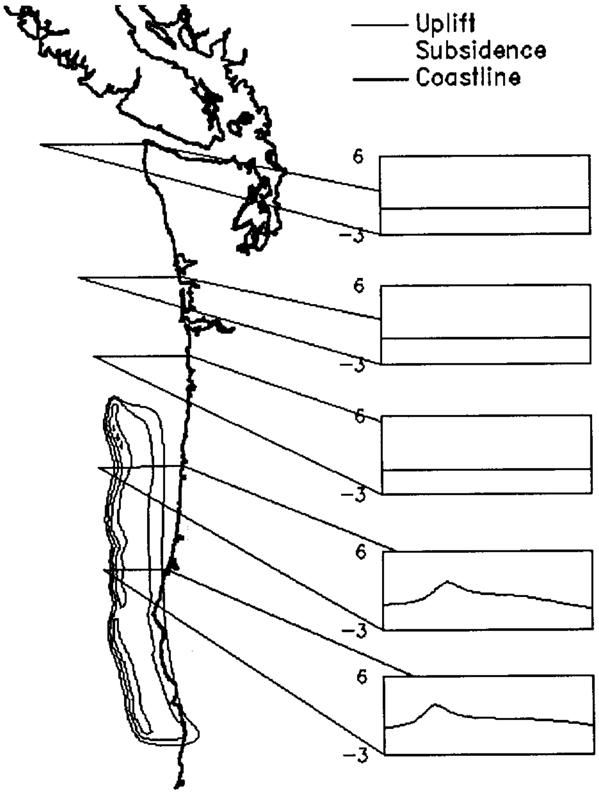

Figure 3.4h Deformation for scenario 2CS.

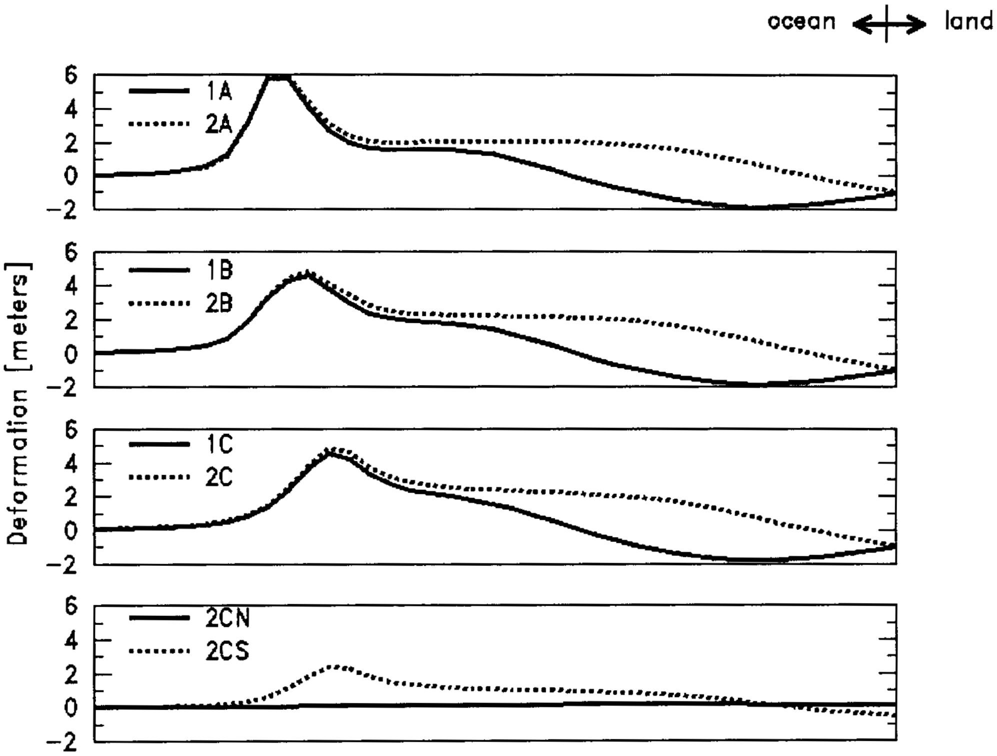

Figure 3.5a Cross section of deformations offshore of Newport, OR.

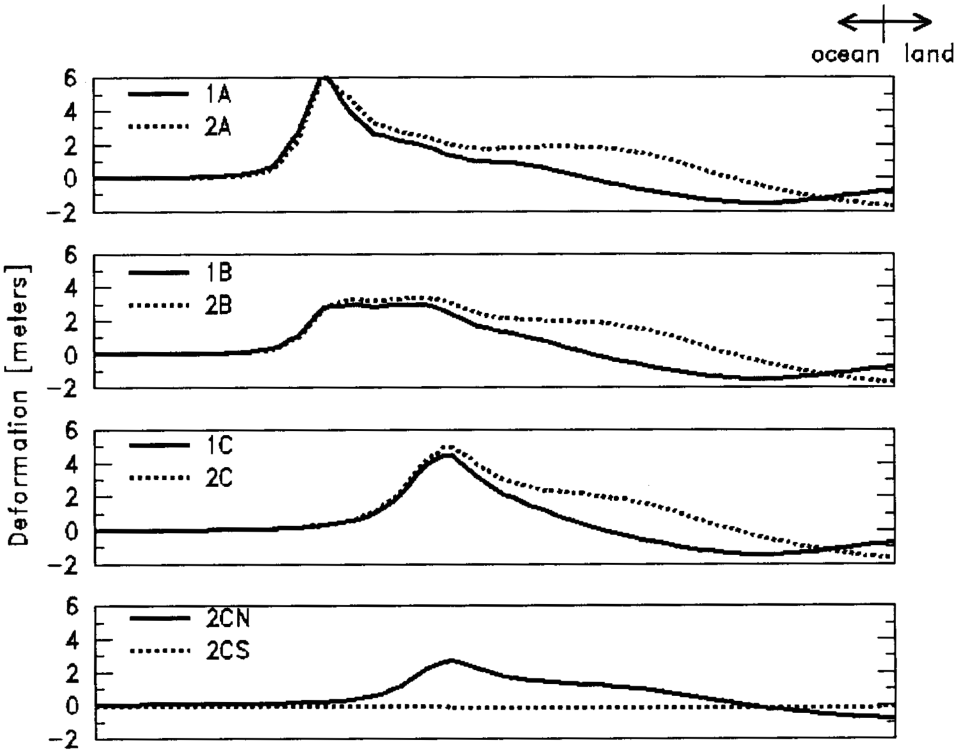

Figure 3.5b Cross section of deformations offshore of Seaside, OR.

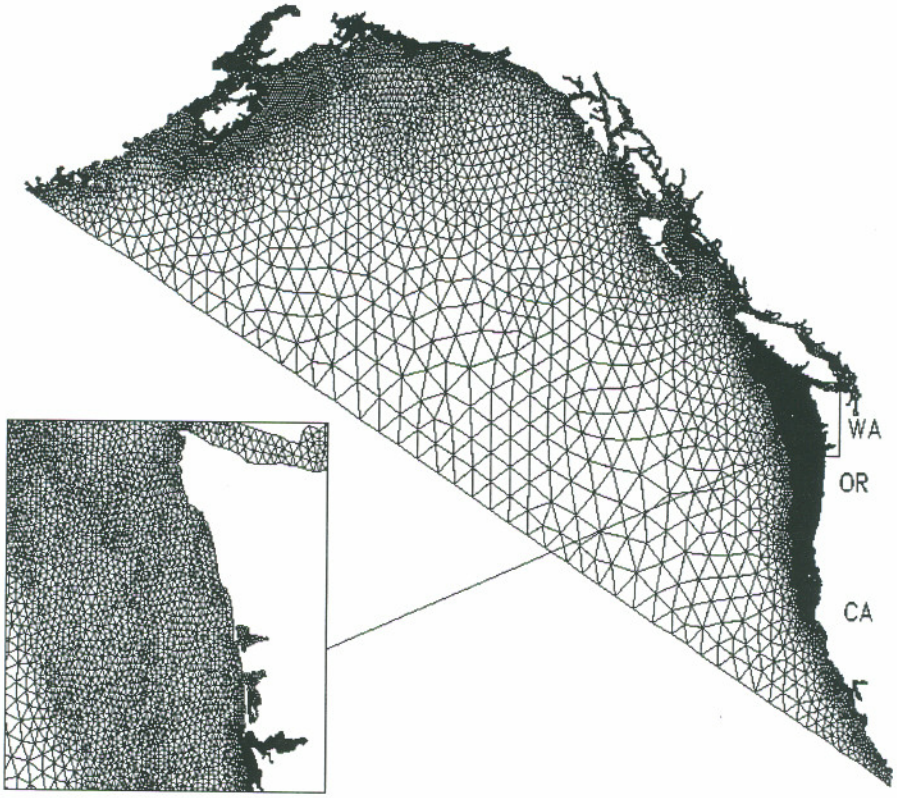

Figure 3.6a Finite element grid 1.

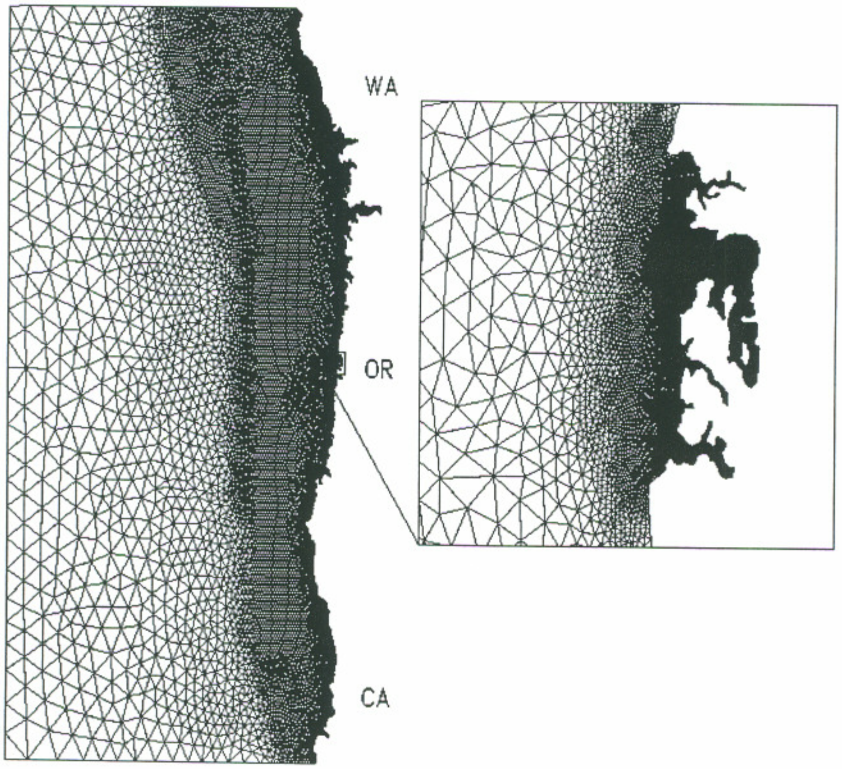

Figure 3.6b Finite element grid 2.

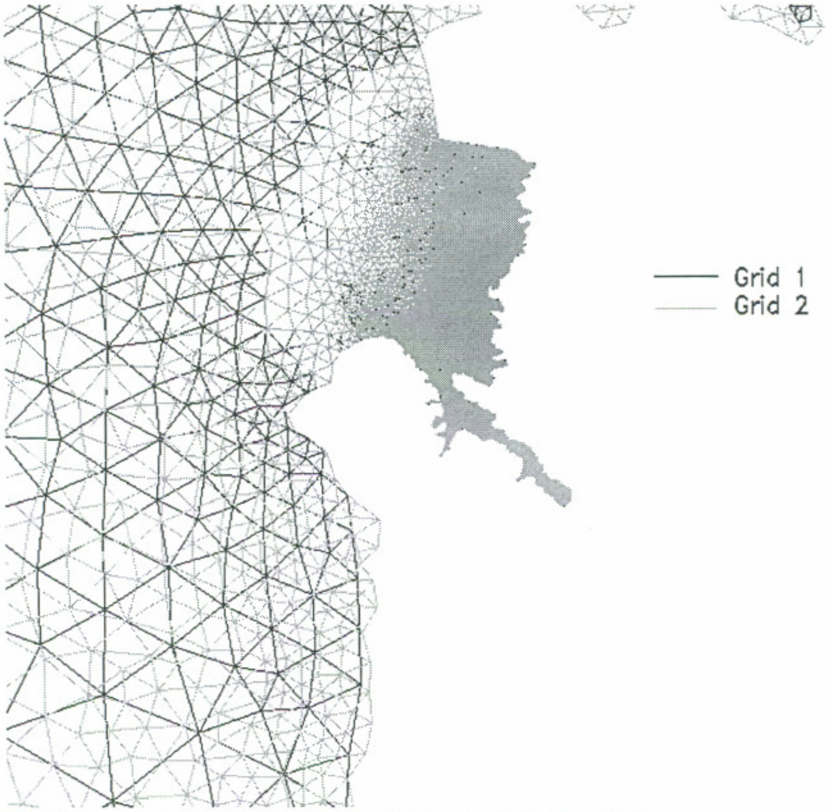

Figure 3.7a Comparison of grids 1 and 2 near Seaside, OR.

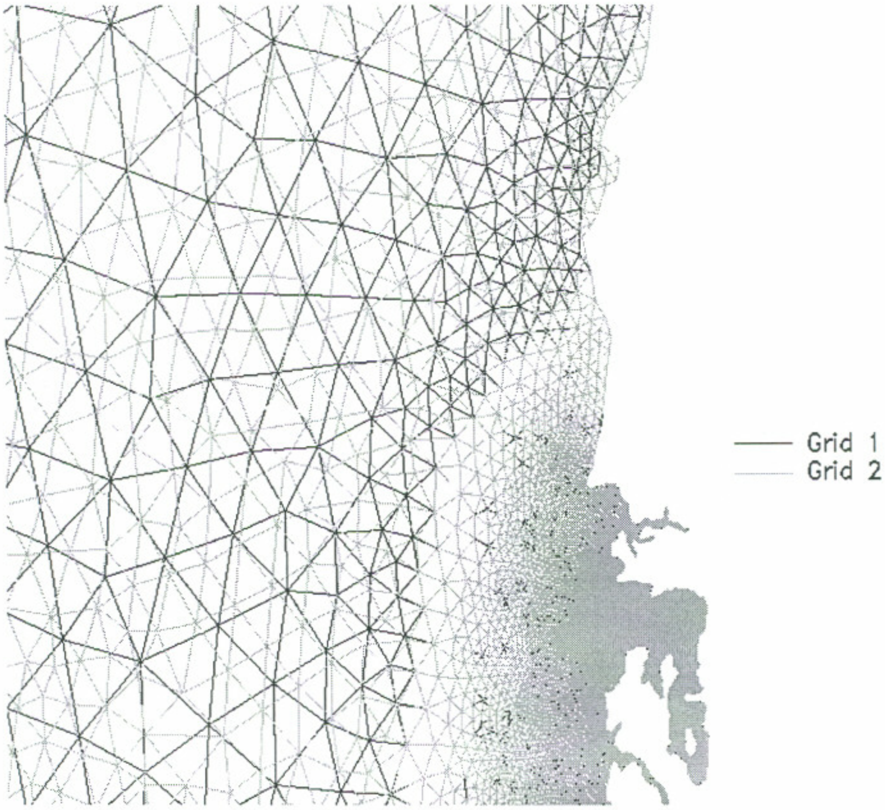

Figure 3.7b Comparison of grids 1 and 2 near Newport, OR.

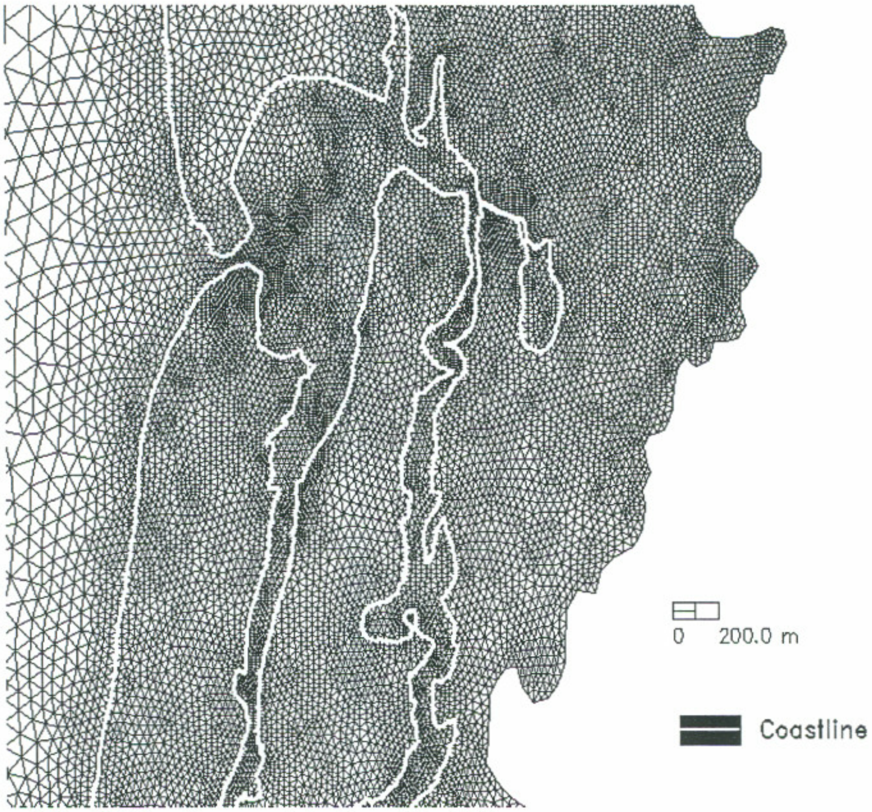

Figure 3.8a Grid refinement in Seaside, OR.

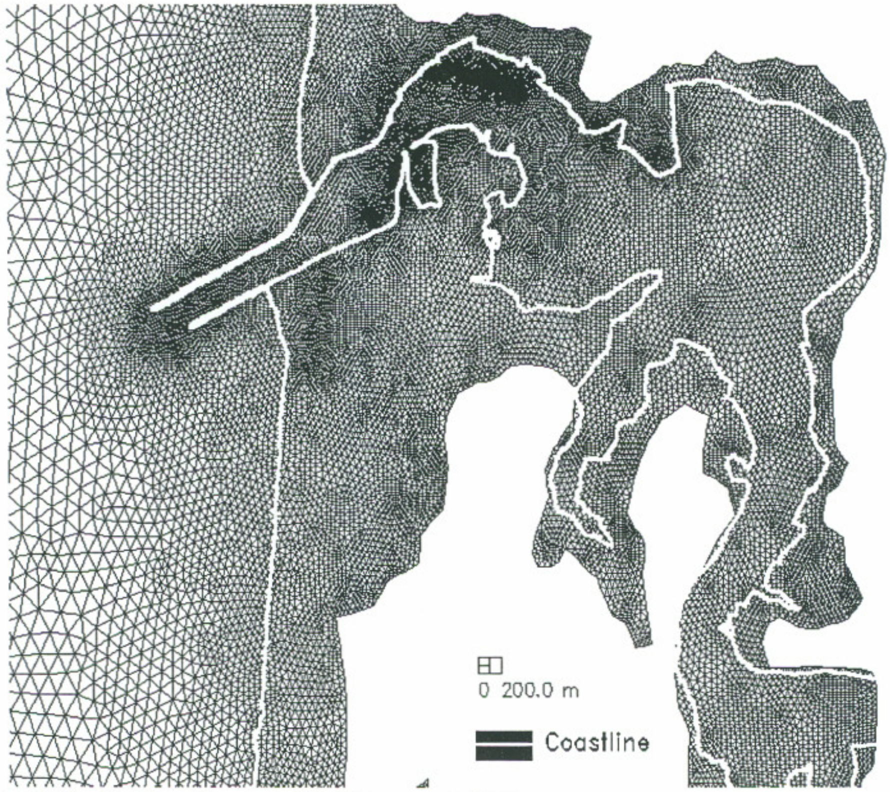

Figure 3.8b Grid refinement in Newport, OR.

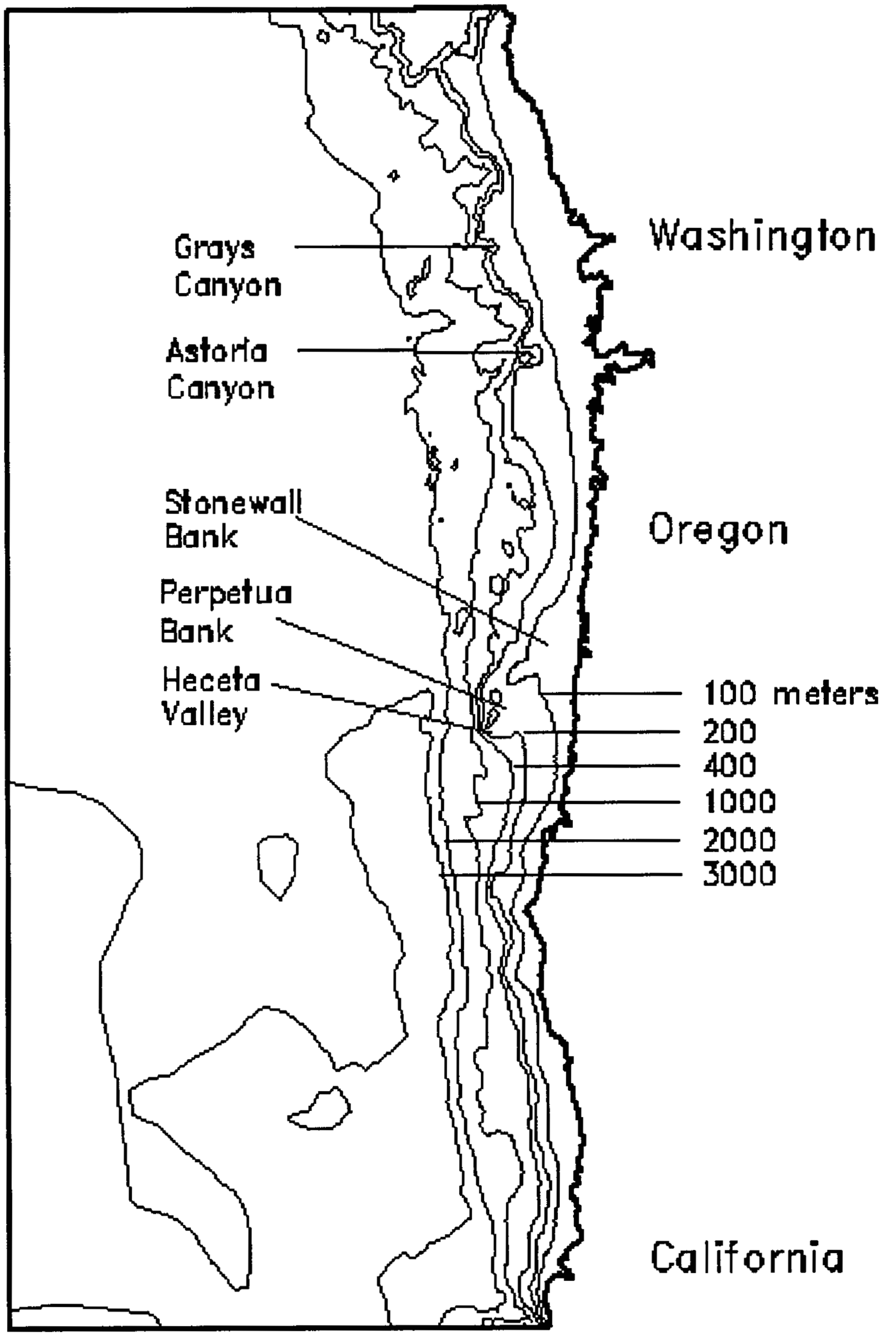

Figure 3.9 Bathymetry throughout the domain.

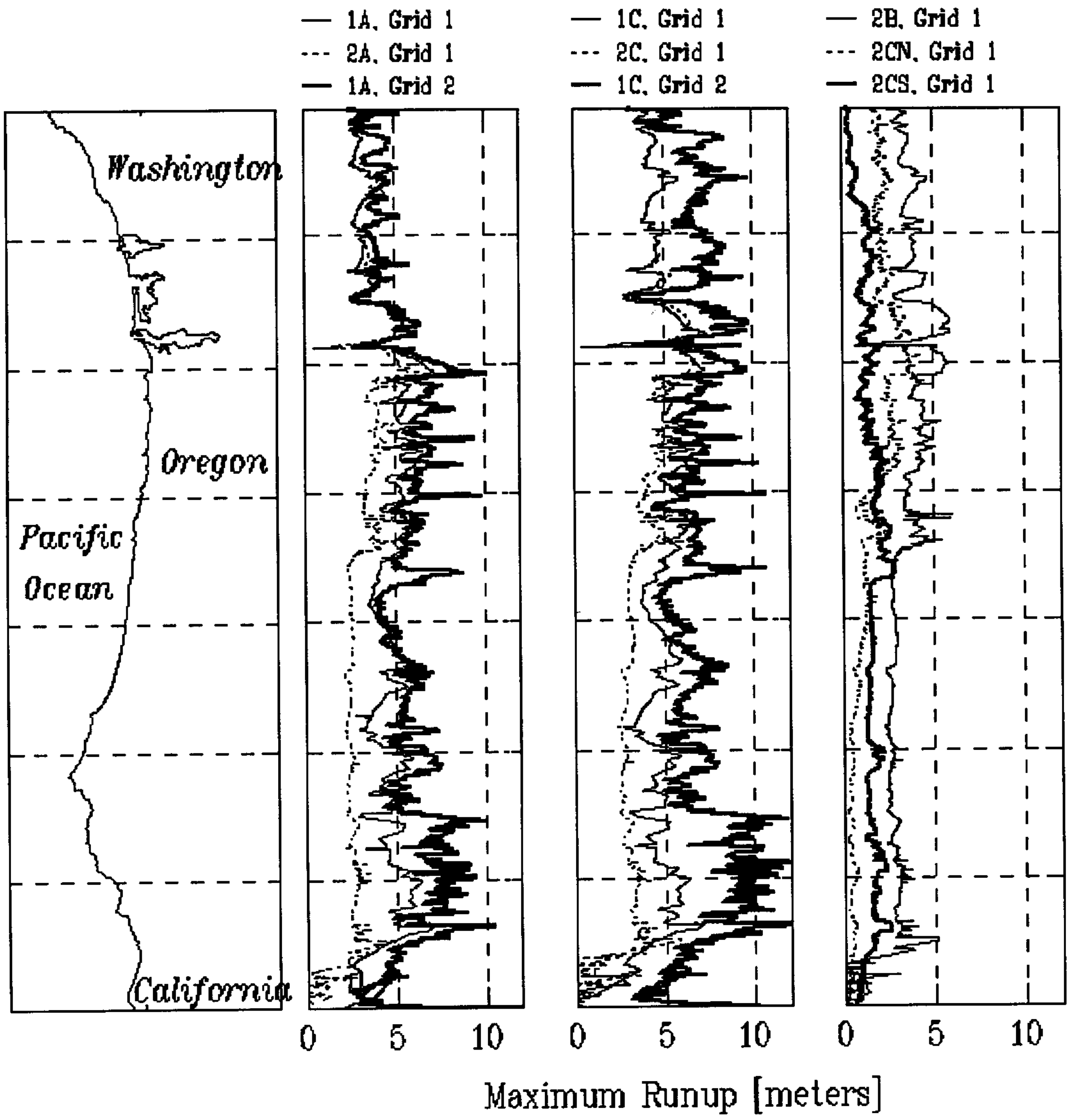

Figure 3.10a Maximum coastal wave elevations.

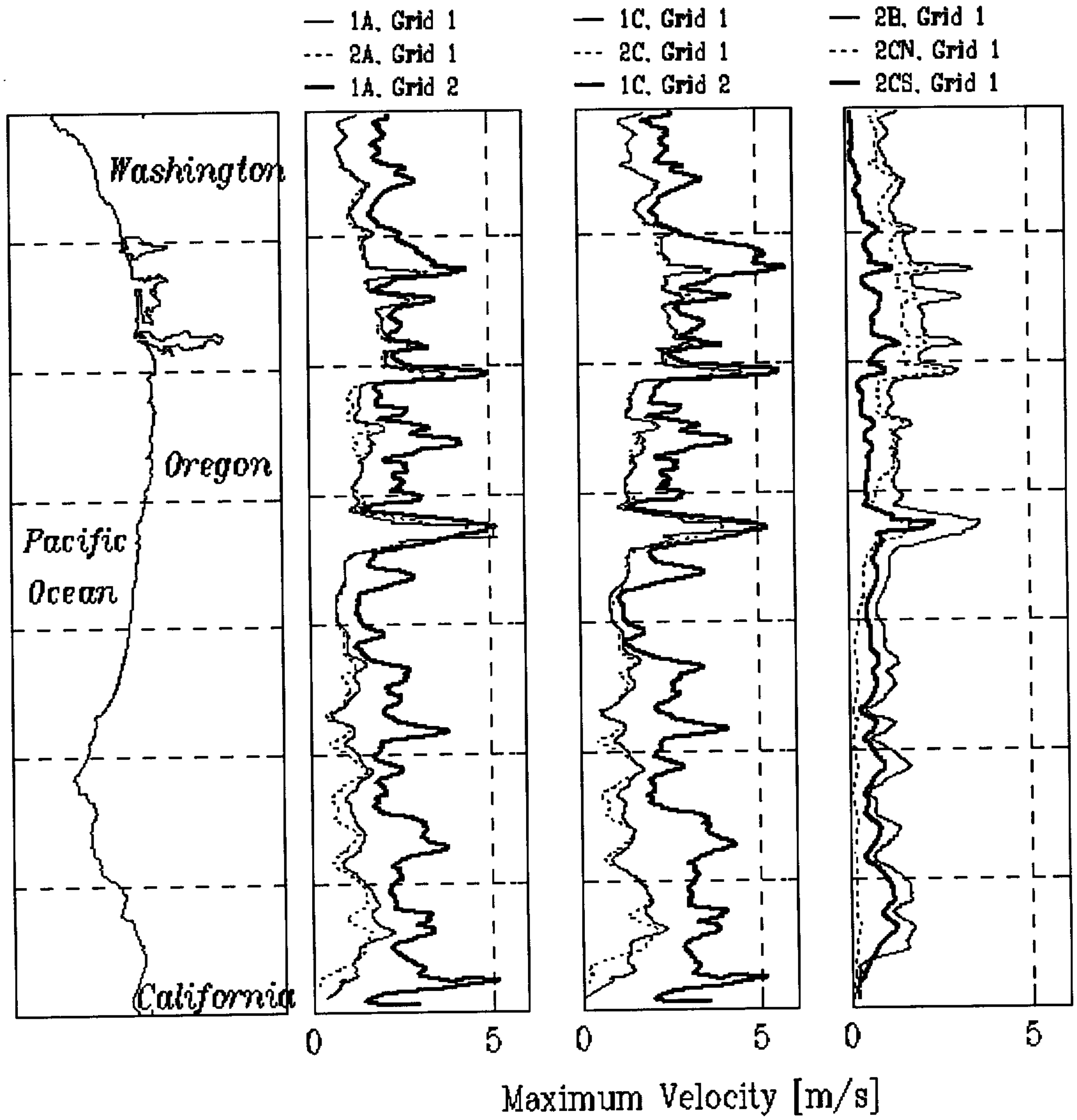

Figure 3.10b Maximum coastal velocities.

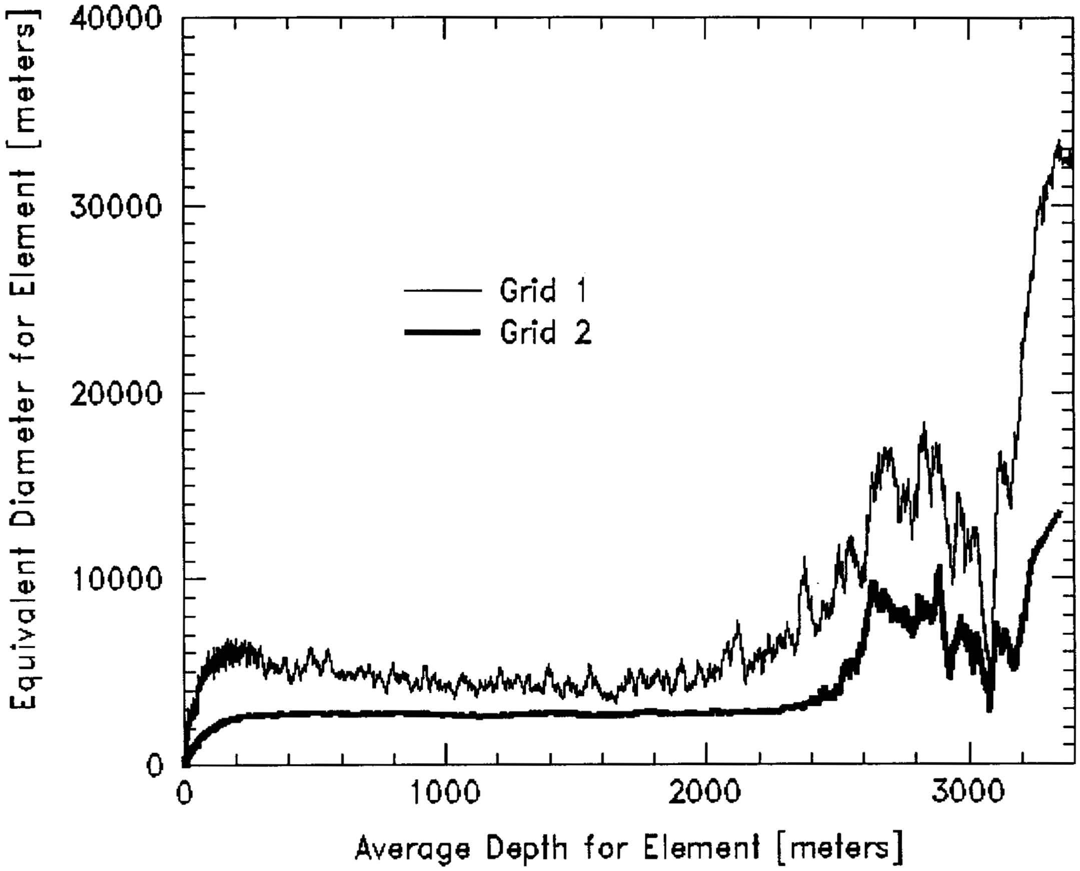

Figure 3.11 Comparison of grid refinement for grids 1 and 2.

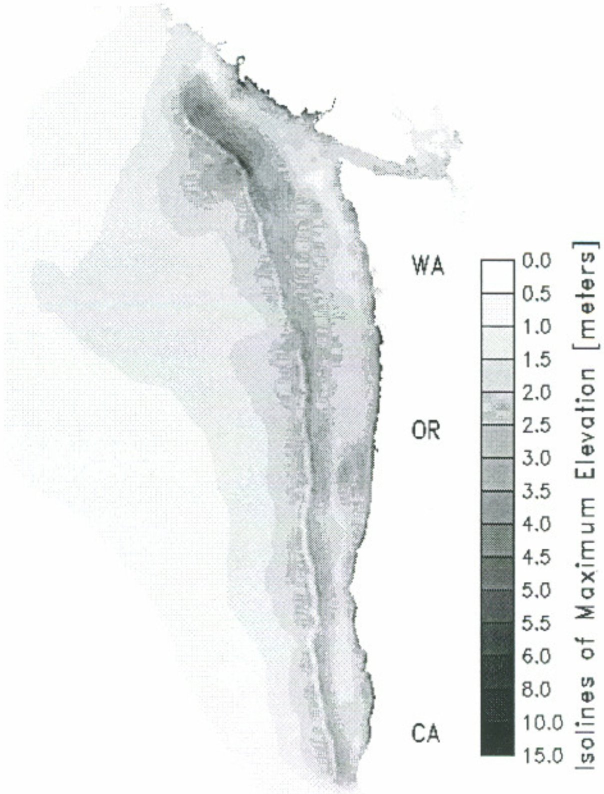

Figure 3.12a Isolines of maximum elevation for scenario 1A.

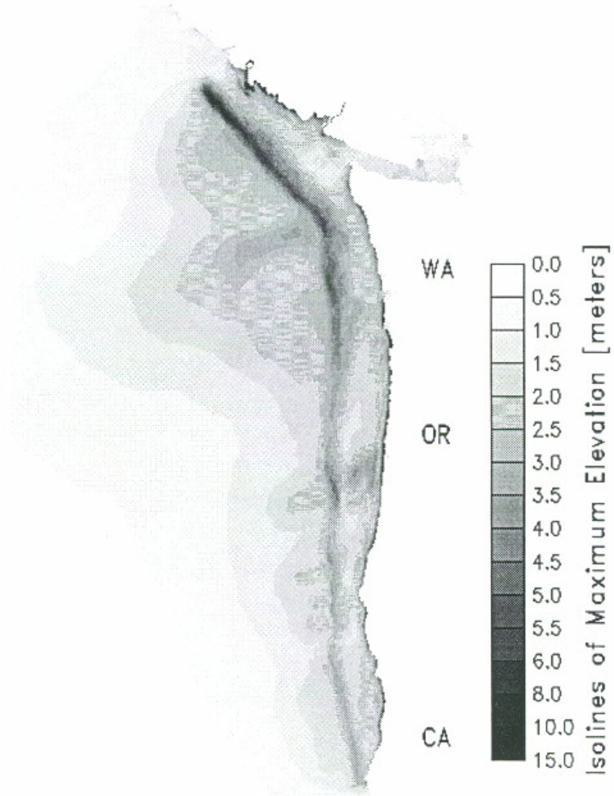

Figure 3.12b Isolines of maximum elevation for scenario 1C.

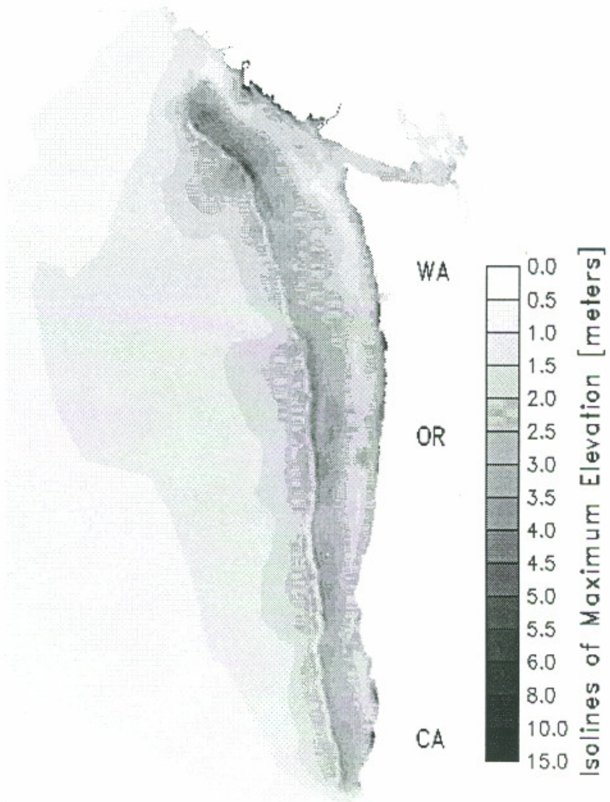

Figure 3.12c Isolines of maximum elevation for scenario 2A.

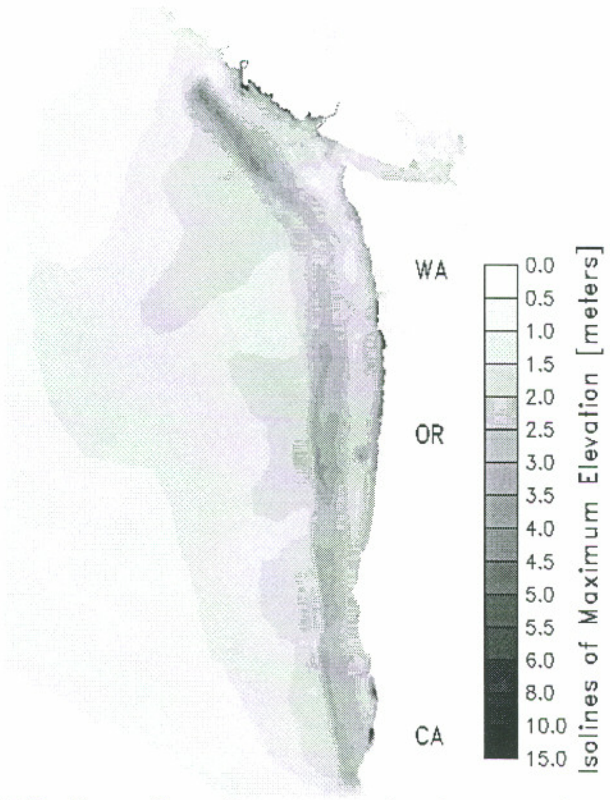

Figure 3.12d Isolines of maximum elevation for scenario 2B.

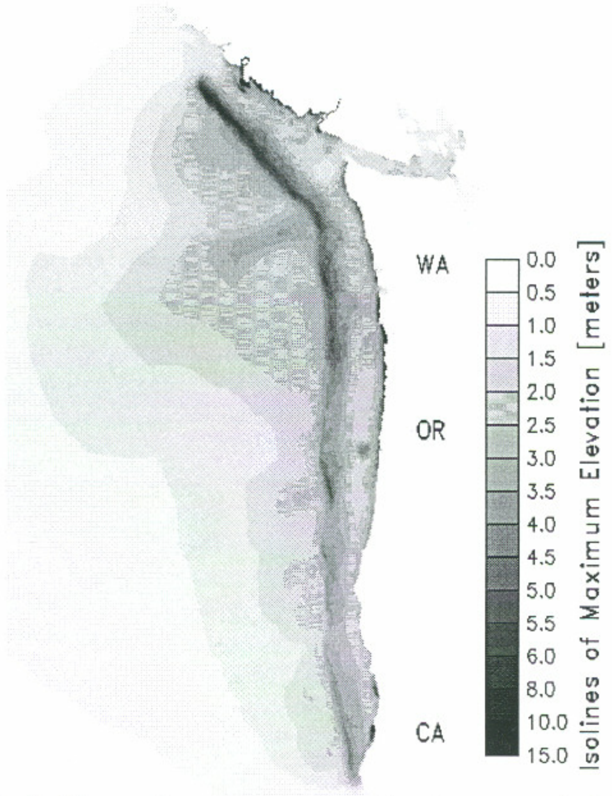

Figure 3.12e Isolines of maximum elevation for scenario 2C.

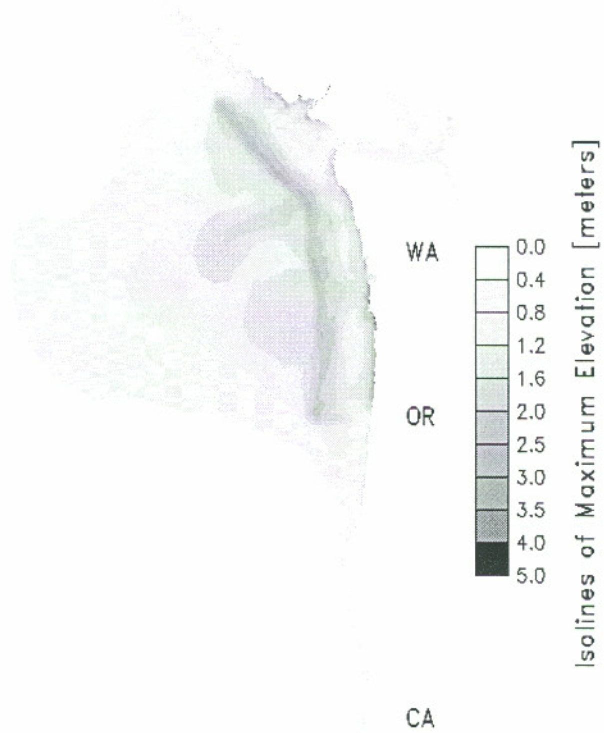

Figure 3.12f Isolines of maximum elevation for scenario 2CN.

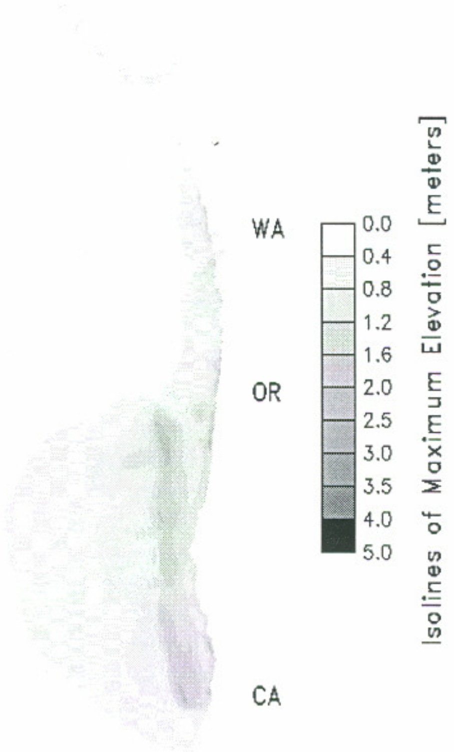

Figure 3.12g Isolines of maximum elevation for scenario 2CS.

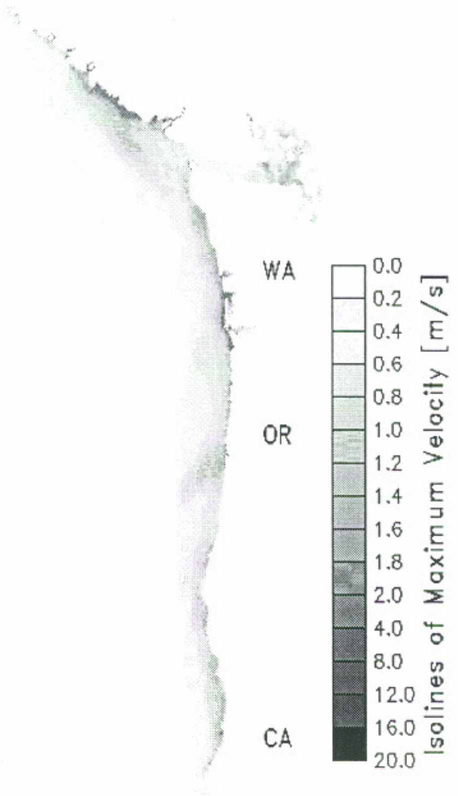

Figure 3.13a Isolines of maximum velocity for scenario 1A.

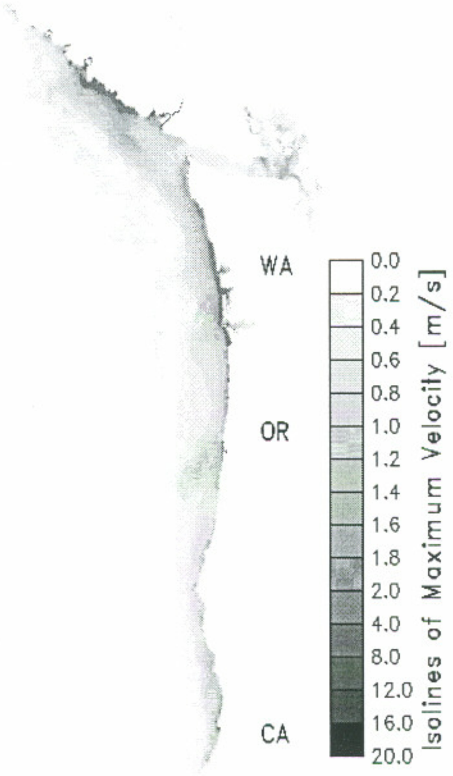

Figure 3.13b Isolines of maximum velocity for scenario 1C.

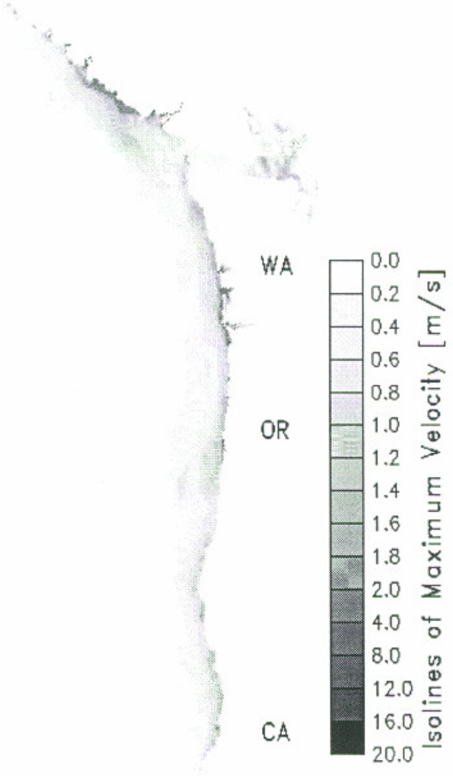

Figure 3.13c Isolines of maximum velocity for scenario 2A.

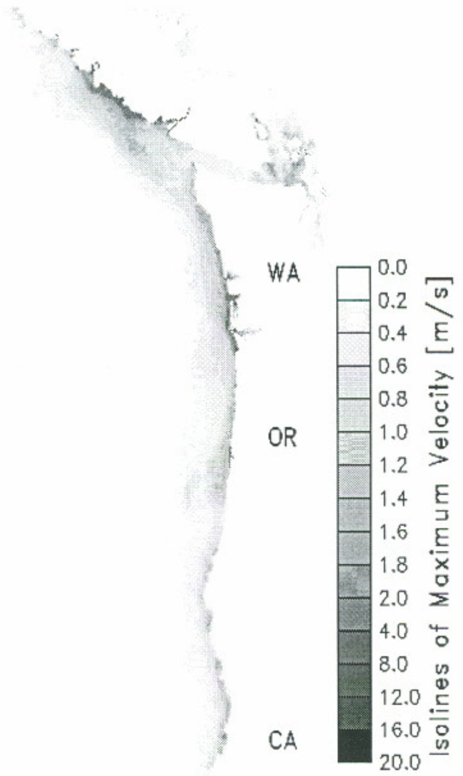

Figure 3.13d Isolines of maximum velocity for scenario 2B.

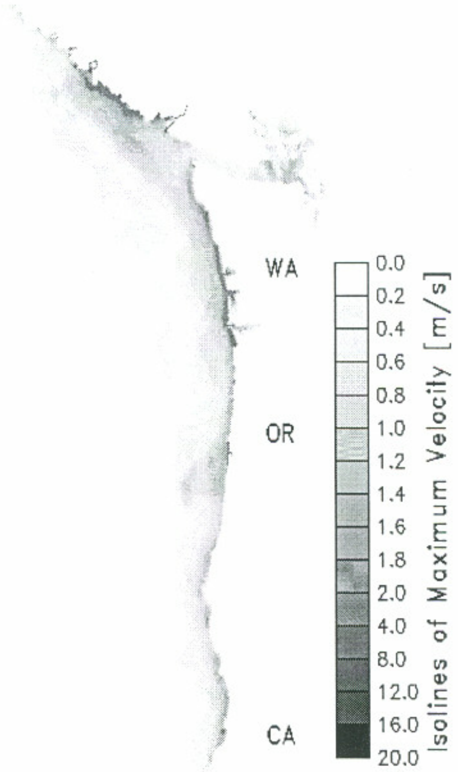

Figure 3.13e Isolines of maximum velocity for scenario 2C.

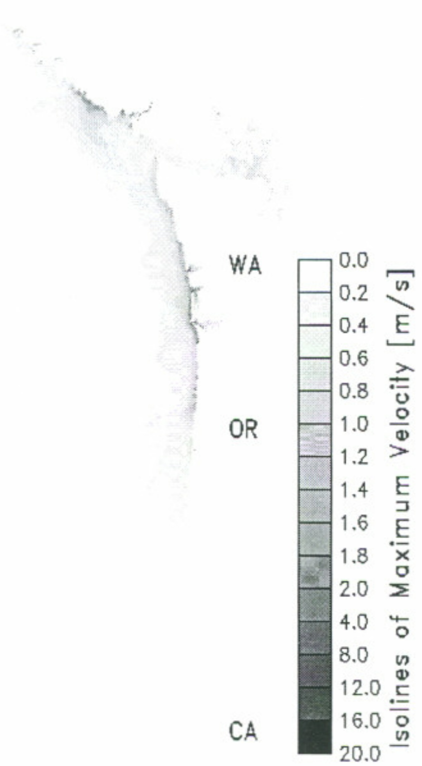

Figure 3.13f Isolines of maximum velocity for scenario 2CN.

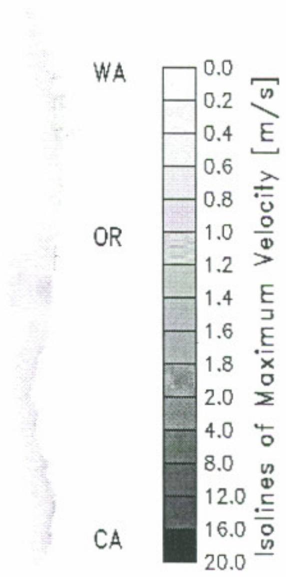

Figure 3.13g Isolines of maximum velocity for scenario 2CS.

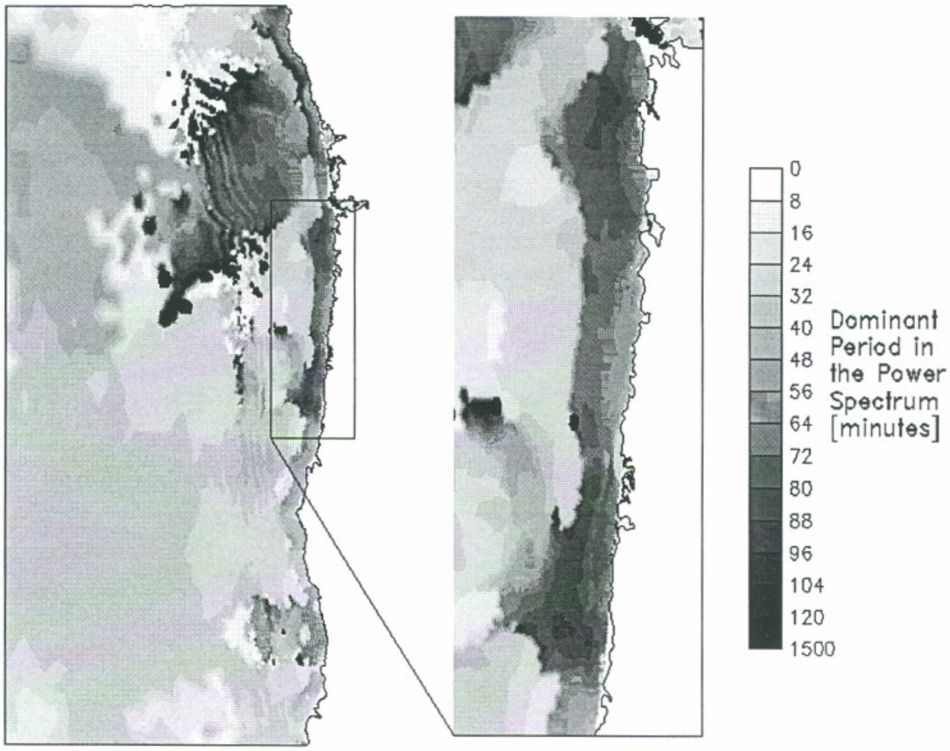

Figure 3.14a Isolines of the dominant period calculated from the power spectrum of 1A, grid 2 elevations.

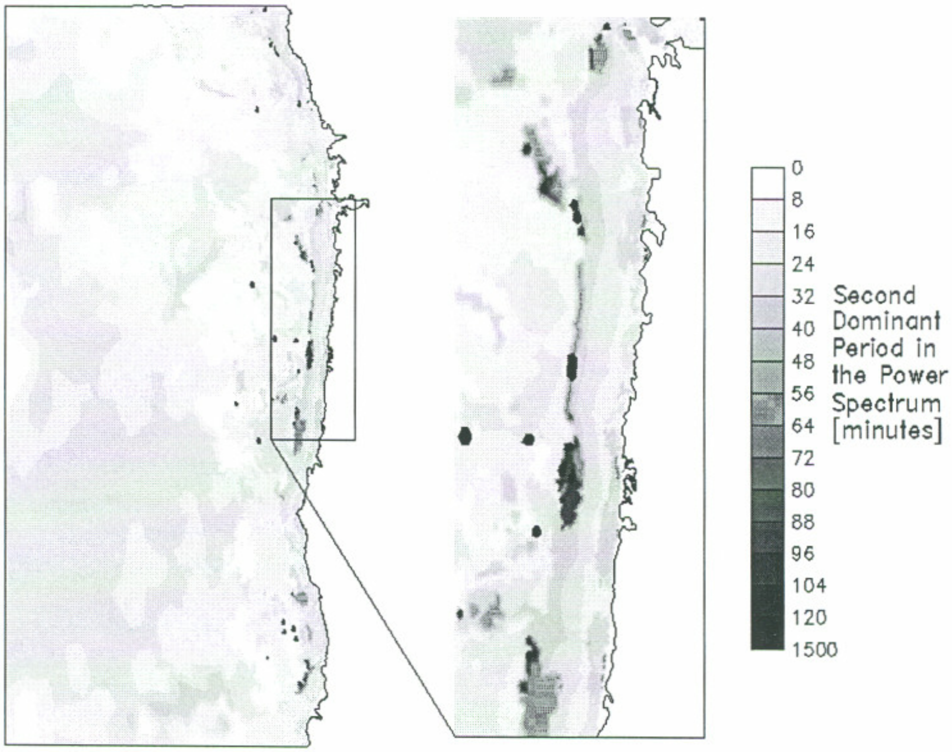

Figure 3.14b Isolines of the second dominant period calculated from the power spectrum of 1A, grid 2 elevations.

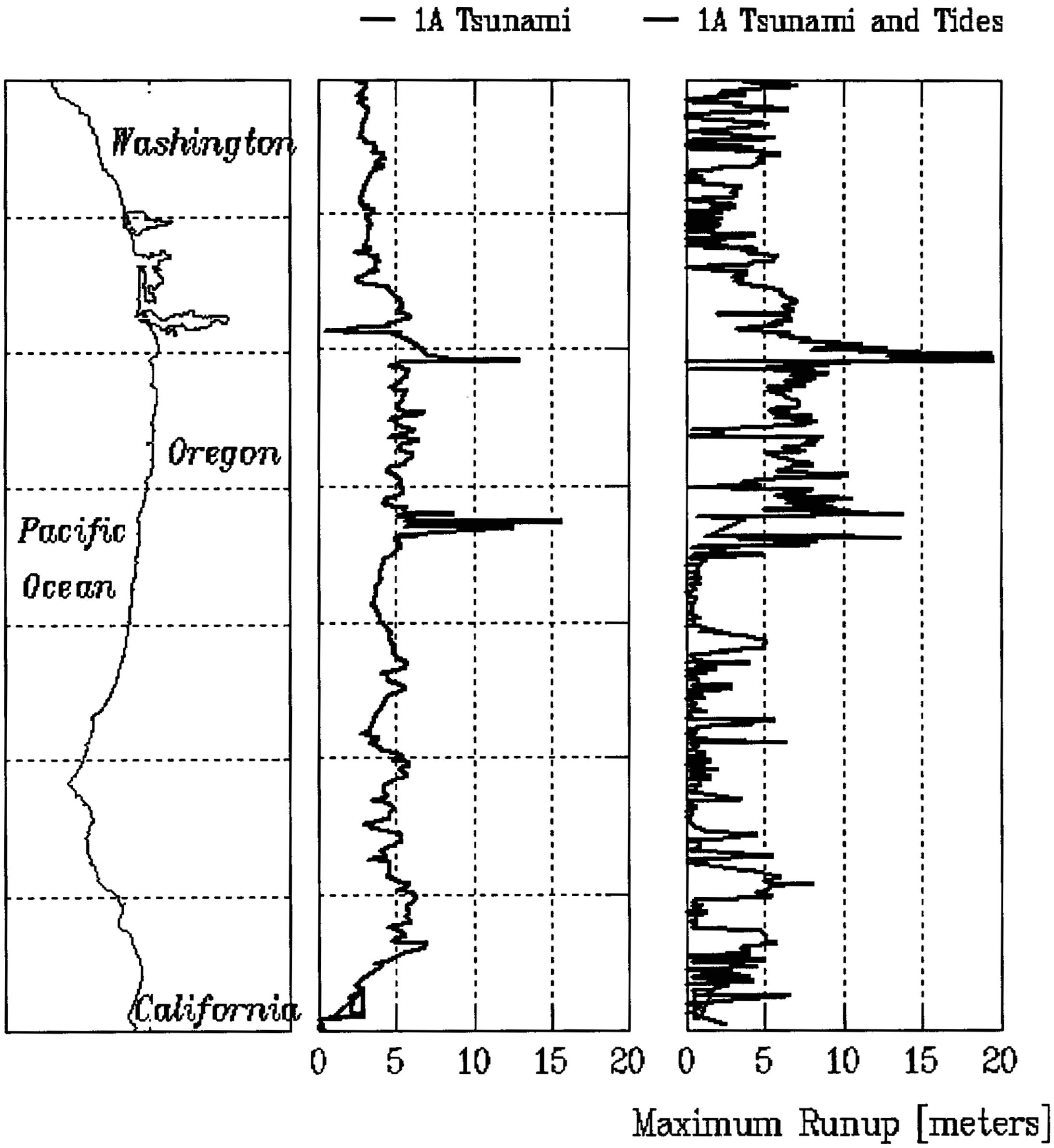

Figure 3.15 Maximum coastal wave elevations with the inclusion of tidal forcing during the 1A grid 1 simulation.

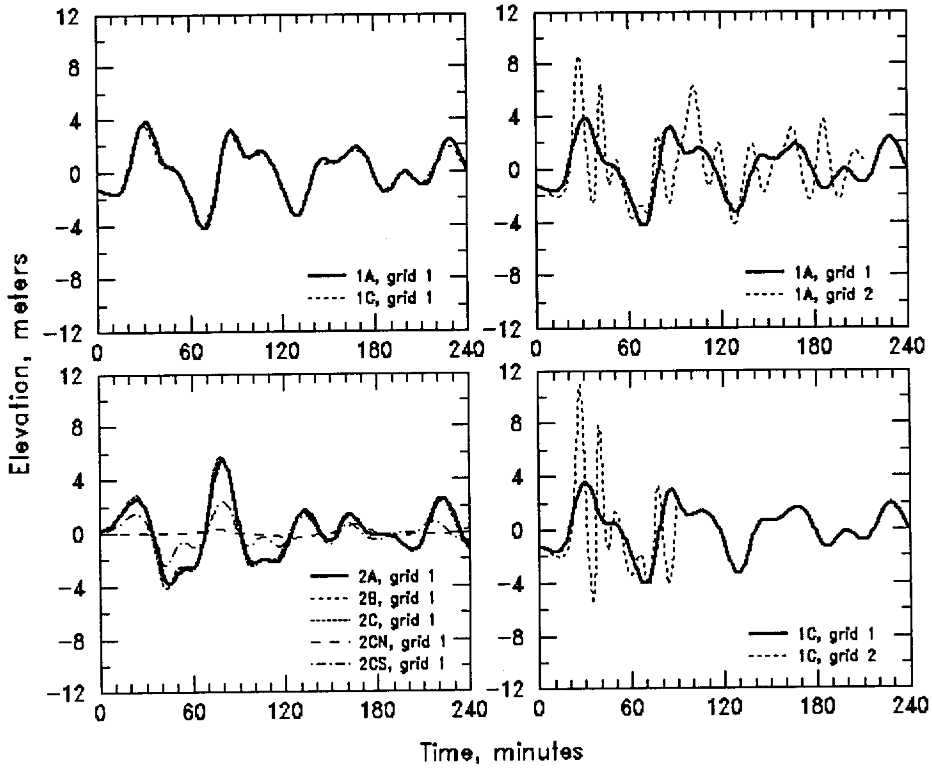

Figure 3.16a Elevation time histories near Klamath, CA.

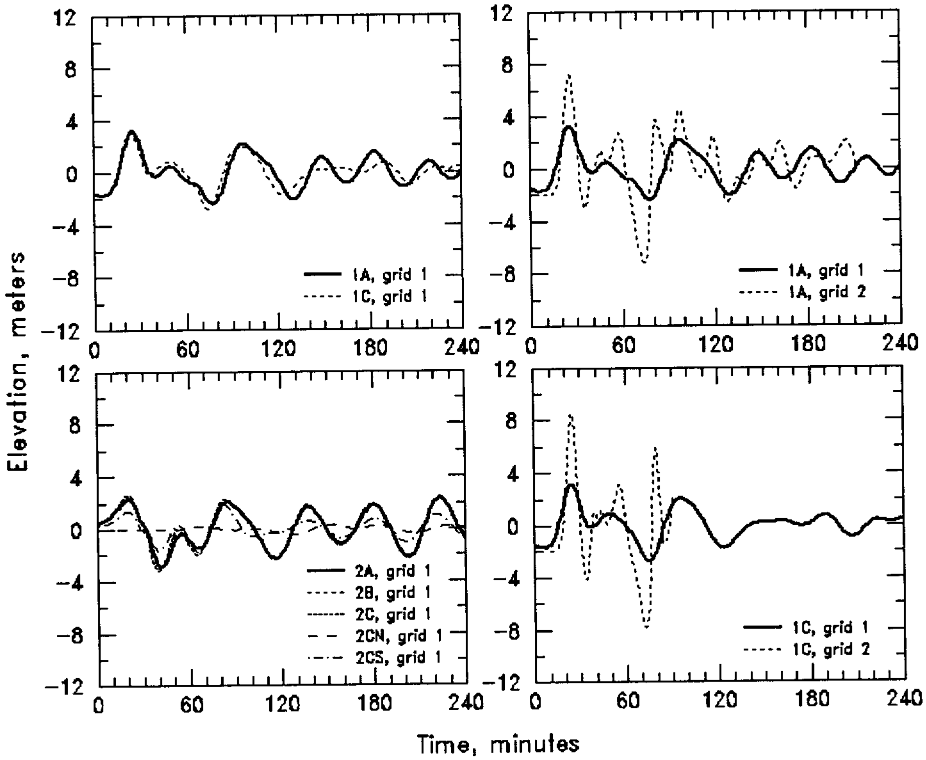

Figure 3.16b Elevation time histories near Crescent City, CA.

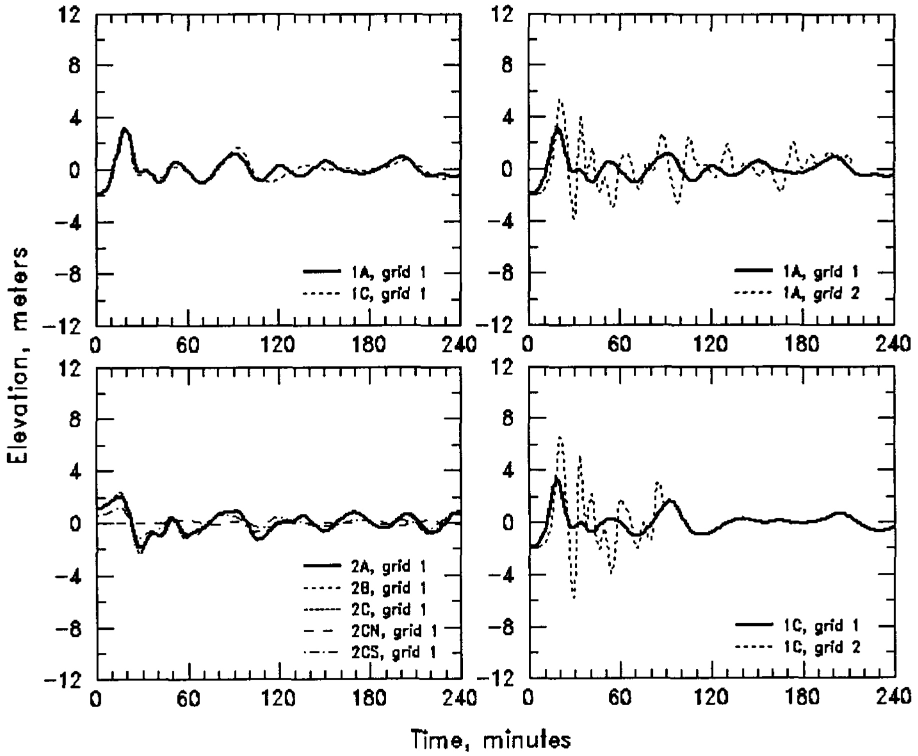

Figure 3.16c Elevation time histories near Brookings, OR.

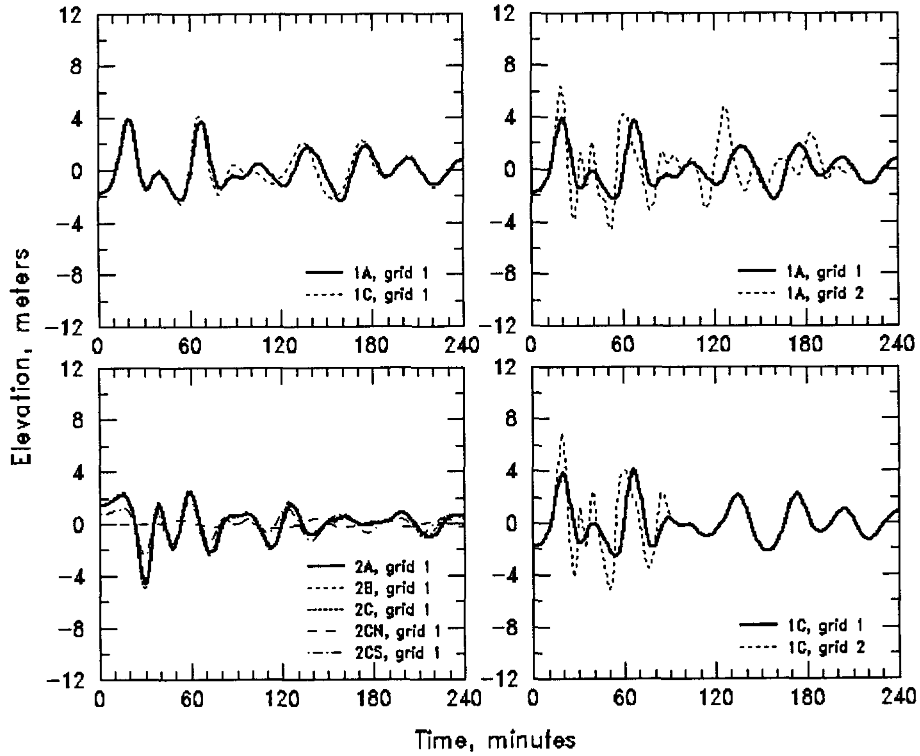

Figure 3.16d Elevation time histories near Gold Beach, OR.

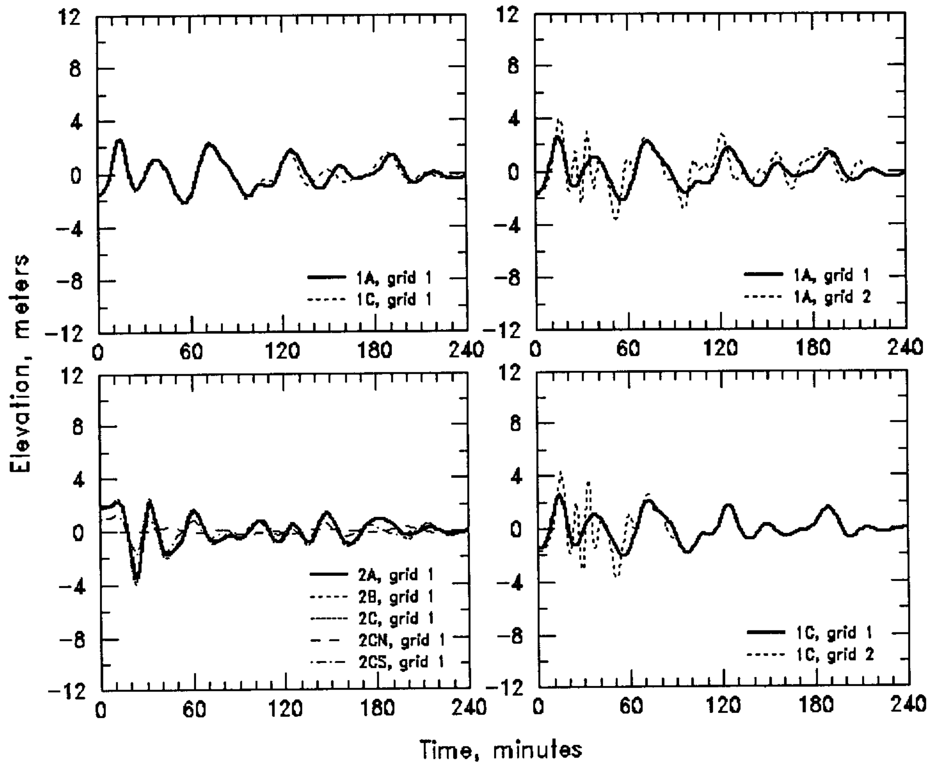

Figure 3.16e Elevation time histories near Port Orford, OR.

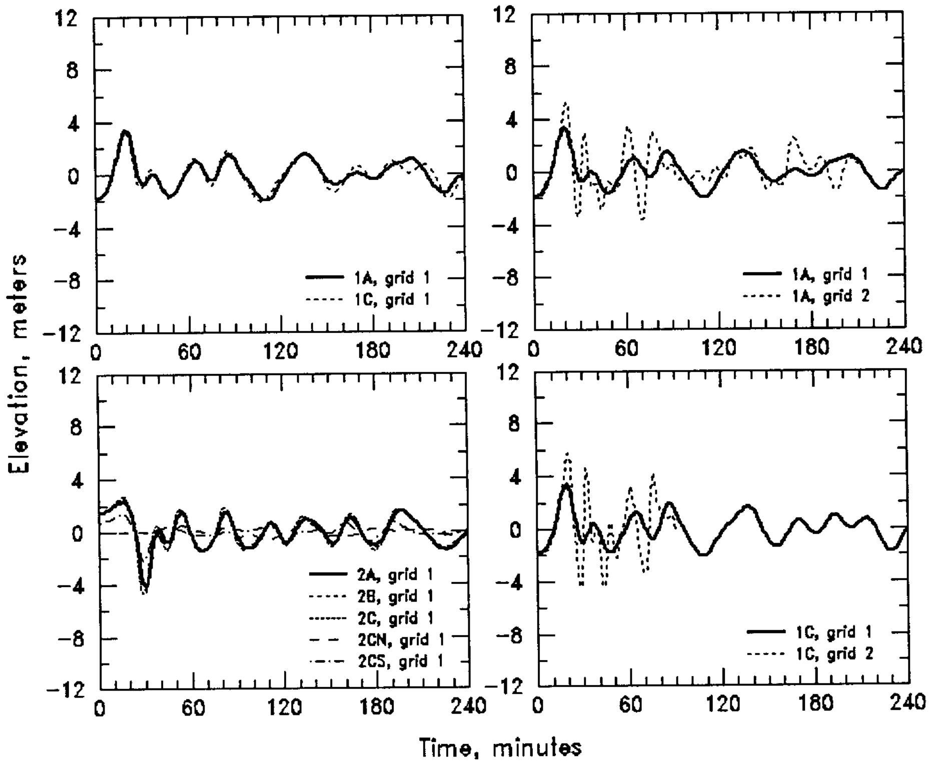

Figure 3.16f Elevation time histories near Bandon, OR.

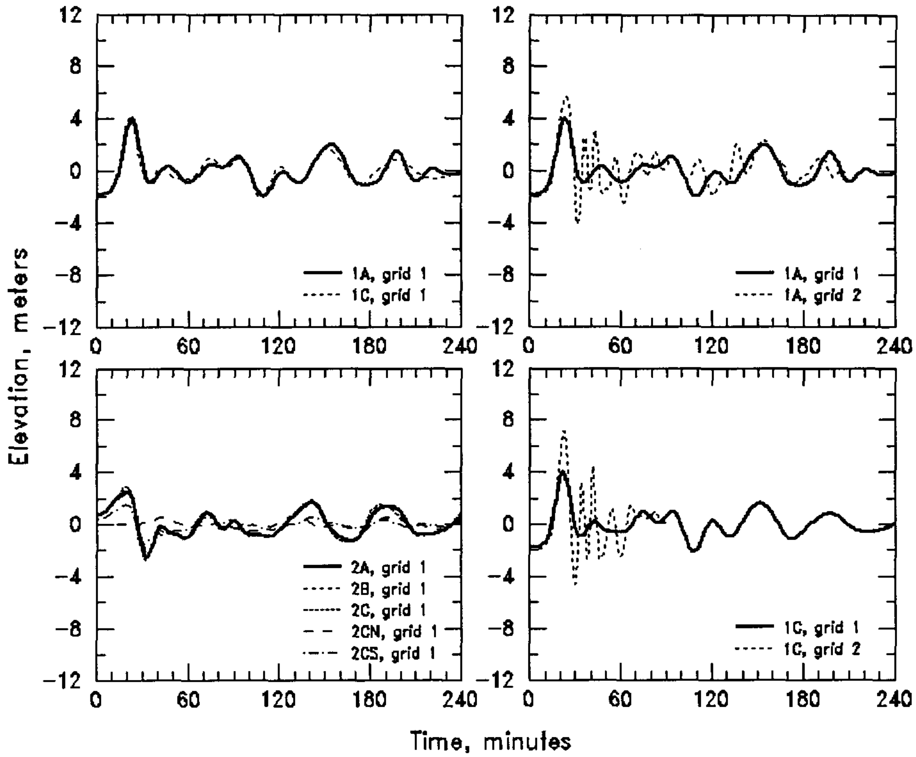

Figure 3.16g Elevation time histories near the entrance of Coos Bay, OR.

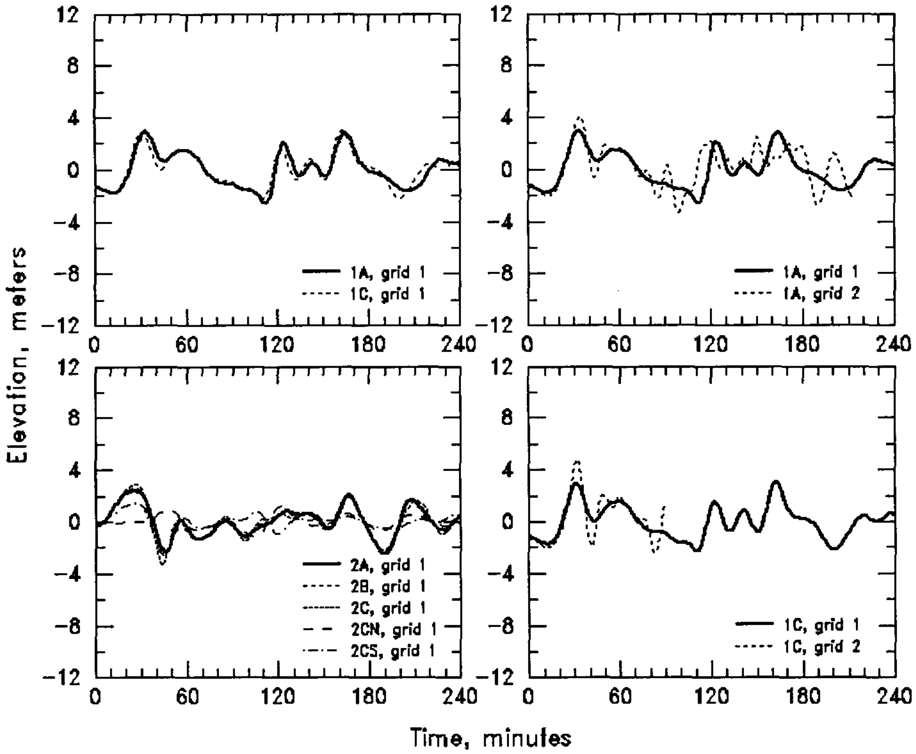

Figure 3.16h Elevation time histories near Florence, OR.

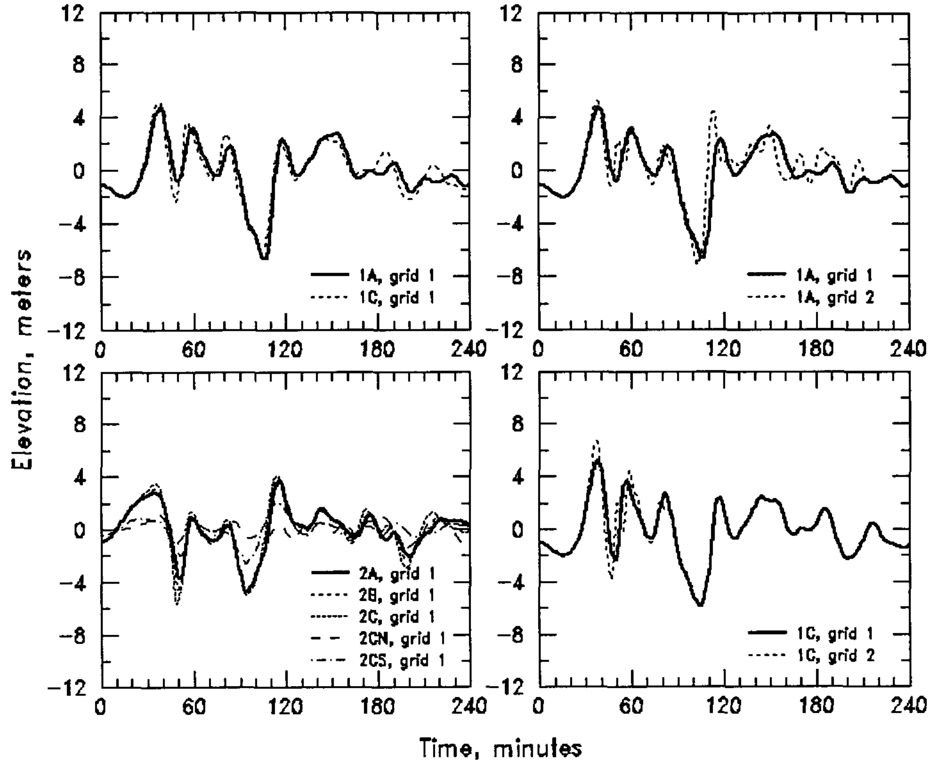

Figure 3.16i Elevation time histories near the entrance of Alsea Bay, OR.

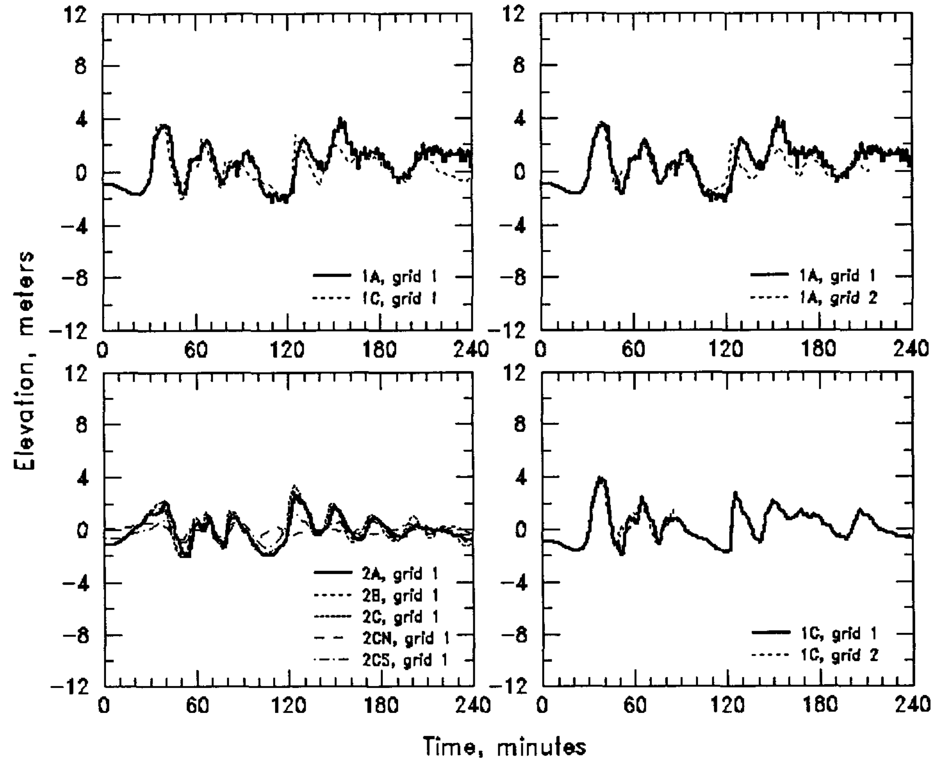

Figure 3.16j Elevation time histories near the entrance of Yaquina Bay, OR.

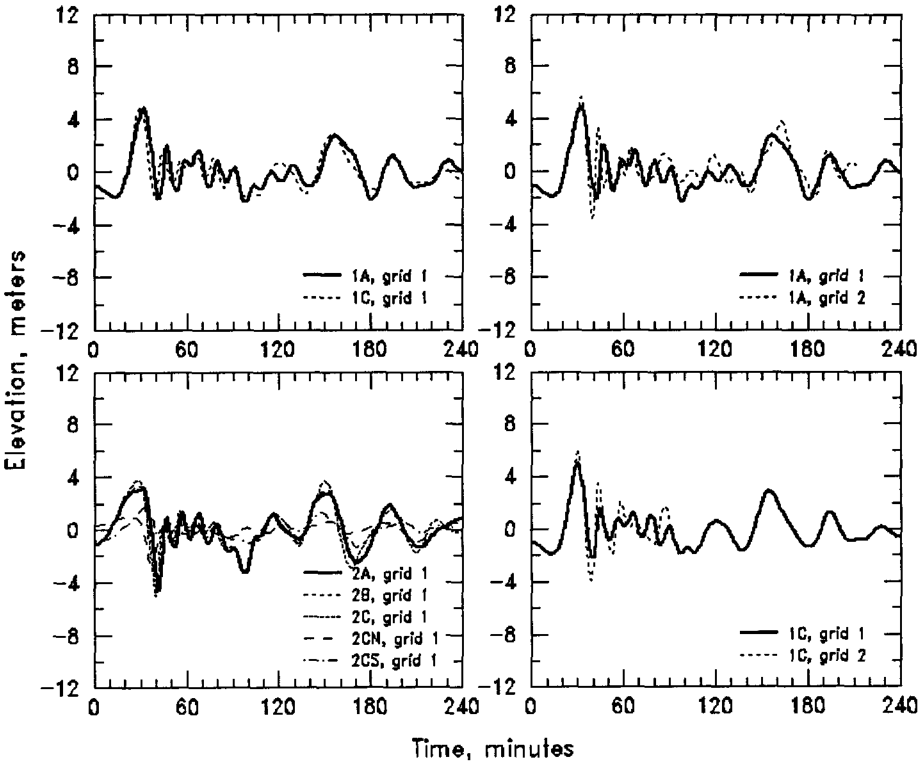

Figure 3.16k Elevation time histories near Lincoln City, OR.

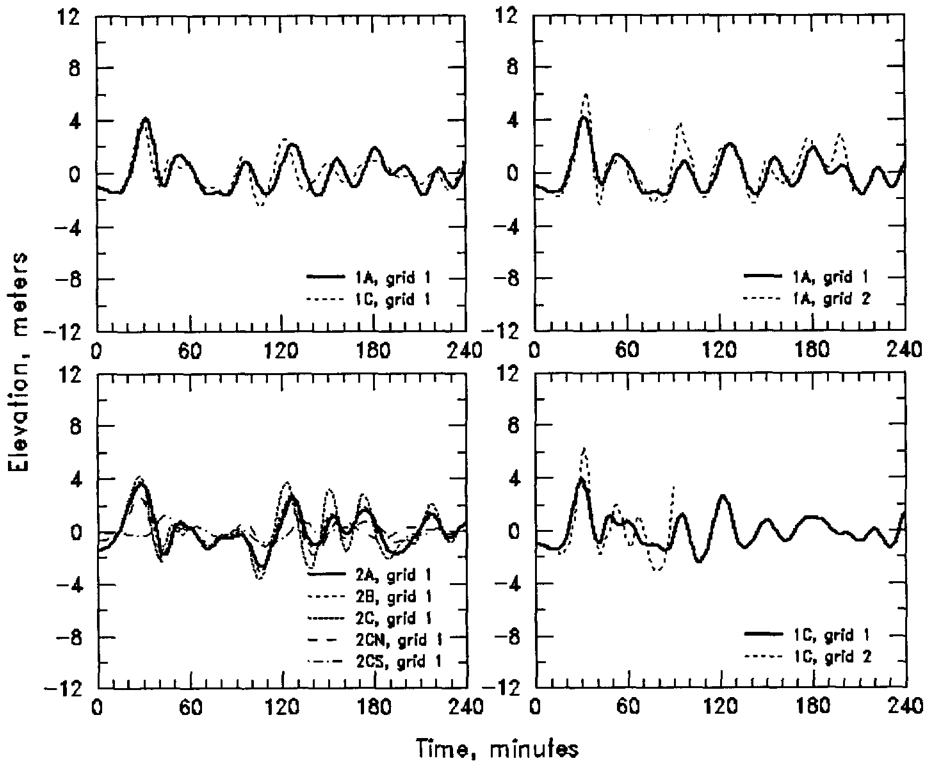

Figure 3.16l Elevation time histories near Netarts, OR.

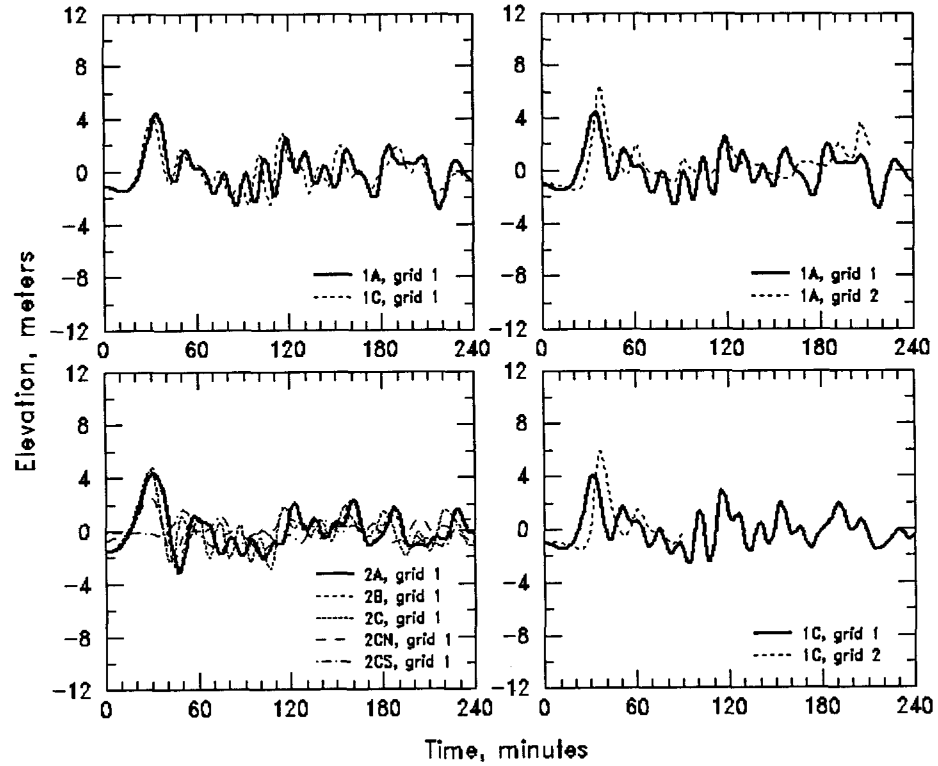

Figure 3.16m Elevation time histories near the entrance of Tillamook Bay, OR.

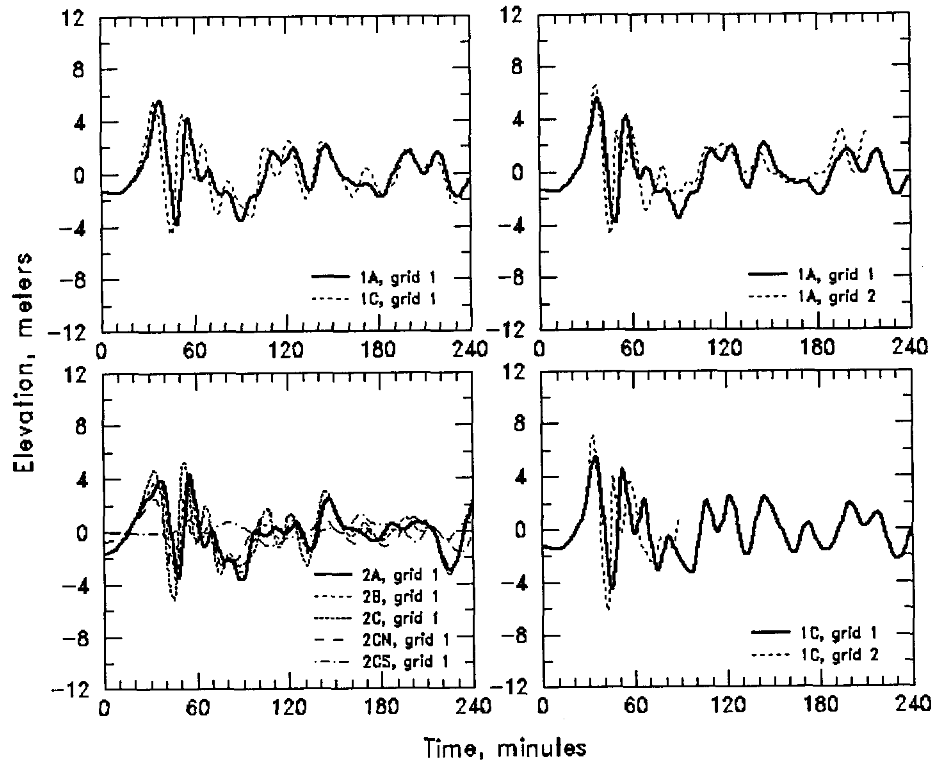

Figure 3.16n Elevation time histories near Cannon Beach, OR.

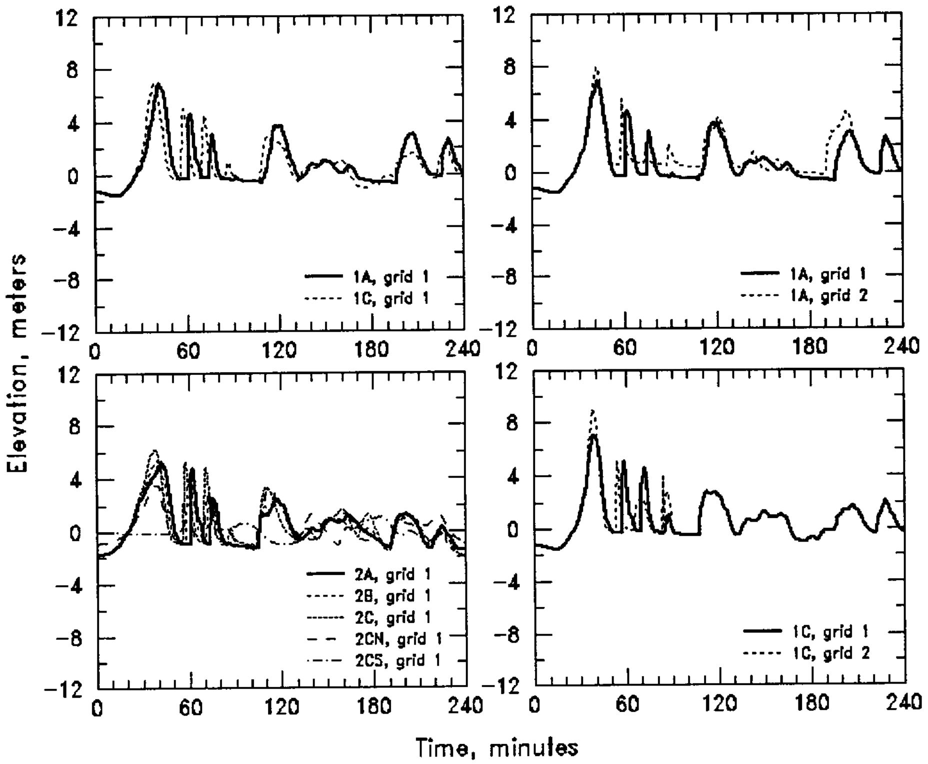

Figure 3.16o Elevation time histories near Seaside, OR.

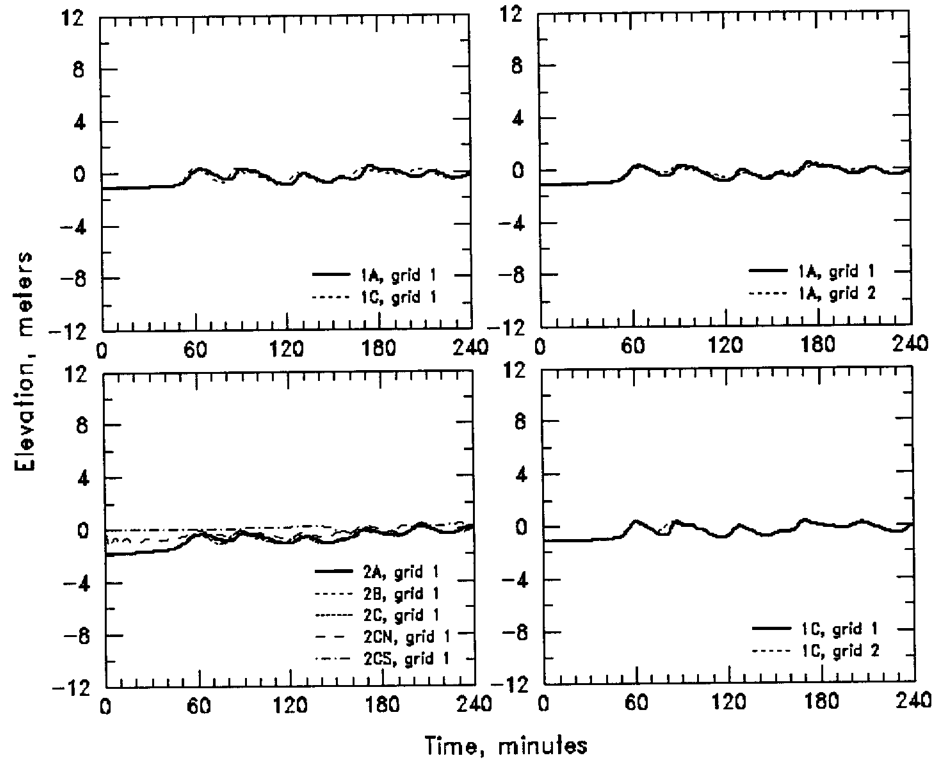

Figure 3.16p Elevation time histories near Astoria, OR.

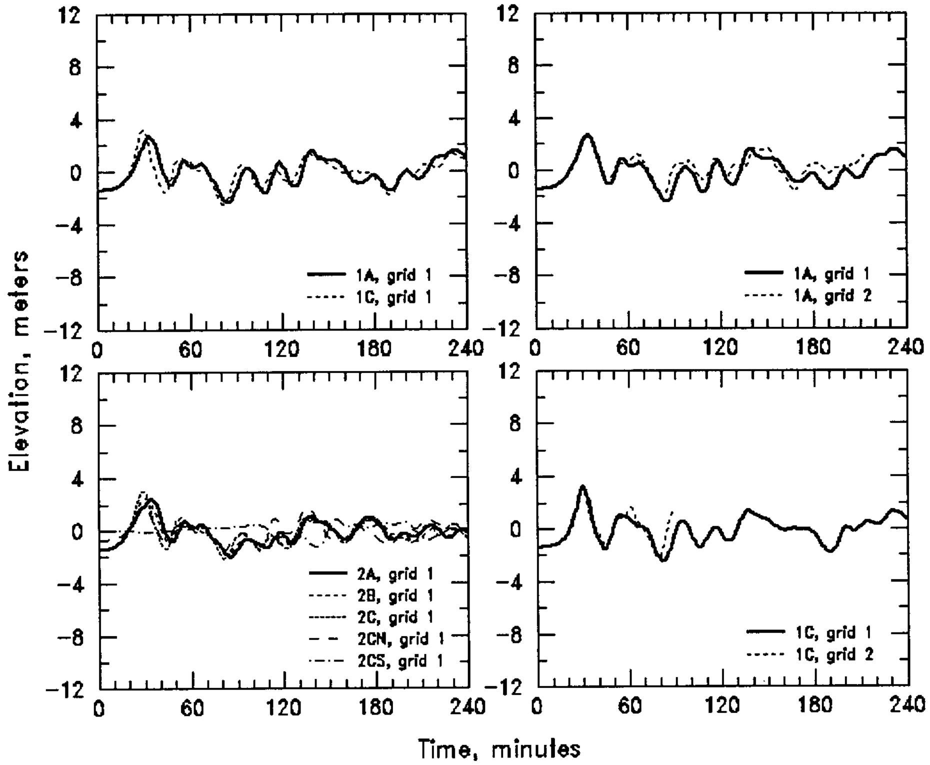

Figure 3.16q Elevation time histories near the entrance of the Columbia River.

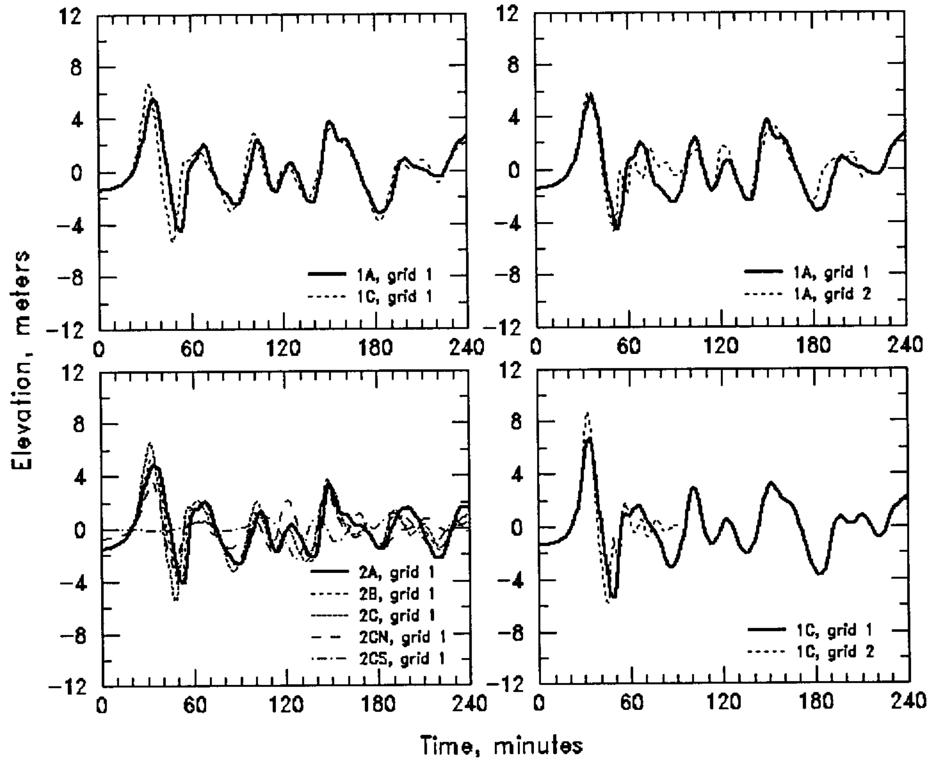

Figure 3.16r Elevation time histories near Long Beach, WA.

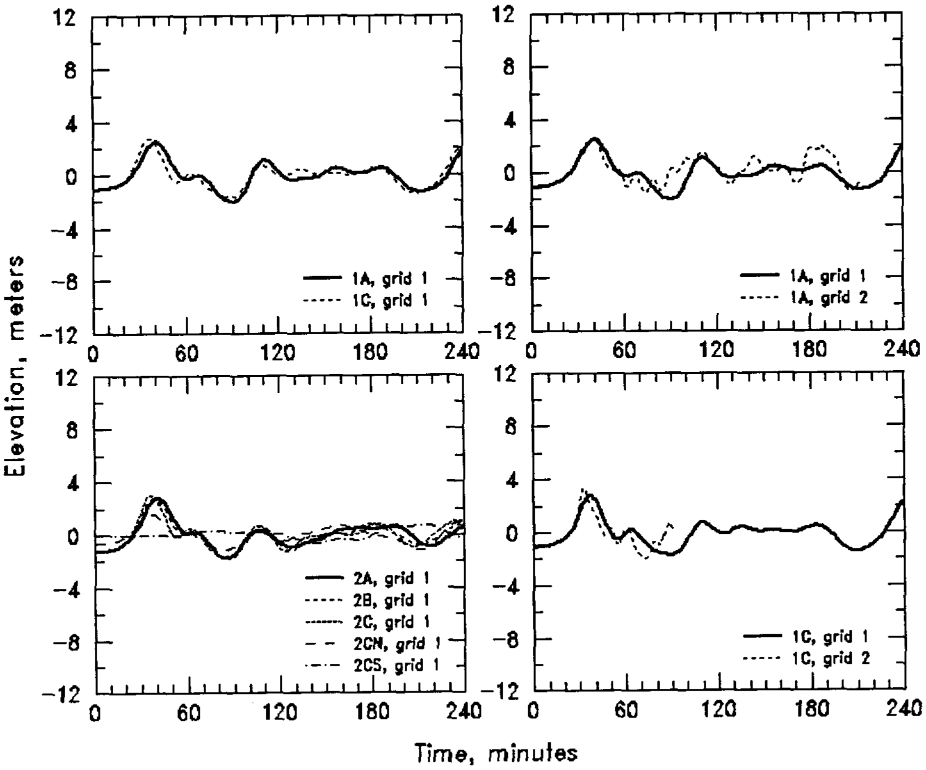

Figure 3.16s Elevation time histories near the entrance of Willapa Bay, WA.

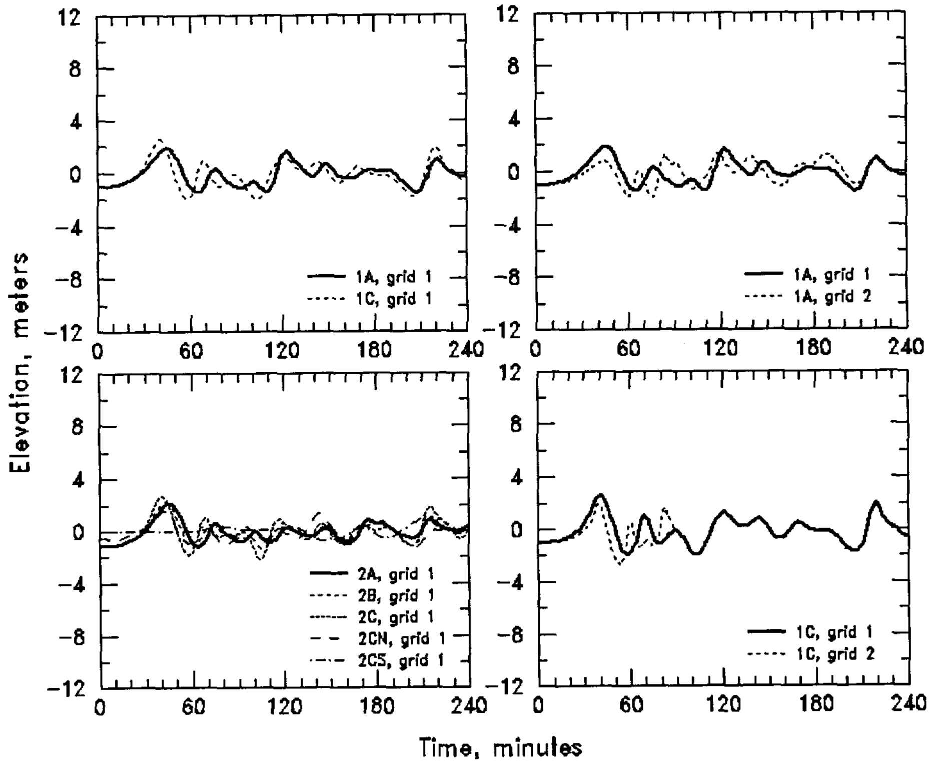

Figure 3.16t Elevation time histories near the entrance of Grays Harbor, WA.

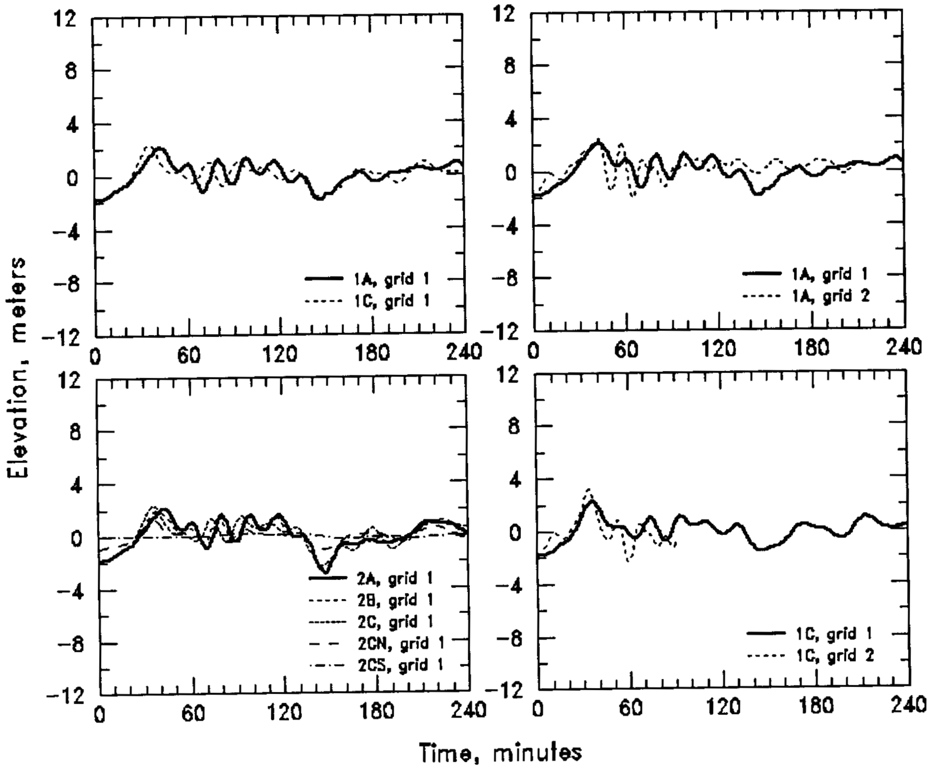

Figure 3.16u Elevation time histories near Neah Bay, WA.

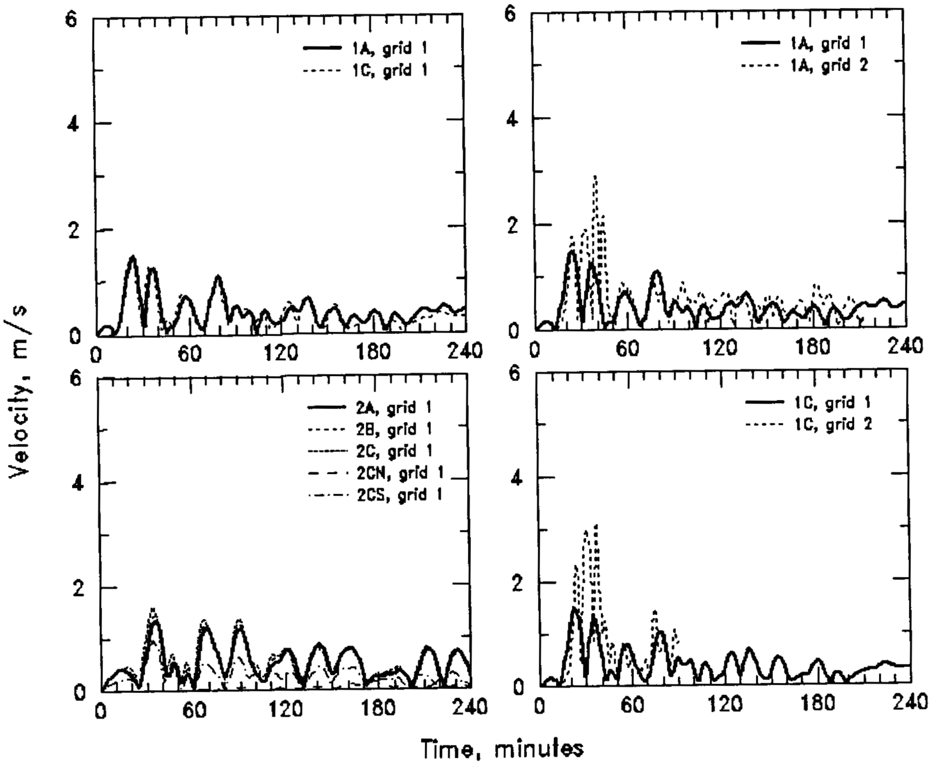

Figure 3.17a Velocity time histories near Klamath, CA.

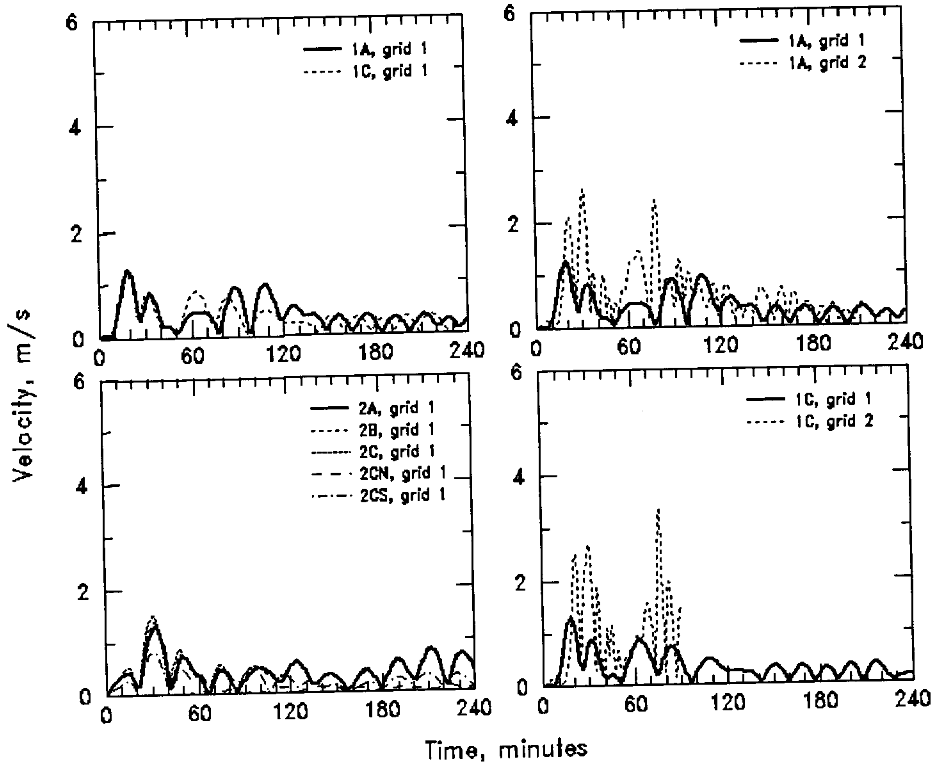

Figure 3.17b Velocity time histories near Crescent City, CA.

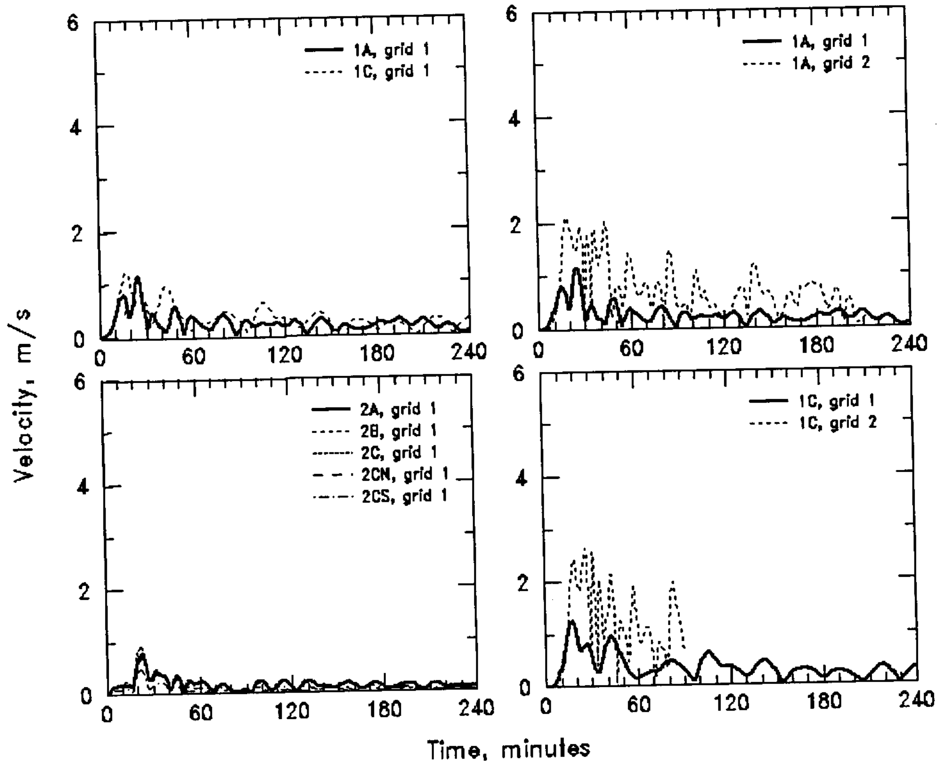

Figure 3.17c Velocity time histories near Brookings, OR.

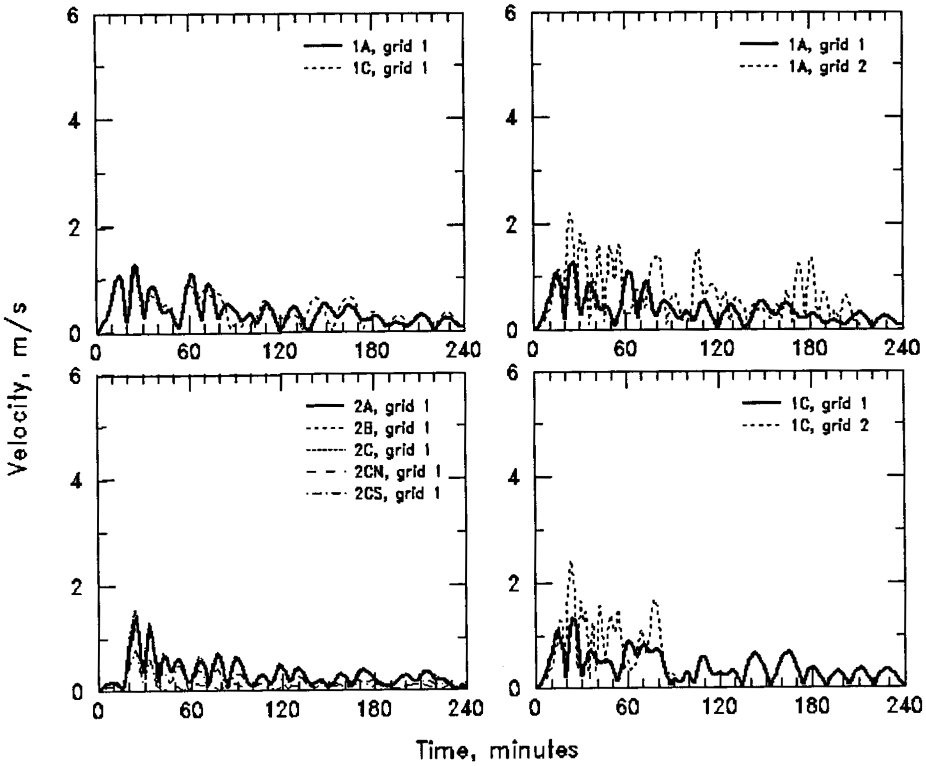

Figure 3.17d Velocity time histories near Gold Beach, OR.

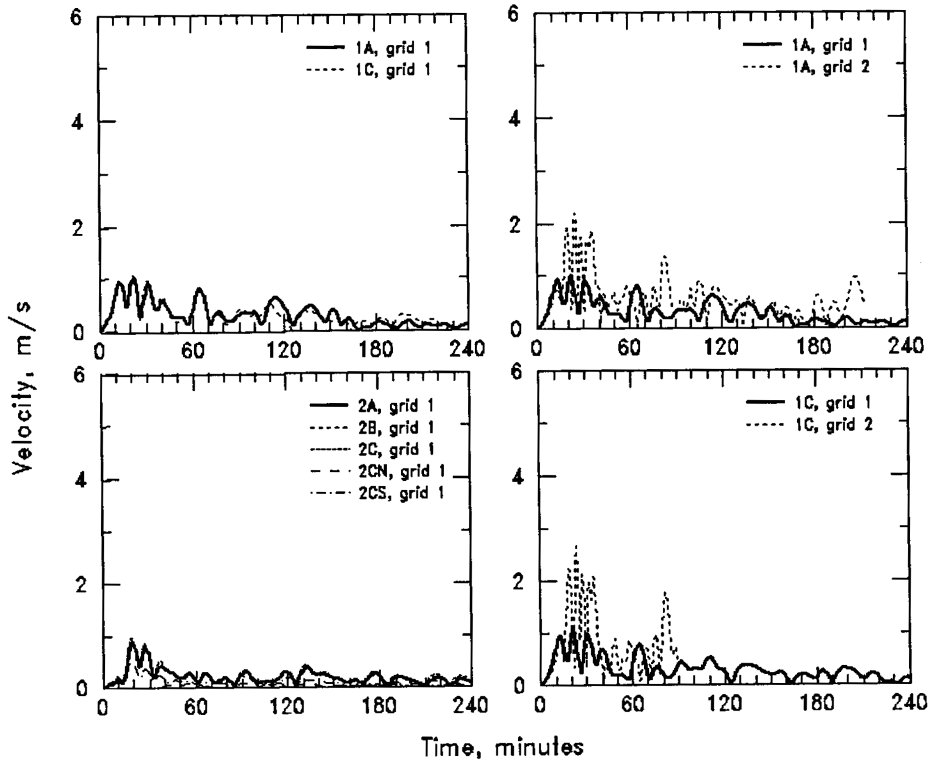

Figure 3.17e Velocity time histories near Port Orford, OR.

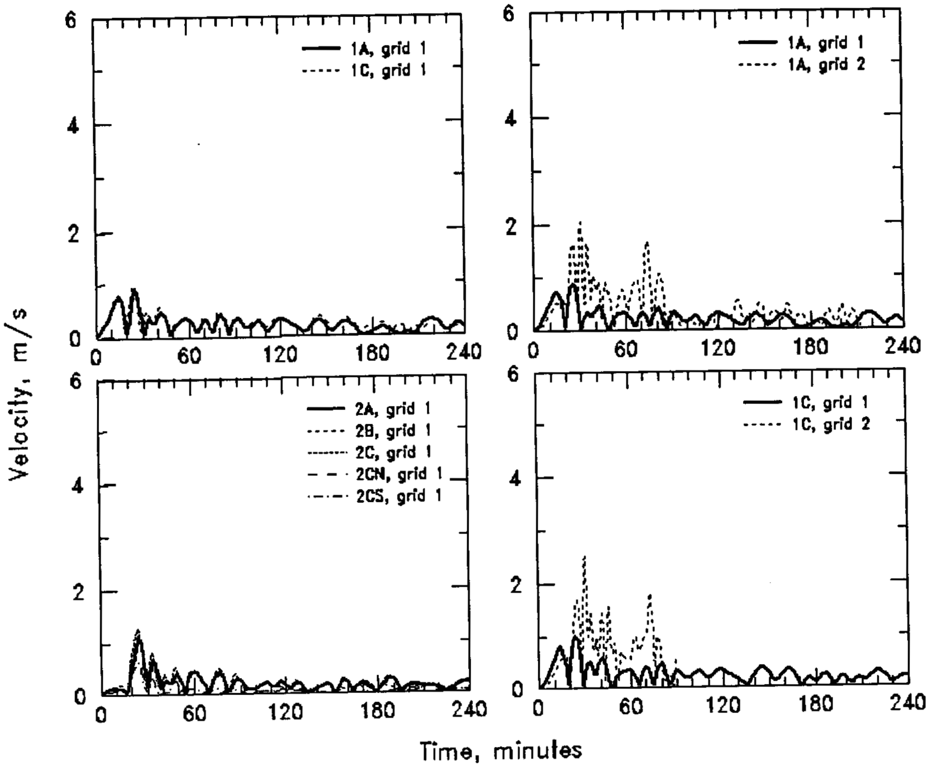

Figure 3.17f Velocity time histories near Bandon, OR.

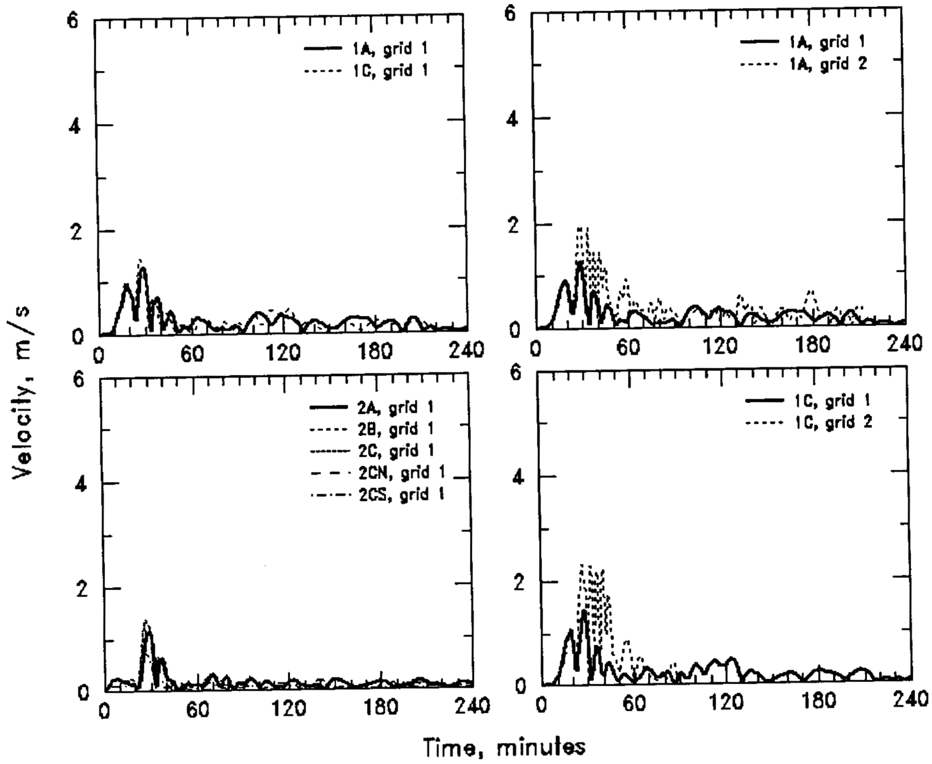

Figure 3.17g Velocity time histories near the entrance of Coos Bay, OR.

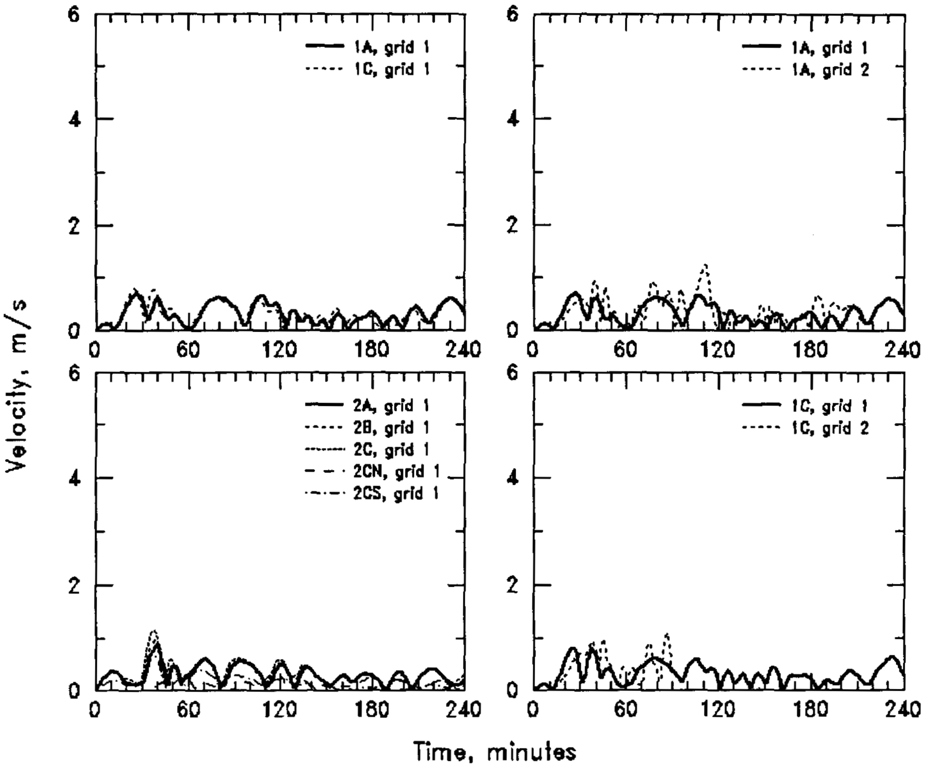

Figure 3.17h Velocity time histories near Florence, OR.

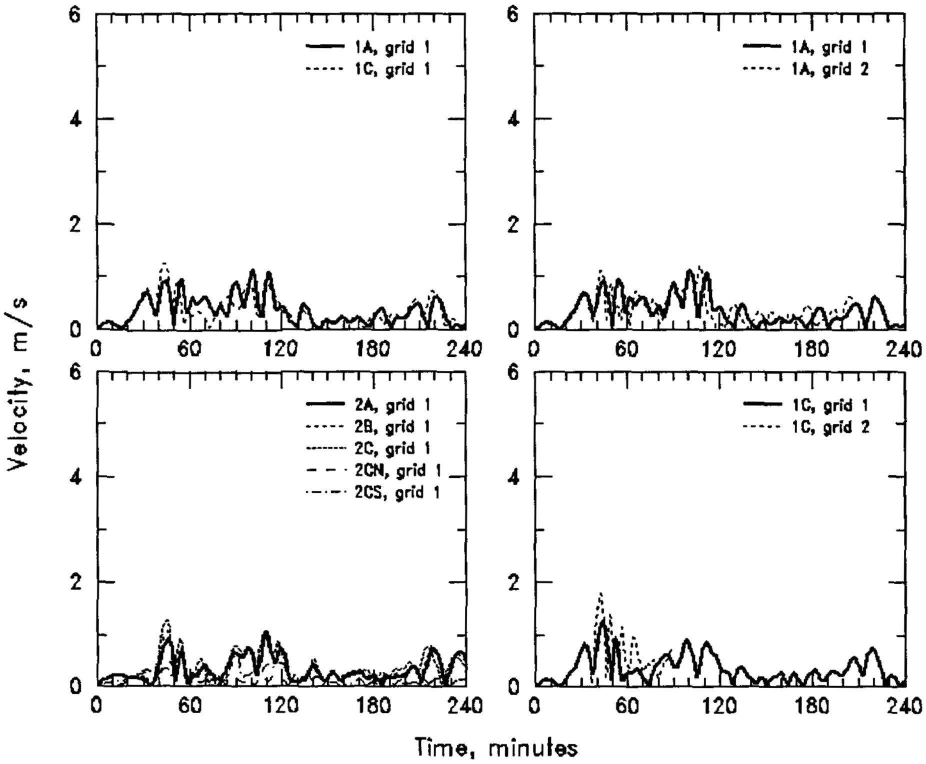

Figure 3.17i Velocity time histories near the entrance of Alsea Bay, OR.

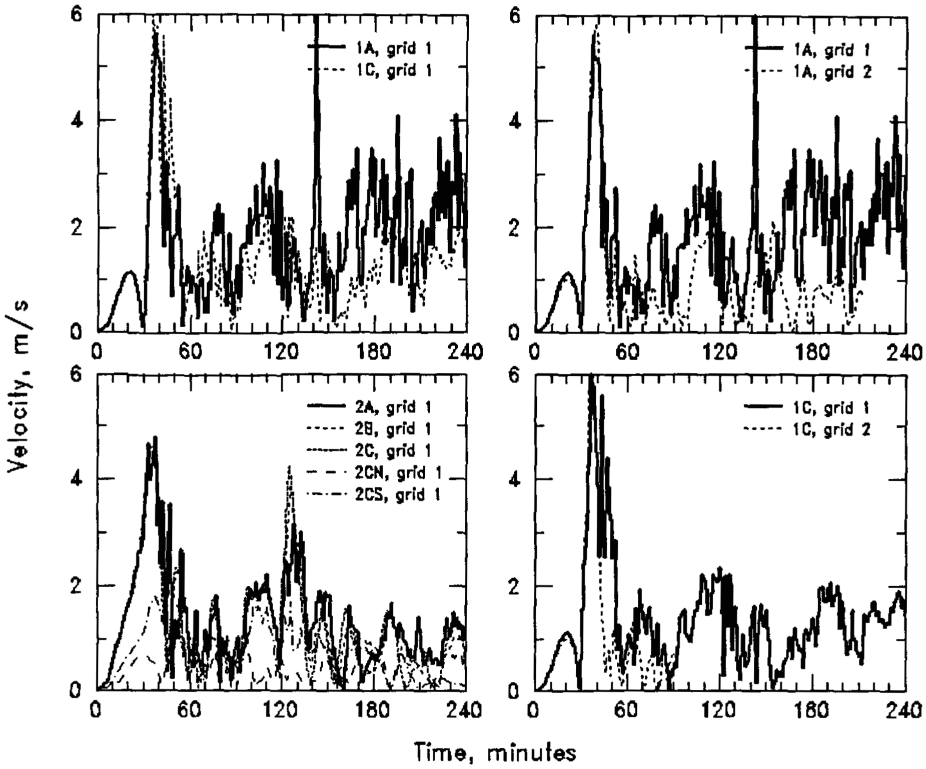

Figure 3.17j Velocity time histories near the entrance of Yaquina Bay, OR.

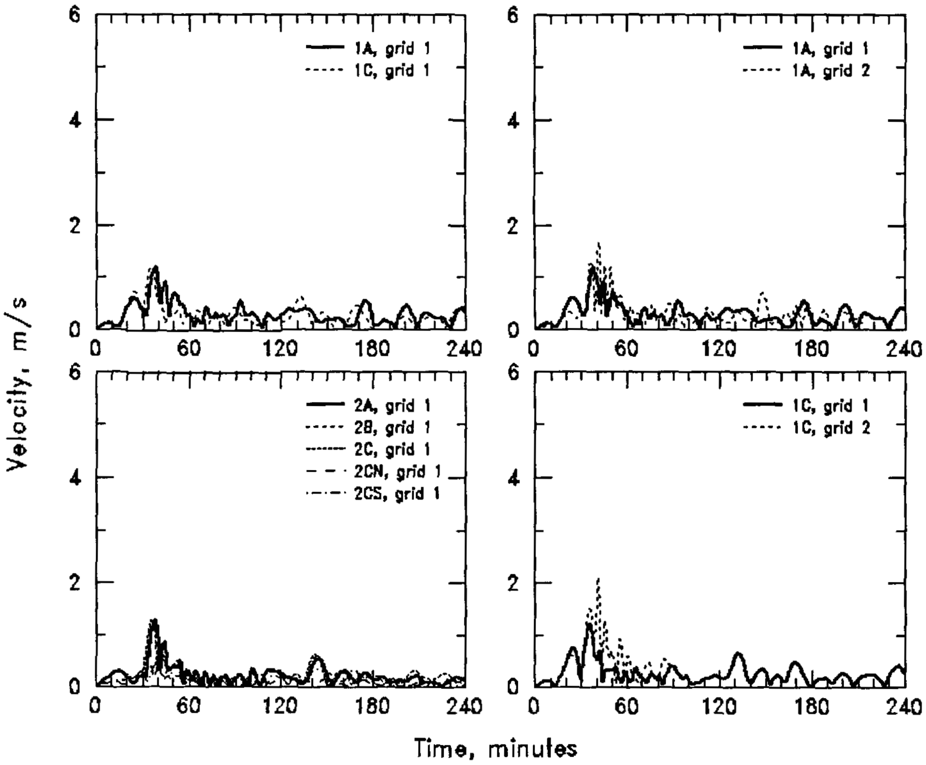

Figure 3.17k Velocity time histories near Lincoln City, OR.

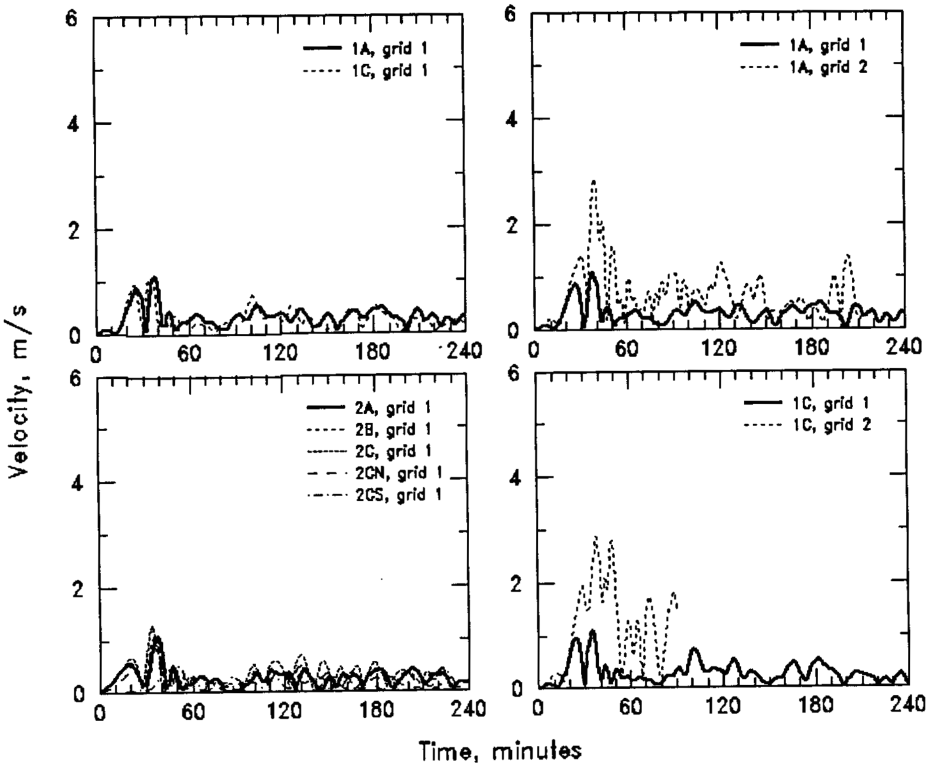

Figure 3.17l Velocity time histories near Netarts, OR.

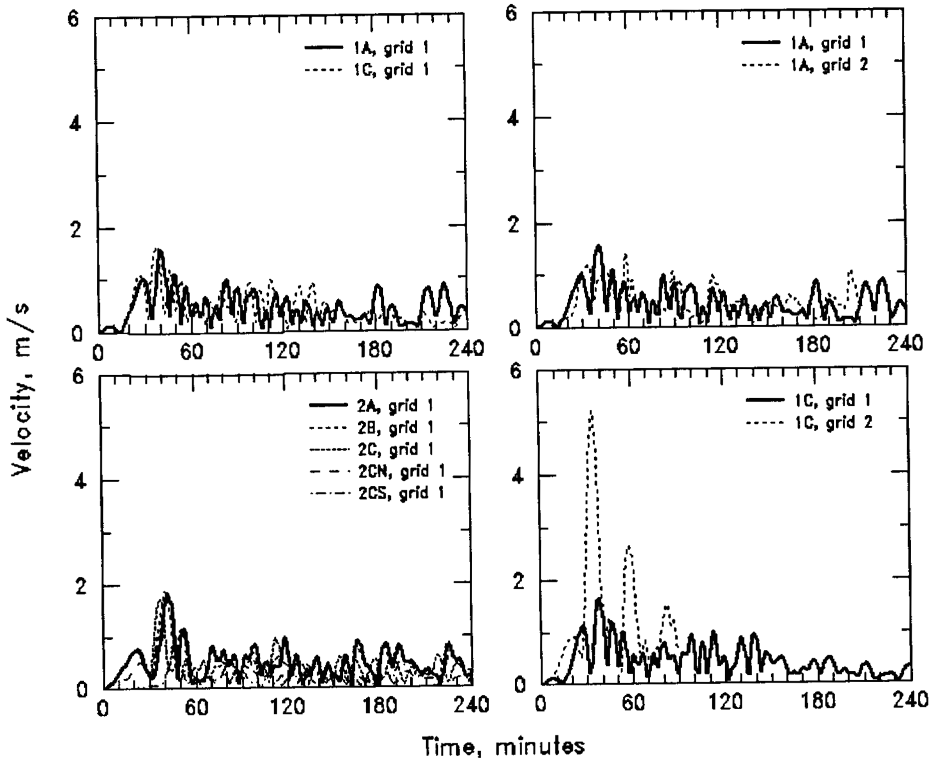

Figure 3.17m Velocity time histories near the entrance of Tillamook Bay, OR.

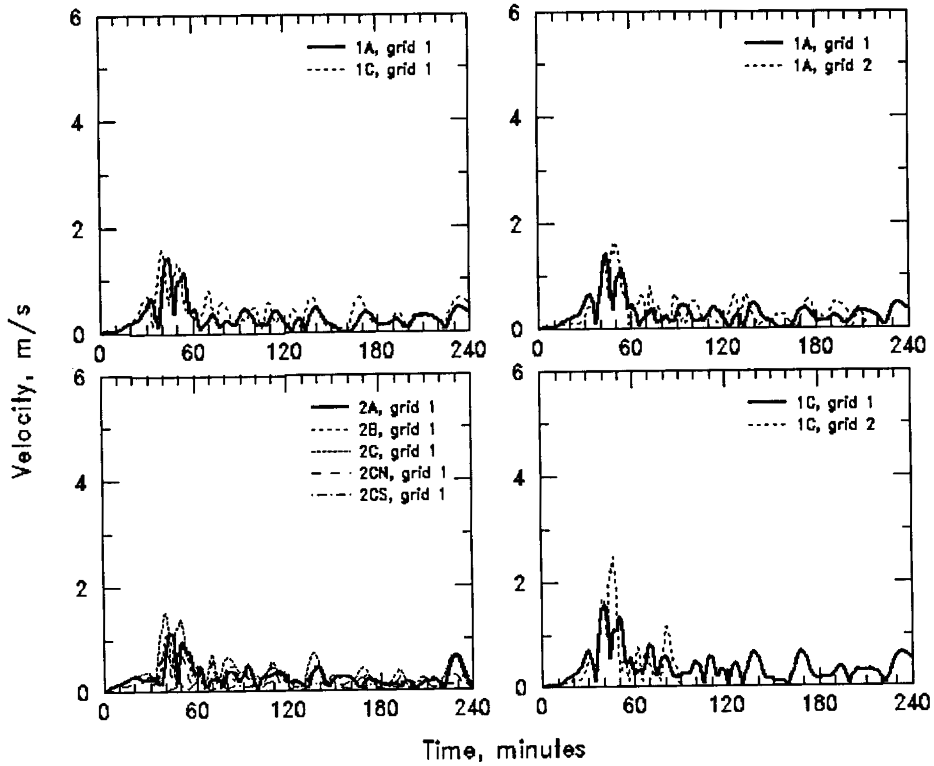

Figure 3.17n Velocity time histories near Cannon Beach, OR.

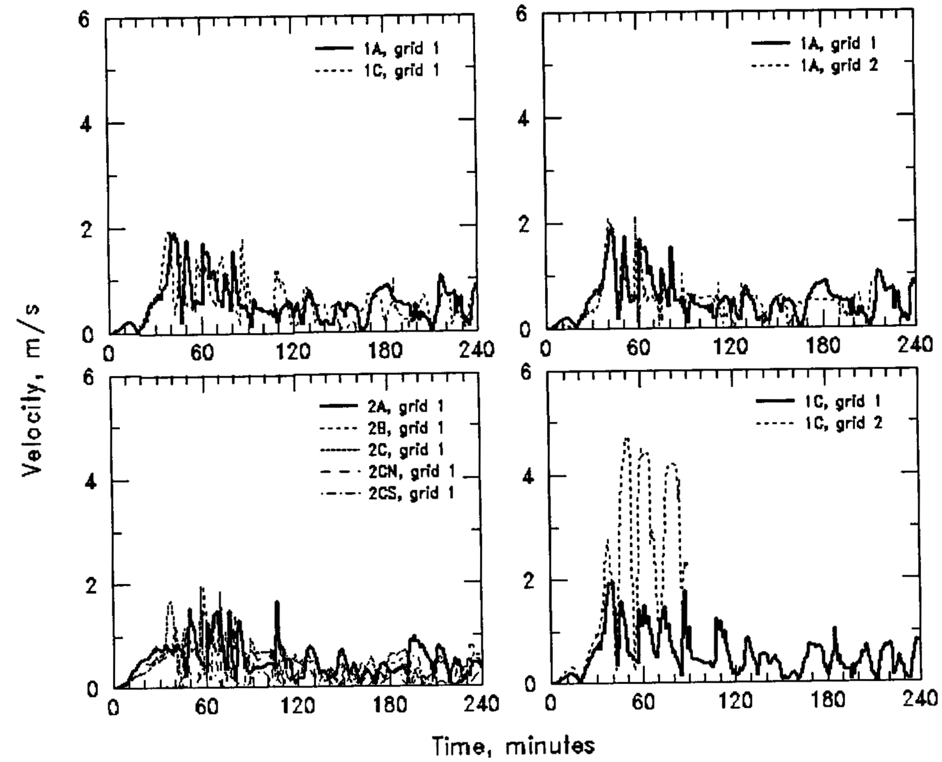

Figure 3.17o Velocity time histories near Seaside, OR.

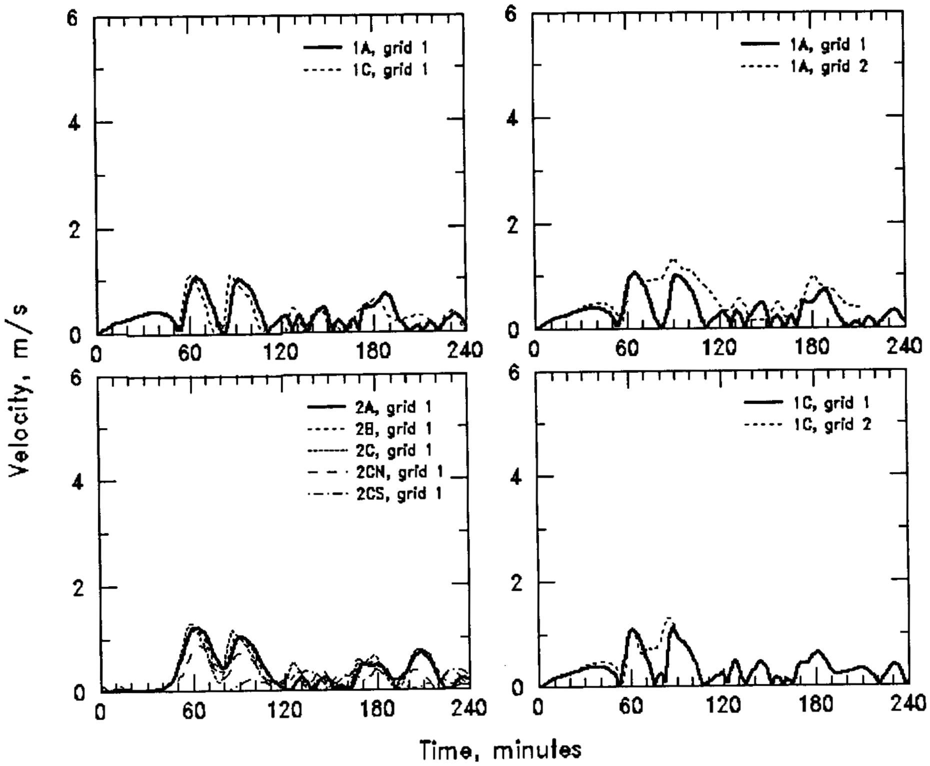

Figure 3.17p Velocity time histories near Astoria, OR.

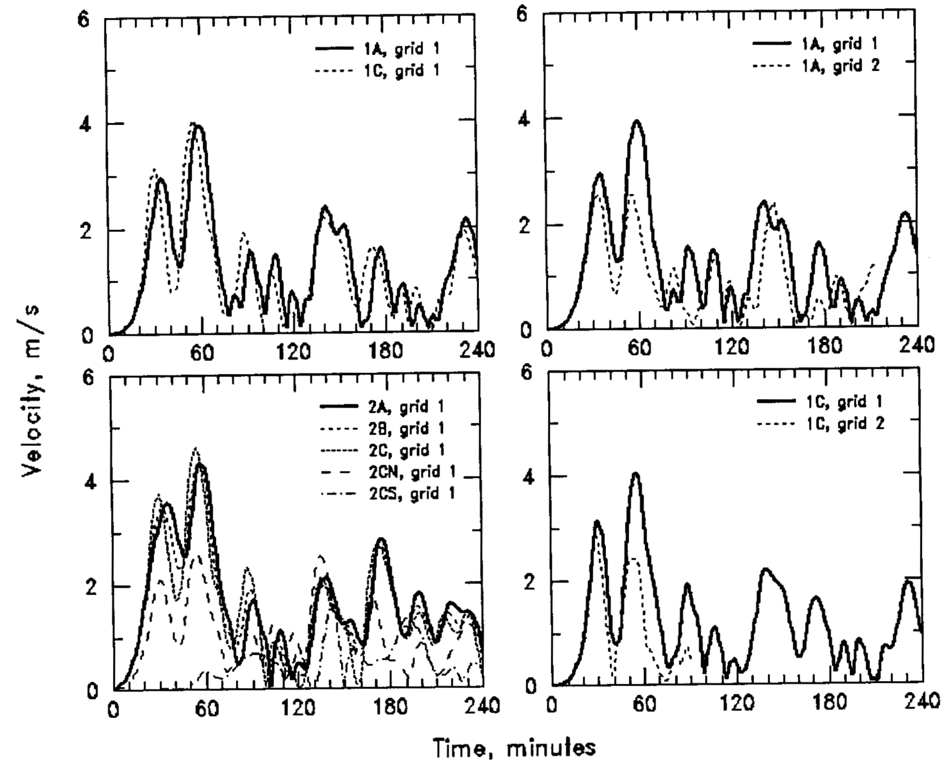

Figure 3.17q Velocity time histories near the entrance of the Columbia River.

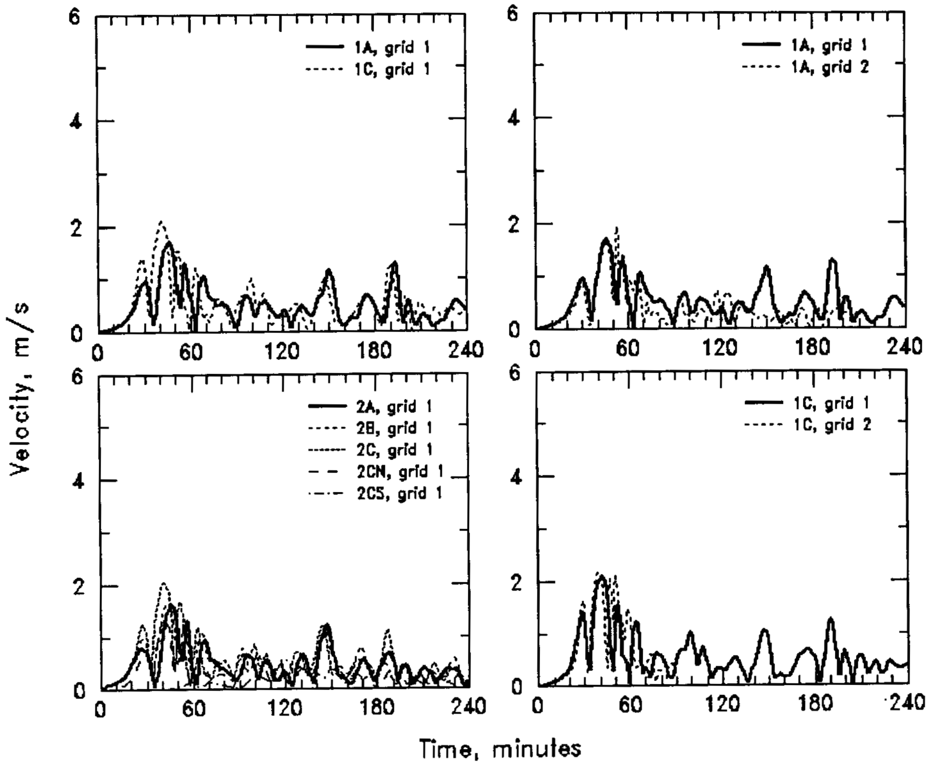

Figure 3.17r Velocity time histories near Long Beach, WA.

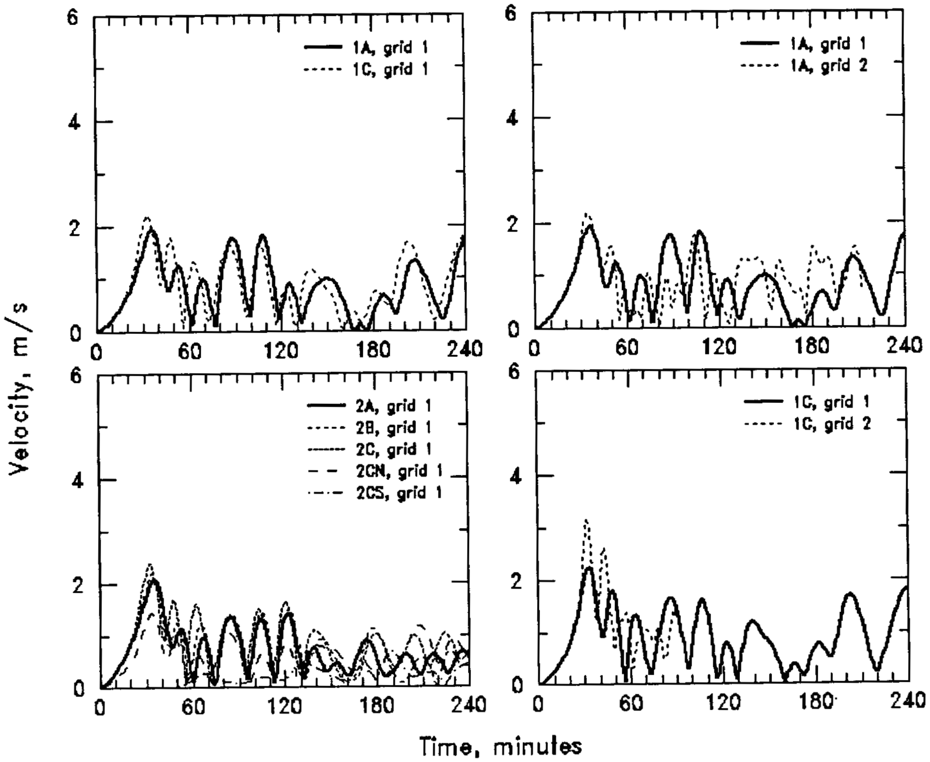

Figure 3.17s Velocity time histories near the entrance of Willapa Bay, WA.

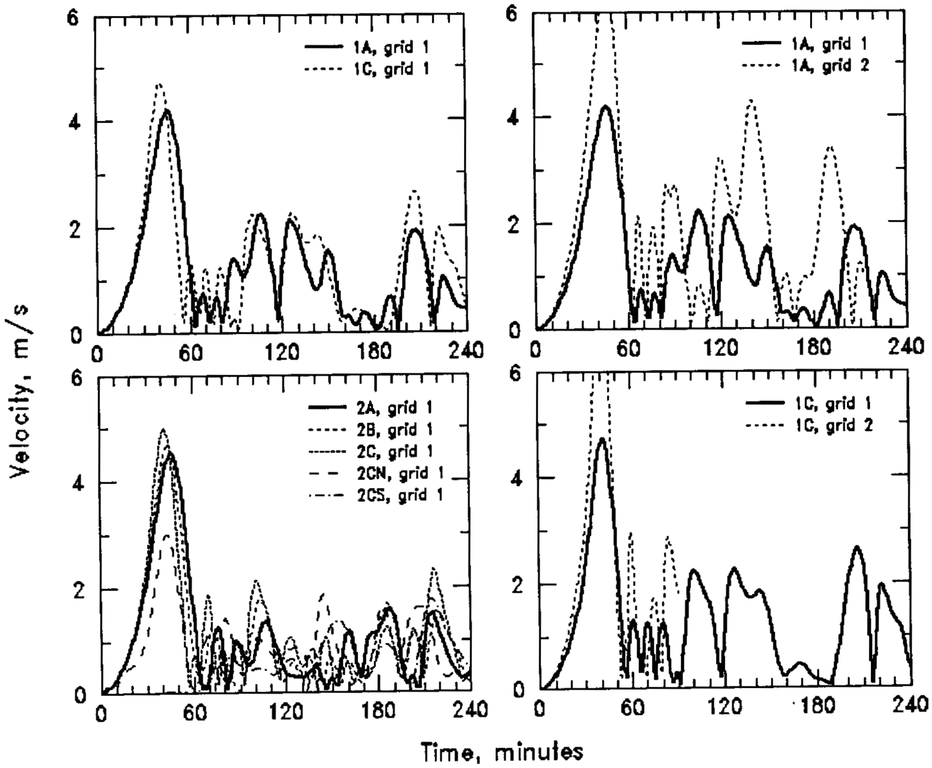

Figure 3.17t Velocity time histories near the entrance of Grays Harbor, WA.

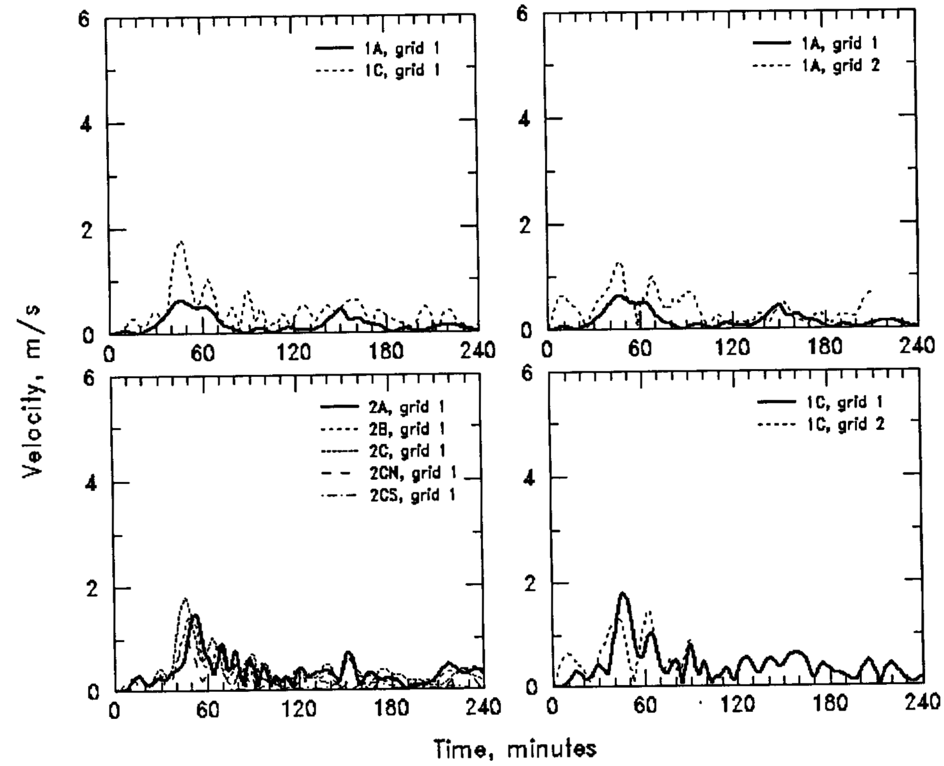

Figure 3.17u Velocity time histories near Neah Bay, WA.

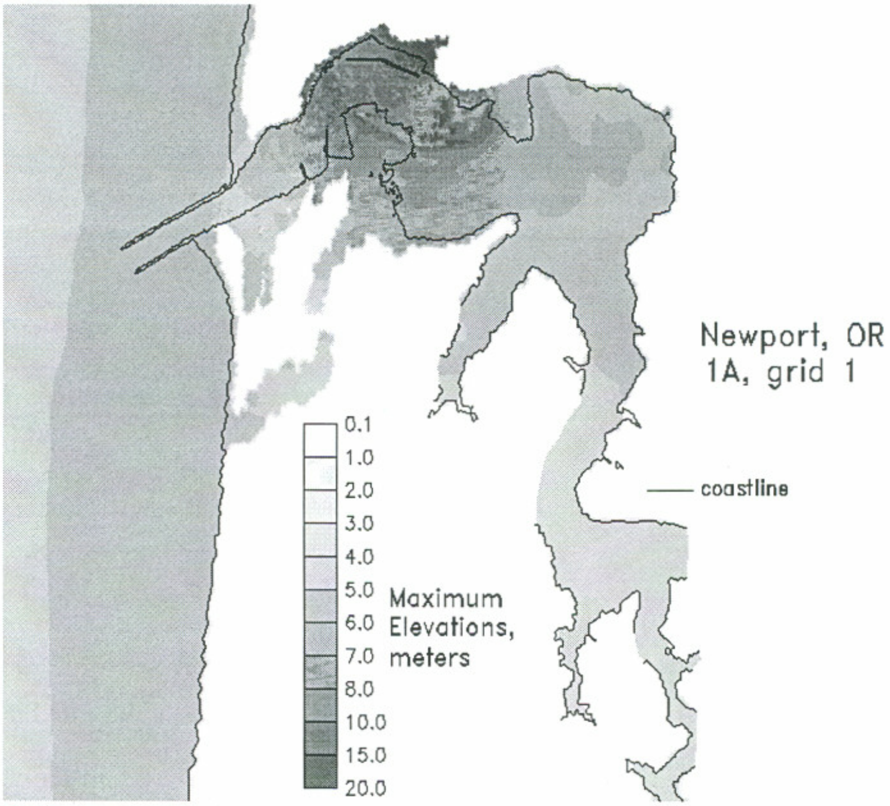

Figure 3.18a Isolines of maximum elevation near Newport, OR for 1A, grid 1.

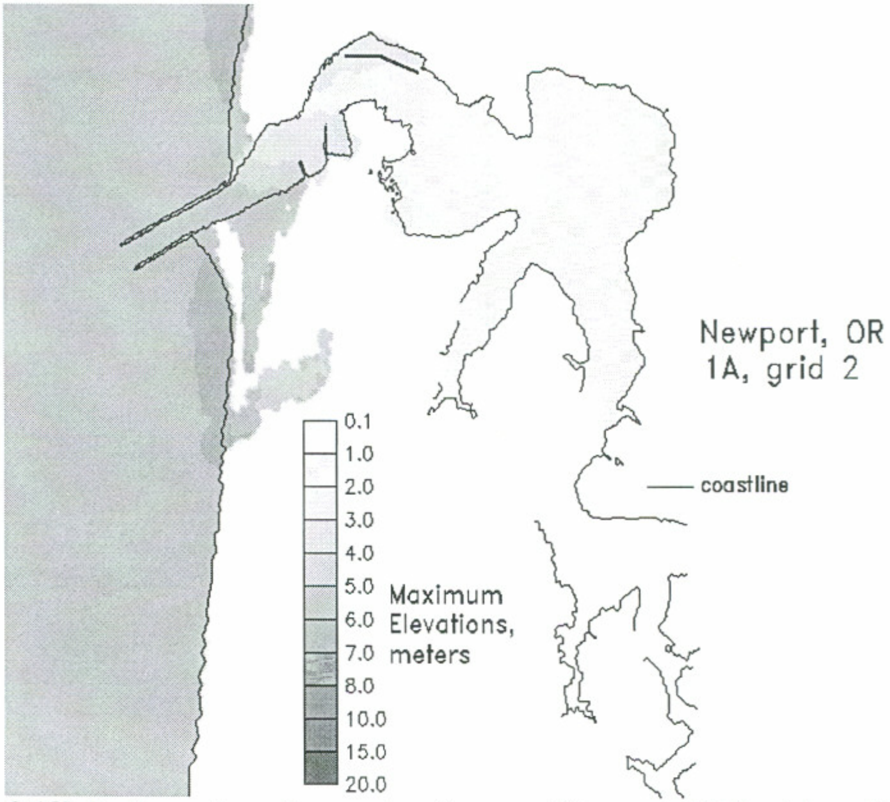

Figure 3.18b Isolines of maximum elevation near Newport, OR for 1A, grid 2.

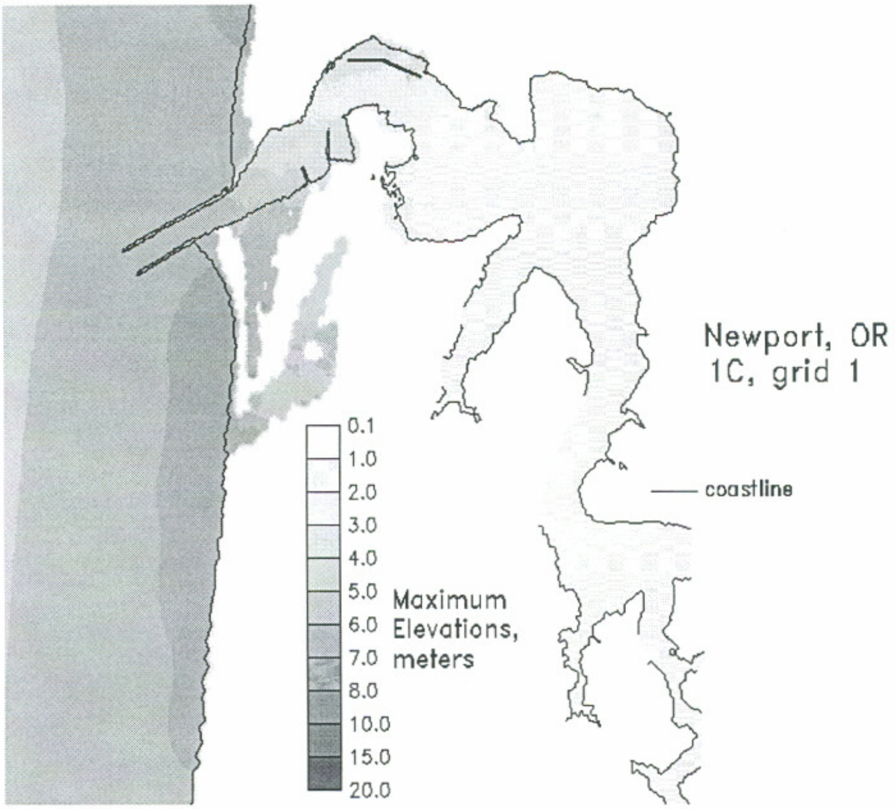

Figure 3.18c Isolines of maximum elevation near Newport, OR for 1C, grid 1.

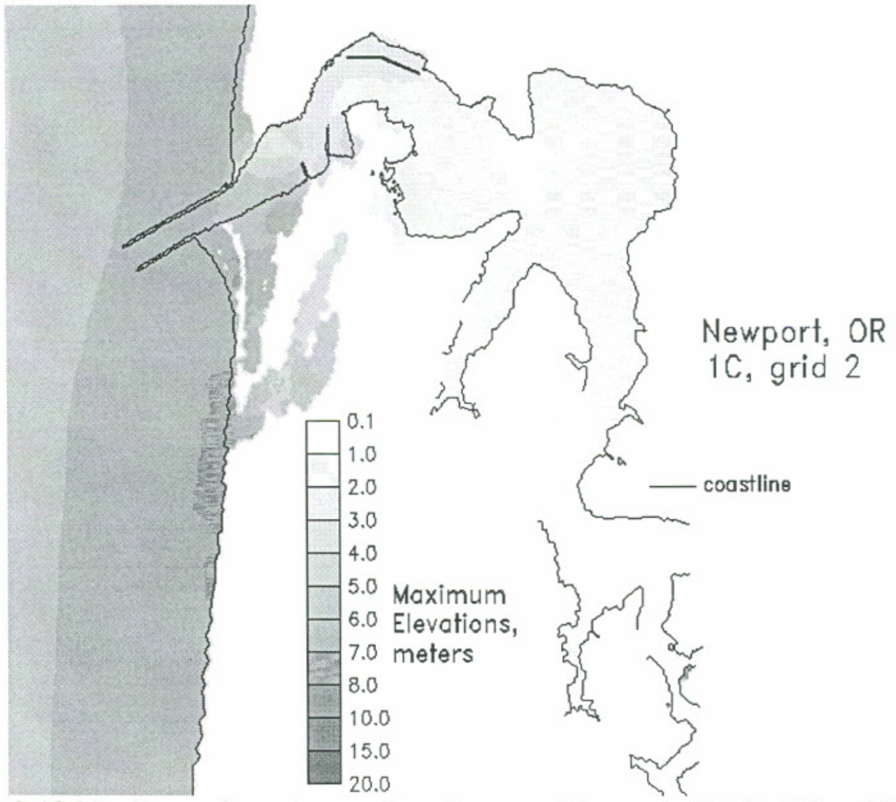

Figure 3.18d Isolines of maximum elevation near Newport, OR for 1C, grid 2.

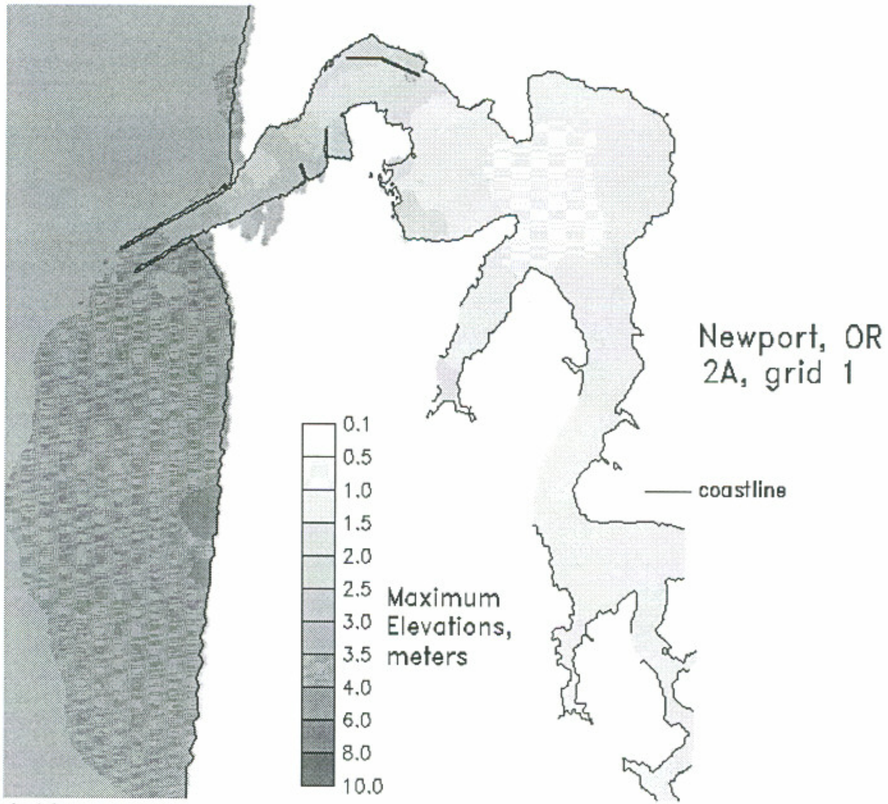

Figure 3.18e Isolines of maximum elevation near Newport, OR for 2A, grid 1.

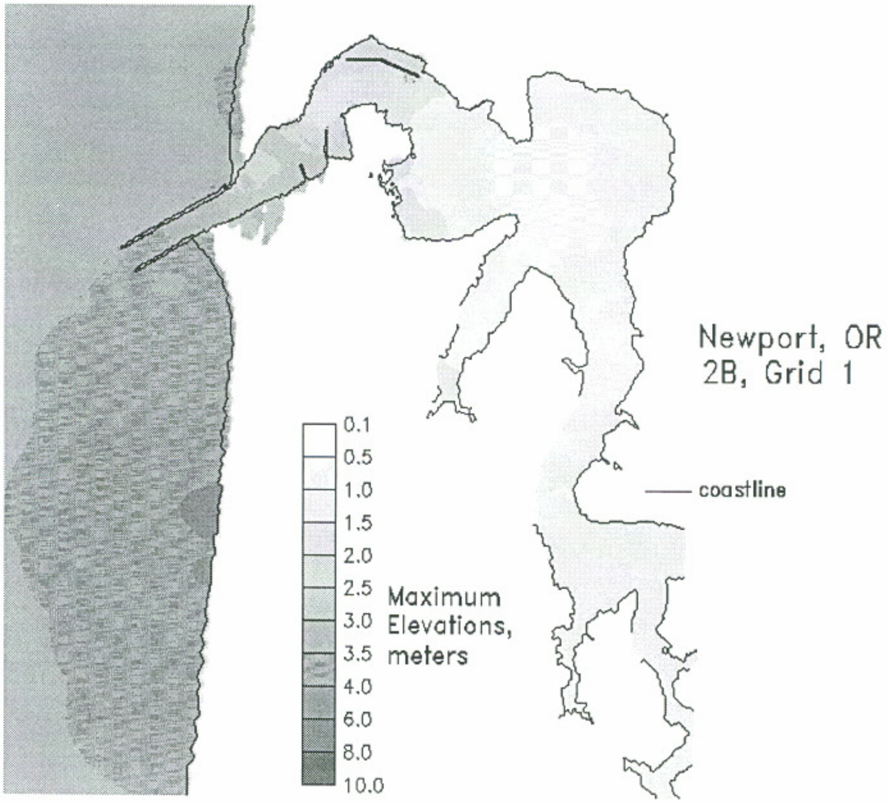

Figure 3.18f Isolines of maximum elevation near Newport, OR for 2B, grid 1.

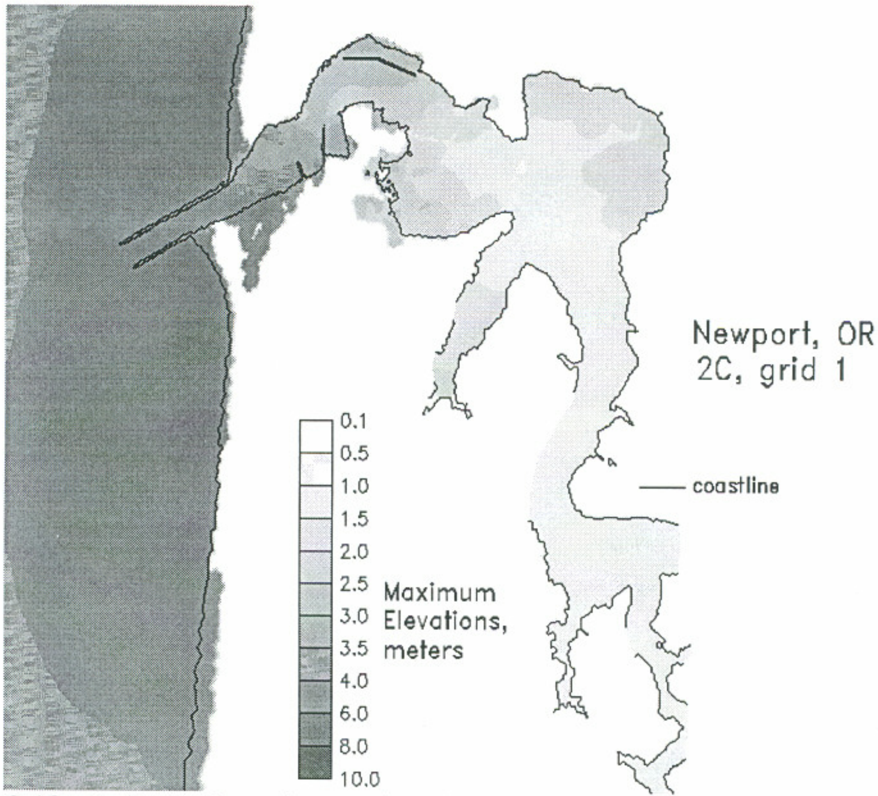

Figure 3.18g Isolines of maximum elevation near Newport, OR for 2C, grid 1.

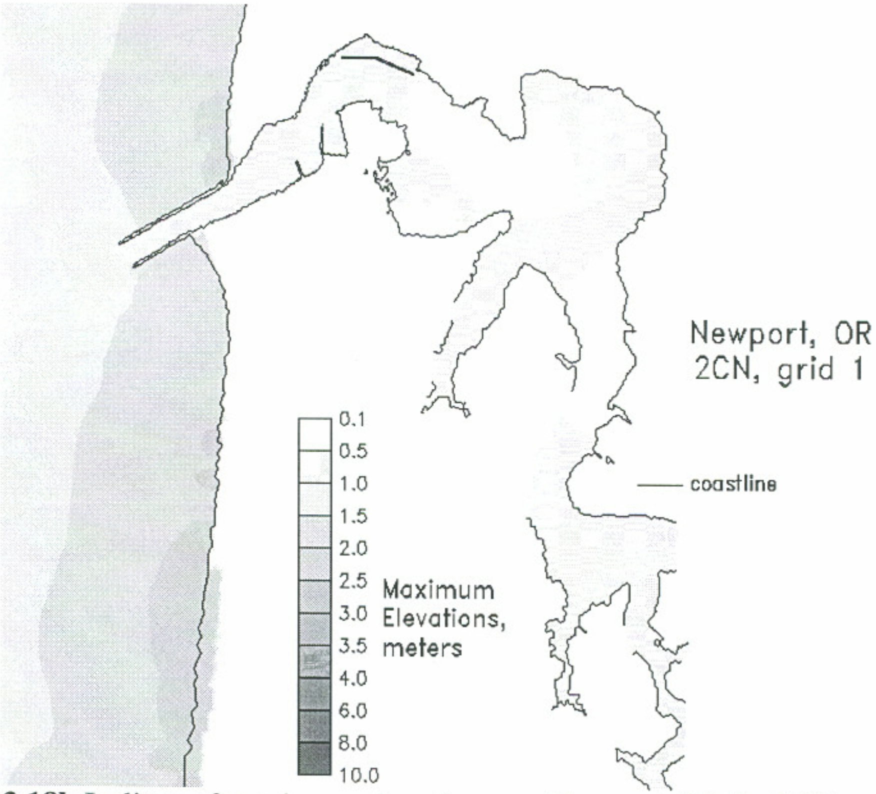

Figure 3.18h Isolines of maximum elevation near Newport, OR for 2CN, grid 1.

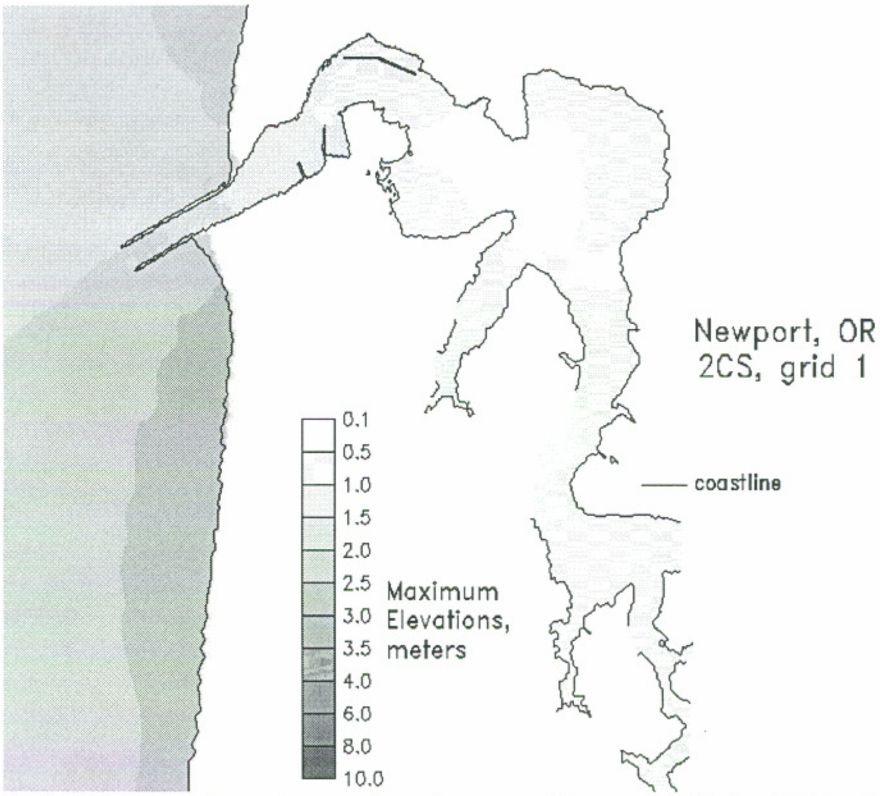

Figure 3.18i Isolines of maximum elevation near Newport, OR for 2CS, grid 1.

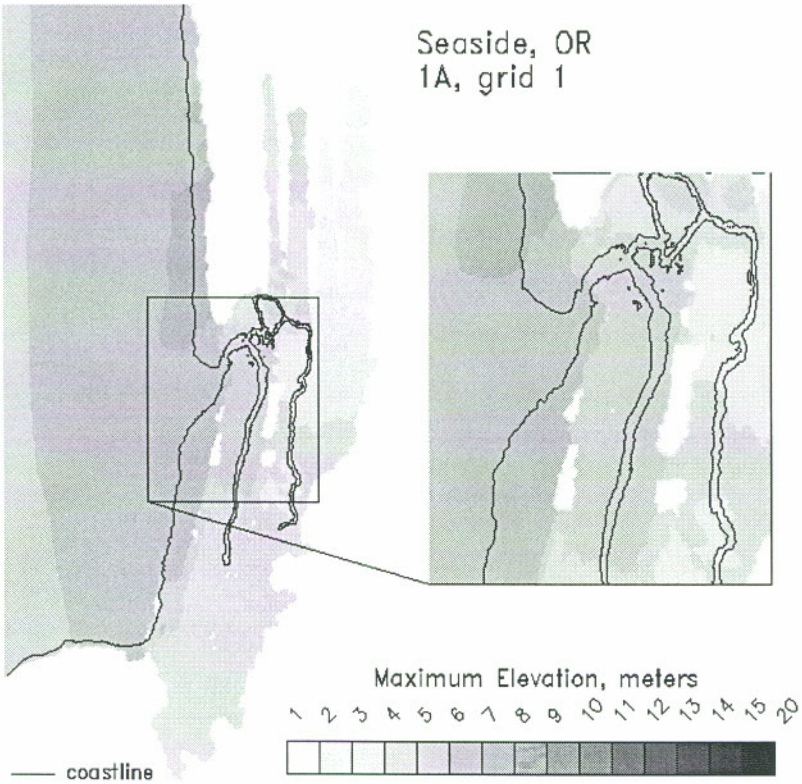

Figure 3.19a Isolines of maximum elevation near Seaside, OR for 1A, grid 1.

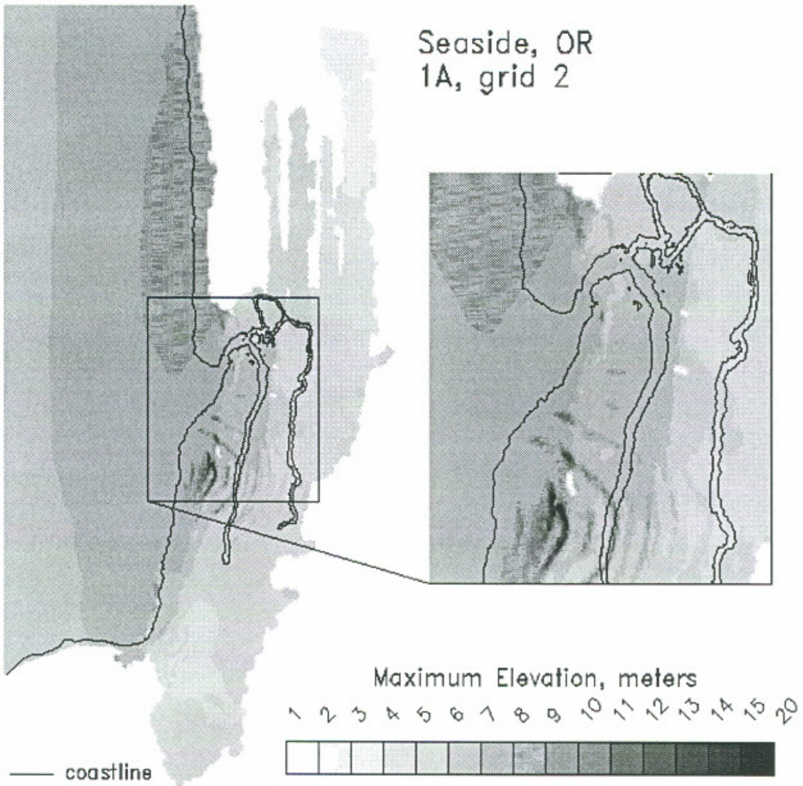

Figure 3.19b Isolines of maximum elevation near Seaside, OR for 1A, grid 2.

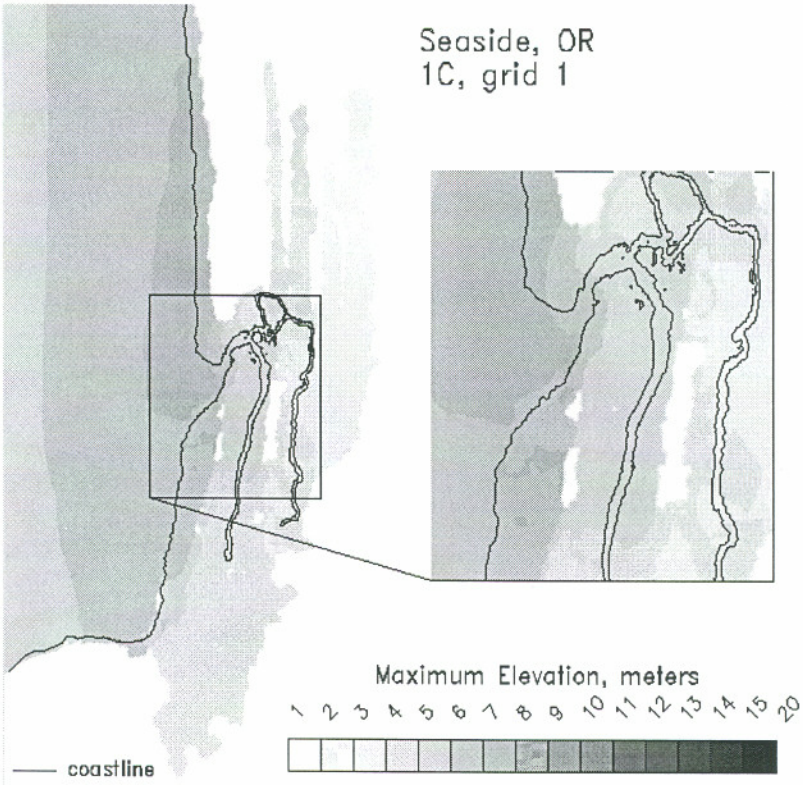

Figure 3.19c Isolines of maximum elevation near Seaside, OR for 1C, grid 1.

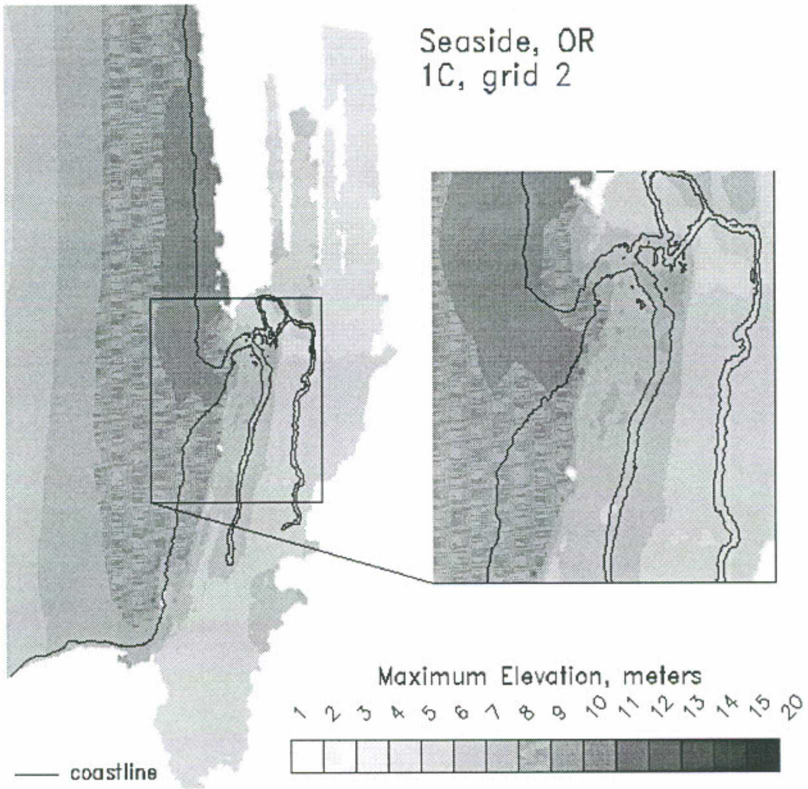

Figure 3.19d Isolines of maximum elevation near Seaside, OR for 1C, grid 2.

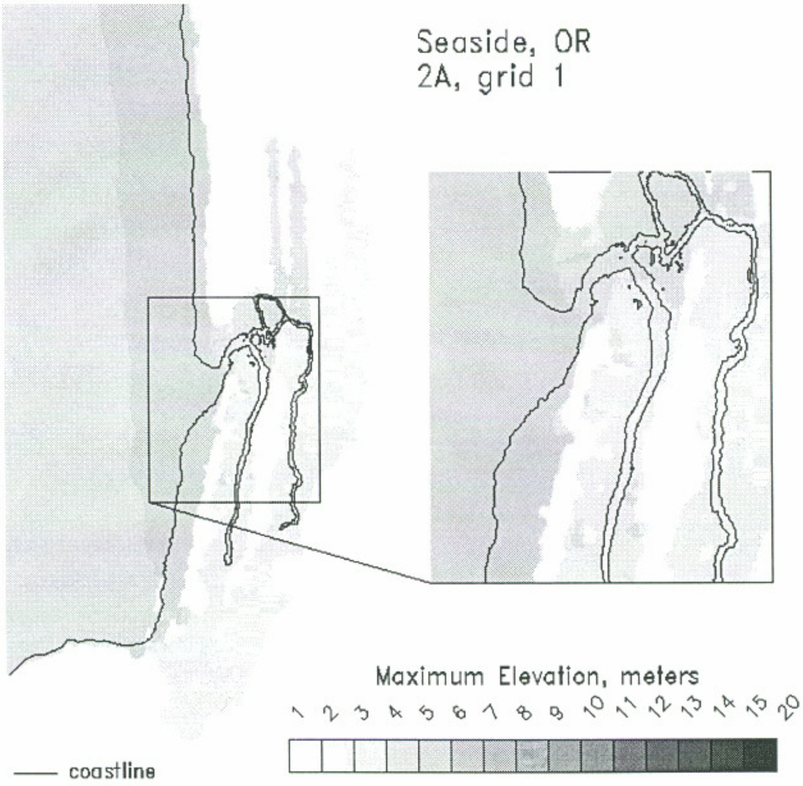

Figure 3.19e Isolines of maximum elevation near Seaside, OR for 2A, grid 1.

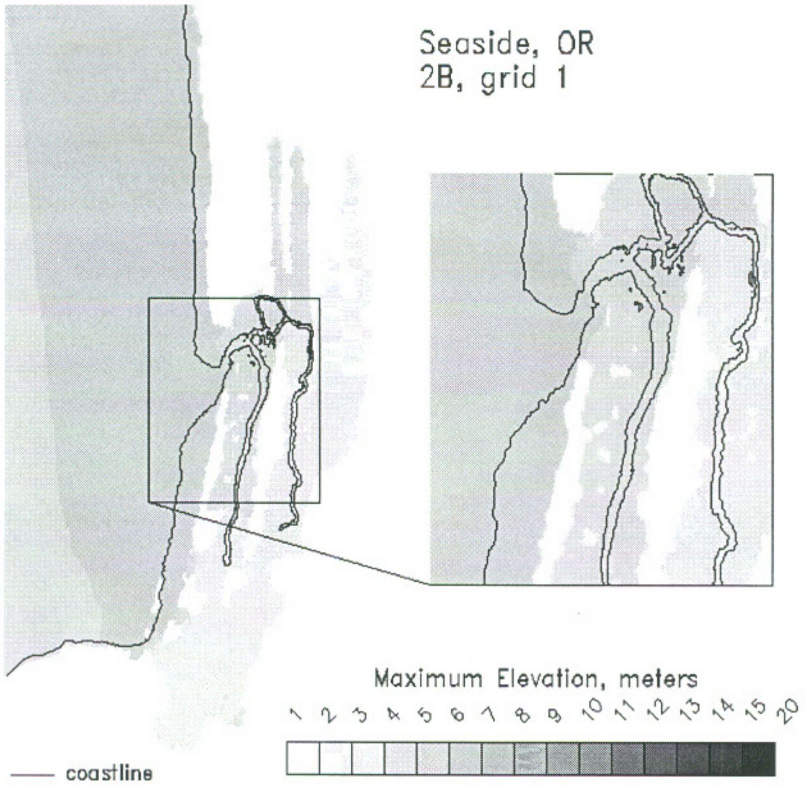

Figure 3.19f Isolines of maximum elevation near Seaside, OR for 2B, grid 1.

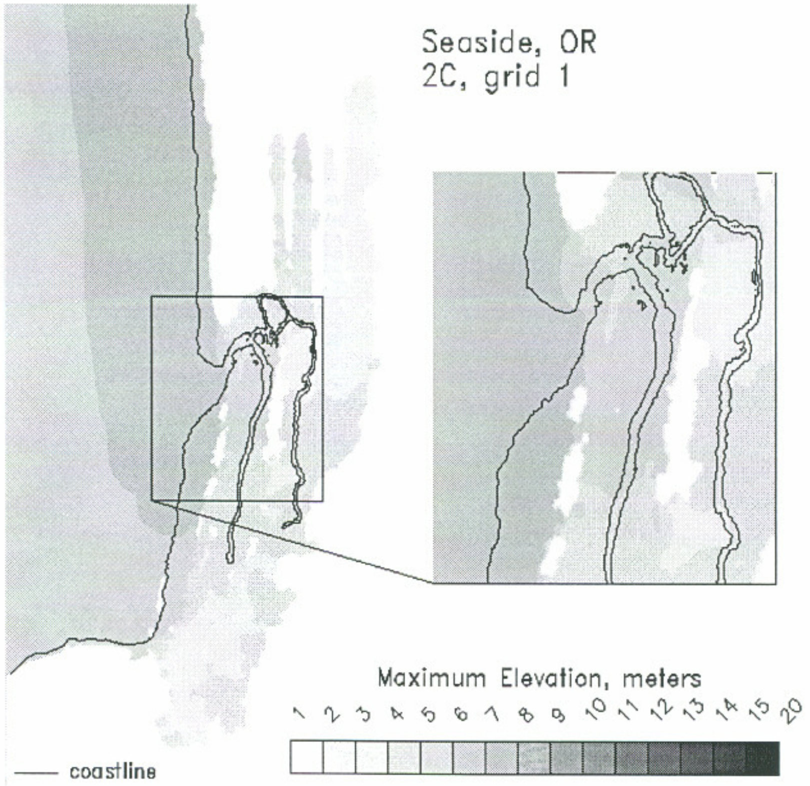

Figure 3.19g Isolines of maximum elevation near Seaside, OR for 2C, grid 1.

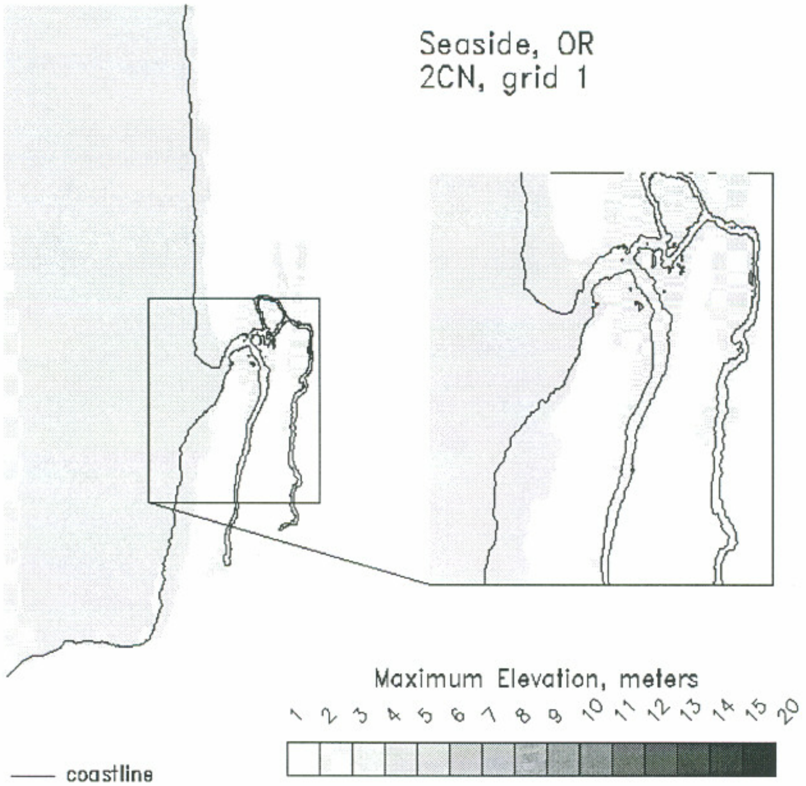

Figure 3.19h Isolines of maximum elevation near Seaside, OR for 2CN, grid 1.

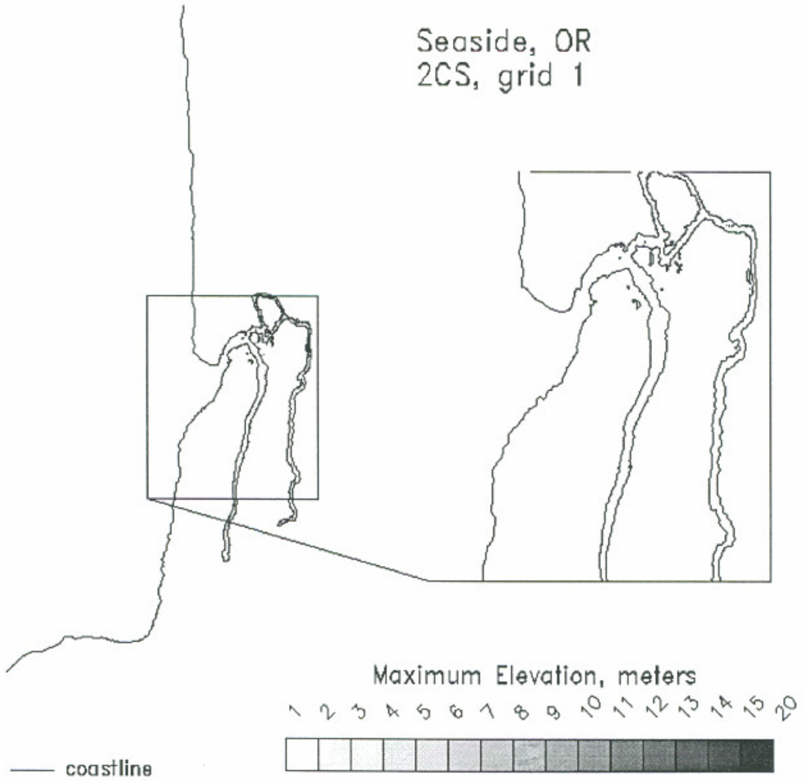

Figure 3.19i Isolines of maximum elevation near Seaside, OR for 2CS, grid 1.

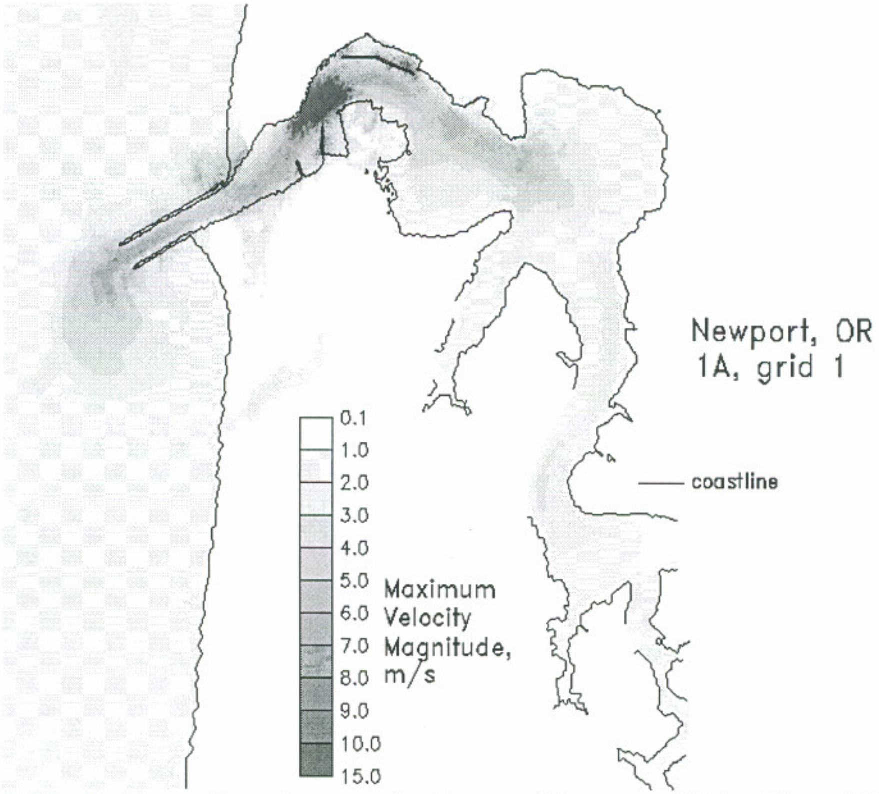

Figure 3.20a Isolines of maximum velocity near Newport, OR for 1A, grid 1.

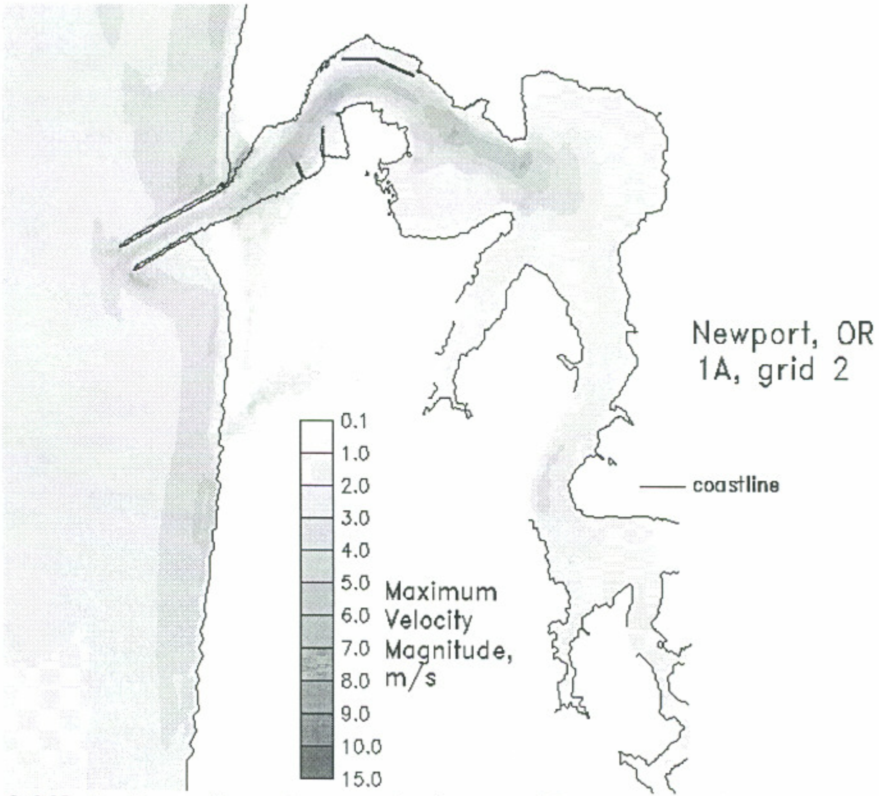

Figure 3.20b Isolines of maximum velocity near Newport, OR for 1A, grid 2.

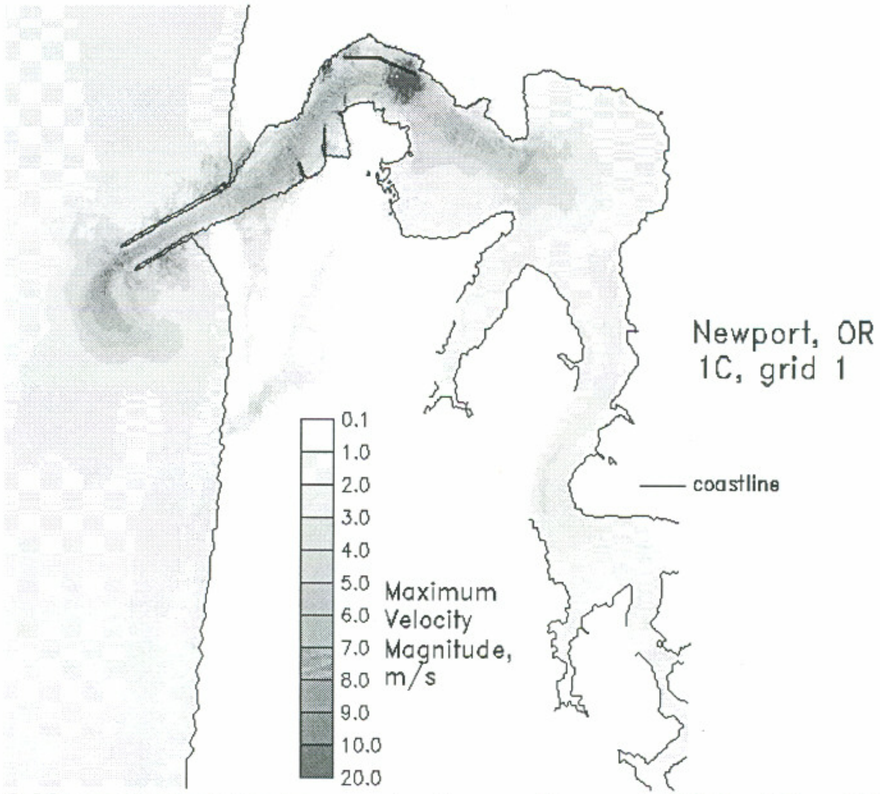

Figure 3.20c Isolines of maximum velocity near Newport, OR for 1C, grid 1.

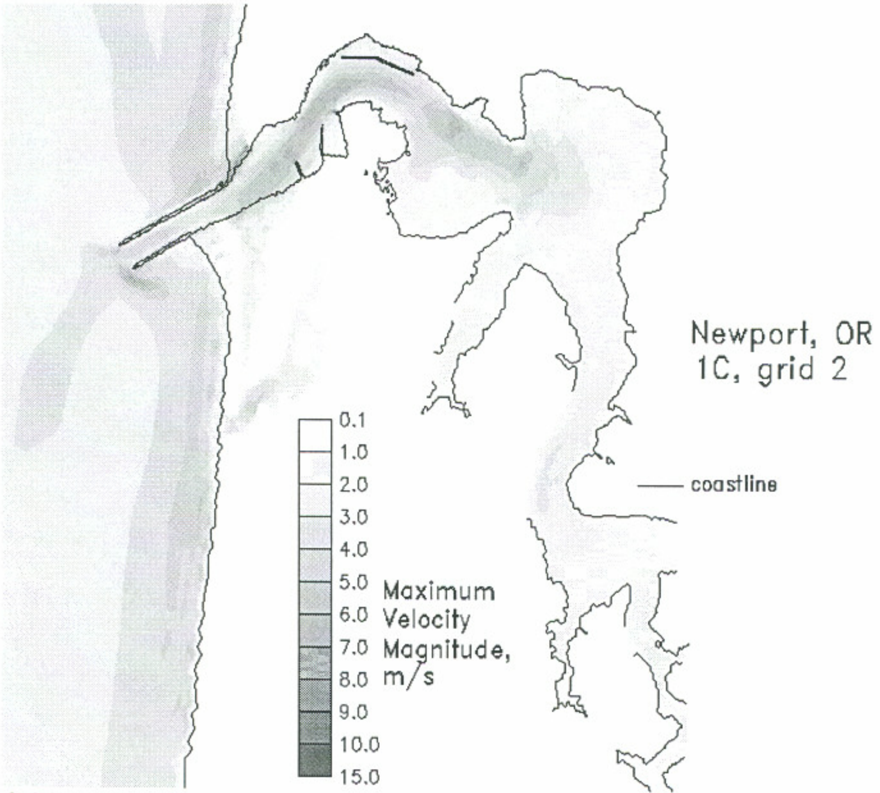

Figure 3.20d Isolines of maximum velocity near Newport, OR for 1C, grid 2.

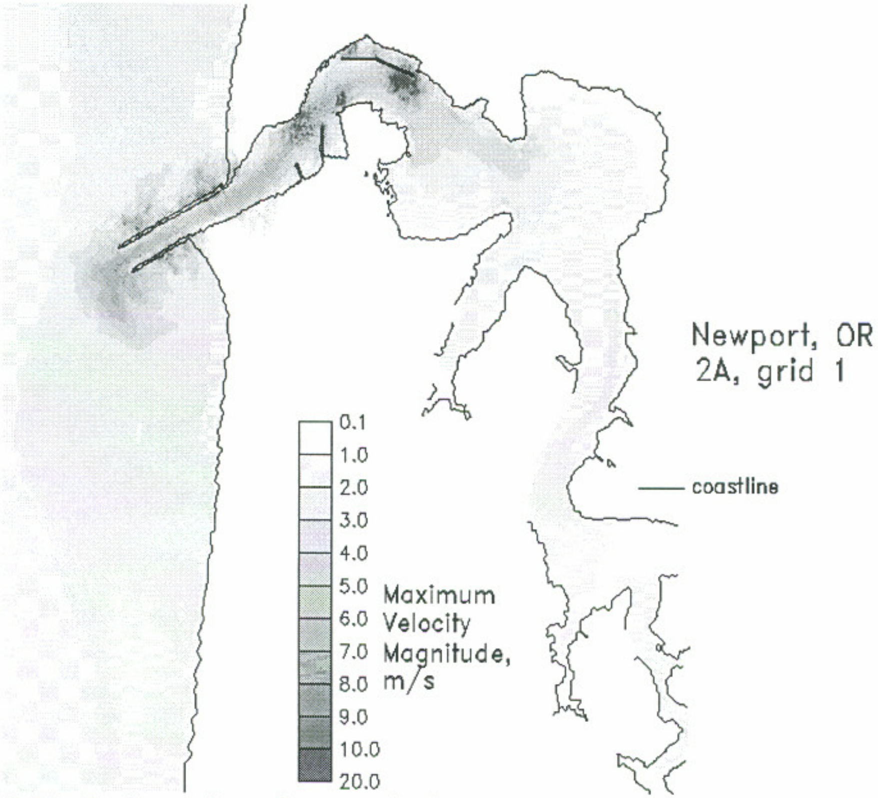

Figure 3.20e Isolines of maximum velocity near Newport, OR for 2A, grid 1.

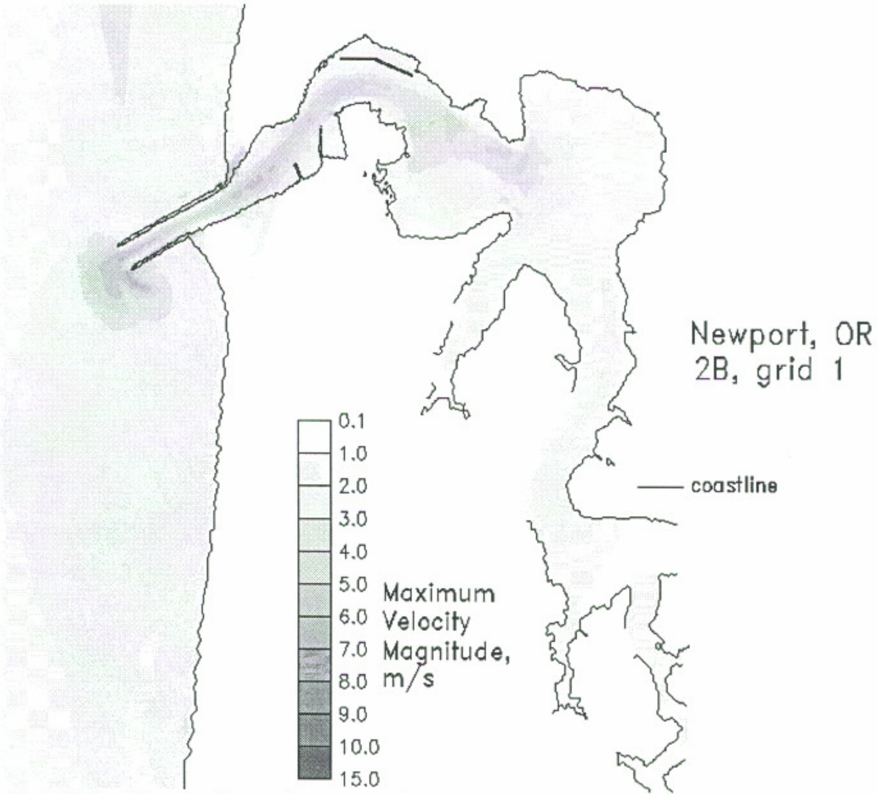

Figure 3.20f Isolines of maximum velocity near Newport, OR for 2B, grid 1.

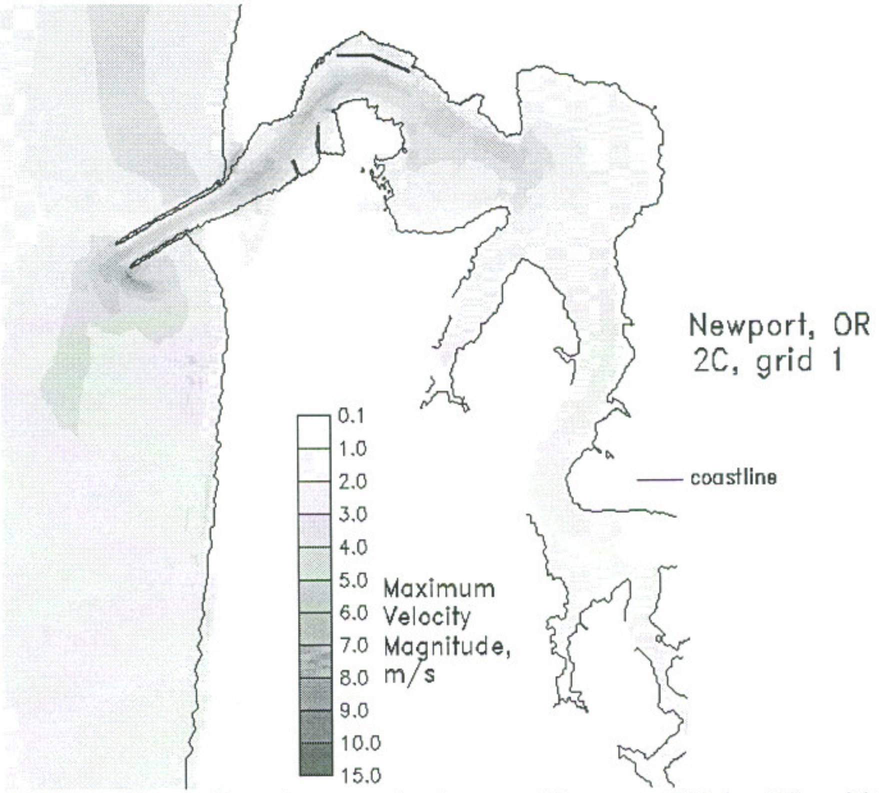

Figure 3.20g Isolines of maximum velocity near Newport, OR for 2C, grid 1.

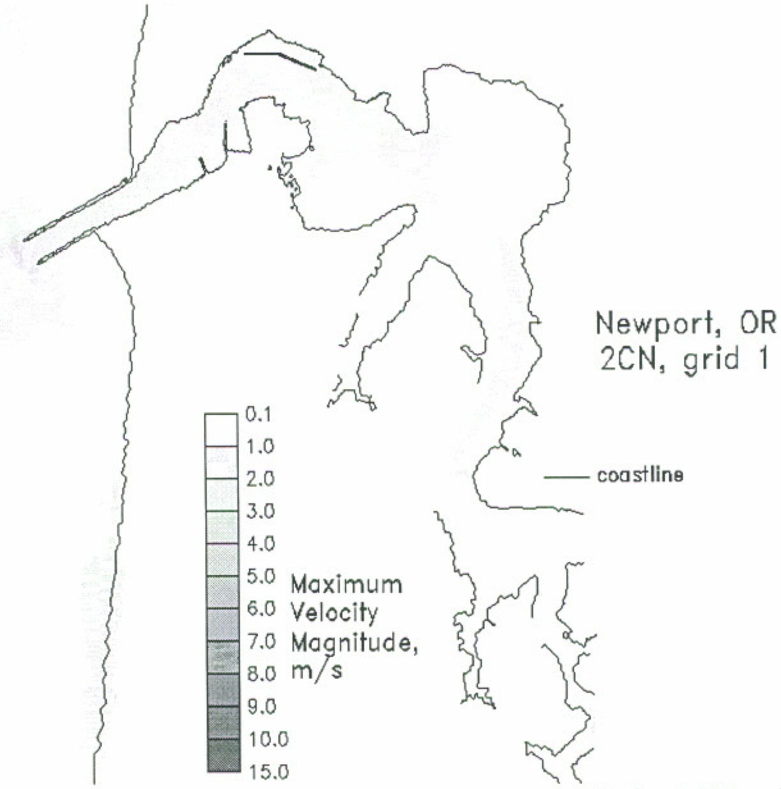

Figure 3.20h Isolines of maximum velocity near Newport, OR for 2CN, grid 1.

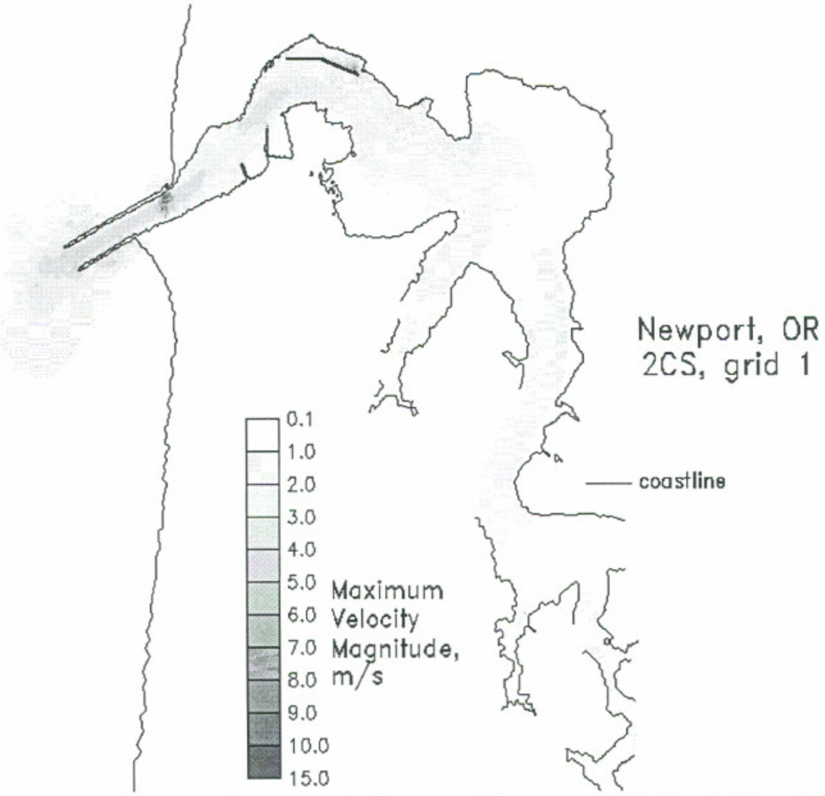

Figure 3.20i Isolines of maximum velocity near Newport, OR for 2CS, grid 1.

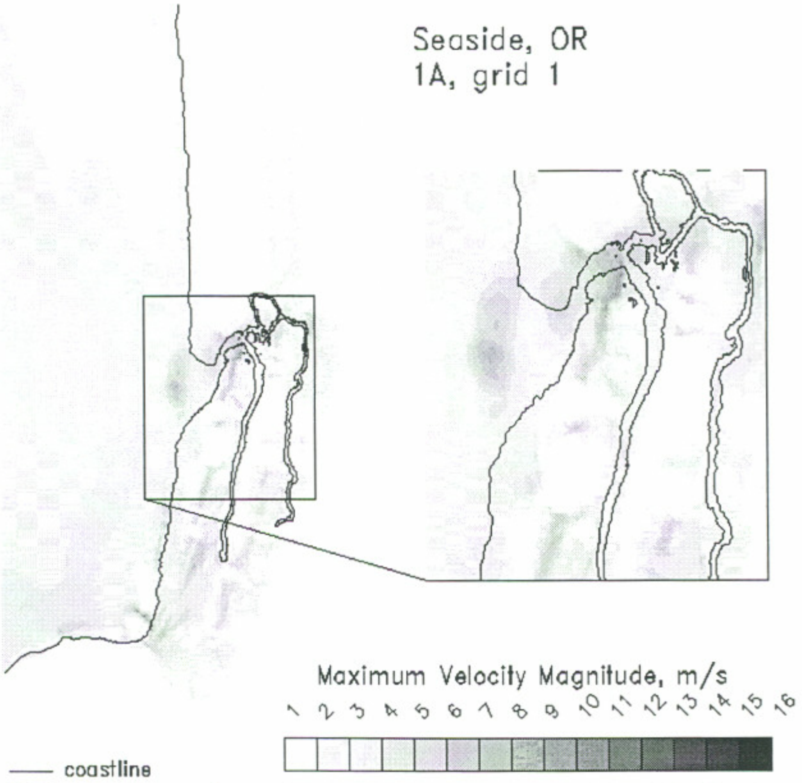

Figure 3.21a Isolines of maximum velocity near Seaside, OR for 1A, grid 1.

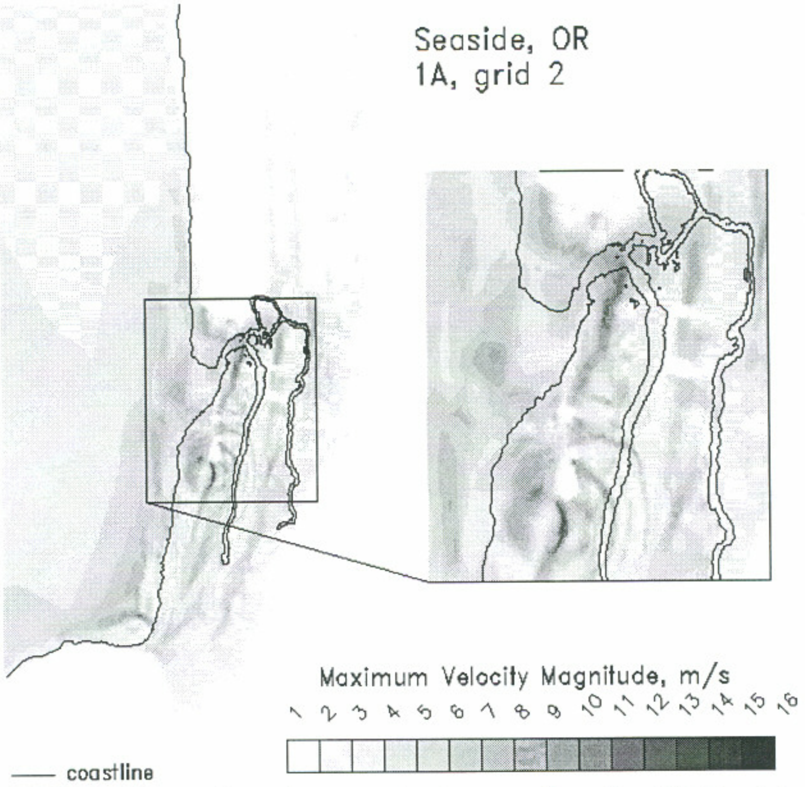

Figure 3.21b Isolines of maximum velocity near Seaside, OR for 1A, grid 2.

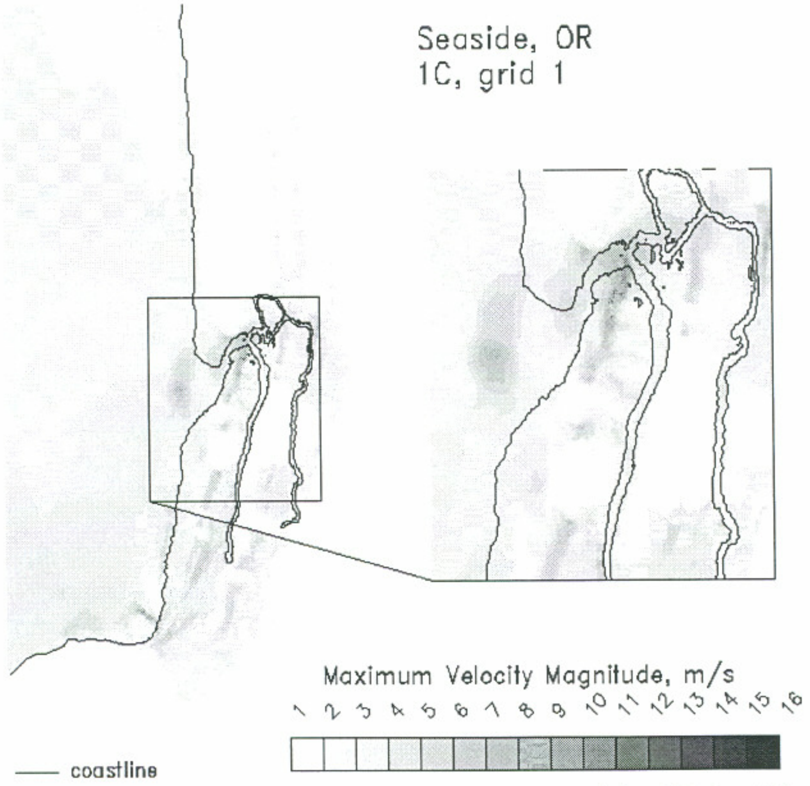

Figure 3.21c Isolines of maximum velocity near Seaside, OR for 1C, grid 1.

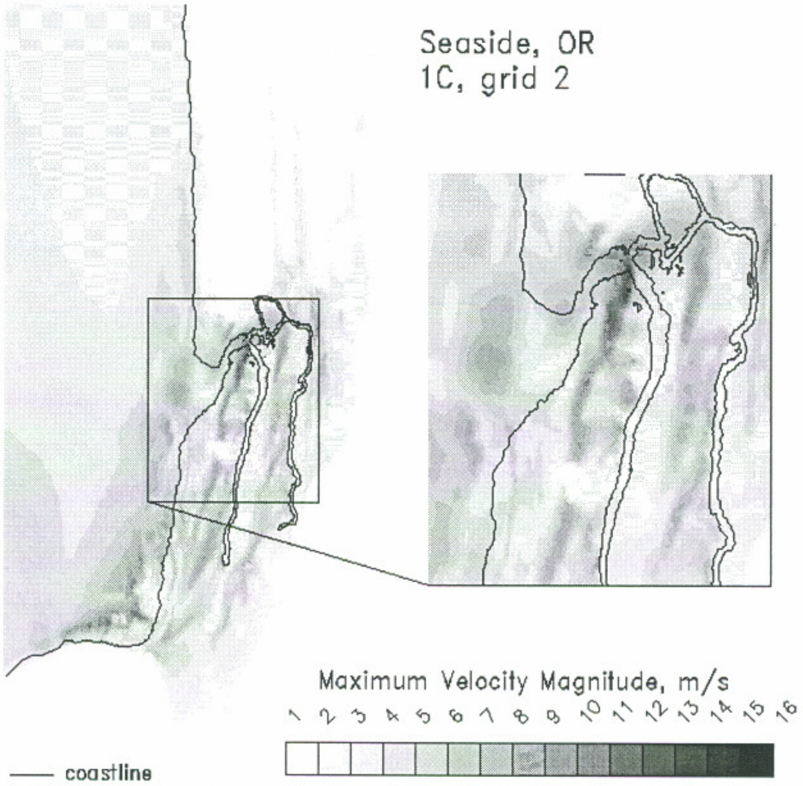

Figure 3.21d Isolines of maximum velocity near Seaside, OR for 1C, grid 2.

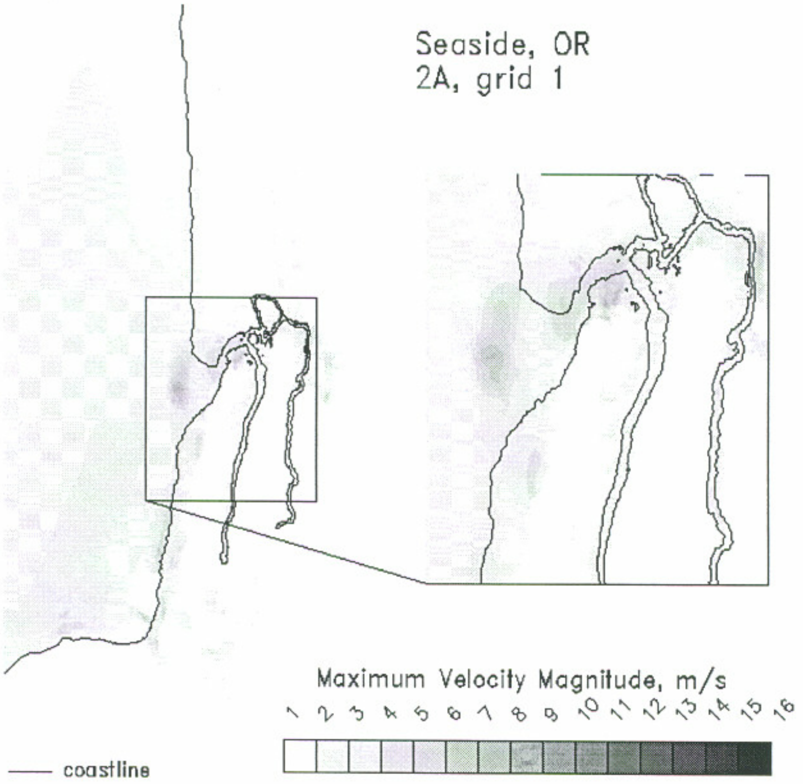

Figure 3.21e Isolines of maximum velocity near Seaside, OR for 2A, grid 1.

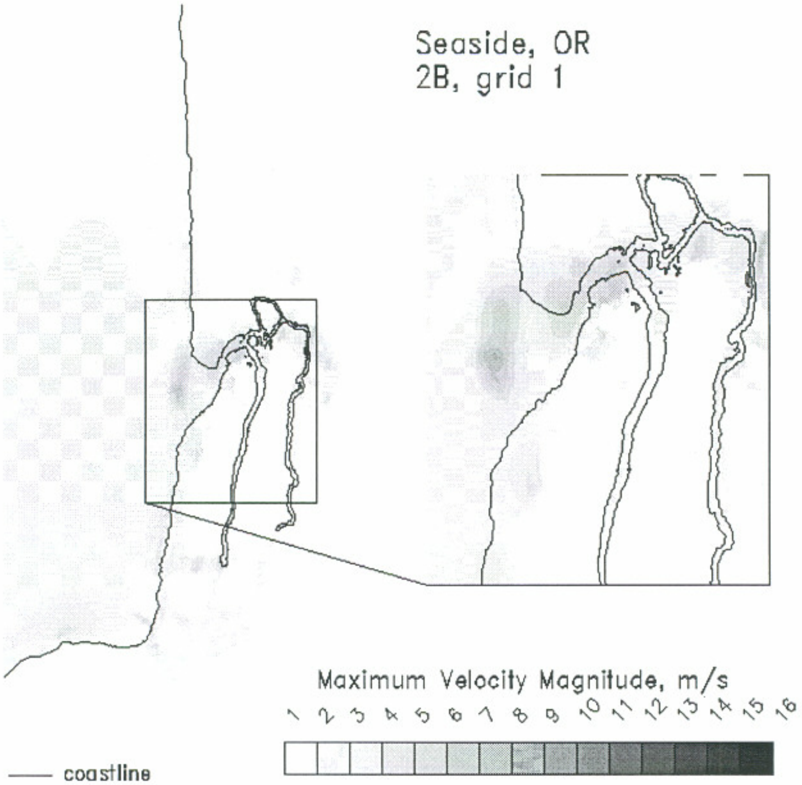

Figure 3.21f Isolines of maximum velocity near Seaside, OR for 2B, grid 1.

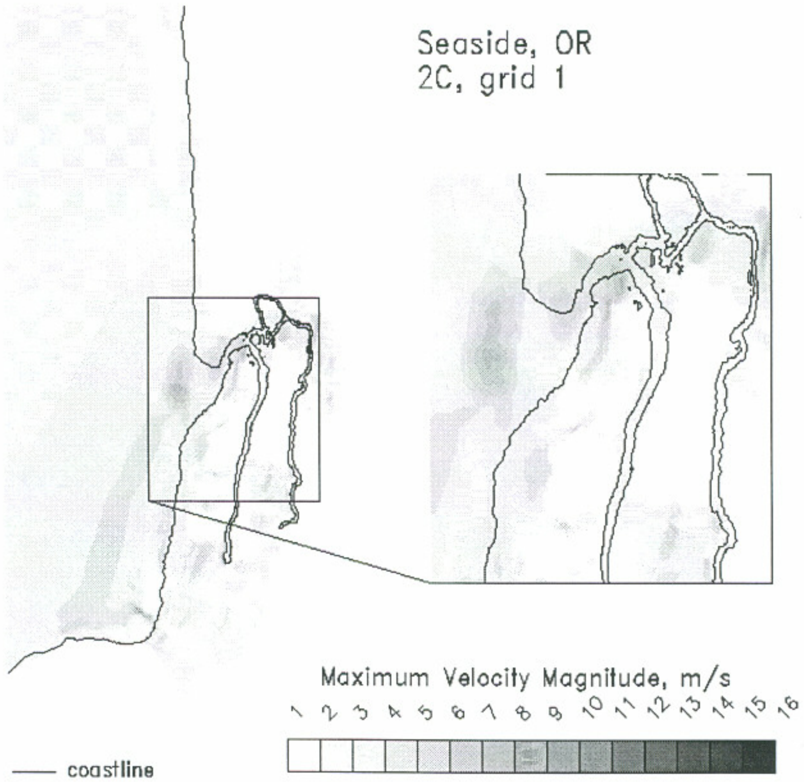

Figure 3.21g Isolines of maximum velocity near Seaside, OR for 2C, grid 1.

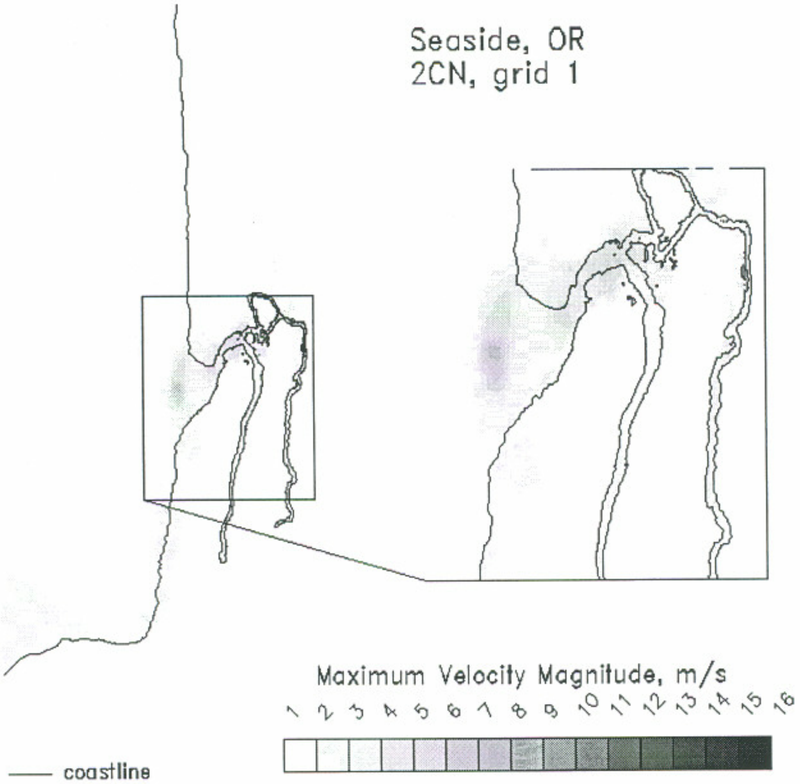

Figure 3.21h Isolines of maximum velocity near Seaside, OR for 2CN, grid 1.

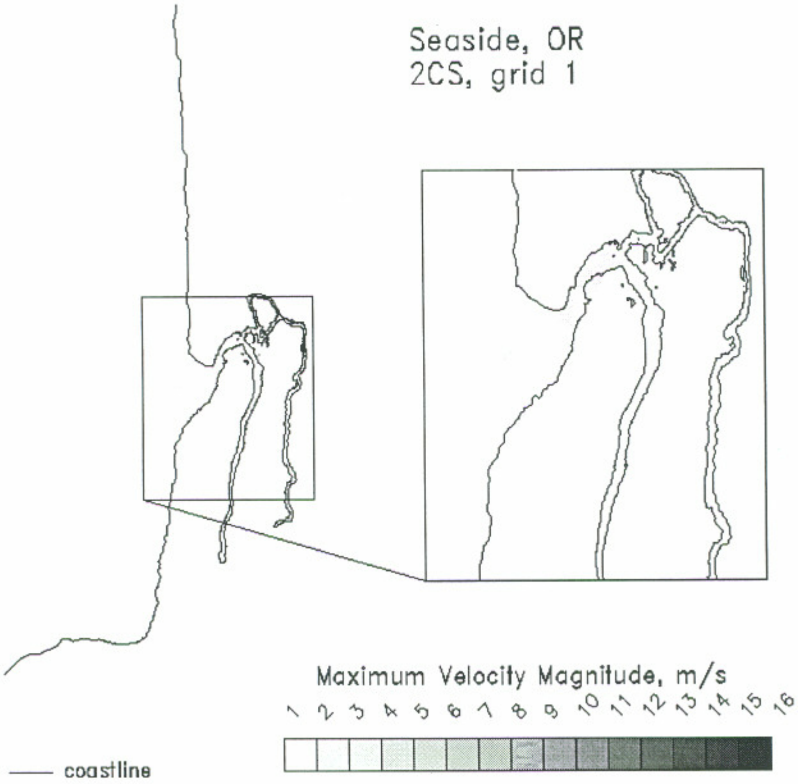

Figure 3.21i Isolines of maximum velocity near Seaside, OR for 2CS, grid 1.

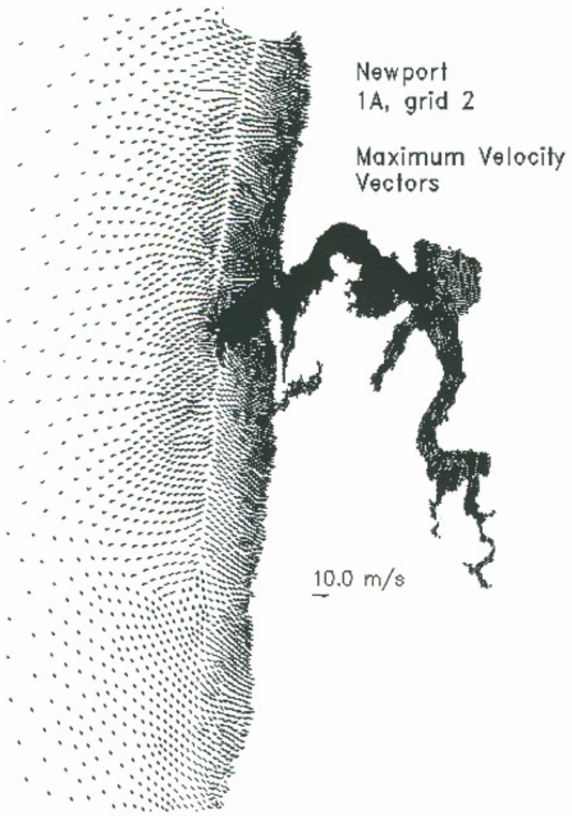

Figure 3.22a Maximum velocity vectors offshore of Newport, OR for 1A, grid 2.

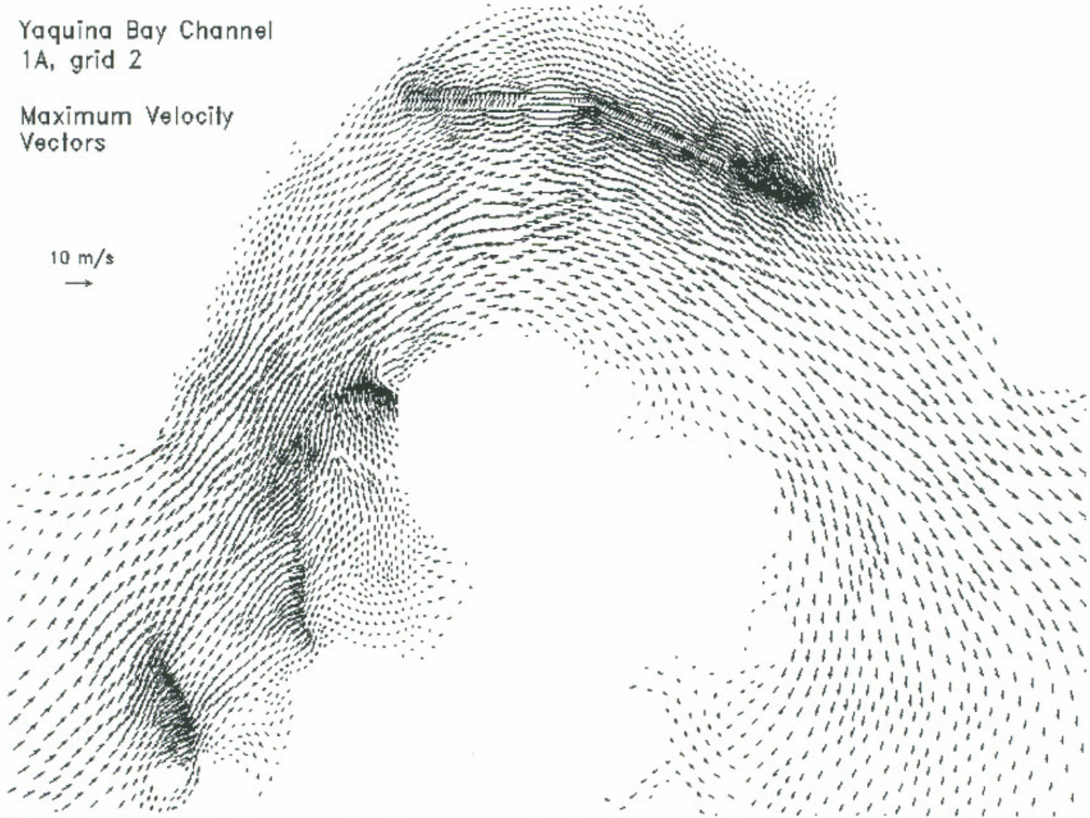

Figure 3.22b Maximum velocity vectors in the Yaquina Bay channel for 1A, grid 2.

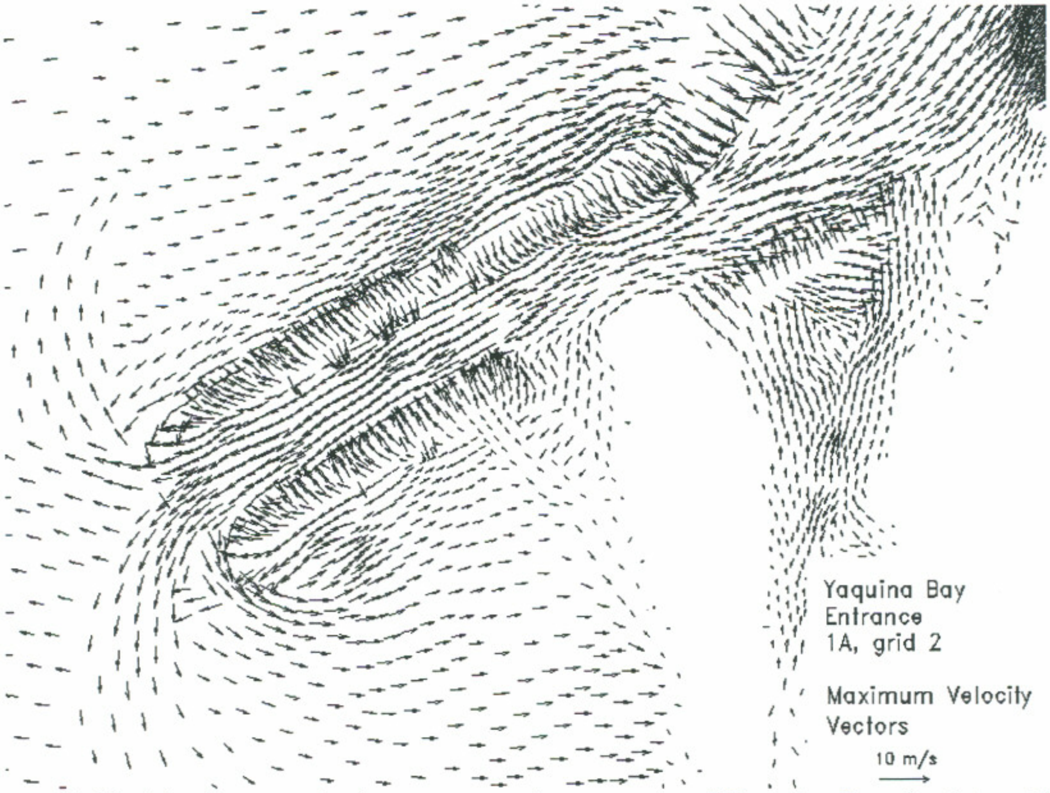

Figure 3.22c Maximum velocity vectors at the entrance of Yaquina Bay for 1A, grid 2.

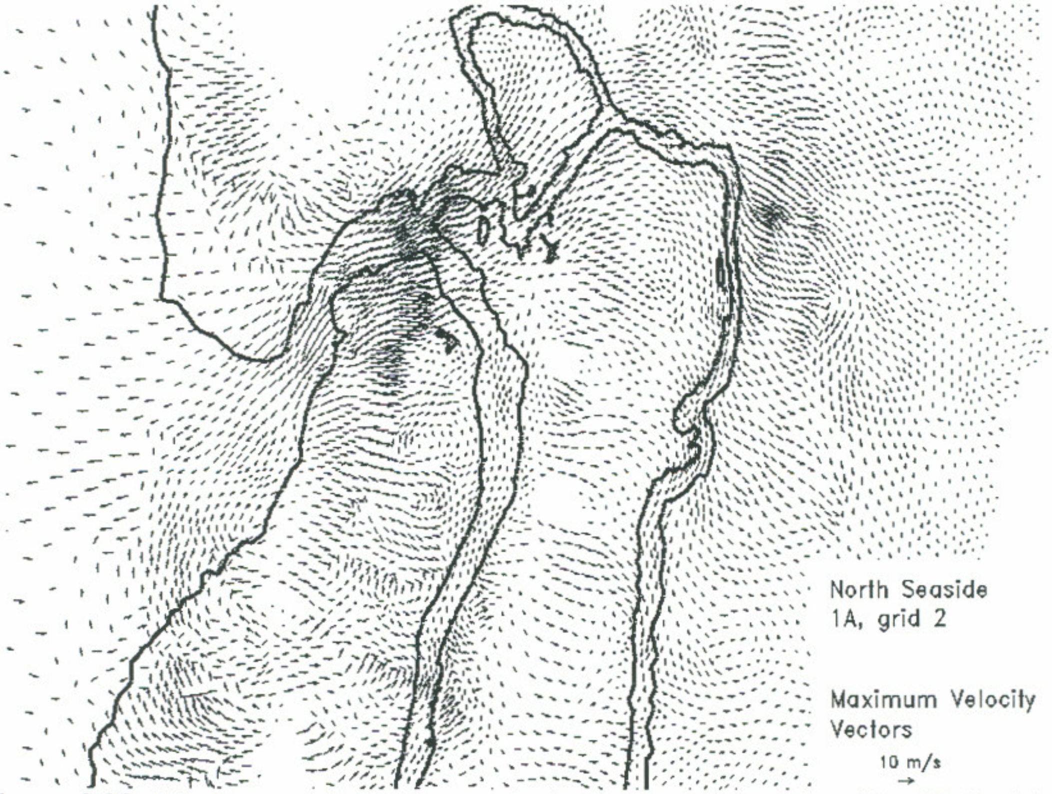

Figure 3.23a Maximum velocity vectors in the northern part of Seaside, OR for 1A, grid 2.

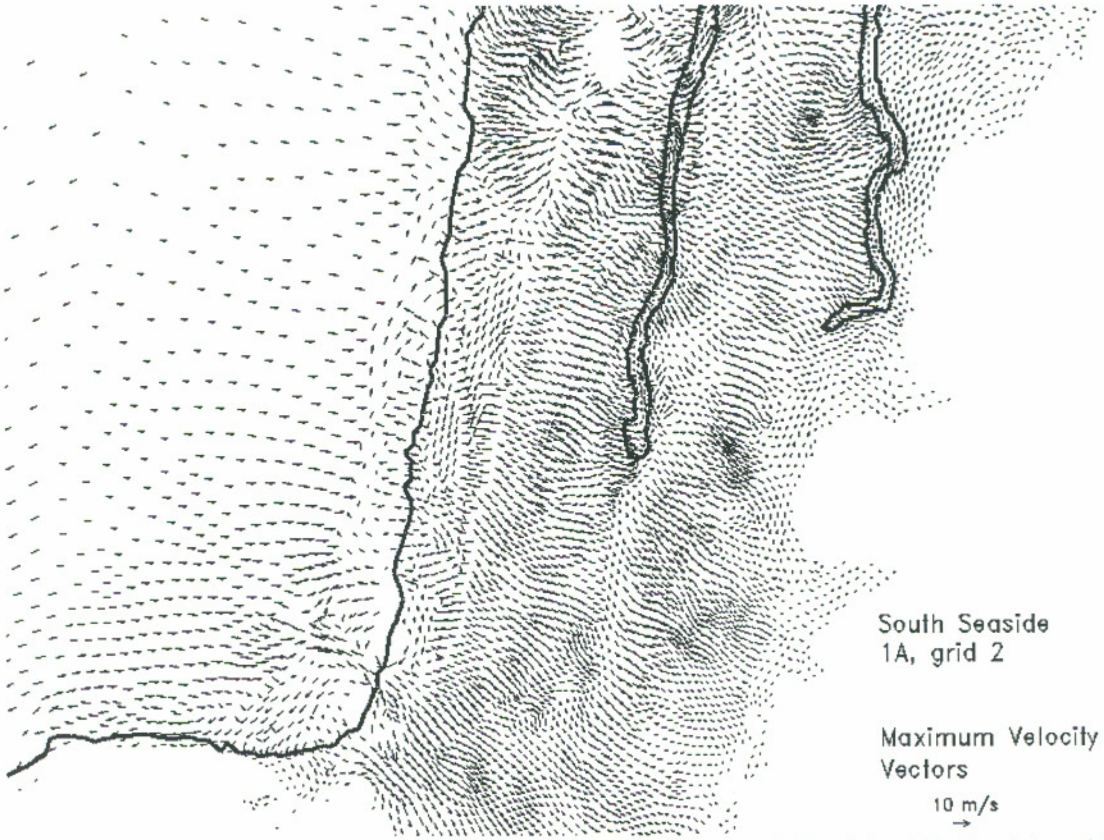

Figure 3.23b Maximum velocity vectors in the southern part of Seaside, OR for 1A, grid 2.

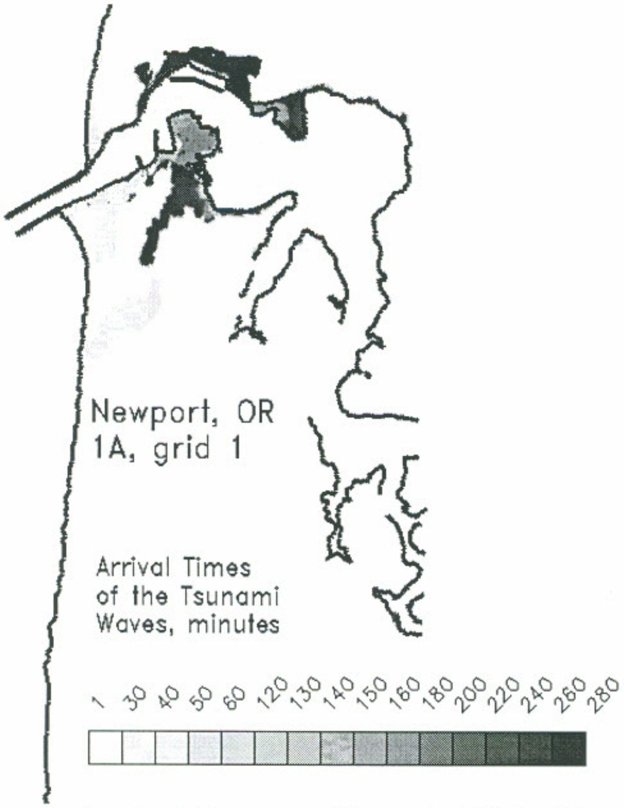

Figure 3.24a Tsunami arrival times near Newport, OR for 1A, grid 1.

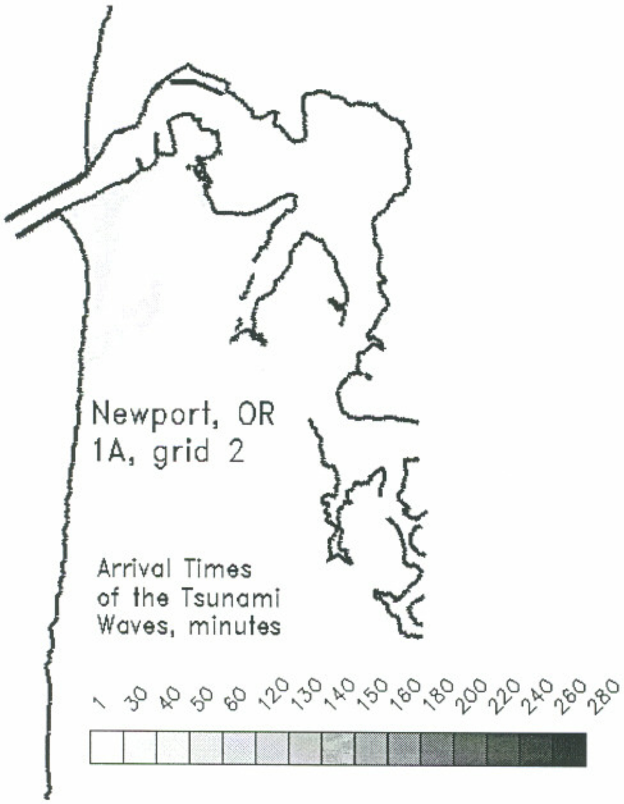

Figure 3.24b Tsunami arrival times near Newport, OR for 1A, grid 2.

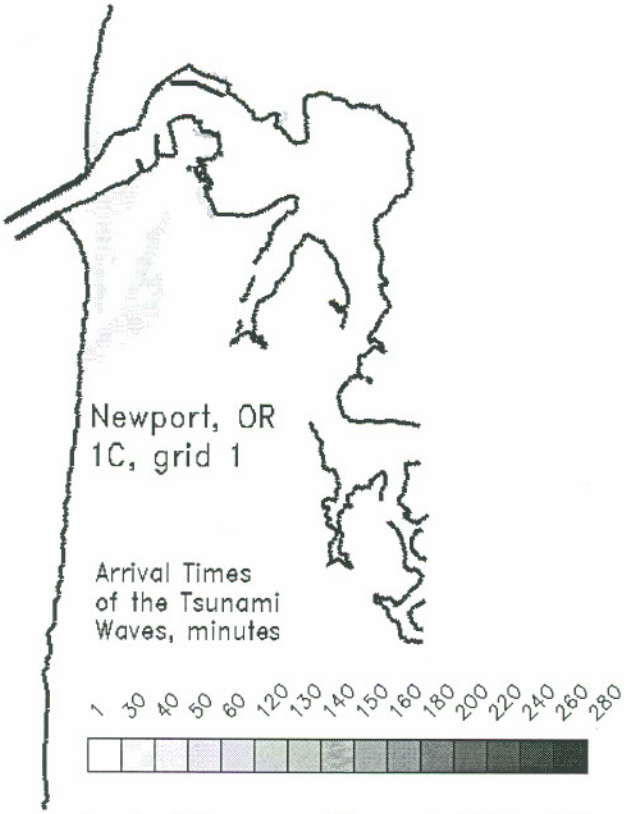

Figure 3.24c Tsunami arrival times near Newport, OR for 1C, grid 1.

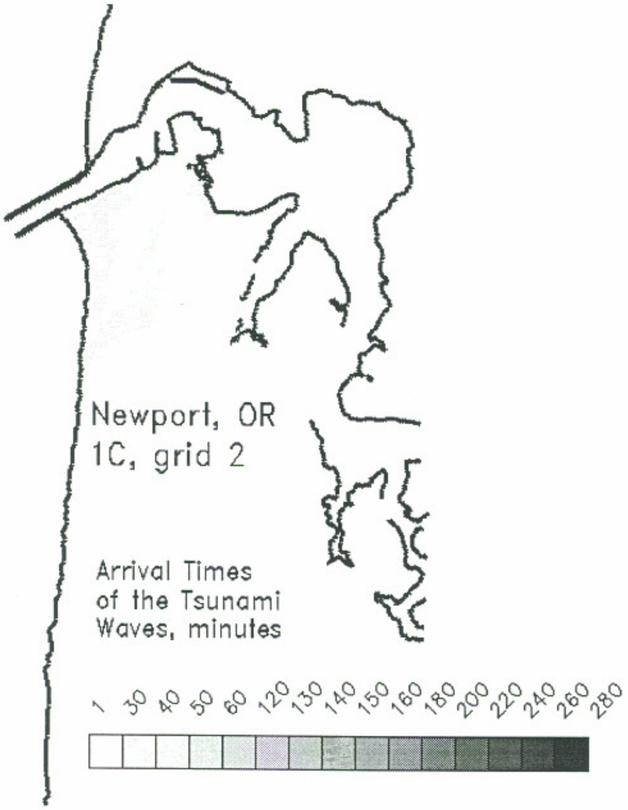

Figure 3.24d Tsunami arrival times near Newport, OR for 1C, grid 2.

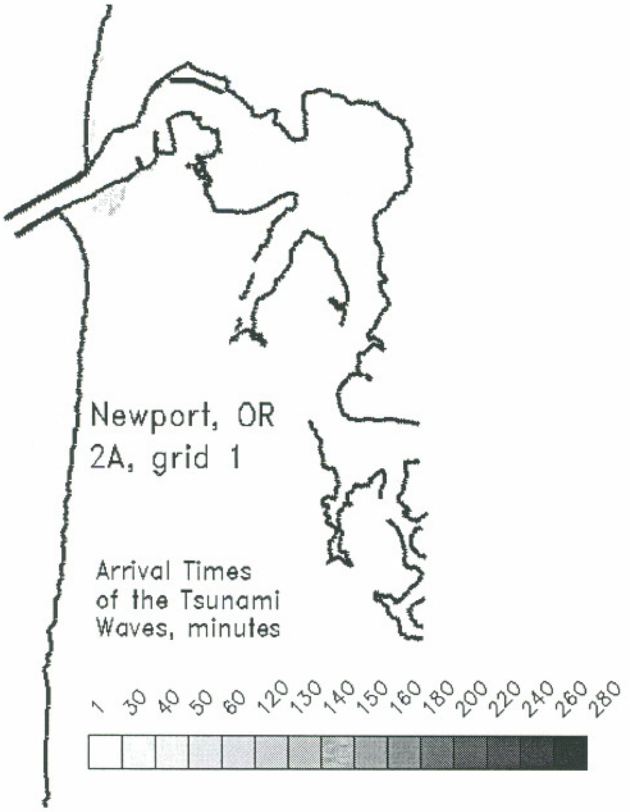

Figure 3.24e Tsunami arrival times near Newport, OR for 2A, grid 1.

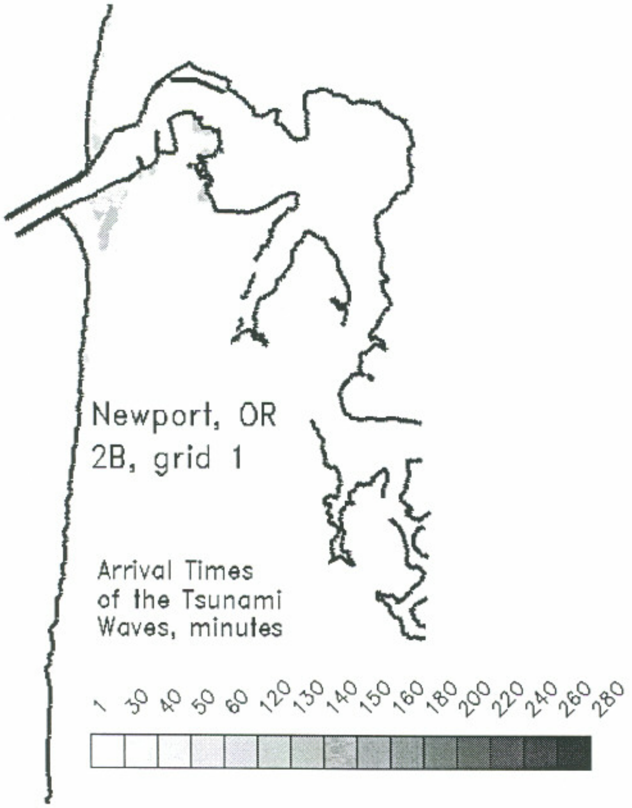

Figure 3.24f Tsunami arrival times near Newport, OR for 2B, grid 1.

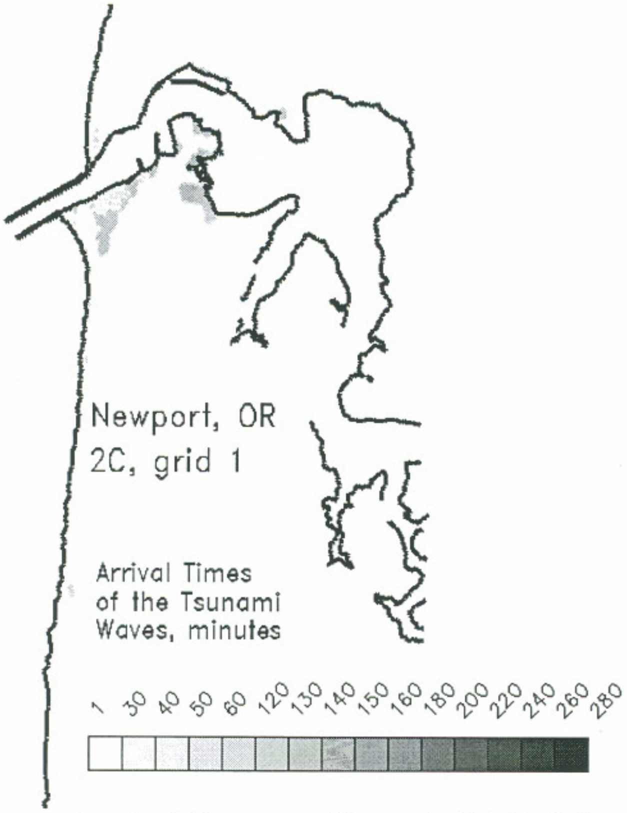

Figure 3.24g Tsunami arrival times near Newport, OR for 2C, grid 1.

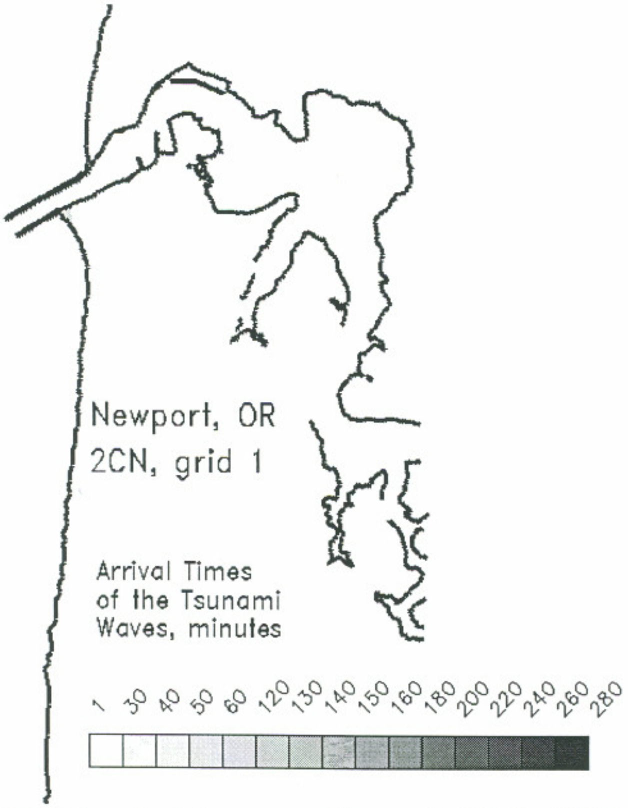

Figure 3.24h Tsunami arrival times near Newport, OR for 2CN, grid 1.

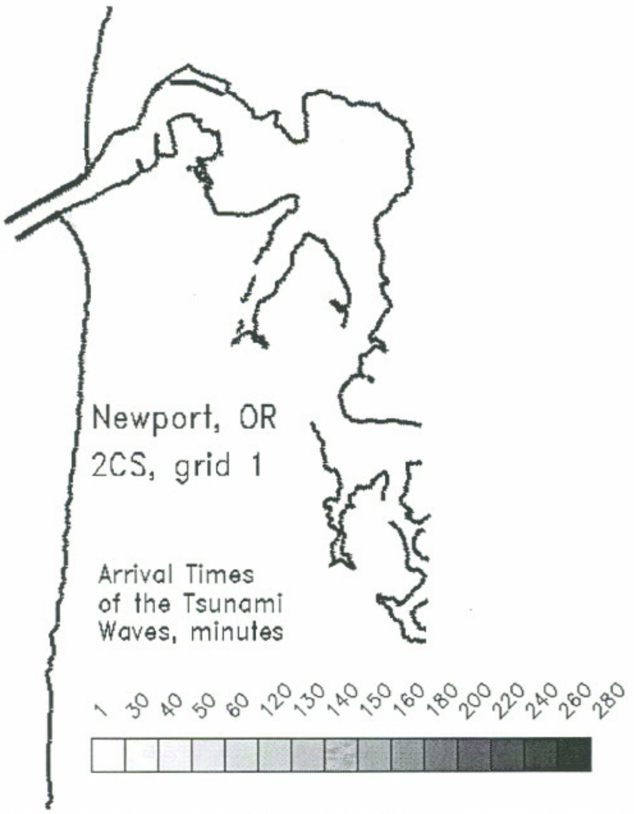

Figure 3.24i Tsunami arrival times near Newport, OR for 2CS, grid 1.

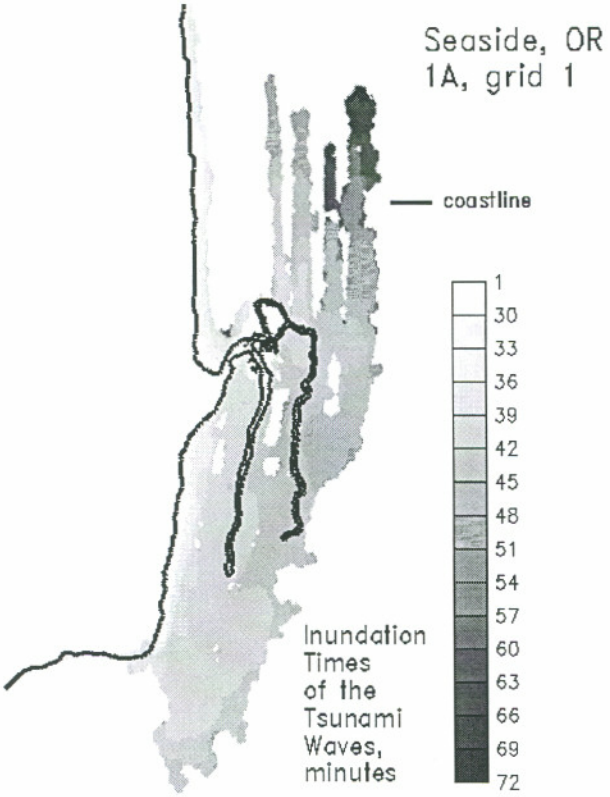

Figure 3.25a Tsunami arrival times near Seaside, OR for 1A, grid 1.

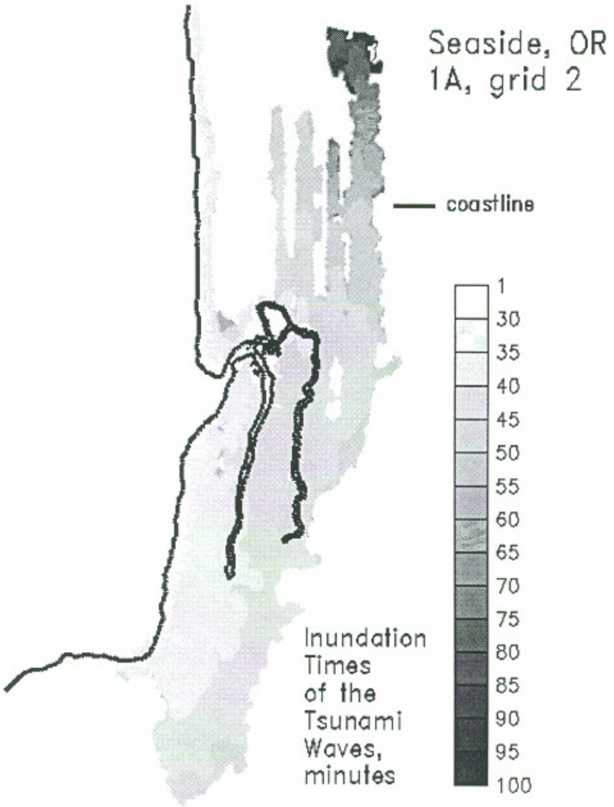

Figure 3.25b Tsunami arrival times near Seaside, OR for 1A, grid 2.

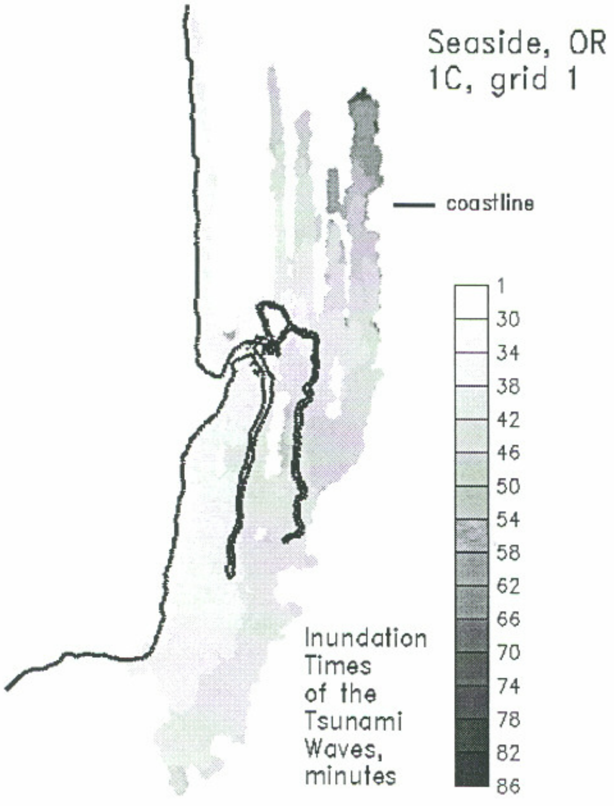

Figure 3.25c Tsunami arrival times near Seaside, OR for 1C, grid 1.

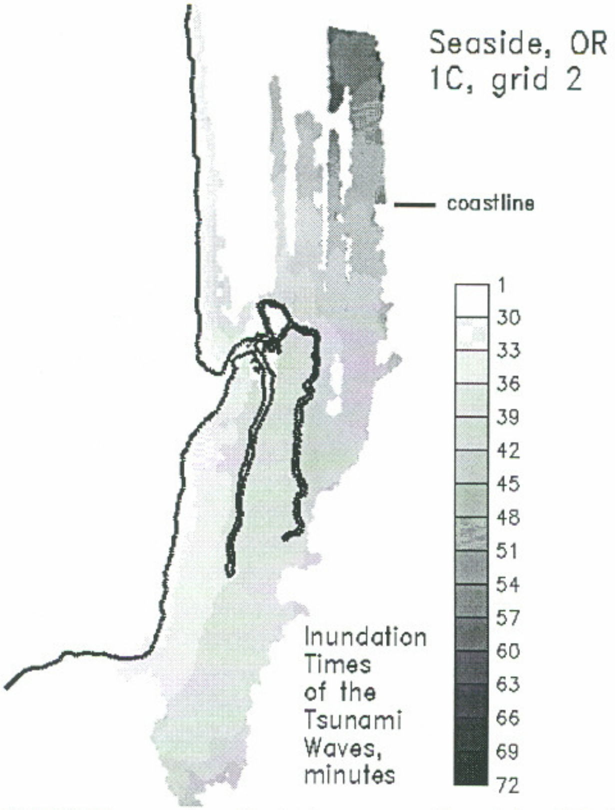

Figure 3.25d Tsunami arrival times near Seaside, OR for 1C, grid 2.

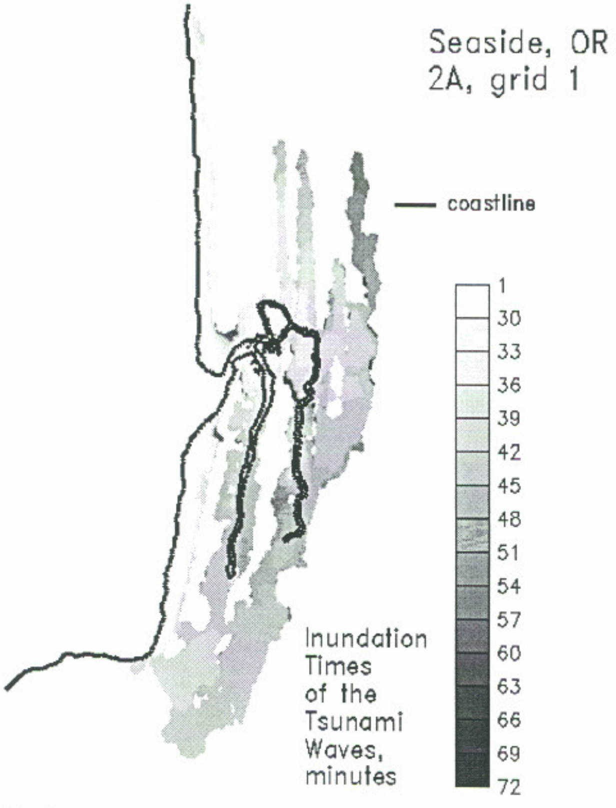

Figure 3.25e Tsunami arrival times near Seaside, OR for 2A, grid 1.

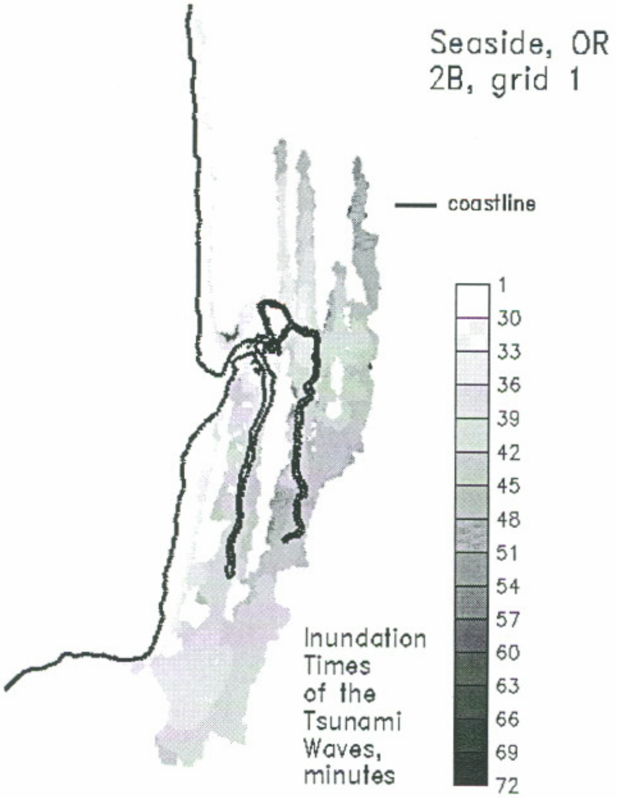

Figure 3.25f Tsunami arrival times near Seaside, OR for 2B, grid 1.

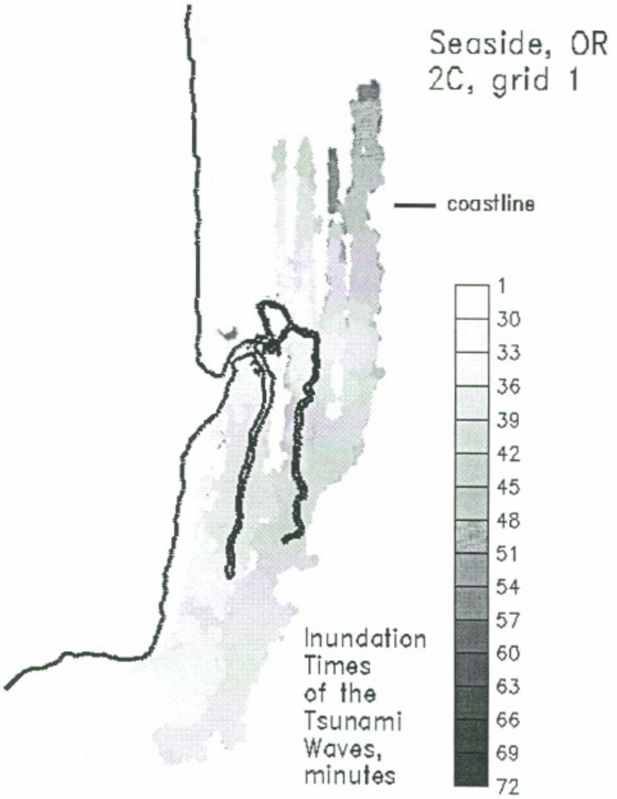

Figure 3.25g Tsunami arrival times near Seaside, OR for 2C, grid 1.

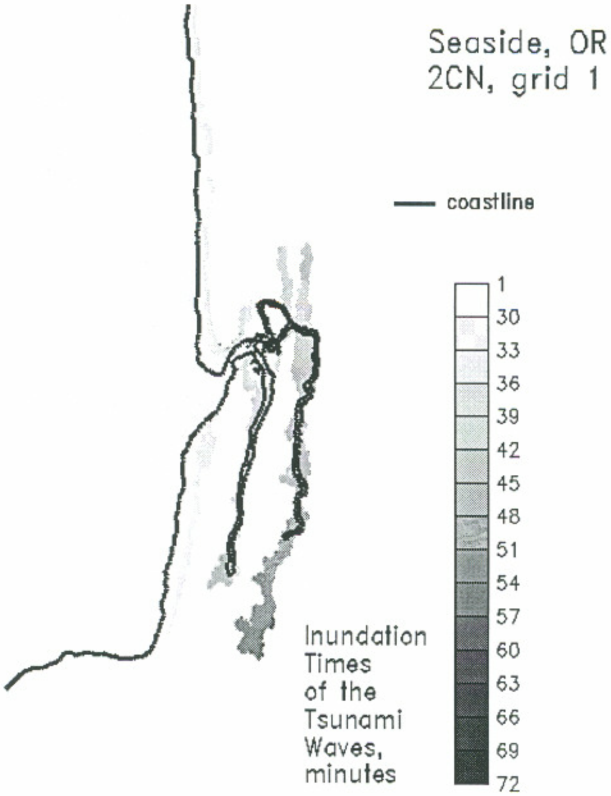

Figure 3.25h Tsunami arrival times near Seaside, OR for 2CN, grid 1.

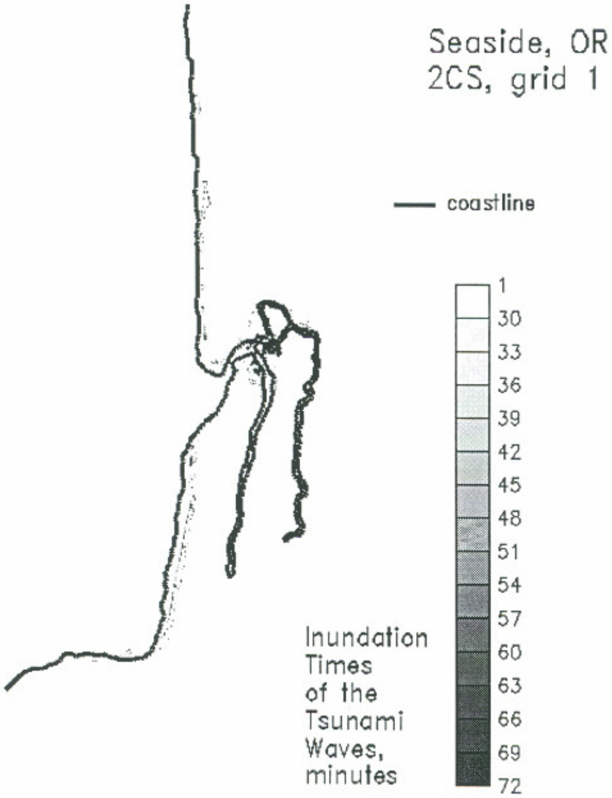

Figure 3.25i Tsunami arrival times near Seaside, OR for 2CS, grid 1.

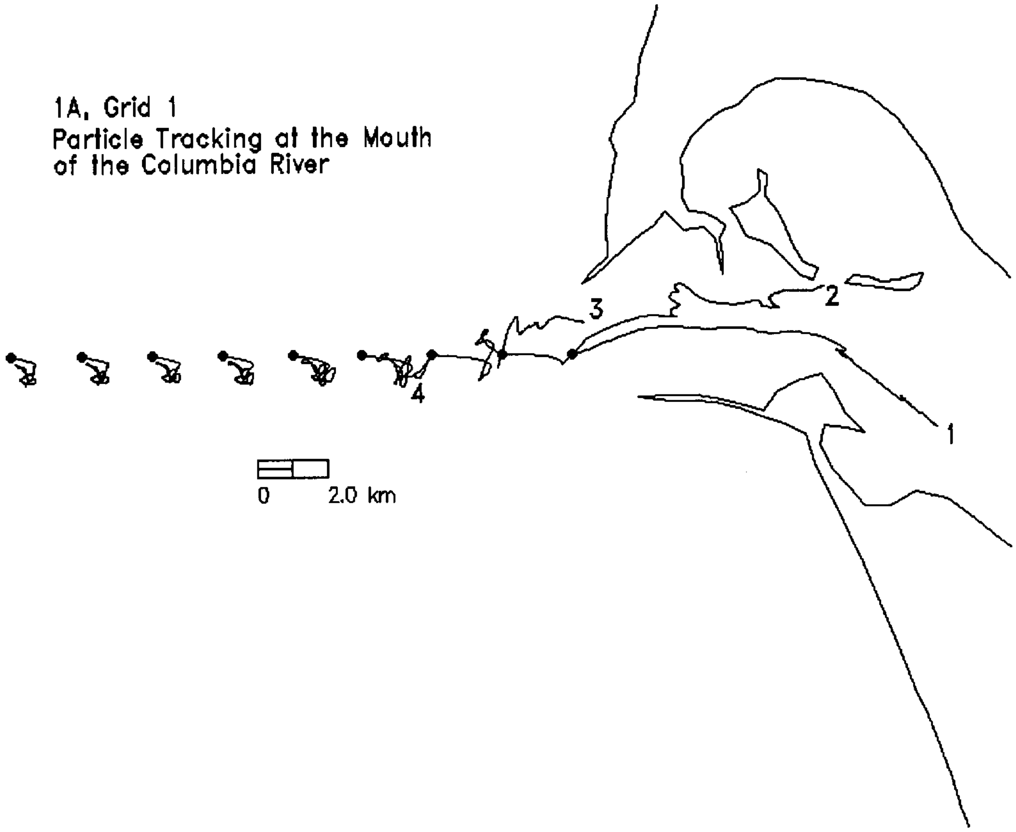

Figure 3.26a Particle tracking near the entrance of the Columbia River for 1A, grid 1.

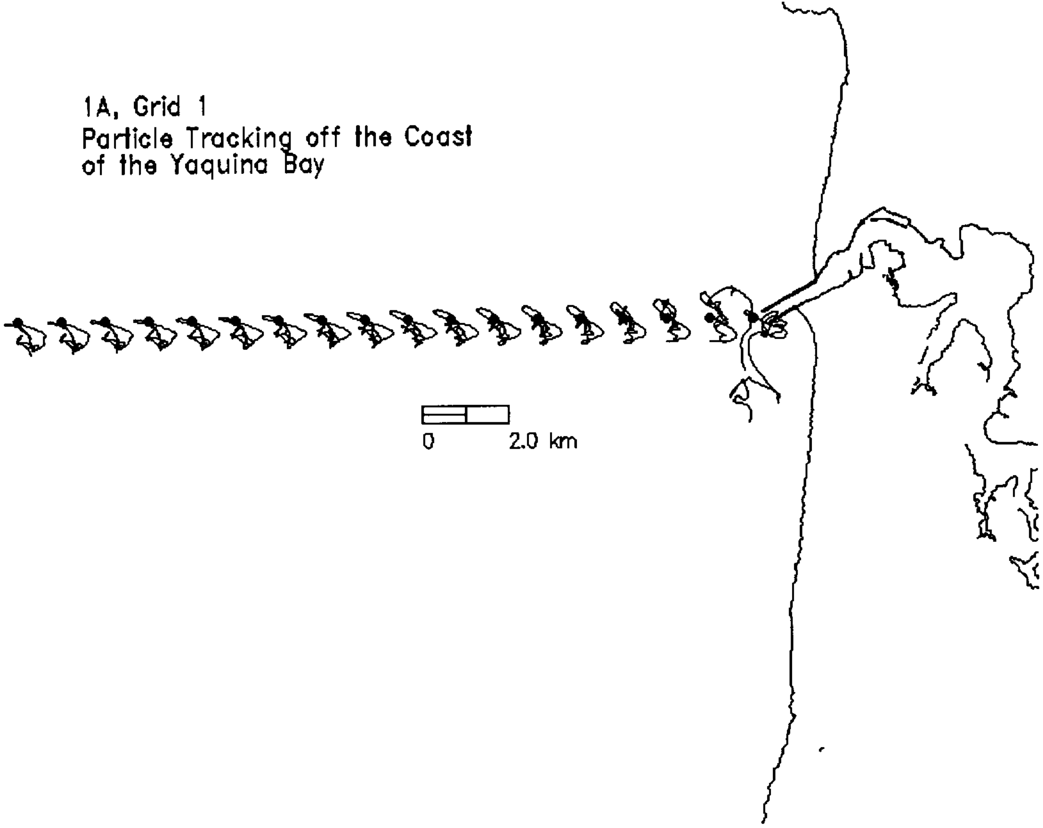

Figure 3.26b Particle tracking near the entrance of Yaquina Bay for 1A, grid 1.

CHAPTER 4

Modeling of Past Tsunamis: One Model's Lessons from the 1993 Hokkaido Nansei-Oki and 1964 Alaska Tsunamis

4.1 Introduction

Tsunamis are natural disasters that occur frequently throughout the world, although most occur in the Pacific ocean. Over the past 200 years, these events have occurred every one to two years on average (Lander et al., 1993). The frequency and magnitude of tsunami events is different for various subduction zones, although each event can impact a wide range of geographical locations. For example, the 1960 Chile tsunami resulted in near-field damage along the coast of Chile and far-field damage in Hawaii, Japan, the west coast of the United States, and other Pacific boundary lands.

Assessment of tsunami hazards in communities at risk to either near-field or far-field tsunamis is thus a critical task to perform in order to minimize future damage from these frequent events. Several tools are currently available to scientists and planners who are seeking to estimate such risks. One of these tools is the use of a hydrodynamic numerical model. Numerical models are used to simulate the propagation and inundation of tsunami waves. They use as input an initial wave profile that is equivalent to the deformation occurring along the underlying ocean floor. One of the primary decisions for scientists and planners, therefore, is the choice of deformation to be used as an initial condition. This selection of the deformation is dependent on the objectives of a particular study. City planners, for example, may be primarily interested in estimating future tsunami impacts from locally generated near-field tsunamis if their city is located near a subduction zone. They may also be interested in estimating the impact from potential far-field tsunamis. Modelers are also interested in estimating future near-field or far-field tsunami hazards. Yet, in order to ensure that the numerical models are adequately representing the physics of these waves, modeling of past events provides an avenue to validate the models' capabilities.

This study addresses one numerical model's capabilities of reproducing past tsunamis. The information gained from evaluating the factors affecting these capabilities can in turn be used to enhance the modeling of future tsunamis. Without question, the most significant obstacle facing modeling of past tsunamis is the estimation of the deformation occurring during the earthquake. There are many approaches to this obstacle, but they can generally be classified as either forward or inverse estimations of the deformation. Forward methods attempt to utilize seismologic and geologic data as input to the model used to compute the deformation. Inverse methods approach the problem by using the data on the front end and working backwards to determine what type of an earthquake and deformation could have created that data. Different types of data can be used for the inversion, including tide gauge recordings of wave elevations. When tide gauge data is used for the inversion, a hydrodynamic numerical model is used to determine what type of an initial wave (i.e. deformation) could be propagated to cause such tide gauge observations.

The problem with forward deformation models is that seismologic data can be quite ambiguous. For example, Myers and Baptista (1995) used seven different forward deformation models as initial conditions to hydrodynamic simulations. The deformations for each of the seven scenarios were significantly different, as were the tsunami waves in the numerical model. The underlying problem is that there is no data pertaining to how the ocean floor deformed during the event and thus no way of verifying which estimate of the deformation is the best. Data is usually available for how various points on land deformed, and this can be used to help constrain the problem. However, the majority of the deformation occurs along the ocean floor, and the land deformation data is thus usually insufficient to verify the estimated deformation.

This paucity of deformation data is also the Achilles' heal of inverse methods. The inverse estimates are further complicated by the fact that they have an inherent reliance on other models that relate the data to the seismic source. For example, inversion with tide gauge recordings is performed by linking the initial deformation with the data through the use of a hydrodynamic model. Any errors that are derived from the hydrodynamic models will, therefore, be embedded into the seismic source. The inversion has the effect of deriving an optimized initial condition for the hydrodynamic model to match the tide gauge observations. In theory, such inversion is an ideal way of determining the source if there are no errors in the hydrodynamic model or other assumptions provided in the inversion process. Yet because there can be significant errors in the model or assumptions and because there is no way of verifying the ocean floor deformation, this leaves too many degrees of freedom in deriving a source.

Without an adequate way of verifying the initial conditions to the hydrodynamic models, it is unfair to discuss a model's ability to reproduce a past tsunami. Perhaps the only way to eliminate this source uncertainty is to have a detailed bathymetric study immediately before and after an earthquake event. At present, acquiring such data is too costly and unfeasible. Until such data is available, the best course of action is to minimize errors in each of the components of the modeling process. For example, ambiguity in the seismic data needs to be minimized, the coverage and accuracy of bathymetric and topographic data need to be enhanced, and errors in the hydrodynamic model need to be minimized. This study addresses this latter component by evaluating the effect of grid refinement, tide and tsunami interactions, energy loss, and (numerical model) parameter selection on the numerical solution. The next two sections introduce the numerical model used in this study, the two events, and the deformations used as initial conditions for each event. The remaining sections after that address the impact of the above mentioned factors on the modeling process.

4.2 Description of the Hydrodynamic Model

The finite element model ADCIRC (Luettich et al., 1991) is used to solve the two-dimensional depth-averaged shallow water equations. Inundation is allowed to occur through the use of an element based wetting and drying algorithm (Luettich and

Westerink, 1995a-b) which utilizes water level gradients to help decide whether elements should be flooded at each time step. The model was also modified by adjusting the kinematic boundary condition to permit the floor of the ocean to deform over the first three time steps. The use of a finite element code allows for variable grid refinement throughout the domain and for the coastline to be better represented. Thus, more refinement can be added in areas where it is needed, such as shallow waters and regions of rapidly changing bathymetry/topography.

ADCIRC solves the generalized wave continuity equation (GWCE) for water elevations and the nonconservative form of the momentum equations for depth-averaged velocities at each time step. The GWCE is used in place of the primitive continuity equation, a technique that has proven to eliminate spurious $2\Delta x$ oscillations that plagued early finite element solutions. The GWCE is formed by adding the time derivative of the continuity equation, the primitive continuity equation weighted by a factor, and the spatial gradient of the conservative momentum equations. The GWCE and momentum equations used by ADCIRC are shown below:

$$\begin{aligned}
&\frac{\partial^2\eta}{\partial t^2}+G\frac{\partial\eta}{\partial t}-\frac{\partial^2\gamma}{\partial t^2}-G\frac{\partial\gamma}{\partial t}+\\
&\frac{\partial}{\partial x}\left\{u\frac{\partial\eta}{\partial t}-uH\frac{\partial u}{\partial x}-vH\frac{\partial u}{\partial y}+fvH-H\frac{\partial}{\partial x}\left[\frac{p_s}{\rho_0}+g(\eta-\alpha\Psi)\right]\right\}+\\
&\frac{\partial}{\partial x}\left\{-E_h\frac{\partial^2\eta}{\partial x\partial t}+\frac{\tau_{sx}}{\rho_0}-(\tau-G)uH\right\}+\\
&\frac{\partial}{\partial y}\left\{v\frac{\partial\eta}{\partial t}-uH\frac{\partial v}{\partial x}-vH\frac{\partial v}{\partial y}-fuH-H\frac{\partial}{\partial y}\left[\frac{p_s}{\rho_0}+g(\eta-\alpha\Psi)\right]\right\}+\\
&\frac{\partial}{\partial y}\left\{-E_h\frac{\partial^2\eta}{\partial y\partial t}+\frac{\tau_{sy}}{\rho_0}-(\tau-G)vH\right\}=0
\end{aligned} \tag{1}$$

$$\begin{aligned}
M\equiv\frac{\partial\vec{u}}{\partial t}+\vec{u}\bullet\nabla\vec{u}+\vec{f}\times\vec{u}+\tau\vec{u}+\nabla\left[\frac{p_s}{\rho_0}+g(\eta-\alpha\Psi)\right]+\\
\frac{E_h}{H}\left[\frac{\partial^2 uH}{\partial x^2}+\frac{\partial^2 vH}{\partial y^2}\right]+\frac{\tau_{sx}}{\rho_0 H}=0
\end{aligned} \tag{2}$$

where η is the free surface elevation, (u, v) are the depth-averaged velocities, H is the total water column, G is a weighting factor, γ is the bottom deformation (positive for uplift), f is the Coriolis factor, α is the effective Earth elasticity factor, Ψ is the Newtonian equilibrium tide potential, E_h is the horizontal eddy diffusion coefficient, $\tau_{s\bar{x}}$ is the applied free surface stress, τ is the bottom friction, c_f is the bottom friction coefficient, p_s is the atmospheric pressure at the free surface, ρ_0 is the reference density of water, and g is the acceleration due to gravity. A Manning formulation is used to represent bottom friction.

Land boundaries have an imposed no-slip condition, although it is ideal to extend the topographic portion of the grid such that the waves can inundate the land but never reach the land boundary (i.e. the boundary is located far enough inland). The open ocean boundaries of a grid can either have an imposed elevation condition (i.e. for tides) or a transmissive boundary condition. The latter permits waves to travel undisturbed through the boundary. This is imposed by first backtracking in the direction of the arriving wave a distance equivalent to how far the wave would travel in one time step. The elevation at that backtracked location from the previous time step is then imposed as the new elevation at the open boundary node.

4.3 The 1993 Hokkaido Nansei-Oki and 1964 Alaska Events

These two case studies were selected because they both generated large tsunamis that had severe coastal impact. Minimization of errors in the modeling of these events will therefore serve as important benchmarks. The two deformation scenarios presented for these events serve as best guesses of what occurred during the earthquake. Comparisons of model results with data will be shown in this study, although the emphasis will be placed on the effect of certain factors on the numerical solution. Therefore, the initial conditions merely serve to be approximate representations of the deformation, although their accuracy will not be a focus in this study.

The July 12, 1993 Hokkaido Nansei-Oki tsunami was generated at 13h 17m GMT just west of the small Japanese island of Okushiri in the Sea of Japan, as shown in Figure 4.1. The magnitude of the earthquake was M_S=7.8 with an epicenter of 42.3°N and 139.4°E. Even though the earthquake occurred late at night (22h 17m local time), the Japanese residents' preparedness for tsunamis helped to minimize the loss of life. There was significant damage, particularly along the coastline of the southern half of Okushiri Island, where tsunami runup values varied approximately between 5 and 30 meters. The largest observed runup was 31.7 meters near Monai on the western coast of Okushiri (Hokkaido Tsunami Survey Team, 1993). Large runups were also observed along the coast of Hokkaido, ranging between one and ten meters. Propagating waves were primarily constrained within the Sea of Japan, affecting the coastlines of Honshu, Korea, and Russia.

The seismic source selected to generate the tsunami waves for the hydrodynamic model was derived by Takahashi et al. (1995). The source was determined by Takahashi et al. by first computing the deformation from 24 proposed seismic parameter scenarios. These deformations were then used as input to a hydrodynamic numerical model, the results of which were compared with runup observations. The scenario which led to the best match in this comparison was then modified by using inversion techniques with tide gauge data and the hydrodynamic model. The final deformation pattern to the sea floor is displayed in the lower portion of Figure 4.1. Note that this particular source scenario actually consists of two fault ruptures, with the northern source generating primarily uplift to the sea floor. The island of Okushiri initially experienced subsidence from the southern source, and the initial waves generated by the lower source affected the island immediately.

The Alaska earthquake occurred almost 30 years before the Hokkaido Nansei-Oki event, as the main shock struck at 17h 36m local time on March 27, 1964 (3h 36m March 28 GMT). This was one of the largest magnitude earthquakes in recorded history, registering between 8.3 and 8.6 on the Richter scale (Committee on the Alaska Earthquake, 1972). The duration of the main shock was 3 to 4 minutes felt over 500,000 mi^2, with crustal deformation occurring over a region twice that area. Damage from this event was extensive, caused both by the intensity of the earthquake and the inundation of generated tsunamis and seiches. Alaskan ports were subjected to intense wave activity for at least 8 to 10 hours, with later waves gaining energy from the incoming high tide. Locally in Alaska, the tsunami waves resulted in 103 deaths and about $80 million in damage. In contrast to the Hokkaido Nansei-Oki tsunami, which was geographically constrained within a smaller basin (Sea of Japan), the Alaska tsunami was able to propagate freely throughout the Pacific Ocean. Due to the orientation of the seismic source, much of the tsunami energy was channeled in a southeastern direction. Thus, the western coastlines of Canada and the United States were prone to the far-field propagation of the tsunami waves. Sixteen lives were lost along the west coast of the continental United States, as the waves arrived approximately four hours after the initial earthquake. Locations of extensive damage included Port Alberni (Canada), the Oregon coast, and Crescent City (California), which incurred damage estimates of $10 million, $1 million, and $7 million, respectively.

The seismic source selected to represent the deformation for the 1964 event was derived by Holdahl and Sauber (1994). The deformation pattern in isoline form is displayed in Figure 4.2. Holdahl and Sauber modeled the source by using geodetic and geologic observations of the crustal deformation to invert for the slip distribution along the fault. The derivation of this source, therefore, differs from that of Takahashi et al. for the Hokkaido Nansei-Oki source in that tsunami waveforms linked via a hydrodynamic model were not utilized in the inversion algorithm. While such an inversion lacks the use of tide gauge recordings of waveforms, it also does not embed any errors from the hydrodynamic model into the source. As mentioned, these errors are discussed in more detail in subsequent sections. Holdahl and Sauber used 67 component planes to represent the complex three-dimensional geometry of the dipping fault surface, as the slip for each plane was solved for through the inversion. Such a representation of this complex faulting mechanism permitted for a more spatially heterogeneous pattern of deformation to be computed. This heterogeneity in the deformation shown in Figure 4.2 can be contrasted to the smoother isolines of deformation shown for the Hokkaido Nansei-Oki event in Figure 4.1.

4.4 Sensitivity of the Simulations to Selected Factors

4.4.1 Effect of Grid Refinement on Tsunami Simulations

The hydrodynamic model used in this study to propagate the tsunami waves is a finite element based algorithm. Since the effect of grid refinement on the hydrodynamic model is one of the factors to be evaluated in this study, three different grids were used. Refinement in the three grids differed primarily along the nearshore regions of Okushiri. The grids have essentially the same refinement elsewhere throughout the domain, shown in Figures 4.3a-b. Figures 4.4a-c portray the nearshore differences among the coarse, medium, and fine grids at the southern tip of Okushiri. The coarse grid has 34,294 nodes and 66,599 elements, with the smallest element being characterized by an equivalent diameter (twice the square root of the division of the elemental area by π) of 21.48 meters. These numbers change to (41629, 80945, 22.40) and (60181, 117004, 10.34) nodes, elements, and smallest equivalent diameter for the medium and fine grids, respectively. A cumulative histogram of the distribution of the elemental equivalent diameters for each of the grids is shown in Figure 4.5. Each value in the graph shows the percentage of elements in a grid with a particular equivalent diameter or less.

Three finite element grids were also set up for the 1964 Alaska tsunami simulations, in order to contrast and evaluate the effect of grid refinement for this event. Figures 4.6a-c display these three grids, each of which spans the same region extending from the Aleutian Islands to central California. The coarse grid is one of the grids used in a modeling study of potential Cascadia subduction zone tsunamis (Myers and Baptista, 1998a), and therefore consists of added refinement off the coasts of Vancouver Island, Washington, and Oregon to represent well an initial Cascadia tsunami waveform. Added refinement was also placed near the Alaska seismic source. Thus, in the regions of these two sources, representation of the continental slope and shelf is more refined than along other portions of the grid. The medium grid was therefore designed to add four times as much refinement to the entire coarse grid, with the exception of the Cascadia subduction zone region where the refinement was already enhanced. In order to further benchmark the effect of grid refinement for these simulations, a fine grid was derived by adding four times as much refinement to the entire medium grid.

Figure 4.7 plots the average element depth with the elemental equivalent depth for each of the Alaska grids. The medium grid is shown to have more refinement in the deep ocean regions as well as in depths of 500 meters or less. The diameters of all elements are approximately decreased in half for the fine grid as compared to the medium grid. The number of elements, number of nodes, and smallest equivalent diameter for the coarse, medium, and fine grids are (68965, 37897, 11.3), (137655, 74576, 11.3), and (550616, 286915, 11.3), respectively. While these Alaska grids each have more nodes than the Hokkaido Nansei-Oki fine grid, the modeling domain for the Alaska simulation is much larger than that for the Sea of Japan.

The effect of the grid refinement on the Hokkaido simulations should be most evident in near-shore regions of Okushiri, since those are the only areas where refinement was added. If the refinement significantly affects the interaction of the waves with the coastline, this effect should be visible in the computed runups from the simulations. These runup calculations are shown in Figure 4.8b for the coastline segments portrayed in Figure 4.8a. The abscissa in each of the graphs are representative of the counterclockwise distance along each of the shoreline segments. Data observations are shown as circles, and the simulation results are displayed in the three lines. As mentioned, the goal of this study is not to match simulations with data observations, and therefore the data is only included here for reference. The computed runups along the first segment are roughly similar among the coarse, medium, and fine grid runs. Segments 2 and 3, however, show a much more striking discrepancy between the runs on the different grids. The medium grid run appears to result in just slightly larger runups than the coarse grid run, yet close examination of the scale shows that some of these differences can be as large as 5 to 10 meters (i.e. on segment 3). The fine grid run clearly permits the runup process to be more enhanced, as exemplified by the more uniform distribution of increases over the other two runs on segments 2 and 3.

Even though the same seismic source is being imposed for these Hokkaido simulations, the grid refinement is clearly affecting the numerical propagation of the tsunami waves. The differences are most pronounced along the shoreline, yet this near-shore interaction will also change the dynamics of the waves as they head back out to the ocean. This can be seen in Figure 4.9, which displays the root mean square difference in elevations between the medium grid run and the coarse grid run and between the fine grid run and the medium grid run. The RMS difference is computed as

$$\mathrm{RMS}=\left\{\frac{1}{N}\sum_{i=1}^{N}\left[\left(\eta_i-\tilde{\eta}_i\right)-\left(\frac{1}{N}\sum_{j=1}^{N}\left(\eta_j-\tilde{\eta}_j\right)\right)\right]^2\right\}^{1/2} \tag{3}$$

where N is the number of points in time, η is the elevation in one simulation, and $\tilde{\eta}$ is the elevation of the other simulation.

Both sets of differences show a local maximum in about five meters of depth. Also note the large differences which are present as the waves runup onto the land (i.e. negative depths). Considering the 1-2 meter RMS differences in shallow water and on land for these simulations as well as the large runup discrepancies between runs shown in Figure 4.8b, the question arises as to what level of grid refinement will be sufficient to minimize such differences. Without a doubt, the solution is tied to the issue of computing capacity. The Hokkaido simulations were performed shortly before the Alaska simulations, yet in that short amount of time, computing capabilities have increased to a level which permits the use of grids larger than the 60,181 node fine grid used for Hokkaido. As will be demonstrated, though, the use of grids with almost 300,000 nodes still leaves the modeler facing the same above-mentioned question.

The grid refinement for the Alaska simulations is slightly different than that of the Hokkaido grids, which placed all of the added refinement in near-shore regions. Conversely, the medium Alaska grid added twice the refinement (i.e. Δx approximately halved) throughout the entire domain except near the Cascadia subduction zone, where refinement was already about twice as enhanced. The fine Alaska grid subsequently added twice the refinement to the medium grid. The setup of these three grids in this manner permitted for an interesting test to be performed. By examining the computed runups in Figure 4.10 along the northwest coast of the United States, the effects of the different styles of refinement can be better understood. For example, the medium grid did not add refinement to the near-shore regions of this portion of the coastline. Yet Figure 4.10 shows that the medium grid run yielded higher runups along this coastline than those of the coarse grid run. Thus, the refinement added elsewhere to the grid permitted the propagating waves in those areas to be better represented, such that larger runups were computed along the northwest coast of the United States. The fine grid run led to runup increases over those of the medium grid, which are approximately equivalent to the increases gained by using the medium grid over the coarse grid. Thus, while this portion of the coastline is about 2,000 km away from the source, computed runups on the fine grid were about one meter larger than those of the coarse grid.

To understand the spatial variability of differences among the three Alaska simulations, Figure 4.11 displays some of the isolines of maximum elevation throughout the domain. A maximum elevation is extracted from the time series of elevation at every node in the domain and plotted in isoline format. It is clear that in the direction that most of the tsunami energy is oriented (~southeast), the isolines extend further into the deep ocean with increased refinement. As the waves reach the Cascadia coastlines and propagate along the continental shelf, the isolines also protrude further towards the ocean with the more refined grids. This has important implications for both regional and transoceanic modeling of tsunamis. It is obvious that even with a grid that has approximately 300000 nodes, the level of refinement necessary to propagate the wave sufficiently has probably not been reached. The word probably is used here because it is unclear what even more refinement will add. It is clear, though that the medium grid was invaluable in its advances it provided over the coarse grid, as was the fine grid in its advances it brought over the medium grid. It is fair to say that more refined grids will probably bring similar advances, yet today's computational limits are preventing that next step. With such significant differences attributed to the effect of grid refinement in regional simulations of this Alaska tsunami, the errors shall be significantly larger for modeling of transoceanic tsunamis that travel even further.

The Hokkaido Nansei-Oki and Alaska simulations exemplify a couple of different effects that grid refinement has on the solution. The Hokkaido simulations showed how near-shore refinement represents better the process of inundation as well as the interactions of the waves with the coastline. In addition to this effect, the Alaska simulations have shown that refinement is also playing a large role in how the waves traverse the deep ocean, the continental slope, and the continental shelf. In order to show how grid refinement is affecting the propagation characteristics in these regions, Figures 4.12b-c show time histories of wave elevations at the locations shown in Figure 4.12a. Only the coarse run and fine run time histories are shown, to emphasize the refinement effect on the amplitude, phase, and frequency of the simulated waves. The frequencies of the waves for the coarse and fine runs show the most striking differences. The fine grid run is better able to support higher frequency information. This, in turn, affects the amplitude and phase of the waves, particularly along the northwest United States coastline where higher amplitude waves are propagated at the higher frequencies.

The only question that remains is whether this higher frequency information is representative of data recorded by tide gauges. Figures 4.13a-f show time histories of elevations at Yakutat (Alaska), Sitka (Alaska), Neah Bay (Washington), Astoria (Oregon), Crescent City (California), and San Francisco. The top graph of each figure compares the tide gauge observation with a coarse grid simulation of both the tsunami and the tides while the bottom graph displays the fine and coarse grid simulations of just the tsunami. While there remain questions as to how well this combination of seismic source, model, and grid were able to reproduce the observations, it is clear that higher frequency information in the observations is not being simulated in the coarse grid simulations. The fine grid tsunami simulation, however, shows that it is propagating such higher frequency waves, in accordance with the data. A simulation of both the tides and the tsunami on the fine grid was not available, due to computational time constraints.

The effect of grid refinement in the deep ocean, the continental slope and shelf, and near-shore regions has been shown to lead to significant solution differences and to be a limiting factor given the limits of today's computers. This does not signify that numerical modeling of tsunamis is not useful, but it does emphasize the amount of attention that needs to be placed on the topic of grid refinement. Efficient placement of grid points to preserve the numerical integrity of tsunami simulations is therefore discussed in more detail by Myers and Baptista (1998b). While such topics are more intensely investigated from a scientific vantage, simultaneous attention should be accorded to numerical models' use as hazard mitigation tools. For example, the Alaska grids used in this study were modified from a grid that was used to estimate potential impacts of Cascadia subduction zone tsunamis on the western coast of the United States. Grid refinement was enhanced in Seaside, OR and Newport, OR in order to examine the local impacts of the waves on these communities. The Seaside area serves as a good cross-case study, given the fact that it is at risk to near-field Cascadia tsunamis as well as being one of the west coast communities which was impacted strongly by the 1964 Alaska tsunami.

Figure 4.14 shows the portions of northern Seaside which were covered by water (figure includes the rivers) in the fine grid simulation of the Alaska tsunami. The circles represent runup observation points from witnesses of this event. It should be noted that even with grid refinement on the order of 10 meters in this area, the bathymetry and placement of the river boundaries carry uncertainty due to the fact that this data was not available for the time of the 1964 event. However, some of the observation points show an interesting relation with the fine grid simulation. Six of the observation points along the land next to the Neawanna River were covered by water in the fine grid simulation, but not by the coarse or medium grid simulations. These results do not include the tides, so the inundation patterns will be different for all three simulations since the wave arrived during a high tide period. However, the important point here is that grid refinement will play a major role in determining the extent of hazards in communities. After all, had we been using this model with the coarse or medium grid in 1963 (i.e. predicting what would happen if such an earthquake were to occur in the future), we may have concluded that none of the Seaside community was at high risk from such an event.

4.4.2 Nonlinear Tide and Tsunami Interactions

A common practice in tsunami modeling is to model the tsunami wave without the influence of tides. For example, the Hokkaido simulations presented in this study do not include tidal forcings. Generally, when tide gauge data is used in conjunction with modeling of just the tsunami (either for inverse or forward modeling purposes), the tidal component of the tide gauge record is extracted (from historical records) to leave only the elevation recording of the tsunami waves. The question posed in this section is, therefore, whether this is a linear process. For example, if nonlinear effects are significantly stronger when the tsunami waves are interacting with the tides, then an extracted "tsunami" wave time history will in actuality be a time history of both tsunami and nonlinear interactions. Modeling results of just the tsunami will therefore not be directly comparable to such an extracted time series. The problem would grow worse for runup observations, as it is more difficult to even extract just the tidal information unless an accurate local tide model is available.

To explore the nature of tide and tsunami nonlinearities, the coarse Alaska grid was utilized in a series of simulations. The coarse simulation of just the tsunami was discussed in the previous section. Using the same grid, tides were simulated for the same time period as the tsunami run. Boundary conditions for the tidal forcing were obtained from a regional tide model of the Eastern North Pacific Ocean developed by Myers and Baptista (1998c). Finally, a third simulation was performed in which both the tides and the tsunami were imposed concurrently. Boundary conditions for this third simulation were imposed using the following relation at the open boundary nodes,

$$\frac{\partial \eta}{\partial t} = -g\frac{\partial \eta}{\partial n} - \eta_{\text{tide}} \qquad (4)$$

where n is the direction of the arriving tsunami wave and η_{tide} is the tidal elevation at the open boundary node. This open boundary condition is designed so as to allow the tsunami waves to travel undisturbed through the open ocean boundary, yet still permit for a Dirichlet tidal forcing to be concurrently imposed.

If nonlinearities associated with tide and tsunami interactions are negligible, then the results of the tsunami simulation added to the results of the tide simulation would equal the results of the tide and tsunami simulation. Nonlinear tide and tsunami interactions were thus computed as the difference between this addition and the tide and tsunami simulation. Figures 4.15a-b show time histories of these nonlinear interactions at the same 18 locations portrayed in Figure 4.12a. Note that the vertical scale is different for each station. The amplitudes of most of these time histories are generally between 0.5 and 1 meter, though it is clearly station dependent. The periodicity of most of the time histories is generally consistent with periods that are more typical of the tsunami, although station 4 (Prince William Sound) does primarily show a tidal periodicity.

In order to gain a better understanding of the frequency of these interactions, the power spectrum was computed for each of the 18 station time histories. The results are displayed in Figures 4.16a-b, with the amplitude of the frequency component being represented on the y-axis of each log-log plot. Power spectrum results are computed and shown for time histories of 1) the nonlinear interaction, 2) the tide results added to the tsunami results, and 3) the tide and tsunami simulation results. Perhaps the most striking result in these figures is the wave period of the last local maximum in the nonlinear interaction power spectrum. The amplitude of this last maximum is significant at each station, and is strongest at locations closer to the seismic source. The wave period of this last maximum at each station, though, is always located at an intermediate point between the longest tsunami period and the M_2 tidal period (744 minutes). It is possible that this last maximum in the nonlinear interaction spectrum represents the generation of a tide-tsunami frequency associated with the nonlinear mixing of the waves. The other maxima in the power spectrum of the nonlinear interactions at each station occur at periods equal to or close to the tsunami periods (as seen in the tide results plus tsunami results). This seems to indicate that these other maxima are more associated with stronger nonlinearities present in a water column of both tides and tsunami.

The primary conclusion from these results, though, is that nonlinearities generated by the interaction of tsunami waves and tides are non-negligible. To emphasize this, Figure 4.17 shows coastal elevations of the tsunami results compared to the tide and tsunami simulation results, as well as of the nonlinear interaction component along the northwest coast of the United States. The first graph in this figure shows the influence of tides on coastal elevations for this Alaska tsunami. Because the tsunami arrived along these coastlines during flood tide, the tide and tsunami simulation results are generally about a meter larger than the tsunami simulation results. For the purposes of hazard mitigation, simulations of potential future tsunamis should attempt to capture this effect by simultaneously forcing tides and the tsunami in model runs. The second graph in Figure 4.17 shows the maximum coastal amplitudes of the nonlinear interactions. Clearly, with many of these coastal locations experiencing 0.5 to 1 meter nonlinear interaction effects, such influences are a critical phenomena in the simulations. Interestingly, Crescent City, California (Station 17) shows large nonlinear effects, which may help to explain the devastating effect the tsunami had on this locality. Figure 4.18 displays the maximum nonlinear component of the elevation for every grid node as a function of distance from the seismic source. There is a clear decrease in these values the farther a point is from the source. It should be noted that some of these differences arise from phase induced offsets or from runup differences. Overall, though, the amplitudes can be discerned to be large at all points and also show an inverse relationship with distance. From the previous section on grid refinement, it is possible that the loss of energy associated with grid refinement may be a contributing factor to the decreasing trend in the nonlinear component amplitude.

4.4.3 Numerical Energy Loss

The effect of grid refinement has been shown to lead to numerical solutions that lose a significant amount of higher frequency information if the refinement is too coarse. This property, by itself, suggests that the energy carried by the numerically propagated waves is being diminished as well. To test this theory, the Hokkaido simulations were altered slightly by converting the open boundaries throughout the Sea of Japan into closed land boundaries. Thus, energy generated by the initial tsunami waves has no way of escaping the domain via open transmissive boundaries and should ideally be conserved through the length of the simulation. Three grids were used for these energy simulations including the coarse and fine grids mentioned previously. Also included was an "extra fine" grid that split each of the fine grid elements into four, resulting in a grid of 237,367 nodes and 468,016 elements.

The potential (E_p), kinetic (E_k), and frictional loss (E_f) components of the total energy are computed as,

$$E_p(t) = \frac{1}{2}\rho g \int_{\Omega} \eta^2 d\Omega \tag{5}$$

$$E_k(t) = \frac{1}{2}\rho \int_{\Omega} \left[\int_{0}^{h+\eta-\gamma} \left(u^2 + v^2\right) dz \right] d\Omega \tag{6}$$

$$E_f(t) = \frac{1}{2}\rho \int_{t_0}^{t} \int_{\Omega} c_f \left(u^2 + v^2\right)^{3/2} d\Omega dt \tag{7}$$

where Ω is the spatial domain, t_0 is the initial time of the simulation, ρ is the density, g is the gravitational acceleration, η is the wave elevation, h is the depth, γ is the deformation along the ocean floor, u and v are horizontal velocities, and c_f is a friction coefficient.

Figure 4.19 shows the energy variation with time for these three simulations, as well as a delineation of the potential and kinetic energy components for the fine grid simulation. The frictional loss of energy is negligible compared to the other components and is therefore not displayed. Each of the simulations shows a diminishing trend of energy preservation. However, the fine grid energy variation becomes steady after losing energy for the first hour and a half, whereas the coarse grid shows energy to be decreasing for the duration of the simulation. The extra fine grid simulation was run for an hour and a half of tsunami time during which the energy decreased, but not as much as the other two simulations. These results clearly exemplify the proportionality between grid refinement and energy preservation, most likely owing to the ability of more refined grids to resolve higher frequency waves more effectively.

However, energy loss may be caused by more than just grid refinement. For example, selection of numerical parameters, shallow water assumptions, or truncation errors may all be culprits in the energy loss issue. These effects are discussed in more detail in Myers and Baptista (1998b) through the use of a channel grid extracted off the coast of Seaside, OR and a synthetic imposition of a tsunami in that channel. Figure 4.20 displays some of the energy results from that study for four grids, each of which was derived by splitting each element of the next coarser grid into four elements. The comparisons among these grids show a similar proportionality between grid refinement and energy preservation as was shown for the Hokkaido simulations. G is the weighting factor in the generalized wave continuity equation (GWCE) and is modified in the last three simulations for the most refined grid. The larger this parameter is, the more the GWCE approaches the primitive continuity equation. And as Figure 4.20 displays, energy is preserved better with larger G values (i.e. more primitive continuity equations). Myers and Baptista (1998b) discuss how these different factors influence energy preservation and the numerical solution.

To provide a feel for how the energy loss is influencing the maximum elevations computed at each node, Figure 4.21 presents the maximum elevation as a function of depth for the four grid simulations using $G=0.08\ sec^{-1}$. Most of the differences occur in either shallow water near the land boundary or along the continental slope. Maximum differences between the most refined grid and the coarsest grid are about 10 meters along the continental slope, and differences of the order of a few meters occur in several different regions.

Energy loss is therefore concluded here to be a symptom of the performance of the model. It is called a symptom because it is a warning sign that grid refinement, shallow water assumptions, or truncation errors are afflicting the numerical solution. Its use as an indicator can help to benchmark how well the model is performing.

4.4.4 Parameter Selection in the Numerical Model

It was demonstrated in the previous section how the weighting factor G can significantly affect the preservation of energy and thus the numerical solution of elevations and velocities. Other parameters that are available for user modification include friction coefficients, the time step, the minimum depth, and a diffusion coefficient. Of these, the first three are the most influential on the numerical solution and are now investigated further. The Hokkaido simulations are used here to benchmark the effects of these parameters on the numerical solutions.

The fine Hokkaido grid was utilized first to perform three new simulations that differ from the original one by the type of friction imposed. The original fine grid simulation used a Manning coefficient of 0.0275 $\mathrm{sec \cdot m^{-1/3}}$ in the friction factor. The first two new simulations used modified coefficients of 0.015 $\mathrm{sec \cdot m^{-1/3}}$ and 0.035 $\mathrm{sec \cdot m^{-1/3}}$. The third simulation used an adapted Manning scheme that permits for a better representation of the friction along topographic interfaces. Time histories of elevations were then compared for all simulations at every node, and root mean square differences between each simulation and the original simulation were computed using equation 3. These RMS differences are shown in Figure 4.22 as a function of depth for these friction sensitivity simulations. All three RMS variations with depth show a distribution centered approximately around five meters of depth. The smaller friction simulation resulted in the most scatter in this distribution, in terms of both the magnitude of the difference and the variation with depth. The other two friction simulations generally led to RMS differences constrained within one meter. While most of the larger differences occurred in 0-10 meters depth, significant differences were also present in the inundation of the waves (i.e. negative depths representing points on land).

Similar RMS difference distributions are plotted in Figure 4.23 for simulations testing the sensitivity of the model to the selection of a time step and a minimum depth. Again, the fine grid was utilized for these sensitivity tests. The time step simulation used a Δt of 0.5 seconds rather than the one second used by the original simulation. While the time step simulation is designed to evaluate the effect of decreasing the time step in half, it should be noted that the original time step of one second did not lead to any numerical instabilities. Generally, instabilities are the primary concern in selecting a time step, so this sensitivity test should help reveal the effect of decreasing the time step further than is necessary to avoid such instabilities. As the top graph in Figure 4.23 shows, the largest RMS differences using a smaller time step occurred on land, thus indicating the importance of the time step selection on the modeled inundation process. Many of the differences in 0-10 meter depths were on the order of one meter with a distribution centered somewhere between 5 and 10 meters of depth.

The minimum depth simulation discarded the land portions of the grid and imposed a minimum depth of 10 meters around the island of Okushiri. This latter simulation is designed to represent nonlinear models that do not have inundation capabilities and therefore must impose a minimum depth to avoid numerical problems associated with wetting and drying. From the previous sensitivity tests, it is apparent that the 0-10 meter depth range is where the tsunami waveforms are very susceptible to changes. Therefore, it is expected that imposing a minimum depth of ten meters will affect the simulation results more than the other sensitivity tests presented in this section. As can be seen in the bottom graph of Figure 4.23, this is indeed the case. Differences on the order of one meter are now occurring in depths of 40 meters and greater, whereas the other sensitivity simulations showed more negligible differences in such depths. Many shallow water points showed differences up to four meters. It should be noted that many of these differences in the RMS plots may be associated with phase errors, yet the overall trend in each case also supports significant amplitude differences.

These sensitivity test results are intended to stress the notion that parameter selection should not necessarily be indelible, and the changes which are made to input parameters can influence the solution in non-negligible ways. The minimum depth simulation showed the importance of a model being capable of handling inundation. The time step simulation revealed that decreasing the time step can affect the solution even if instabilities are not an issue. The only effective way to eliminate such time step differences is to continue to decrease the time step until differences are no longer seen. This, however, is bounded by the capabilities of the computer since further decreases would result in simulations that would require lengths of time on the order of months to compute. The friction sensitivity tests tread on a different quagmire, in the sense that friction parameterization is difficult to quantify for such large domains. Choosing a Manning factor or a friction parameterization scheme is not a cut and dried process, particularly for points on land experiencing inundation. Obtaining adequate friction factors is sometimes based on friction optimization for tide models, yet this is still subject to much uncertainty. Clearly the selection of parameters is open to debate, and each selection should be individually optimized as much as possible in the effort to eliminate errors in the modeling of tsunamis.

4.5 Summary

The critical components to the instruction set of any numerical model are the initial and boundary conditions. Tsunami simulations use the deformation to the floor of the ocean as initial conditions, yet the deformation itself relies on many assumptions regarding its computation by either forward or inverse algorithms. It is common to use hydrodynamic models and tsunami data to find optimal seismic sources that could have induced such waves. Without an adequate way to verify the accuracy of these derived sources along the ocean floor, many degrees of freedom are introduced in the uncertainties. Until such verification is achieved, or when there is less uncertainty involved in computations of deformation which are derived independently of a hydrodynamic model (i.e. forward models), attempts should be made to ensure that the other components of the tsunami modeling process are as sound as possible.

This study looked at the modeling of the 1993 Hokkaido Nansei-Oki and 1964 Alaska tsunamis from the vantage of analyzing which modeling components carry significant uncertainty and the extent of those uncertainties. A finite element model was used for the simulations, so it is possible that some of these uncertainties are unique to finite element algorithms. However, it is believed that most of the sources of uncertainty presented here have common denominations in most models. Added grid refinement was shown to lead to better propagation of higher frequency waves in the solution. Allowing for the waves to propagate at higher frequencies also permitted them to sustain larger amplitudes and, in some cases, slightly different phases. The statement that grid refinement is a significant factor in numerical solutions seems like an obvious one, yet the results indicate that even grids which have hundreds of thousands of nodes in the domain are not at a sufficient level to adequately propagate all of the frequency information in the waves. This is exemplified by the energy computations, which can serve as a benchmark of the errors that are occurring in a solution. The most refined grids were still showing energy loss on the order of one half of the initial energy in the system. This amount of energy loss surely will influence wave propagation computations of elevations and velocities. Tides were shown to interact nonlinearly with tsunami waves, and the magnitude of these interactions stresses the importance of their inclusion in the modeling process. Finally, parameters such as the GWCE weighting factor, friction, the time step, and a minimum depth can also greatly influence the solution, particularly in nearshore shallow waters.

These results have significant implications for using models in hazard mitigation studies. If physical or numerical factors are not accounted for properly, the models may underestimate the impact of tsunami waves. While nonlinear tide-tsunami interactions were scrutinized in this study, there will also be a linear superposition of these two types of waves. Hazard mitigation studies should try to account for both the linear and nonlinear influences of the tides on the tsunami waves. Until there is less uncertainty in the modeling components described in this paper, factors of safety should be considered in estimating damage from potential events that may occur in the future. Recognition of these uncertainties and the need to design sounder modeling solutions implores close cooperation between policy makers and the numerical modelers.

Several factors were not mentioned in this study, including the accuracy and coverage of bathymetric/topographic data and conversions of this data to equivalent vertical reference levels. The factors that were addressed, though, are most pertinent to the application of the hydrodynamic model using the assumptions of a particular seismic source and data set. While the underlying theme in this study is that of a caution flag in the use of numerical models, it is in no way deterring their use as a tool in understanding the physics of past tsunamis and the hazards of future ones. Rather, it urges judicious use of numerical models by pointing out the factors to which close attention should be paid, the result of which will help advance our understanding of these events.

4.6 References

Committee on the Alaska Earthquake of the Division of Earth Sciences National Research Council, 1972. *The Great Alaska Earthquake of 1964*, Oceanography and Coastal Engineering, National Academy of Sciences, Washington, D.C.

Hokkaido Tsunami Survey Group, 1993. Tsunami Devastates Japanese Coastal Region, *EOS Transactions*, AGU, 74(37), 417.

Holdahl, S.R. and J. Sauber, 1994. Coseismic Slip in the 1964 Prince William Sound Earthquake: A New Geodetic Inversion, *Pure and Applied Geophysics*, 142(1), 55-82.

Lander, J.F., P.A. Lockridge and M.J. Kozuch, 1993. *Tsunamis Affecting the West Coast of the United States 1806-1992*, National Geophysical Data Center Key to Geophysical Records Documentation No. 29.

Luettich, R.A. and J.J. Westerink, 1995a. *An Assessment of Flooding and Drying Techniques for Use in the ADCIRC Hydrodynamic Model: Implementation and Performance in One-Dimensional Flows*, Dept. of the Army, U.S. Army Corps of Engineers, Vicksburg, MS.

Luettich, R.A. and J.J. Westerink, 1995b. *Implementation and Testing of Elemental Flooding and Drying in the ADCIRC Hydrodynamic Model*, Dept. of the Army, U.S. Army Corps of Engineers, Vicksburg, MS.

Luettich, R.A., J.J. Westerink and N.W. Scheffner, 1991. *ADCIRC: An Advanced Three-Dimensional Circulation Model for Shelves, Coasts, and Estuaries*, Dept. of the Army, U.S. Army Corps of Engineers, Washington, D.C.

Myers, E.P. and A.M. Baptista, 1995. Finite element modeling of the July 12, 1993 Hokkaido Nansei-Oki tsunami, *Pure and Applied Geophysics*, 144(3/4), 769-801.

Myers, E.P. and A.M. Baptista, 1998a. Finite Element Modeling of Potential Cascadia Subduction Zone Tsunamis, (submitted to *Science of Tsunami Hazards*).

Myers, E.P. and A.M. Baptista, 1998b. Numerical Considerations in Finite Element Simulations of Tsunamis, (submitted to *International Journal for Numerical Methods in Fluids*).

Myers, E.P. and A.M. Baptista, 1998c. Inversion for Tides in the Eastern North Pacific Ocean, (submitted to *Advances in Water Resources*).

Takahashi, To., Ta. Takahashi, N. Shuto, F. Imamura and M. Ortiz, 1995. Source Models for the 1993 Hokkaido Nansei-Oki Earthquake Tsunami, *Pure and Applied Geophysics*, 144(3/4), 747-767.

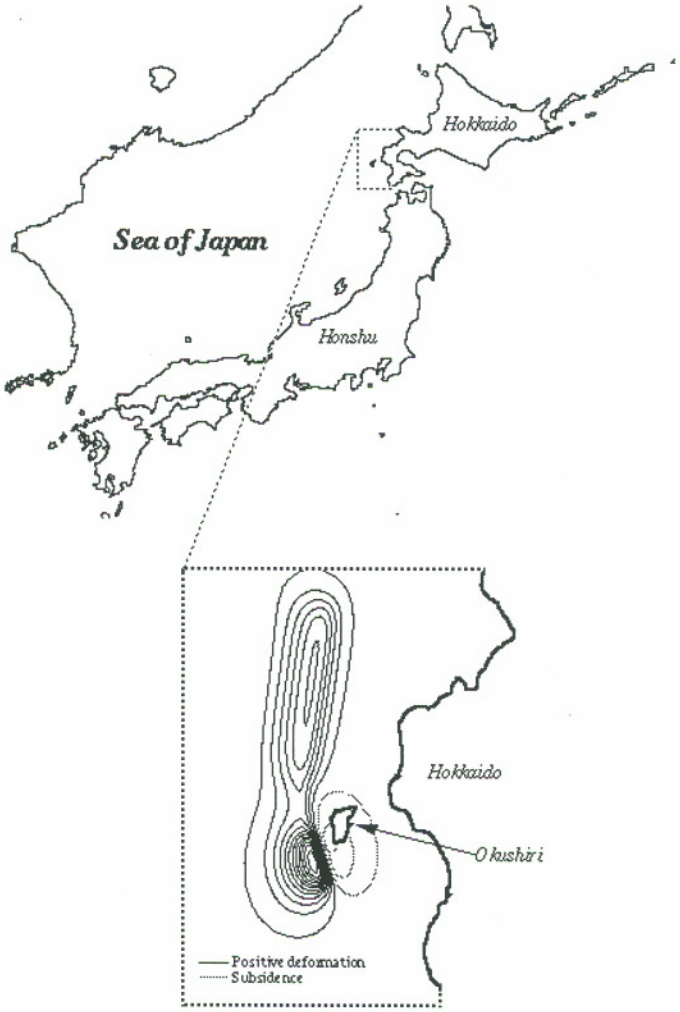

Figure 4.1 Regional domain and ocean floor deformation for the 1993 Hokkaido Nansei-Oki tsunami.

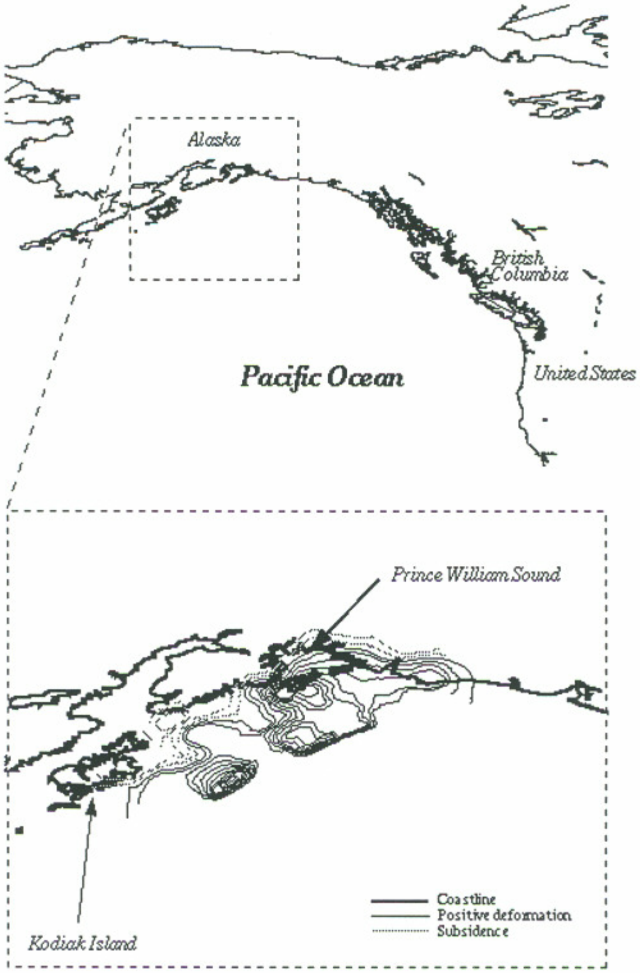

Figure 4.2 Regional domain and ocean floor deformation for the 1964 Alaska tsunami.

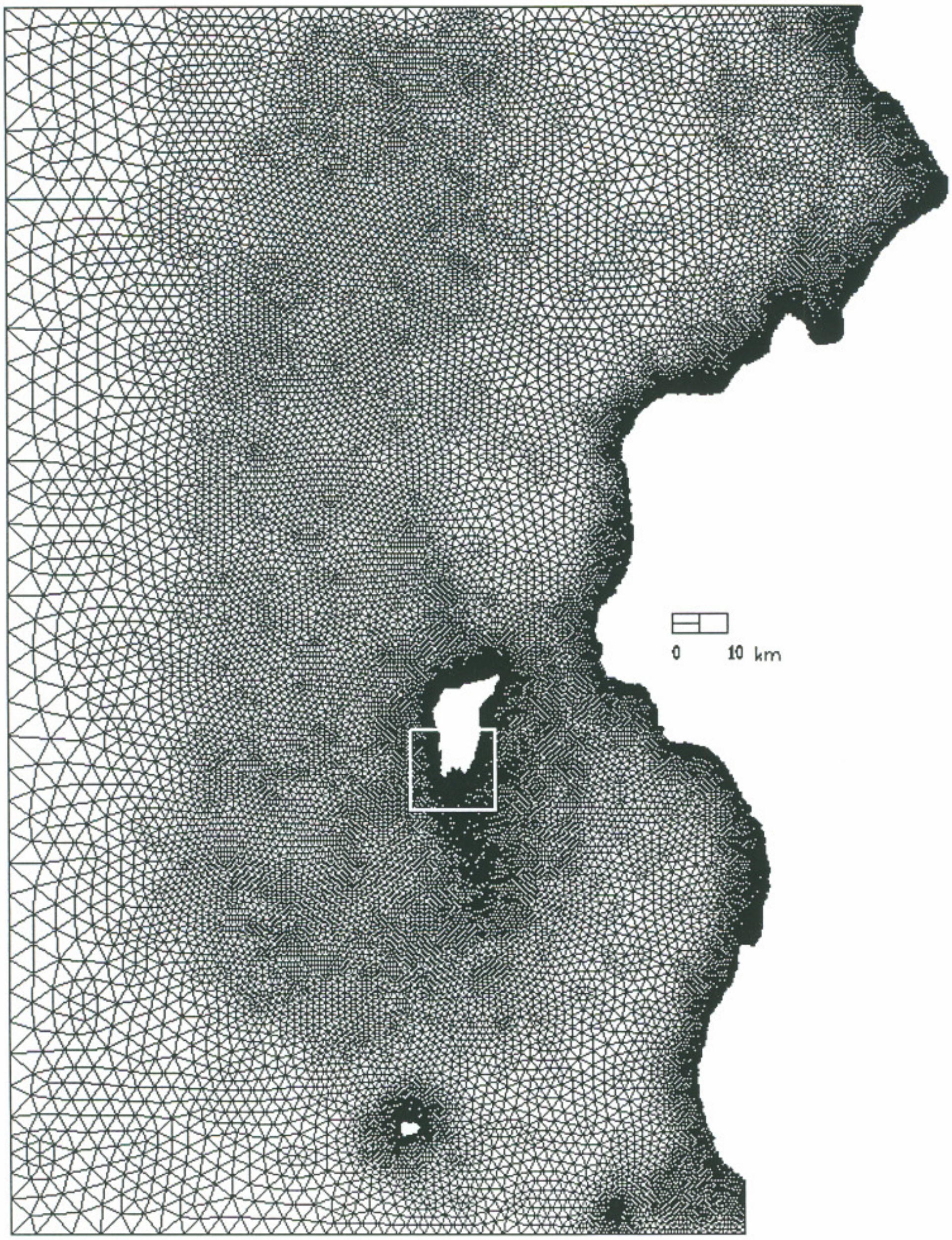

Figure 4.3a Finite element grid used for the Hokkaido tsunami simulations.

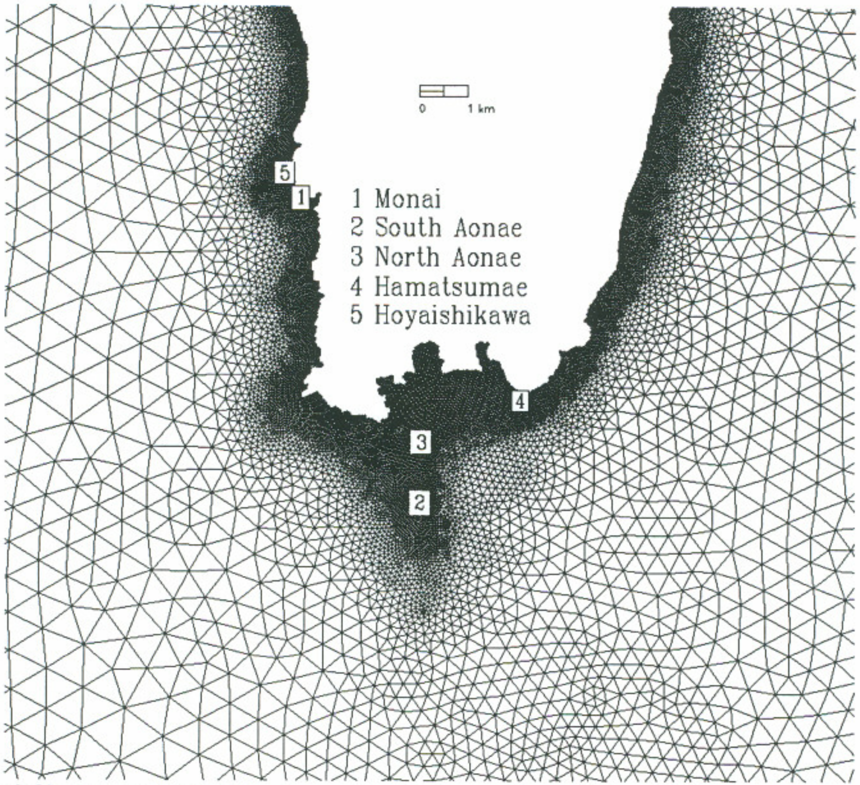

Figure 4.3b Zoom of finite element grid in southern Okushiri.

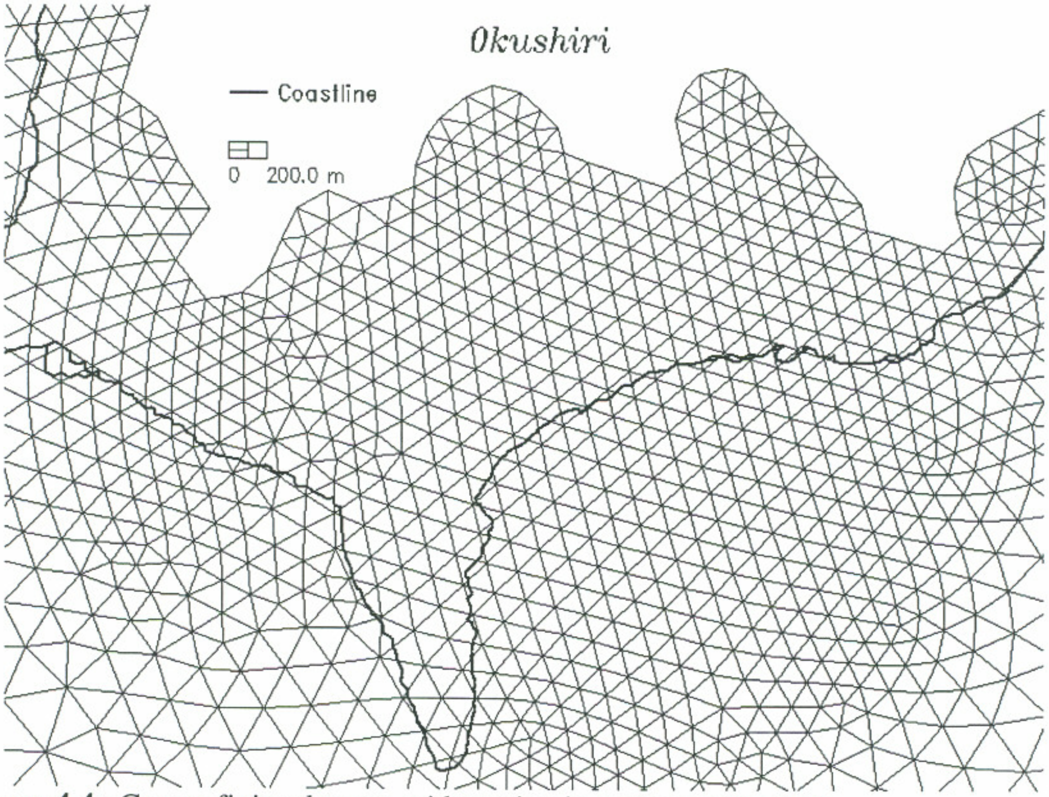

Figure 4.4a Coarse finite element grid spacing in southern Okushiri.

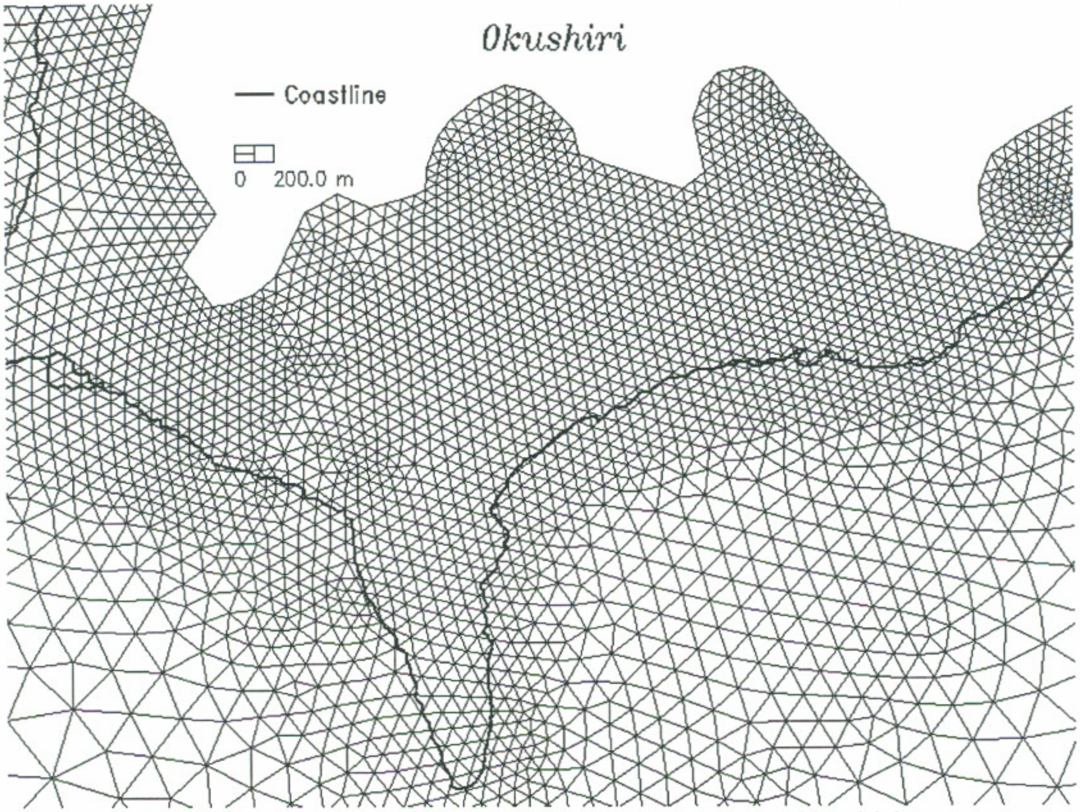

Figure 4.4b Medium finite element grid spacing in southern Okushiri.

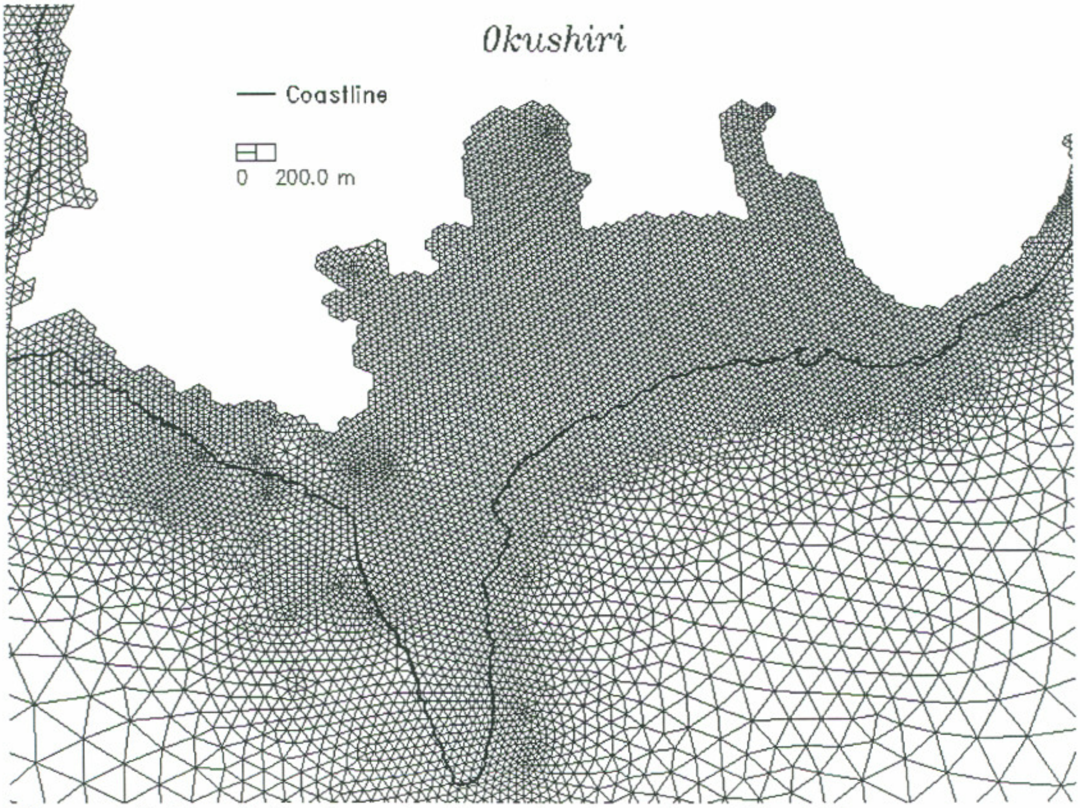

Figure 4.4c Fine finite element grid spacing in southern Okushiri.

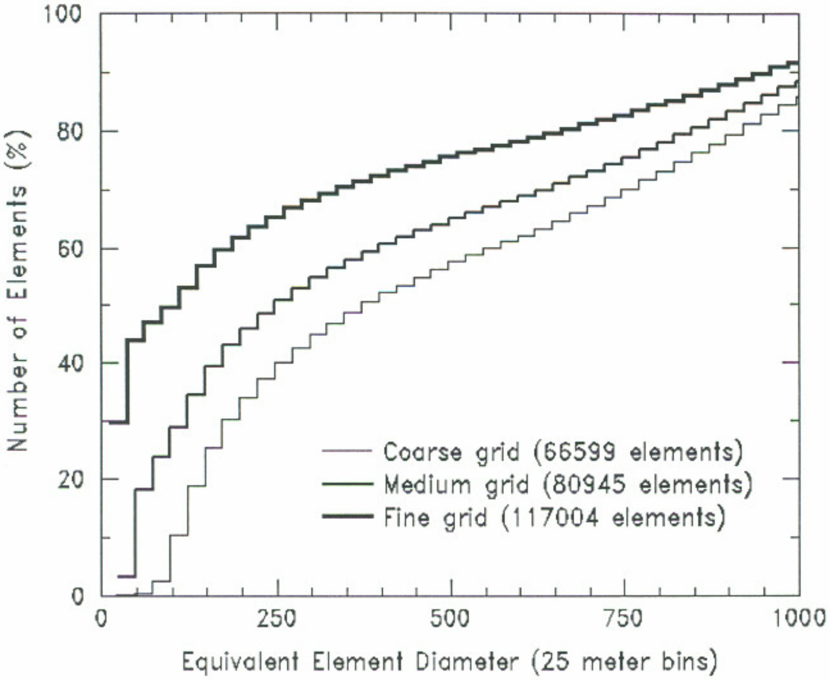

Figure 4.5 Histogram of grid refinement for the three finite element grids.

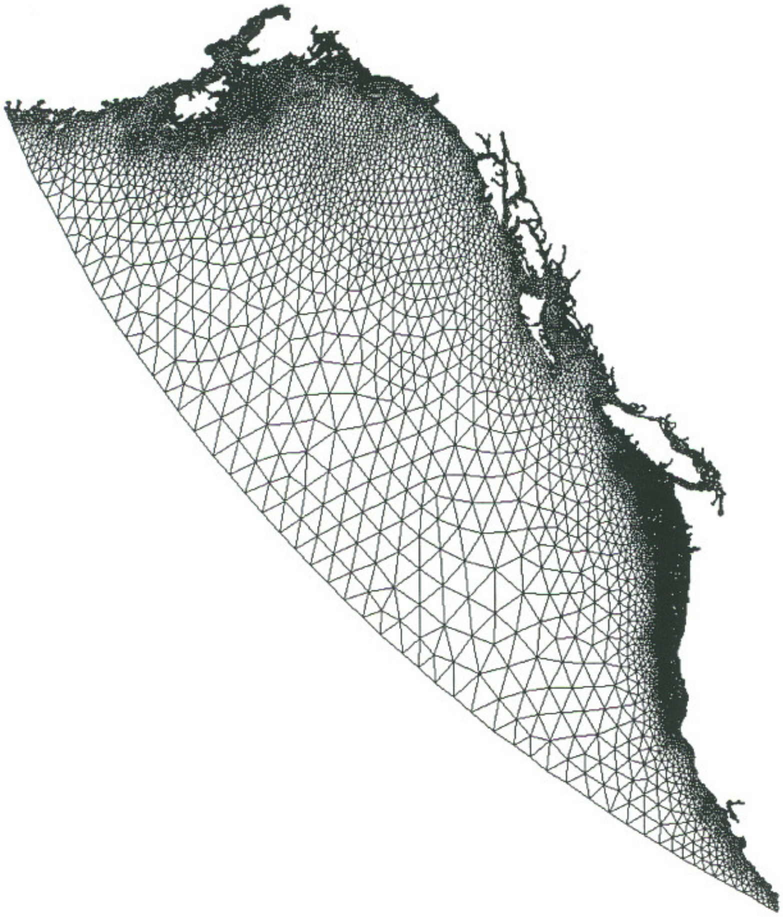

Figure 4.6a Coarse finite element grid used for the Alaska simulations.

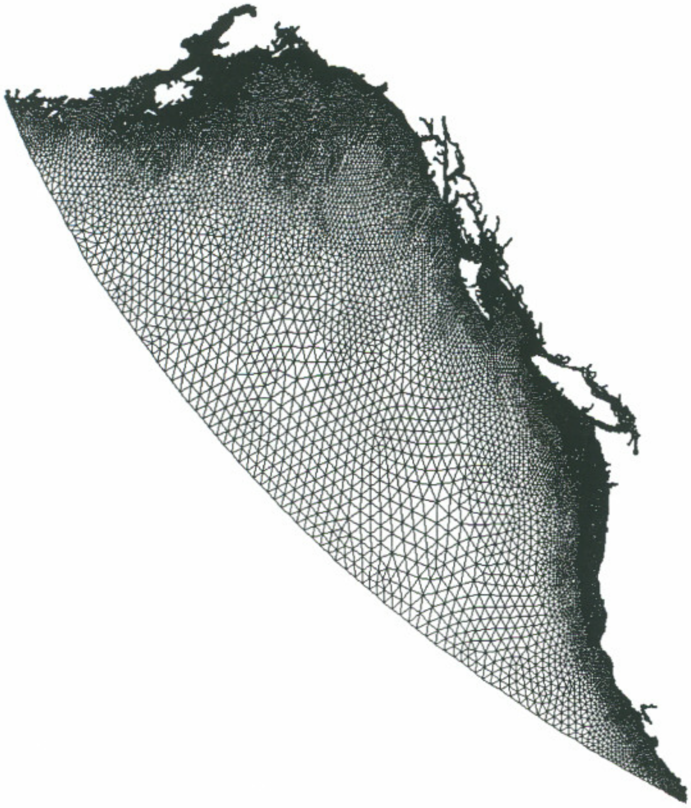

Figure 4.6b Medium finite element grid used for the Alaska simulations.

Figure 4.6c Fine finite element grid used for the Alaska simulations.

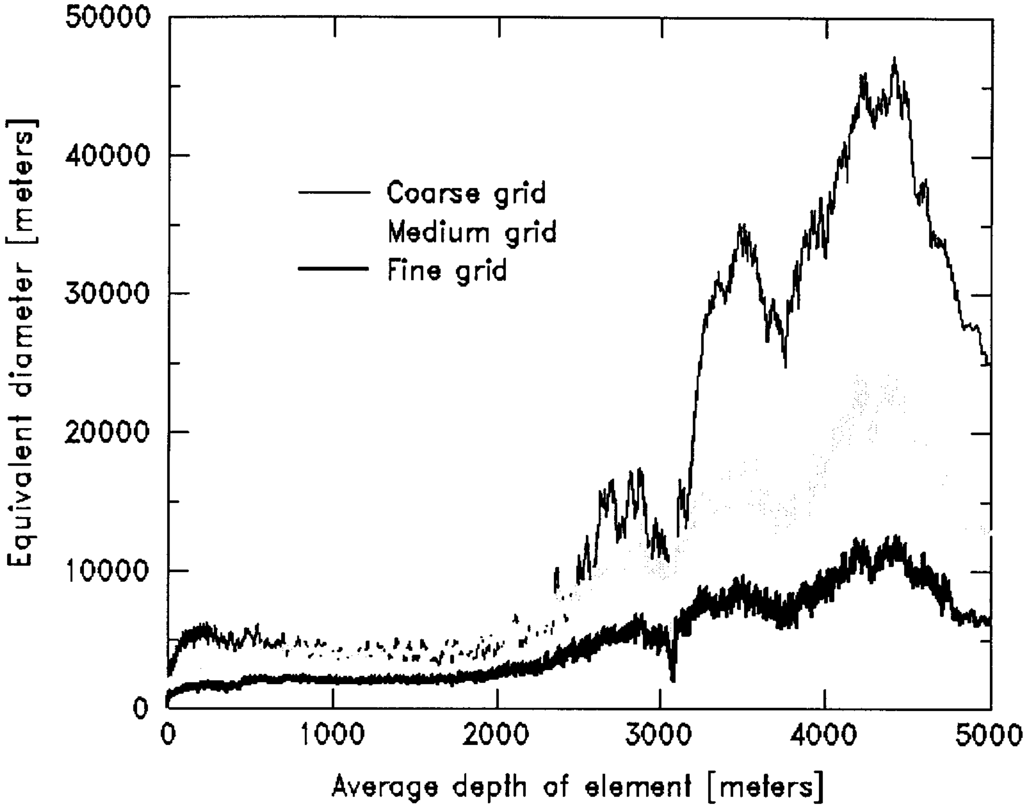

Figure 4.7 Grid refinement as a function of depth for the Alaska grids.

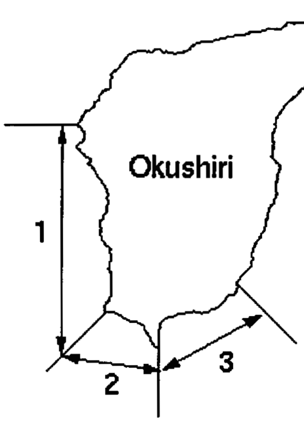

Figure 4.8a Coastline segments along Okushiri for results in 8b.

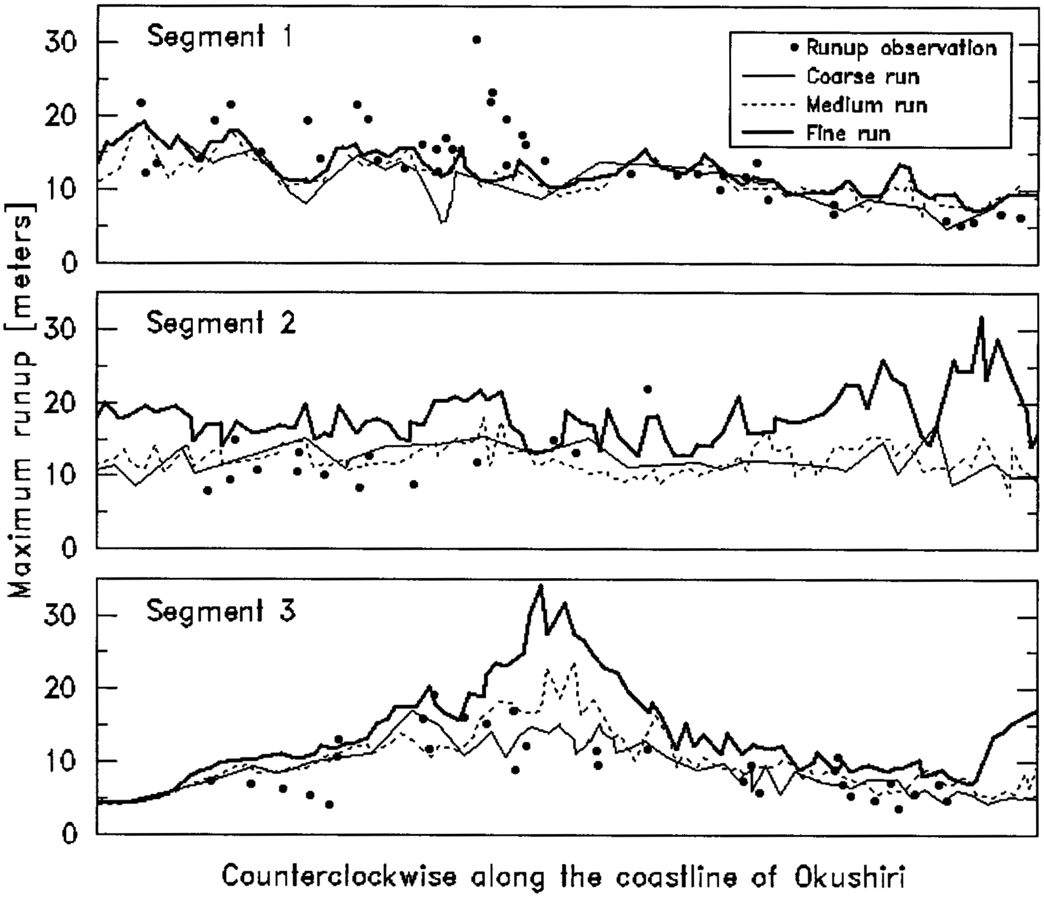

Figure 4.8b Computed and observed runups along the three coastline segments shown in 8a.

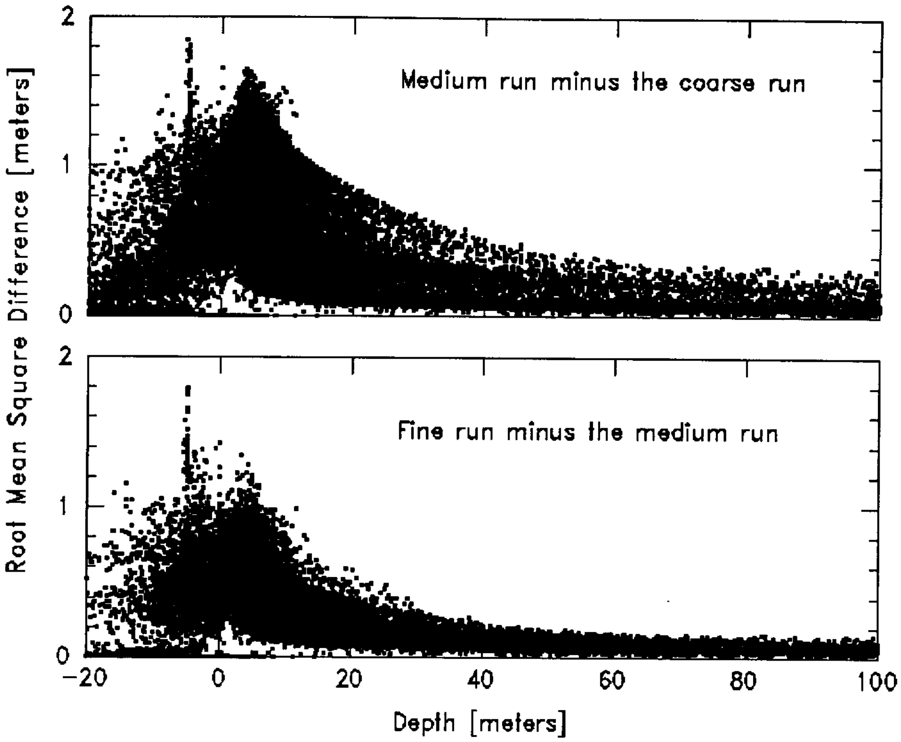

Figure 4.9 Nodal RMS elevation differences between the medium and coarse runs and between the fine and medium runs.

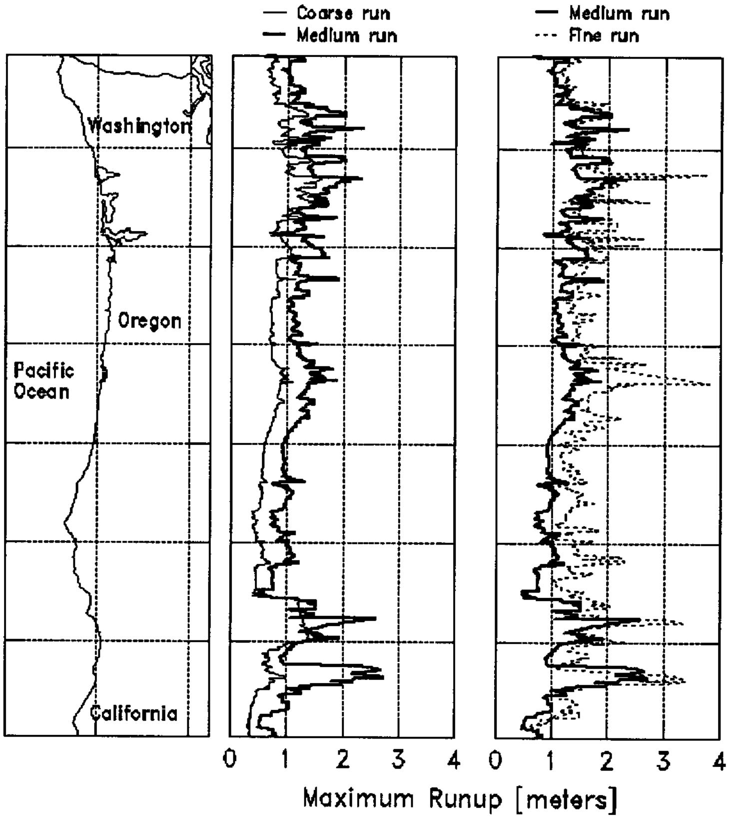

Figure 4.10 Computed runups for the 1964 Alaska tsunami along the Washington, Oregon, and northern California coastlines.

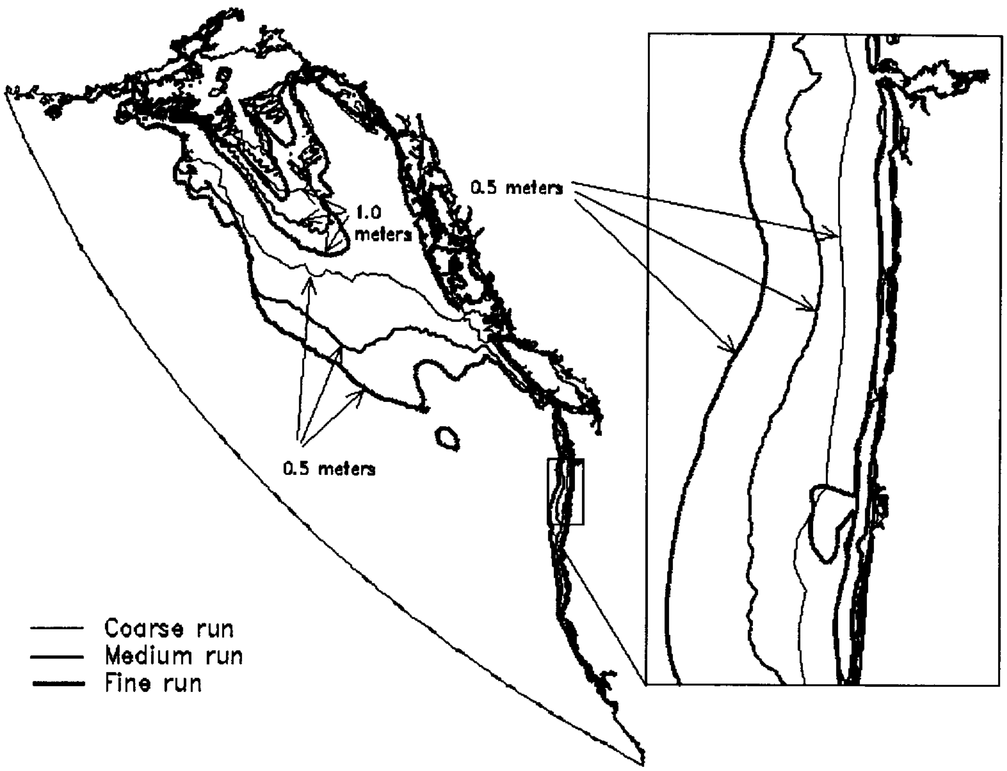

Figure 4.11 Isolines of maximum elevation for the Alaska simulations on different grids.

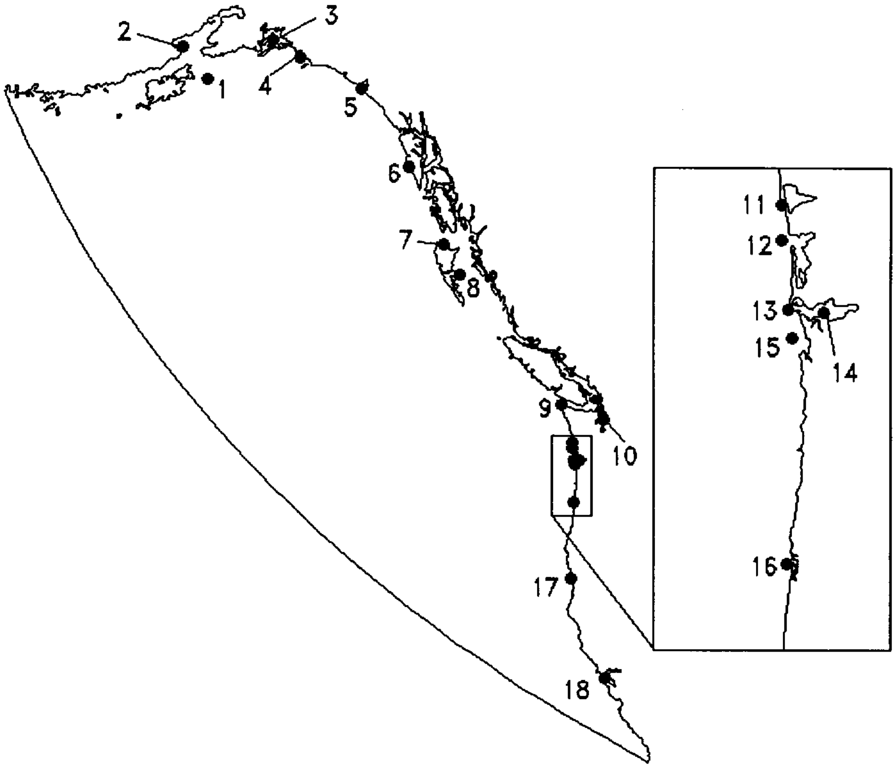

Figure 4.12a Station locations for results presented in 12b-c.

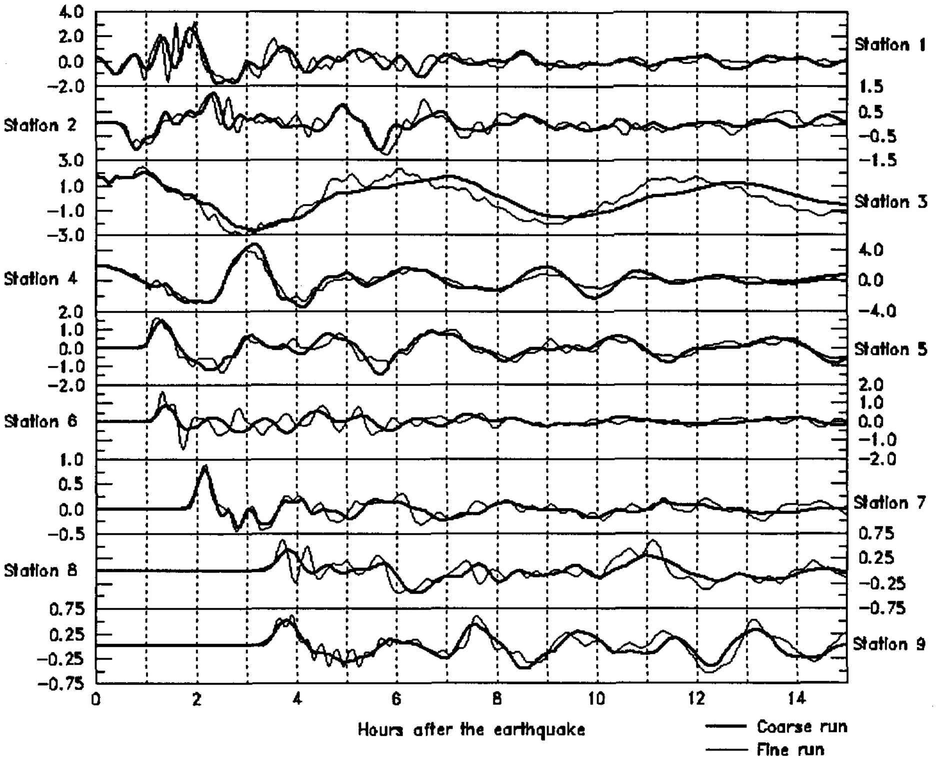

Figure 4.12b Comparison of elevation time histories computed on the fine and coarse grids for stations 1-9.

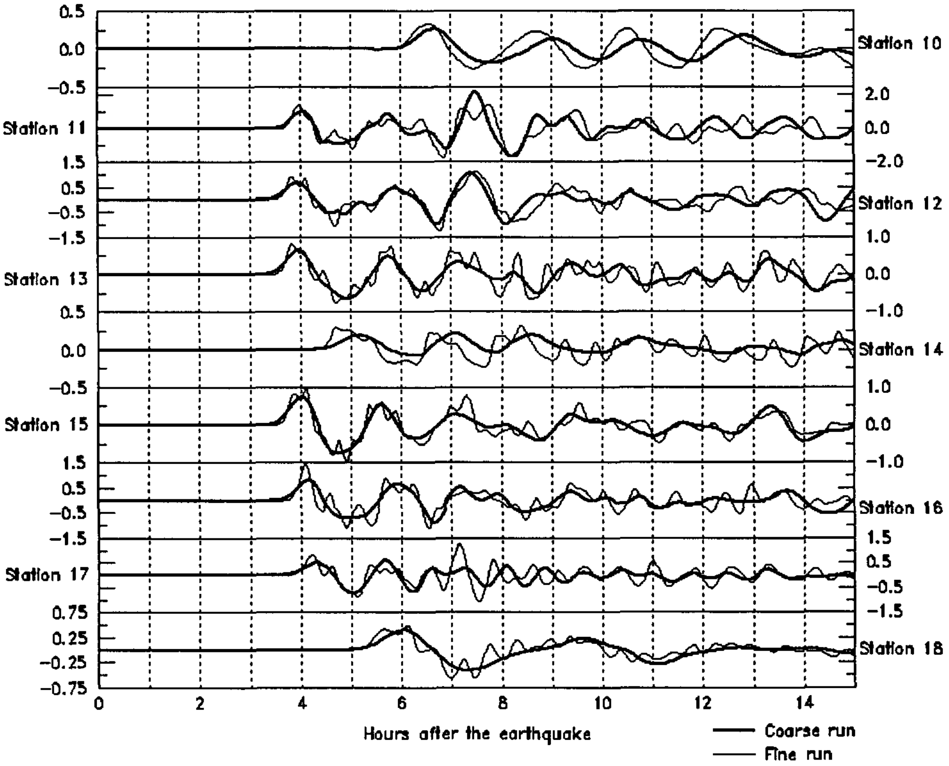

Figure 4.12c Comparison of elevation time histories computed on the fine and coarse grids for stations 10-18.

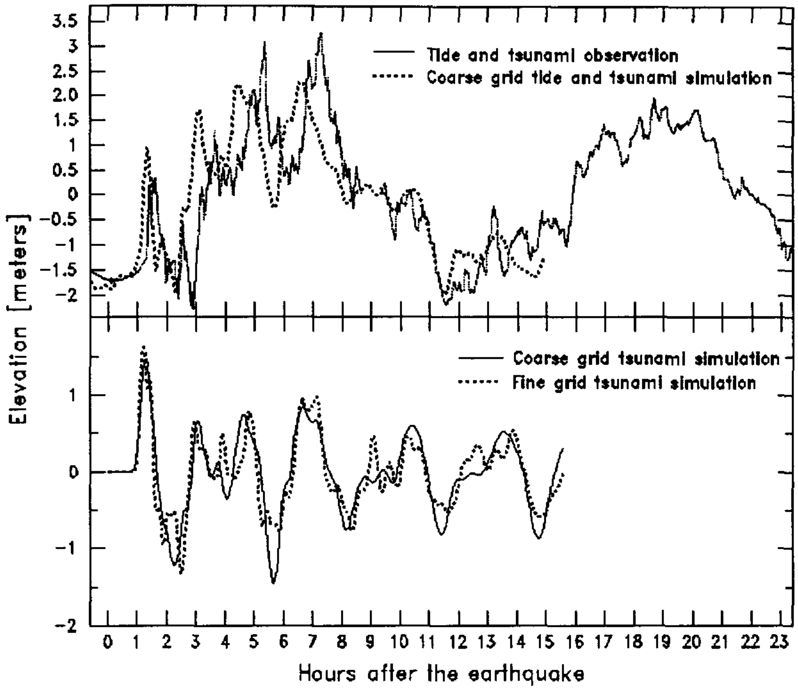

Figure 4.13a Modeled tide and tsunami elevations (from coarse grid) compared to tide gauge recordings at Yakutat, AL. Bottom graph shows fine and coarse grid computations of just the tsunami. Observations shown in 4.13a-f were extracted from the Committee on the Alaska Earthquake of the Division of Earth Sciences, National Research Council (1972) with permission from the National Academy of Sciences.

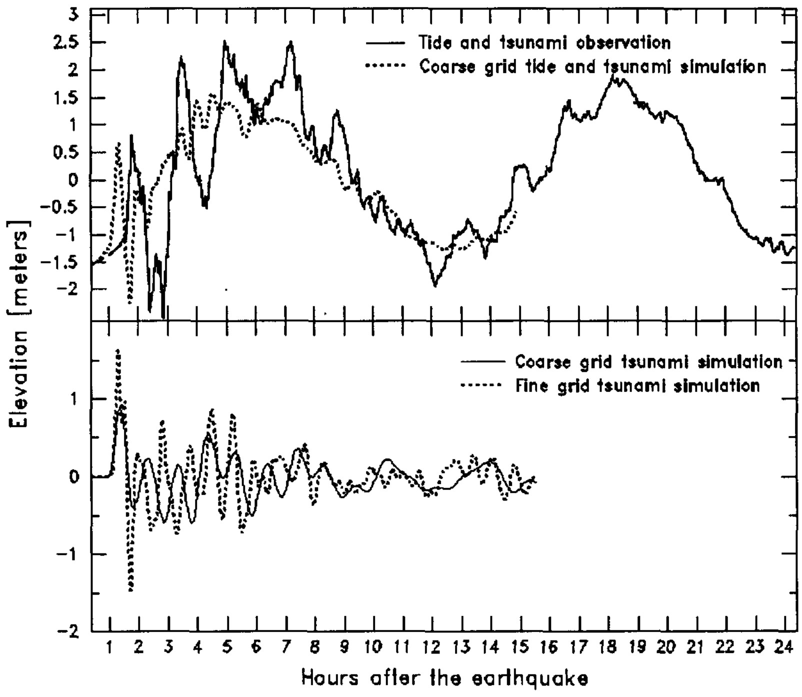

Figure 4.13b Modeled tide and tsunami elevations (from coarse grid) compared to tide gauge recordings at Sitka, AL. Bottom graph shows fine and coarse grid computations of just the tsunami.

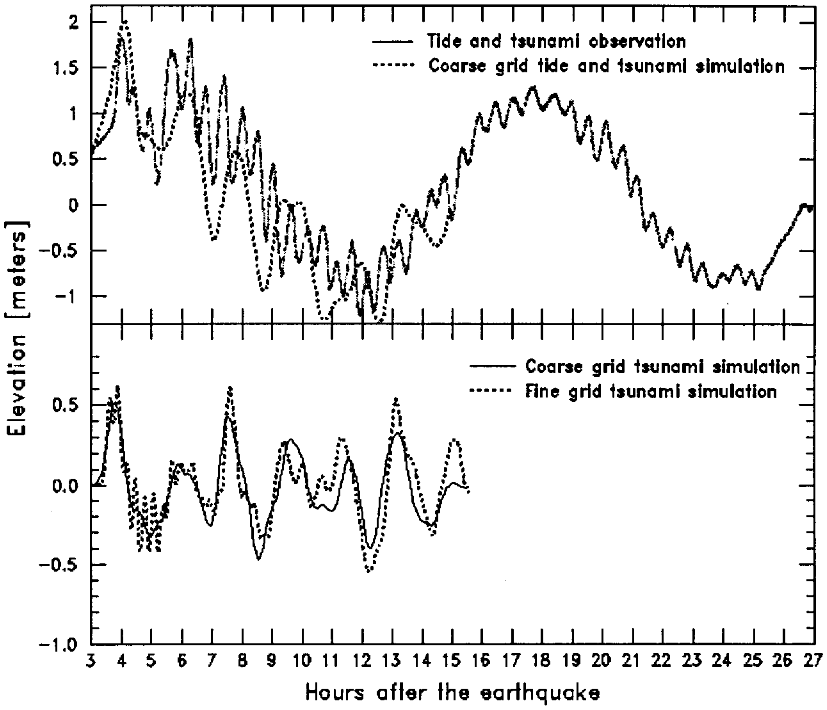

Figure 4.13c Modeled tide and tsunami elevations (from coarse grid) compared to tide gauge recordings at Neah Bay, WA. Bottom graph shows fine and coarse grid computations of just the tsunami.

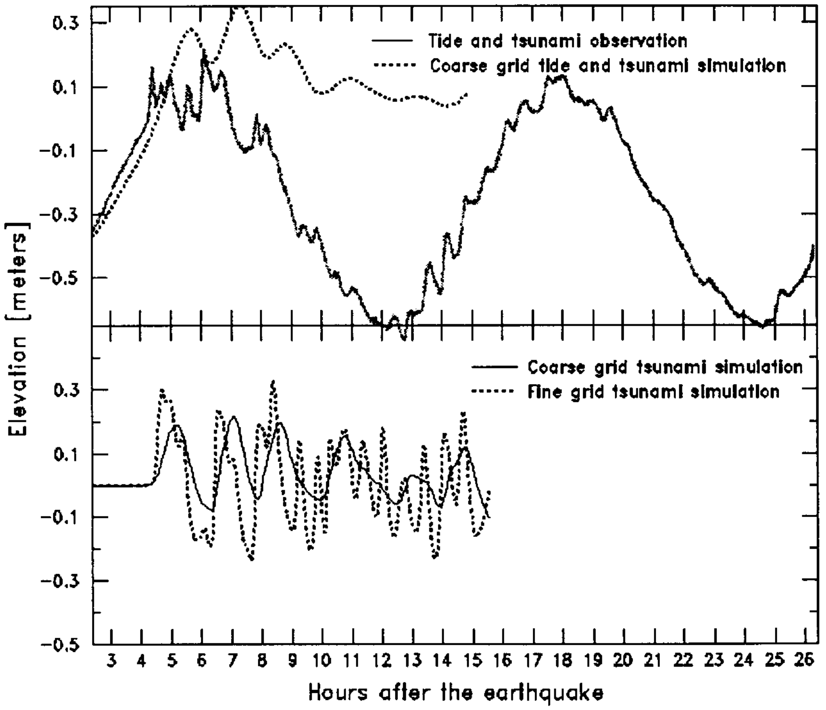

Figure 4.13d Modeled tide and tsunami elevations (from coarse grid) compared to tide gauge recordings at Astoria, OR. Bottom graph shows fine and coarse grid computations of just the tsunami.

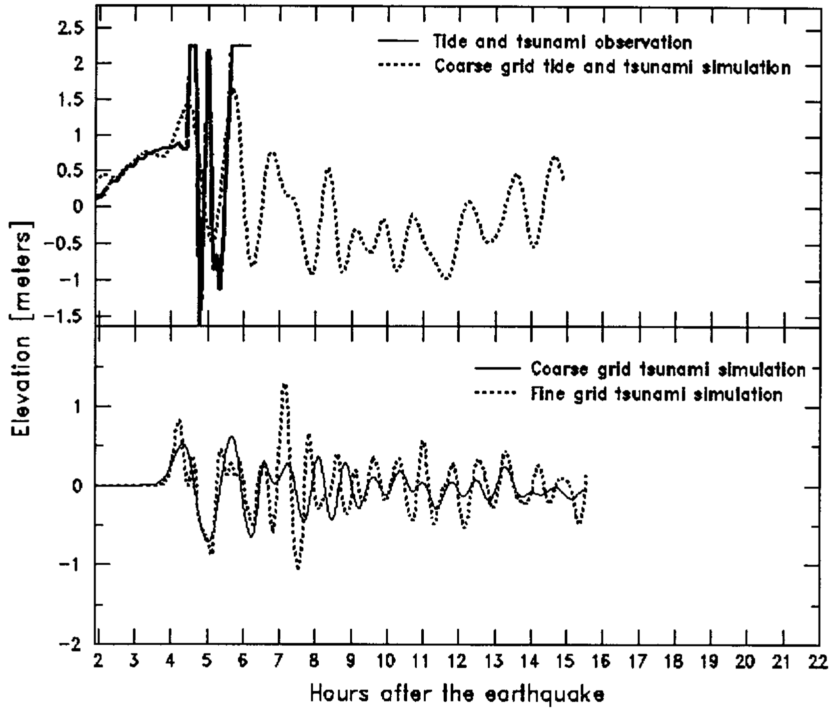

Figure 4.13e Modeled tide and tsunami elevations (from coarse grid) compared to tide gauge recordings at Crescent City, CA. Bottom graph shows fine and coarse grid computations of just the tsunami.

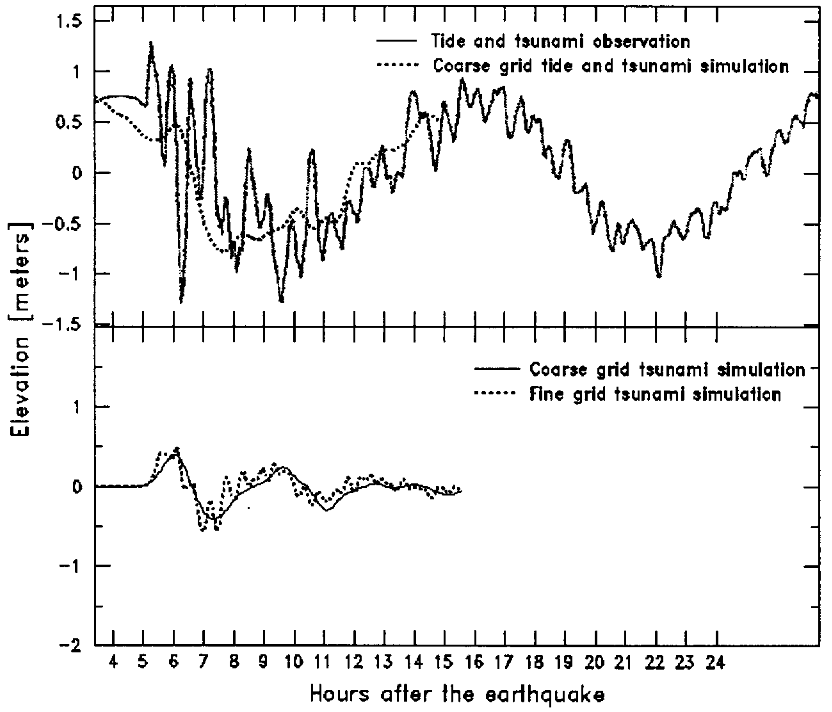

Figure 4.13f Modeled tide and tsunami elevations (from coarse grid) compared to tide gauge recordings at San Francisco, CA. Bottom graph shows fine and coarse grid computations of just the tsunami.

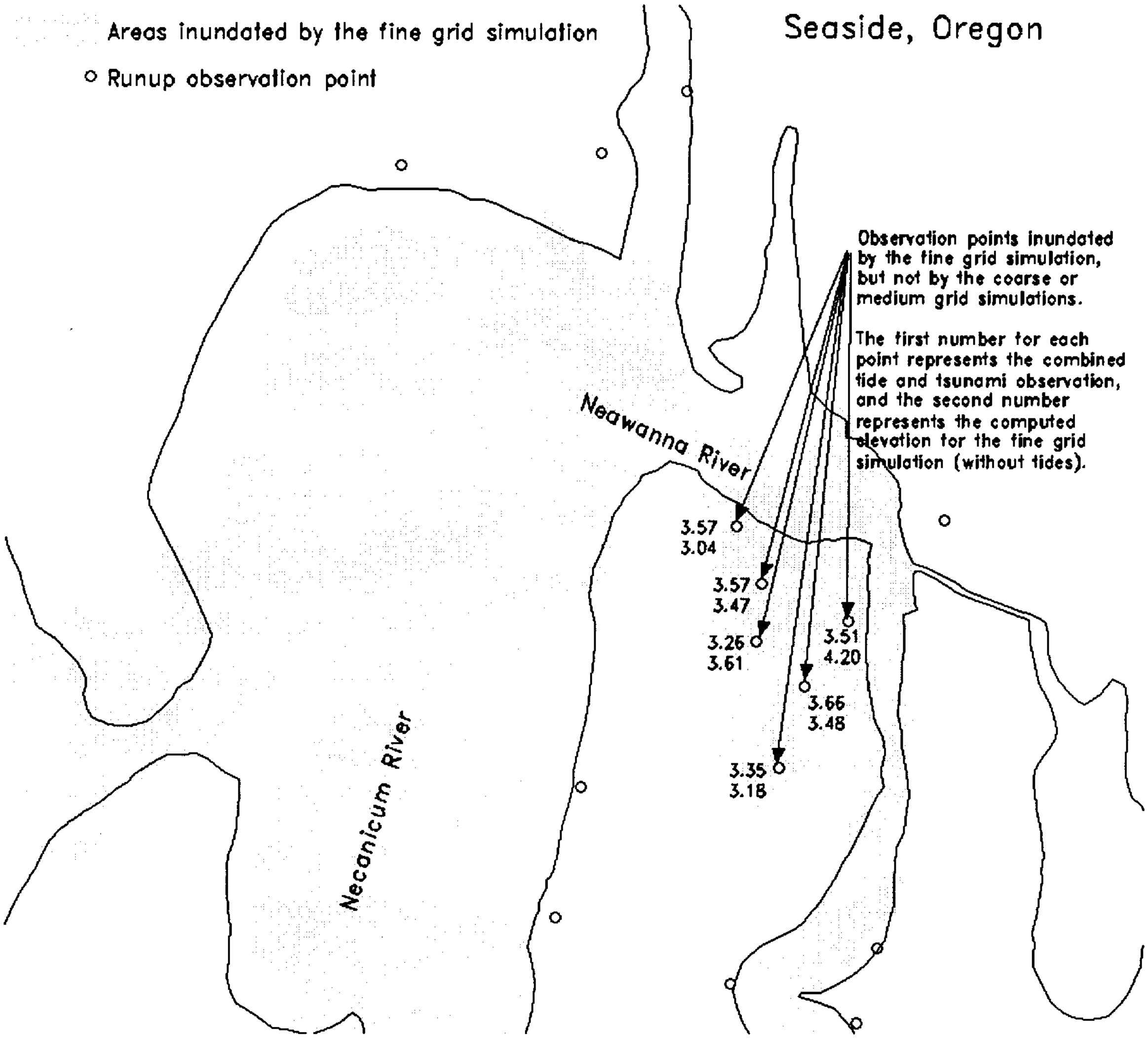

Figure 4.14 Fine grid inundation in Seaside, OR from the 1964 Alaska tsunami compared to runup observations.

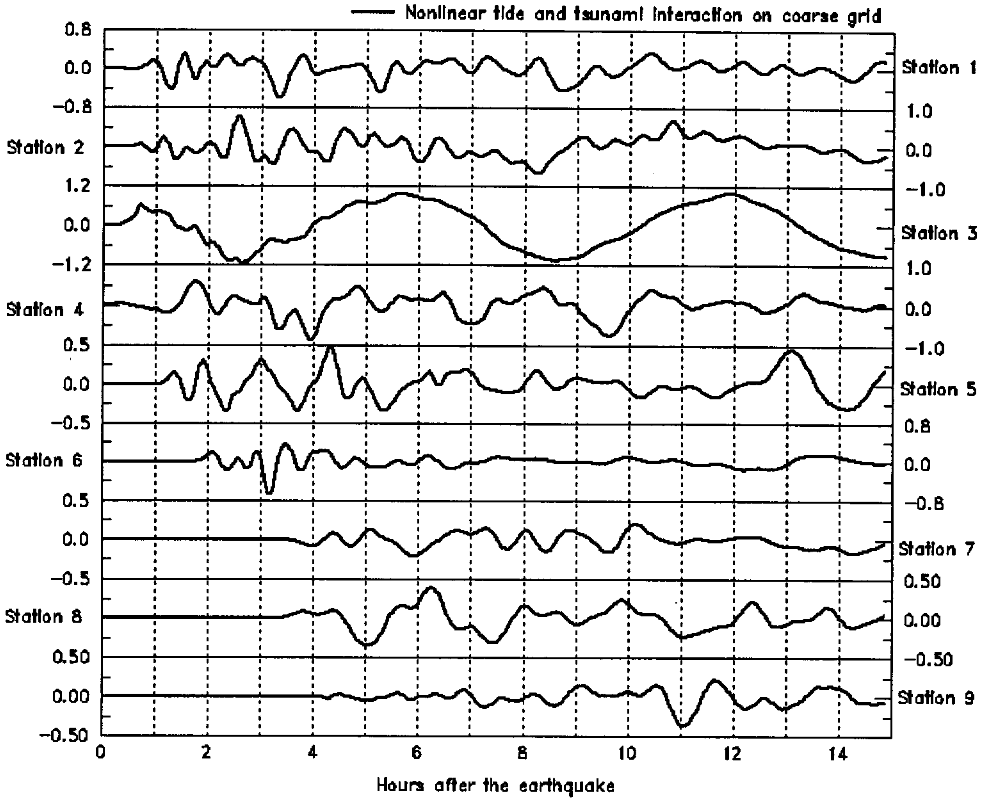

Figure 4.15a Nonlinear tide and tsunami interactions as time histories for stations 1-9.

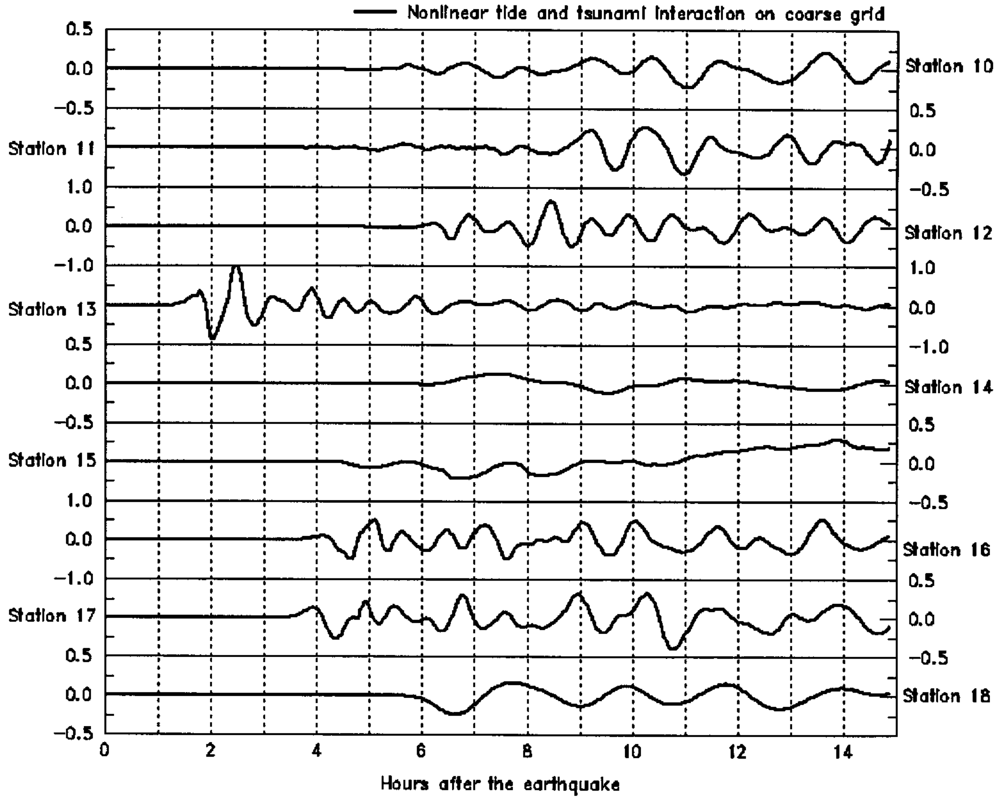

Figure 4.15b Nonlinear tide and tsunami interactions as time histories for stations 10-18.

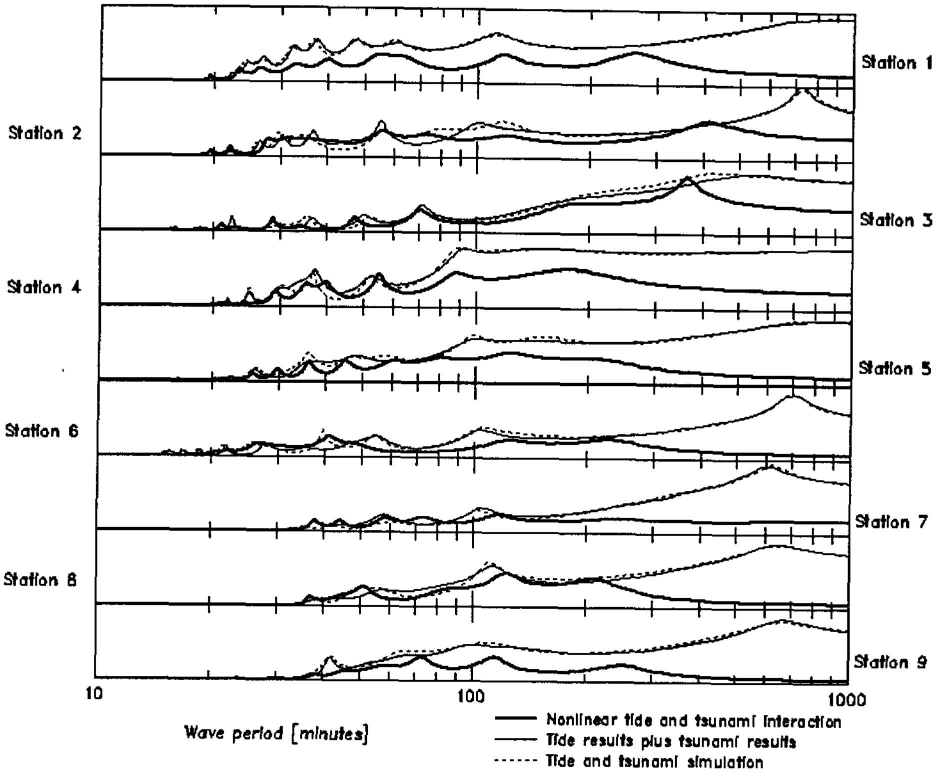

Figure 4.16a Power spectrum results showing the frequency differences associated with nonlinear tide and tsunami interactions at stations 1-9.

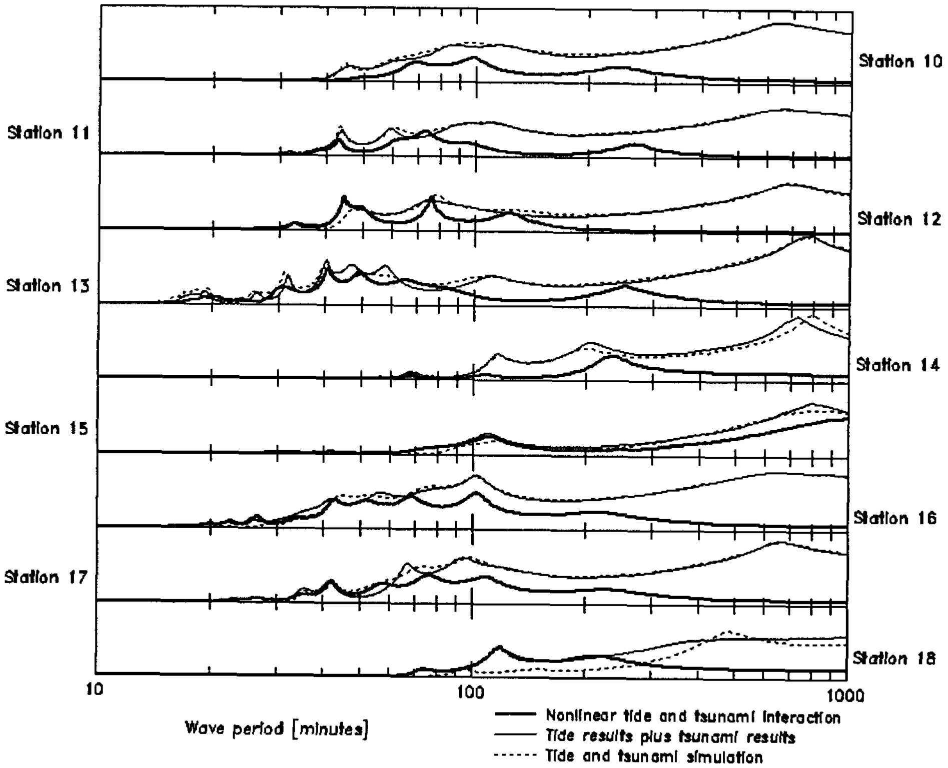

Figure 4.16b Power spectrum results showing the frequency differences associated with nonlinear tide and tsunami interactions at stations 10-18.

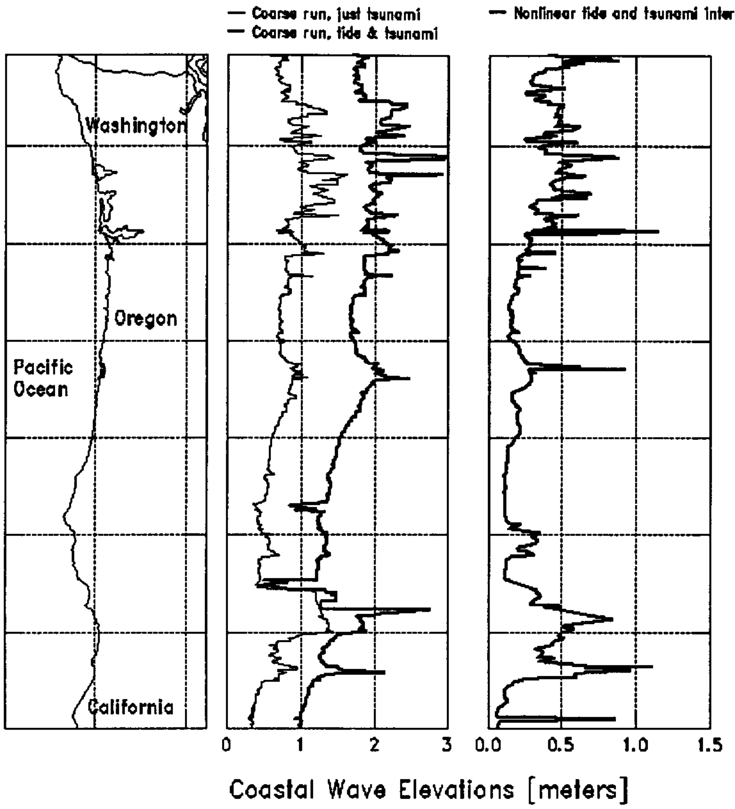

Figure 4.17 Influence of tidal interactions on computed coastal elevations along Washington, Oregon, and northern California.

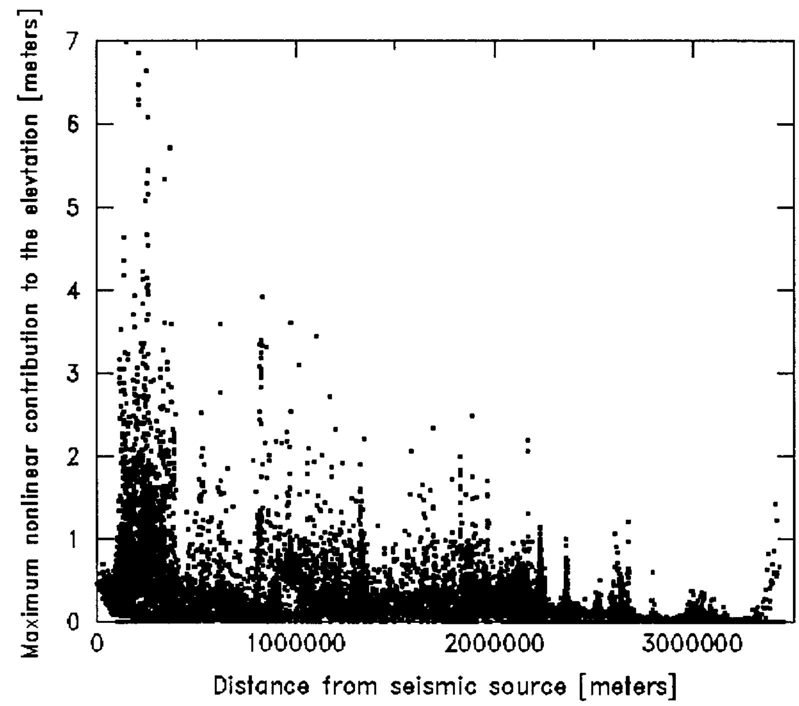

Figure 4.18 Maximum nonlinear differences as a function of distance from the Alaska seismic source.

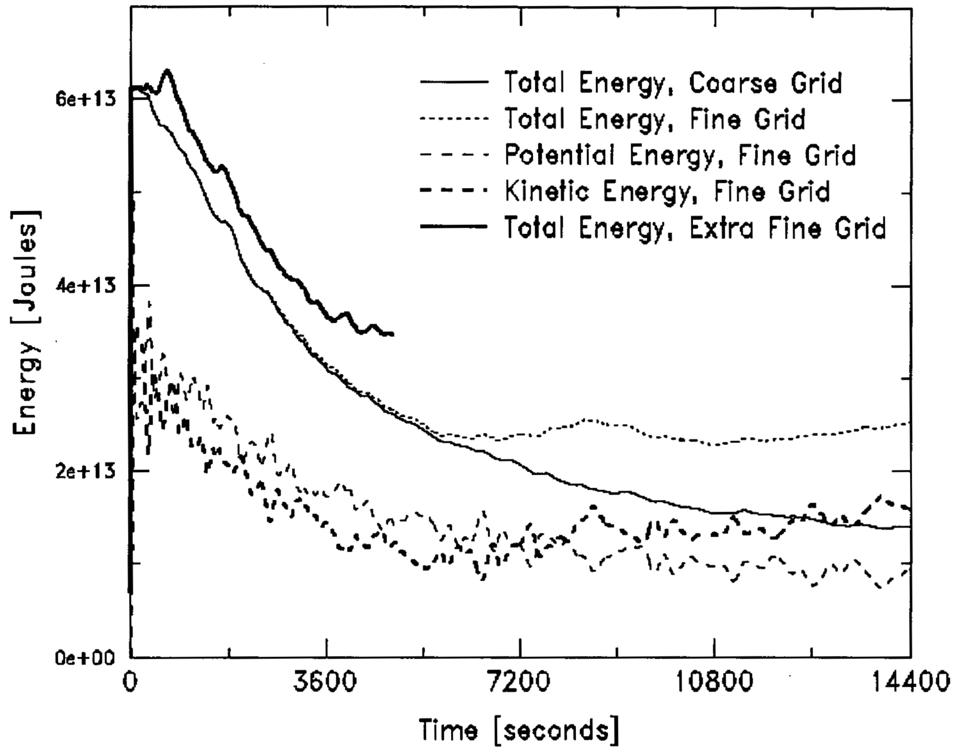

Figure 4.19 Energy loss in tsunami simulations of the 1993 Hokkaido Nansei-Oki event.

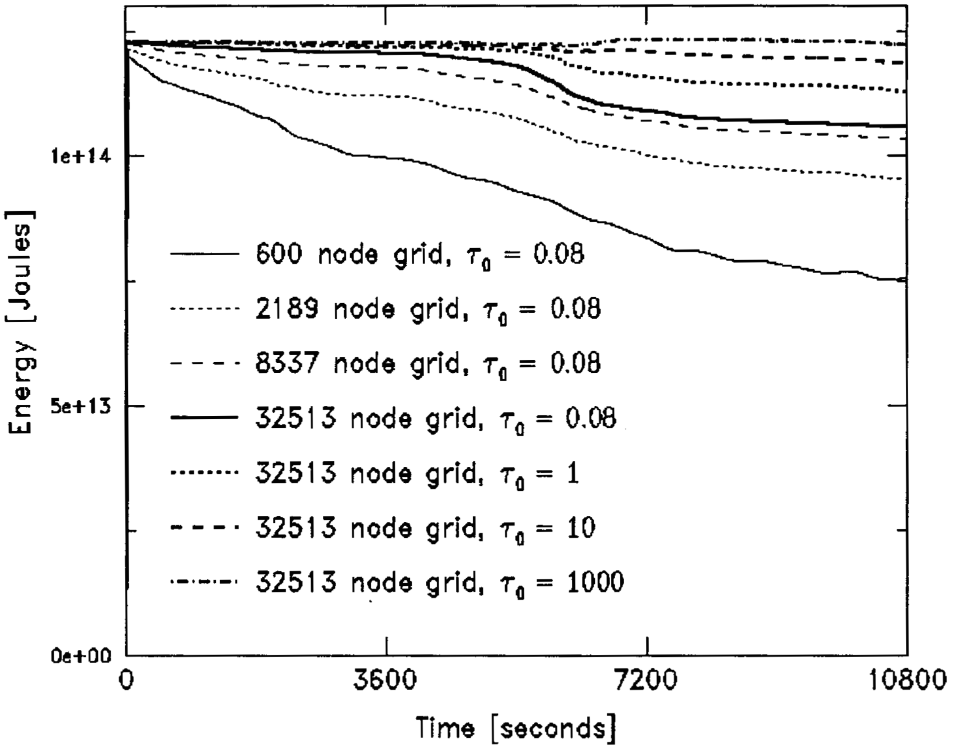

Figure 4.20 Energy variation in time for a synthetic channel grid simulation of a tsunami.

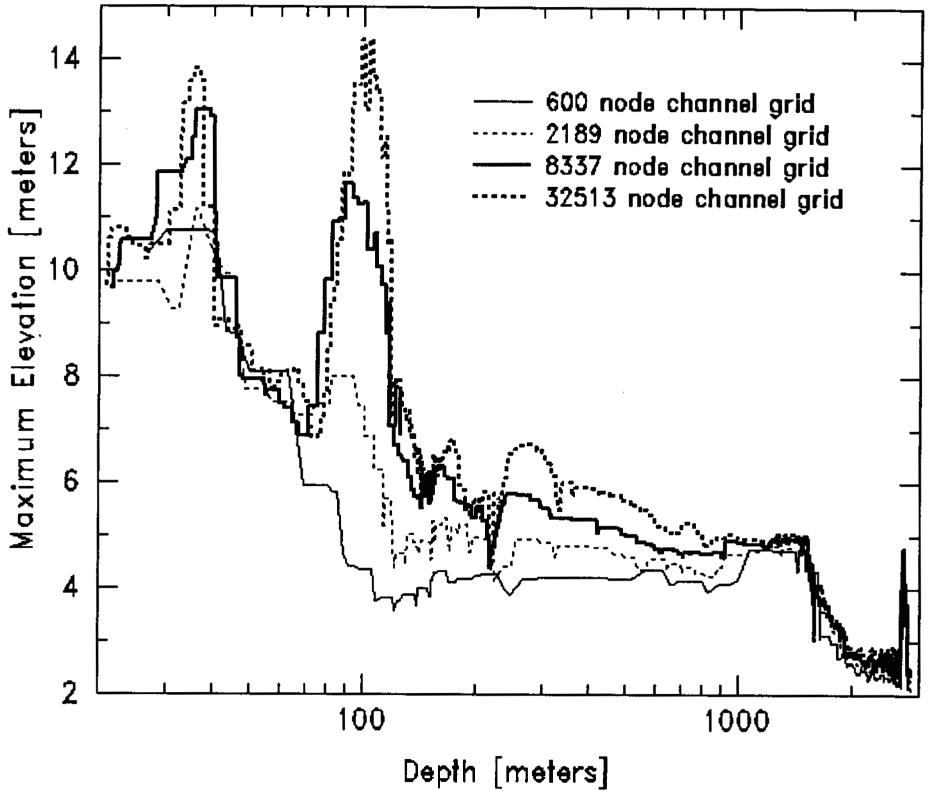

Figure 4.21 Influence of energy loss on maximum elevations in the channel grid simulations.

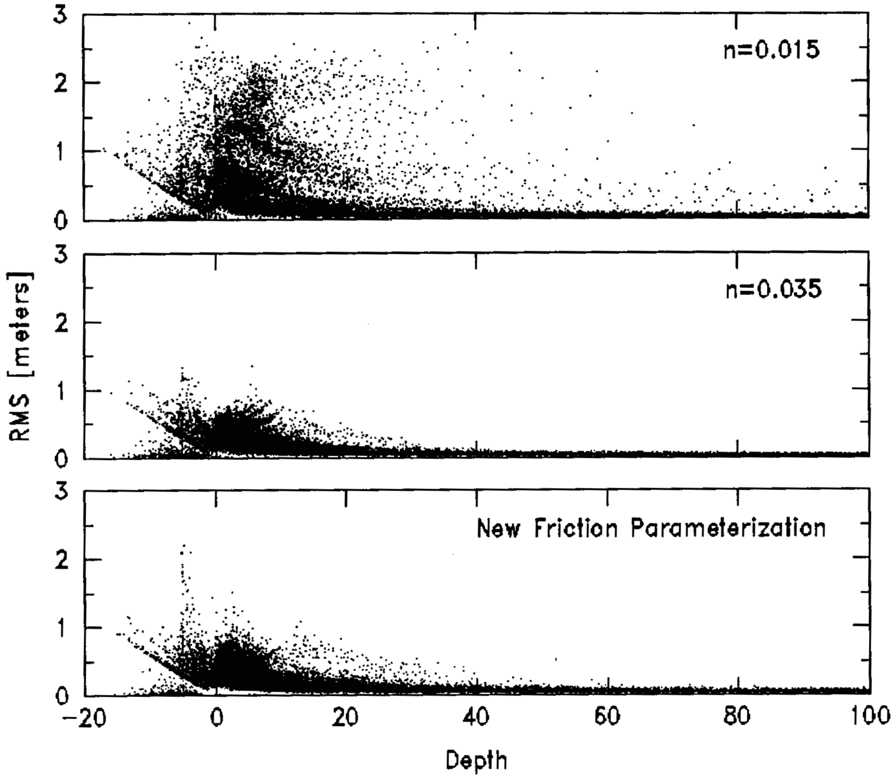

Figure 4.22 RMS differences between friction sensitivity simulations and the original Hokkaido Nansei-Oki tsunami simulation.

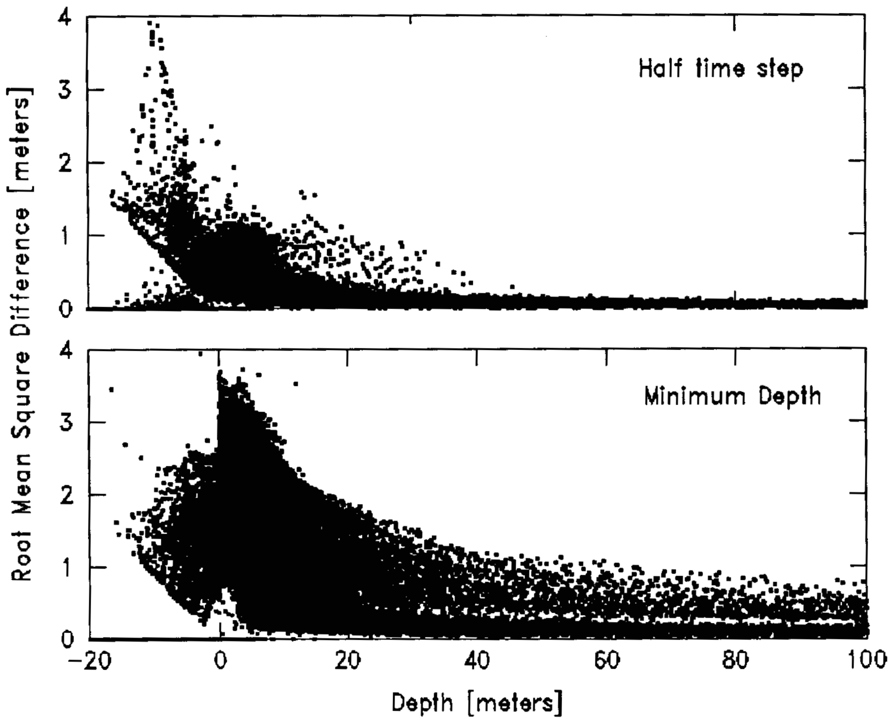

Figure 4.23 RMS differences between time step and minimum depth simulations and the original Hokkaido Nansei-Oki tsunami simulation.

CHAPTER 5

Numerical Considerations in Finite Element Simulations of Tsunamis

5.1 Introduction

Numerical simulations of tsunamis face the daunting task of dissecting sources of errors between model results and observations. This problem primarily arises due to the fact that it is presently difficult to validate whether initial conditions are defined properly. Initial conditions for tsunami simulations are derived from the deformation to the floor of the ocean resulting from motion between crustal plates during a subduction earthquake. In order to ascertain what this ocean floor deformation is for a given earthquake, accurate bathymetry needs to be available for the relevant geographic area before and after the event. Such data sets are practically infeasible to collect, owing to the expense of bathymetric surveys, the accuracy needed to extract deformation patterns, and the uncertainty in forecasting where future events will occur.

Currently, tsunami simulations use initial conditions derived from deformation models of the fault plane motion and/or inversion techniques. As mentioned above, and as discussed by Myers and Baptista (1998a), there is still an abundance of uncertainty embedded within these computed deformations. Part of this uncertainty derives from the fact that the tsunami modeling process as a whole relies on several components, including the deformation model, seismic parameters, fault plane geometry, the hydrodynamic tsunami model, bathymetric/topographic data, and tsunami observational data. Each of these components individually carries its own uncertainties, which become amalgamated into the uncertainty of the final tsunami modeling results. Dissecting this conglomerated uncertainty into the component uncertainties proves to be a difficult process, particularly given that the initial conditions cannot be verified.

From a hazard mitigation vantage, numerical modeling of tsunamis can still serve as a useful tool for evaluating tsunami hazards in communities at risk of enduring such events. Yet from a scientific vantage, it is imperative to begin effectively quantifying errors and the sources of those errors in order to advance our understanding of the underlying physical processes. One way this may be done is to isolate each of the components and analyze their respective errors. Myers and Baptista (1998a) addressed some of the sources of errors in the hydrodynamic modeling component used to simulate the propagation and inundation of tsunami waves. The study presented here further explores the nature of errors produced by the hydrodynamic numerical model and investigates ideas that would help ameliorate such conditions.

Two governing principles serve as the roots for the investigation here. The first root originates from the notion that, once the tsunami waves have been generated within the model, the energy in those waves should be preserved throughout the length of the simulation. The second root looks at the minimization of differences between the numerical model's representation of the partial differential equations (PDEs) of mass and momentum preservation and the PDEs in their original form, such differences representing the truncation errors of the model. Thus, ideally the energy of the tsunami waves should be preserved and the truncation errors minimized. As will be shown in this analysis, though, these roots are not always efficiently upheld. The culprits of their weakening will be evaluated in a manner that will help identify how to correct them.

The next two sections address the approaches used to compute energy errors and truncation errors. A channel test case is then introduced as a mechanism for evaluating the nature of these errors in tsunami simulations. Finally, results from the test case are analyzed, corrective measures are investigated, and appropriate conclusions are made.

5.2 Energy Errors

Once the energy of the earthquake is transmitted to the water in the form of tsunami waves, that energy should remain constant with the exception of losses due to friction and diffusion. In this study, the test case considered will be frictionless and without diffusion. Therefore, only the potential and kinetic components of the energy need to be evaluated here. The potential energy (E_p) and kinetic energy (E_k) of the tsunami waves at a point in time and space are evaluated as:

$$E_p = \frac{1}{2}\rho g \eta^2 \tag{1}$$

$$E_k = \frac{1}{2}\rho H\left(u^2 + v^2\right) \tag{2}$$

where ρ is the density of the water, g is the gravitational acceleration, η is the water elevation, H is the water column height, and (u, v) are depth-averaged velocities.

The total tsunami energy throughout a spatial domain, E_T, can be calculated by integrating E_p and E_k over the domain Ω,

$$E_T = \frac{1}{2}\rho g \int_\Omega \eta^2 d\Omega + \frac{1}{2}\rho \int_\Omega H\left(u^2 + v^2\right) d\Omega \tag{3}$$

E_T should remain constant once the ocean floor motion has finished generating the initial tsunami waves. As will be shown, this is not always the case. Since E_T only provides a measure of the energy of all the waves in a spatial domain, a different measure is needed to assess where these energy errors are originating. Such a control measure can be derived by applying the finite element method (FEM) to an equation representing the residual. The residual is defined here to be the change in total energy over one time step at a point in space,

$$\frac{dE_T}{dt} = \frac{E_T^n - E_T^{n-1}}{\Delta t} \tag{4}$$

where n is the current time step, n-1 is the previous time step, and Δt is the time step. Thus, applying the FEM to this residual using Galerkin weighting functions leads to the following,

$$\int_{\Omega}\left(\frac{E_T^n - E_T^{n-1}}{\Delta t}\right)\varphi_j d\Omega = 0 \quad j = 1, NP \tag{5}$$

where NP is the number of nodes in the finite element grid and φ_j is the weighting function for node j. Since the FEM involves integrating over the spatial domain, the change in energy over one time step is being integrated in a global sense. This is ideal, considering that we would like the global integration of the energy change to ideally be zero. The FEM inclusion of a weighting function multiplication factor can provide a measure of a single node's contribution to the global energy error.

The finite element model used in this research, ADCIRC (Luettich et al., 1991), is formulated from the two-dimensional, depth-averaged shallow water equations. It uses a generalized wave continuity equation (GWCE) to solve for elevations and the non-conservative form of the momentum equations to solve for depth-averaged velocities. Most hydrodynamic numerical models use this general approach of solving one equation representing the conservation of mass and another equation representing the conservation of momentum. Thus, such models do not strictly enforce conservation of energy. If energy were conserved, then the above equation applying the FEM to the energy change per time step would in fact be equal to zero, as is stated on the right-hand side (RHS) of the equation. However, instead of trying to enforce this equation, simply evaluating the RHS will provide a measure of the nodal energy error. The elevations and velocities solved for by ADCIRC at the two time steps can therefore be used to compute the nodal energy error per time step, ε_j^n,

$$\varepsilon_j^n = \int_{\Omega}\left(\frac{E_T^n - E_T^{n-1}}{\Delta t}\right)\varphi_j d\Omega = \int_{\Omega}\left(\frac{E_p^n - E_p^{n-1}}{\Delta t}\right)\varphi_j d\Omega + \int_{\Omega}\left(\frac{E_k^n - E_k^{n-1}}{\Delta t}\right)\varphi_j d\Omega \tag{6}$$

The results pertaining to energy errors are therefore presented using the above relation. One of the conveniences of this nodal energy error formulation is that the sum of the nodal errors at each time step is equal to the global change in energy:

$$\sum_{j=1}^{NP}\varepsilon_j^n = \frac{dE_T}{dt} \tag{7}$$

5.3 Truncation Errors

Hirt (1968) presented a method by which to evaluate the stability of finite difference solutions of partial differential equations. The method involves expanding the differential equation's terms in a Taylor series and subtracting off the continuous form of the equation. What remains is the truncation error, which can serve as a measure of the computational stability of a numerical scheme.

Truncation error analysis has been extensively used to help guide grid refinement schemes, including examinations of atmospheric models (Skamarack, 1989), elliptic grid generation problems (Knupp and Luczak, 1995), and tsunami simulations (Imamura and Goto, 1988). The latter of these studies is most relevant to the research presented here, as it focused on the nature of truncation errors in finite difference modeling of tsunamis. Imamura and Goto examined these errors in a linear, one-dimensional formulation of the shallow water equations. They showed that the truncation error plays a prominent role in affecting the numerical dissipation of tsunami simulations, the extent of which depends on the frequencies of the tsunami waves and the distance those waves have traveled.

Hagen and Westerink (1995, 1996) investigated truncation errors in linear, one-dimensional finite element simulations. They showed that such analysis could be utilized as a more appropriate controlling factor in grid generation than the dimensionless wavelength criteria. The research presented here explores the behavior of truncation errors in the two-dimensional, fully nonlinear shallow water equations of a similar finite element model. Since tsunamis consist of vast amounts of energy distributed among a wide range of frequencies, nonlinearities play a significant role in determining the manner in which this energy is redistributed among the many frequencies. Thus, these tsunami simulations will prove to be an ideal test case for investigating truncation errors from a two-dimensional, nonlinear vantage.

For the purposes of this study, the finite element grids used are set up in a manner that facilitates efficient expansion of terms in a Taylor series. They consist of regularly spaced elements in both the x and y directions, every node of which is surrounded by the same configuration of elements portrayed in Figure 5.1. Nodal truncation errors are also only computed for the generalized wave continuity equation (GWCE), the equation ADCIRC uses to solve for elevations. This is done because results from tsunami simulations are generally most significant in terms of the elevation patterns which develop and because the GWCE is the more sensitive of the equations used by ADCIRC. The GWCE, shown below, is formed by adding the time derivative of the continuity equation, the primitive continuity equation weighted by a factor, and the spatial gradient of the conservative momentum equations,

$$\begin{aligned} &\frac{\partial^2\eta}{\partial t^2}+\tau_0\frac{\partial\eta}{\partial t}-\frac{\partial^2\gamma}{\partial t^2}-\tau_0\frac{\partial\gamma}{\partial t}+ \\ &\frac{\partial}{\partial x}\left(u\frac{\partial\eta}{\partial t}-uH\frac{\partial u}{\partial x}-vH\frac{\partial u}{\partial y}+fvH-gH\frac{\partial\eta}{\partial x}-c_f u\sqrt{u^2+v^2}+\tau_0 uH\right)+ \\ &\frac{\partial}{\partial y}\left(v\frac{\partial\eta}{\partial t}-uH\frac{\partial v}{\partial x}-vH\frac{\partial v}{\partial y}-fuH-gH\frac{\partial\eta}{\partial y}-c_f v\sqrt{u^2+v^2}+\tau_0 vH\right)=0 \end{aligned} \tag{8}$$

where η is the free surface elevation, u and v are the depth-averaged velocities, H is the total water column, τ_0 is a weighting factor, γ is the bottom deformation (positive for uplift), f is the Coriolis factor, c_f is the bottom friction coefficient, and g is the acceleration due to gravity.

The first step in the truncation error analysis is therefore to compute the weighted residual statement for the GWCE for a typical interior node as shown in the center of Figure 5.1. For example, after multiplying the time-discretized GWCE through by Δt^2, one of the contributions to the GWCE weighted residual statement from the first term in the above equation will look like:

$$\sum_{el=1}^{6}\sum_{j=1}^{3}\eta_j^{n+1}\int_{A_{el}}\varphi_i\varphi_j\,dA_{el}=\frac{A_{el}}{6}\left(\sum_{j=1}^{6}\eta_j^{n+1}+A_{el}\eta_i^{n+1}\right) \tag{9}$$

where φ_i is the weighting function for the interior node of interest, φ_j is the j^th^ shape function, j=1, 3 nodes for each element, el=1,6 elements surrounding the interior node, and A_{el} is the element area. Each of the GWCE terms is expanded in a similar manner. Since i represents the interior node of interest, each of the surrounding j nodes are next expanded in a Taylor series around node i in order to evaluate the numerical expression of the GWCE at the interior node. Nodes 2 and 5 are expanded in a Taylor series in a different manner than the other surrounding nodes. For example, terms for node 2 are evaluated as one half being expanded around node 3 and the other half being expanded around node 1. These new one-half terms are then expanded around the interior node. Individual variables in nonlinear terms are first expanded in a Taylor series before being multiplied. For example, a UH term would have U expanded and H expanded, with the resulting expanded expressions then being multiplied by each other. All 0-5th order derivatives were kept in this expansion and subsequently grouped based upon the orders of the terms. To continue the example above, the term from the last equation would, after Taylor series expansion, look like:

$$\frac{A_{el}}{6}\left[\begin{array}{l} 3\left(\eta_j+\frac{\Delta x^2}{2}\frac{\partial^2\eta_i}{\partial x^2}+\frac{\Delta x^4}{24}\frac{\partial^4\eta_i}{\partial x^4}\right)+3\left(\eta_i+\frac{\Delta y^2}{2}\frac{\partial^2\eta_i}{\partial y^2}+\frac{\Delta y^4}{24}\frac{\partial^4\eta_i}{\partial y^4}\right)+\Delta y\Delta x\frac{\partial^2\eta_i}{\partial x\partial y}+\frac{\Delta x^3\Delta y}{6}\frac{\partial^4\eta_i}{\partial x^3\partial y} \\ +\frac{\Delta y^2}{2}\frac{\partial^2\eta_i}{\partial y^2}+\frac{\Delta x^2\Delta y^2}{4}\frac{\partial^2\eta_i}{\partial x^2\partial y^2}+\frac{\Delta x\Delta y^3}{6}\frac{\partial^4\eta_i}{\partial x\partial y^3}+\frac{\Delta y^4}{24}\frac{\partial^4\eta_i}{\partial y^4}+\Delta x\Delta y\frac{\partial^2\eta_i}{\partial x\partial y}+\Delta x\Delta y^3\frac{\partial^4\eta_i}{\partial x\partial y^3} \\ +\frac{\Delta x^2}{2}\frac{\partial^2\eta_i}{\partial x^2}+\frac{\Delta x^2\Delta y^2}{4}\frac{\partial^2\eta_i}{\partial x^2\partial y^2}+\frac{\Delta x^3\Delta y}{6}\frac{\partial^4\eta_i}{\partial x^3\partial y}+\frac{\Delta x^4}{24}\frac{\partial^4\eta_i}{\partial x^4} \end{array}\right] \qquad (10)$$

In this particular term expansion, the odd-ordered terms cancel each other out because of the assumed equal spacing in the grid, leaving just even-ordered terms. Many, but not all, of the other terms will also have their odd-ordered expansions cancel away. The terms that remain, however, are significant enough for the analyses in this study.

Finally, an expression equivalent to the continuous form of the GWCE is subtracted from the Taylor series expanded GWCE weighted residual statement, the remainder of which represents the truncation error of the finite element scheme for an interior node. Unfortunately, in two-dimensional nonlinear simulations of actual tsunami events, analytical solutions are not available. Therefore, as an approximation, the continuous form of the equations is estimated within ADCIRC for each point using the solutions for elevations and velocities at each time step. All derivatives in the continuous form as well as the Taylor series form of the GWCE are computed by means of polynomial expressions. Since derivatives up to the fifth order are desired, polynomials are evaluated by using values at seven points (the node of interest, and three nodes to each side of this node). Derivatives of the polynomials are subsequently evaluated from these expressions.

5.4 Channel Grid Case Study: Setup

This case study is designed to examine the effect of certain parameters on the propagation of tsunami waves in a realistic situation. One of these parameters is the grid spacing, and it is therefore necessary to consider a smaller domain to investigate the use of a wide range of grid spacings. A channel grid off the coast of northern Oregon was therefore selected, and bathymetry from this region is interpolated onto each of the grids. The ocean floor deformation which was assumed to generate the initial tsunami waves was derived for a study on finite element modeling of potential Cascadia subduction zone tsunamis (Myers and Baptista, 1998b). The deformation scenario was "1A" from that study, and was actually transposed further into the ocean for this study, to force the waves to travel further before reaching the coastline.

Figure 5.2 displays the bathymetry of the channel in this region as well as cross sections of both the bathymetry and the deformation through the center of the channel. The total length of the channel is approximately 545 km. The deepest portion of the domain is about 3,000 meters near the left boundary, and the shallowest region is around 20 meters near the right boundary. Therefore, this case does not consider situations where inundation is occurring, to avoid complicating matters. All the boundaries are considered no-flow land boundaries, so energy inside the system is not allowed to exit. The orientation of the deformation is such that the waves will initially be moving mostly back and forth in the x-direction, although latter waves will ultimately be propagating in all directions. The bottom of the channel is considered to be frictionless, such that there is no energy loss to friction. Likewise, no diffusion is considered in the numerical simulations, to avoid diffusional energy losses.

The simulations are arranged to investigate the impact of three numerical model parameters on truncation errors and energy errors. The first of these parameters, as mentioned, is the assumed grid spacing. Five grids were constructed with the element configuration shown in Figure 5.1, each with a different Δx ($=\Delta y$). Grid spacings of 4583, 4125, 2750, 2063, and 1375 meters were used to define the five grids. The respective number of nodes in each of these grids is 840, 931, 2200, 3724, and 8379. The number of floating point operations in the truncation error analysis was large enough to render larger-node simulations computationally limiting. The second and fourth grids required a slightly different domain size, yet the difference from the other grids is small compared to the length scales of interest.

The time step in the model is the second parameter whose impact on truncation errors and energy errors will be examined. The coarsest of the above grids is used for these test simulations in which only Δt is altered. Time steps of 0.5, 1, 2, 4, 8, 12, and 16 seconds are used. Since the deformation is imposed over the first three time steps, all results are translated appropriately in time to account for the different ending times of the initial wave generation.

Finally, the effect of the GWCE weighting factor is also investigated. Kolar et al. (1994) evaluated criteria for selecting an optimal value of τ_0. Too large a value may lead to spurious $2\Delta x$ oscillations in the solution, whereas too small a value may cause mass conservation problems. Thus, this parameter could play an important role in determining the extent of energy and truncation errors. Values of 0.001, 0.01, 0.02, 0.04, 0.06, 0.08, and 0.1 seconds^{-1} (larger τ_0 values led to numerical oscillations) were tested in this analysis.

5.5 Results

5.5.1 Effect of Grid Spacing on Errors

The first set of simulations use the five grids mentioned above. All other model parameters are kept constant. These fully nonlinear simulations used a time step of 4 seconds, a GWCE weighting factor of 0.08 sec^{-1}, and a simulation time of 3 hours. Seven recording stations were designated within the grid domain, as shown in Figure 5.3, to record results of errors at locations with different depths. Note that the scales on the two y-axes are different from the x-axis scale in Figure 5.3.

Figures 5.4a-g show time histories of truncation errors and energy errors at stations 1-7, respectively. Because our interest here is in determining the effect of the different grid spacings on the errors, magnitudes are not explicitly labeled in these figures. The truncation errors (top graph) show decreases that are proportional to the decreases in grid spacings. The energy errors also appear to diminish proportionally to the selection of Δx. However, the formulation of the energy errors is different from that of the truncation errors in that the energy errors are dependent on the number of nodes in the grid. It was shown earlier that the sum of the energy errors over all of the nodes is equal to the global change in energy. Thus, the nodal energy error is a measure of that node's contribution to the global change in energy.

The lower graph in Figure 5.5 displays the energy errors at station 7 again, this time adjusted by multiplying each data set by the number of nodes in that particular grid. Adjusting the errors in this manner helps to account for the differences in the number of nodes on each grid, but does not necessarily make the errors from different grids directly comparable. As may be seen, these adjusted energy error time histories are now closer in magnitude in the earlier portions of the time history. In these earlier moments (i.e. less than 3240 seconds for station 7), though, the results seem to suggest that the adjusted errors are larger for grids with smaller Δx. The upper graph in Figure 5.5 shows the global change in energy over time, and demonstrates that this change is smaller for the grids with smaller grid spacings. Thus, it is apparent that in the early portion of the time history, the contribution of other nodes in the global summation is resulting in smaller global energy changes on the more refined grids and larger changes for the coarser grids. In the latter portions of the time history (i.e. greater than 4140 seconds for station 7), the differences between the adjusted energy errors are larger and again show a trend of larger errors on more refined grids. The reason for this trend, though, appears to be evident in the time histories of the global energy change in the upper graph. It is evident that in these later moments of the simulation, there are points in time where the global energy change is actually more intense on the more refined grids. This phenomenon will be revisited in a later section, as it appears to pertain more to the nature of energy loss as the waves reflect off a boundary as opposed to energy loss as the waves propagate through the water.

The phase differences in the errors shown in Figures 5.4a-g, particularly in the later waves, indicate wave propagation differences on the different grids. It is also noticed that the maxima in the energy errors time histories generally occur around the same time as the maxima in the truncation errors. However, in some cases the energy error maxima have the same sign as the truncation error maxima, whereas in other cases the signs are opposite. To investigate this further, two simulations were designed: one in which only the positive deformation generates an initial positive wave, and another in which only the negative deformation generates an initial depression wave. The truncation error and energy error results at one of the stations are shown in Figure 5.6. They clearly show that with positive waves, the energy error and truncation error maxima have opposite signs, whereas with negative waves the maxima of these two errors have the same signs.

Figure 5.7 displays the total energy throughout the simulation in the top graph and the total mass error for the length of the simulation in the bottom graph. The mass errors were computed using the algorithm presented by Kolar et al. (1994) and are scaled by the volume of the initial wave profile (i.e. the mass introduced to the system). These mass errors become larger with increased grid spacing, yet the percentage of these errors compared to the initial wave volume is sufficiently small to conclude that mass is essentially conserved.

The energy preservation plot shows a few interesting trends. First, the energy associated with the initial wave is different among the various grids, particularly the Δx=4125 grid. While the coarse grid deformation was interpolated onto each of the other grids, not all of the grids had overlapping points. The Δx=4125 grid was one of these grids which did not have similar points, and it is interesting to note how much different the initial energy for this simulation was. This has implications for tsunami modeling in general, in that it is critical to have proper grid refinement in the area of the seismic source. If we examine the Δx=4583, 2750, and 1375 grid results (which do have similar overlapping points), the ultimate decrease in energy is proportional to Δx, exemplifying the importance of grid refinement in optimizing energy preservation.

5.5.2 Effect of the Time Step on Errors

Imamura et al. (1988) showed that the truncation errors in finite difference simulations are in part dependent on the Courant number. The Courant number, defined as $\sqrt{gH}\,\Delta t / \Delta x$, depends both on the grid spacing and the time step. The previous section looked at the effect of the grid spacing, whereas here we investigate the effect of the time step on truncation errors and energy errors. The Δx=4583 grid is used for these time step simulations. All the model parameters are kept the same as before, except now time steps of 0.5, 1, 2, 4, 8, 12, and 16 seconds are used.

Figures 5.8a-g display the truncation errors and energy errors at stations 1-7, respectively, for these time step simulations. The truncation error results appear to be approximately proportional to the time step as well. However, the energy errors are approximately the same for each of these simulations. This would appear to indicate that the truncation errors are not directly influencing the amount of energy being lost in the system. The dissimilarity of both truncation errors and energy errors in the Δx and Δt simulations would thus suggest that the two errors are independent of one another for this tsunami scenario.

It should be noted that the domain considered here does not extend into water shallower than 20 meters. The effect of the time step on tsunami simulations in shallower regions and on land (if the model includes inundation) could be more important in the numerical solutions. This was evident in numerical simulations of the 1993 Hokkaido Nansei-Oki tsunami (Myers and Baptista, 1998a), in which the time step was shown to be an important factor in the numerical solution of elevations and velocities in shallow regions and in representing the inundation process (even though the Courant numbers were all less than one). For the purposes of this analysis, though, it is clear that the time step has a proportional relation with truncation errors and is not significantly affecting the energy errors.

5.5.3 Effect of the GWCE Weighting Factor on Errors

The effect of the GWCE weighting factor, τ_0, is specific to most finite element simulations of tsunamis, since finite difference models generally use the primitive form of the continuity equation. Selecting too large a weighting factor may lead to spurious oscillations, and too small a value may cause mass leakage problems. Values of 0.001, 0.01, 0.02, 0.04, 0.06, 0.08, and 0.1 sec^{-1} were selected to test the dependence of truncation errors and energy errors on τ_0.

Figures 5.9a-g show the station time histories of truncation errors and energy errors for the different values of τ_0. The results are mixed for these sensitivity tests. For most of the stations, the truncation errors are generally larger with increased values of τ_0. The smaller value, 0.001 sec^{-1}, clearly led to oscillations in the truncation error, the behavior of which was different than that of the other τ_0 tests. For most of the stations, the initial energy error undulations are larger with smaller values of τ_0, thus showing an opposite trend than was seen with the truncation errors. The energy error results for later waves show more ambiguity, although it is clear that there are propagation differences between the different tests.

Since global mass conservation is more sensitive to τ_0 than other model parameters, it is instructive to examine the global mass and energy preservation patterns. Figure 5.10 shows these trends for the various τ_0 sensitivity tests. The 0.001 sec^{-1} simulation again exemplifies its anomalous behavior here, showing large mass leakage problems near the end of the simulation and anomalous global energy oscillations near the middle of the simulation. Otherwise, Figure 5.10 shows that as τ_0 is increased, both energy and mass are better conserved.

5.6 Solutions

It has been shown that both energy errors and truncation errors show slightly different dependencies on the GWCE weighting factor, and the energy errors showed little sensitivity to the time step whereas the truncation errors showed stronger time step dependence. These observations indicate that the energy errors and truncation errors, at this scale, are independent of each other.

The question then arises as to which is a more appropriate tool for ameliorating the accuracy of tsunami simulations. The numerical model produces elevations and depth-averaged velocities at each time step. The computed elevations serve as a good measure for judging the accuracy of the model, particularly since the wave heights are an important parameter output from tsunami simulations. Since the time step affected the truncation errors approximately as much as the grid spacing affected the energy errors, the wave elevations computed in both sets of simulations can be contrasted to decide whether the truncation errors or energy errors are more useful with these tsunami simulations. Figure 5.11 displays the maximum wave elevations incurred throughout the length of each of the grid spacing simulations. The differences in wave elevations among these five simulations clearly demonstrate the heterogeneity in the solutions, as added grid refinement can account for elevation differences ranging from a few meters to 15 meters. The maximum elevations in the time step simulations were also computed but are not shown here because they are virtually identical.

From these results, it is apparent that measures of the energy errors can serve as a more effective tool in determining the robustness of a numerical tsunami simulation. While such error measures provide useful *a posteriori* information as to the nature and origin of errors in the solution, they can also serve as a tool for constructing a better numerical setup of the problem. For example, the computation of the energy errors utilize the elevations solved for in the GWCE and the depth-averaged velocities produced from the momentum equations, which yields the following energy error matrix:

$$\begin{bmatrix} f_{1,1} & & & f_{1,NP} \\ & \ddots & & \\ & & \ddots & \\ & & \ddots & \\ f_{NP,1} & & & f_{NP,NP} \end{bmatrix} \begin{bmatrix} s_1 \\ \vdots \\ \vdots \\ \vdots \\ s_{NP} \end{bmatrix} = \begin{bmatrix} \varepsilon_1 \\ \vdots \\ \vdots \\ \vdots \\ \varepsilon_{NP} \end{bmatrix} \qquad (11)$$

where the left hand-side (LHS) is a function of the already known elevations and velocities (s_i), the elemental areas, and the time step. Since the elevations and velocities are functions of all the parameters in the GWCE and momentum equations, the LHS of the above matrix is also dependent on these parameters. The energy errors presented in this paper were computed using all the known values on the LHS to compute the unknown errors (ε_i) on the right-hand side (RHS). Suppose, though, that we know *a priori* a maximum energy error that ideally would not be exceeded in a simulation. Using the above matrix equation, any one of the functional parameters on the LHS could then be selected as an unknown. Numerical parameters that may be selected for this optimization include the grid spacing, the time step, and the GWCE weighting factor. As an example, let the elemental area be the unknown. Since there are always more elements than nodes in a finite element grid (NE>NP), the LHS is instead formulated based on a representative area surrounding each node. The new set of equations would be derived as:

$$\begin{bmatrix} f'_{1,1} & & & f'_{1,NP} \\ & \ddots & & \\ & & \ddots & \\ & & \ddots & \\ f'_{NP,1} & & & f'_{NP,NP} \end{bmatrix} \begin{bmatrix} \text{area}_1 \\ \vdots \\ \vdots \\ \vdots \\ \text{area}_{NP} \end{bmatrix} = \begin{bmatrix} \varepsilon_1 \\ \vdots \\ \vdots \\ \vdots \\ \varepsilon_{NP} \end{bmatrix} \qquad (12)$$

where each f'_{ij} now has the area dependence removed and the elevation/velocity solutions (s_i) included.

It has been demonstrated in Figure 5.11 that the elevation/velocity solutions can be quite different, depending on the chosen numerical parameters (i.e. grid spacing) and their effect on the energy preservation. However, as these numerical parameters become better optimized, it is expected that the estimate of the grid spacings (in the example above) will also converge to optimized values. To test this, estimates of the required grid spacings were derived from each of the previously discussed grid spacing simulations for a range of desired energy errors. Results of these required areas are shown in Figures 5.12a-b for stations 1-7. These results clearly show that estimates of the required grid spacing at these stations decrease as the solution is better optimized. This makes sense, since sharper gradients of elevation are represented on the more refined grids, and smaller areas required to maintain a certain energy error are in turn necessary.

From these considerations, it is clear that attaining the appropriate level of grid refinement for a particular tsunami scenario is an iterative process. A simulation is first made in which the required grid spacings are computed for a certain level of energy error. A new grid is then constructed based on this computed grid spacing configuration. A simulation is made using this new grid, and grid spacings required to keep energy errors below the same value are again computed. Another new grid is constructed, and this process is repeated until the computed grid spacings no longer differ from simulation to simulation.

Also note in Figures 5.12a-b that the required grid spacings are generally much lower than the grid spacings used in each of the simulations. The imposed energy errors in these cases were within a reasonable range of values derived from the previous sections' results. Therefore, in order to keep the energy errors from surpassing these realistic values, the most refined grid simulation was indicating that grid spacings of 20-25 meters would at least be required at these stations. The parabolic nature of the curves in these figures also suggests that more stringent grid refinement is required for smaller imposed maximum energy errors.

This iterative process of deriving better grids through error analysis can also be applied to the truncation errors, if desired. Because the truncation error formulations are dependent on several orders of Δx, root-finding algorithms such as eigenvalue methods can be used to solve for Δx based upon a prescribed level of maximum truncation error.

This again was performed for the original Δx simulations to determine required grid spacings to keep the truncation errors below certain levels. The results of these required grid spacings are shown in Figures 5.13a-b for stations 1-7. Similar to the energy error results, these figures show a parabolic trend between the imposed maximum truncation error and the required Δx.

These Δx estimates from each of the grid spacing simulations were used to generate new grids that would theoretically maintain the level of energy preservation dictated by the prescribed values. For example, the Δx=4583 meter simulation was used to produce estimates of what the grid spacing should be around each node in order to keep the energy errors below a specified amount. A finite element grid generator (Turner and Baptista, 1991) was then used to create a new grid with variable grid spacings consistent with what would be required from the error analysis. Figure 5.14 shows a grid which was generated from the results of the Δx=4583 meter simulation. Increased grid refinement is seen to be required in shallow regions (near the right side of the grid) and near the seismic source, a result which is consistent with traditional approaches to refining grids for tsunami simulations. The surprising result from this generated grid is that significant levels of refinement are also required in deeper waters for this tsunami scenario. Generally, less refinement is placed in deeper regions since the tsunami wavelengths increase here. If the domain for a particular tsunami scenario is such that the waves which propagate away from land are unimportant (i.e. they leave the numerical grid boundary via transmissive boundaries), then the added grid refinement in deeper waters may not be necessary. However in many cases these outgoing waves are critical (i.e. in studies of transoceanic tsunamis), and grid refinement based on energy preservation could be a critical tool in the deeper waters as well as in shallower regions.

Each of these new grids generated from the errors in the five Δx simulations were used in new simulations of the tsunami. The global energy loss was computed for each of these new simulations and compared with the amount of energy loss that the original Δx simulations predicted would occur with such grid spacing configurations. Figure 5.15 shows the computed global energy losses contrasted with their predicted energy losses.

As can be seen, the predicted energy loss became a better estimate of the actual energy loss in the more refined grids. Thus, in the iterative process of attaining an energy-preserving simulation discussed before, our estimates of the energy preservation become more accurate as our solutions are ameliorated with increased refinement.

The Δx=1375 meter simulation was further used to generate five more grids which would allow for only 10%, 20%, 30%, 40%, and 50% predicted losses in total energy throughout the three hour simulation. The global energy variation over time is displayed in Figure 5.16, the top graph of which focuses on the first 1.5 hours of the lower graph. Also included in this figure are the results from a simulation that had as much refinement as was computationally feasible, with Δx ranging from 1375 meters in deep waters to 5 meters in shallow waters. This refined grid simulation was designed to represent the maximum amount of refinement that could practically be used on today's state-of-the-art computers. The lower graph of Figure 5.16 shows that there are two critical phases where none of the simulations are able to avoid significant energy losses. These occur a little over an hour into the simulation and around two hours as well, both points in time coinciding with when the waves are reflecting off the shallow water land boundary. In between these two points, energy is better preserved with the grids that were designed to provide better energy preservation. If the entire simulation did not involve any reflections off land boundaries, it is expected that the estimates of how much energy should be lost would become closer to observed energy losses in the new grid simulations.

To understand why grid refinement can play such a key role in energy preservation during the non-reflection phases of wave propagation, the wave elevation and energy error time histories were frequency analyzed using power spectrum analysis to determine if the grid spacings were capable of handling the frequencies inherent in this tsunami scenario. Figures 5.17a-g display these power spectrum results on three of the Δx simulations at stations 1-7, respectively. The energy error power spectrum did not account for the nodal differences among the three grids, so the power spectrum amplitudes in the lower graphs will generally show more power being contained in the larger Δx simulations. The interesting trends in both the energy error and wave elevation power spectrum amplitudes pertain more to the changes in amplitudes across the various frequencies. For these simulations, it is evident that higher frequency signals in both the energy errors and wave elevations are being lost on the coarser grids. Such frequencies (i.e. on the order of minutes) have traditionally been perceived as irrelevant in tsunami simulations. However, if this is contributing to the observed energy losses in numerical simulations, grids capable of resolving such higher frequency information would be necessary.

While use of energy errors can help to construct numerical simulations which maintain better energy preservation during the propagation phases of the event, there still remains the question of what is causing energy loss as the waves reflect off land boundaries. Two theories are considered for why this may be occurring. The first is that it is possible that the sharp gradients in elevations during the reflection are not being fully represented. However, the refined grid simulation presented in Figure 5.16 did not prove to avoid the energy losses during the reflection phases, even though Δx values on the order of 5 meters were used near the boundary in that simulation. Thus, unless finer grid spacing is required, it is likely that something else is the culprit for these losses. The second theory pertains to the assumptions used to derive the shallow water equations. The derivation of these equations neglects certain vertical acceleration terms. However, as waves reflect off a land boundary, these vertical acceleration terms may be non-negligible. To determine the importance of these terms, a three-dimensional simulation was set up in which the shallow water equations are used to solve for surface elevations and an internal mode equation is used to compute the vertical profile of velocities. The maximum velocities from this simulation are displayed in Figure 5.18 as a function of depth in shallow waters. The top graph shows the maximum vertical velocity at the surface, the center graph shows the maximum depth-averaged velocity, and the lower graph shows the maximum rate of change of the vertical velocity. Since the vertical velocities are on the order of one tenth of the depth-averaged horizontal velocities, they appear to be a non-negligible component of the simulation. The time rate of change of the vertical velocities, however, seem to be significantly less than other accelerations such as gravity. Thus, the nature of the vertical velocities in these simulations suggests that they are most likely non-negligible, though their impact on energy loss is difficult to predict.

5.7 Conclusions

Numerical modeling of tsunamis provides an invaluable tool for evaluating the physics by which the generated waves propagate to the shoreline and inundate the land. Their use, however, needs to be complemented with analyses of the robustness of the model application. Without such analyses, it is difficult to ascertain the quality of the results, particularly since the initial conditions can usually not be verified.

We have presented here two approaches for investigating the nature of errors in finite element simulations of tsunamis. The first approach looks at truncation errors in an effort to determine the quality of the model's representation of the governing equations. The results from the truncation error analyses indicate that they are dependent on each of the numerical parameters considered: the grid spacing, the time step, and the GWCE weighting factor. These results have important implications for simulations in which truncation errors serve as barometers of the quality of the solution for elevations and velocities. For the tsunami scenario considered here, the solutions among the simulations in which the truncation error varied significantly (i.e. the time step simulations) were very similar. Thus, while truncation errors are important to different types of numerical simulations, they did not appear to be critical to the solutions considered here.

The second approach for evaluating errors in tsunami simulations involved determining energy errors throughout the domain. At each time step, the nodal contributions to global energy loss could be computed. This provides an *a posteriori* tool for examining which areas in a spatial domain are contributing most to energy loss in a simulation. While it is difficult to compare nodal energy errors for simulations made on grids of varying Δx, the global energy errors unequivocally show that increased grid refinement can significantly reduce energy errors. While the energy errors did not show significant sensitivity to the time step, they did indicate a dependence on the GWCE weighting factor. The numerical solutions are more sensitive to the energy errors, thus indicating that these errors are more useful in tsunami simulations than truncation errors.

Both of these measures of errors in finite element tsunami simulations can also be used to help improve further numerical simulations. By specifying a maximum error (either truncation or energy) which ideally should not be exceeded in a simulation, the formulations can be rearranged to solve for the values of numerical parameters necessary to keep the errors below the specified level. This approach was applied to solving for the grid spacings required to keep energy and truncation errors below specified levels. The results indicate that as the solutions became better, the grid spacing requirements became more stringent. Eventually such requirements converge as the solution simultaneously converges. The grid spacing parameter was used in a set of tests designed to keep energy below specified levels. The results showed that energy preservation was ameliorated during the propagation phases of the simulation, most likely because higher frequency information was better preserved. However, energy losses as the waves reflected off the land boundary could not be avoided, no matter how much refinement was used. It is possible that either the sharp elevation gradients are not being adequately represented during this reflection, or that the assumptions inherent in the shallow water equations are not entirely valid for tsunami scenarios.

Tools such as those presented in this study should be an integral part of presenting numerical modeling results of tsunami events. In doing so, our knowledge of the physical processes occurring during past events will be improved, as will our estimation of future tsunamis generated from active subduction zones.

5.8 References

Hagen, S.C. and J.J. Westerink, 1995. Finite Element Grid Resolution Based on Second and Fourth-Order Truncation Error Analysis, *Computer Modeling of Seas and Coastal Regions II*, 283-290.

Hagen, S.C. and J.J. Westerink, 1996. Utilizing an Imposed Multiple of Change in Finite Element Grid Generation, *Proceedings of the Third Asian-Pacific Conference on Computational Mechanics*, 1817-1822.

Hirt, C.W., 1968. Heuristic Stability Theory for Finite Difference Equations, *Journal of Computational Physics*, 2, 339-355.

Imamura, F. and C. Goto, 1988. Truncation Error in Numerical Tsunami Simulation by the Finite Difference Method, *Coastal Engineering in Japan*, 31(2), 245-263.

Kolar, R.L., J.J. Westerink and M.E. Cantekin, 1994. Aspects of Nonlinear Simulations Using Shallow-Water Models Based on the Wave Continuity Equations, *Computers and Fluids*, 23(3), 523.

Knupp, P. and R. Luczak, 1995. Truncation Error in Grid Generation: A Case Study, *Numerical Methods for Partial Differential Equations*, 11(6), 561-571.

Luettich, R.A., J.J. Westerink and N.W. Scheffner, 1991. *ADCIRC: An Advanced Three-Dimensional Circulation Model for Shelves, Coasts, and Estuaries*, Dept. of the Army, U.S. Army Corps of Engineers, Washington, D.C.

Myers, E.P. and A.M. Baptista, 1998a. Modeling of Past Tsunamis: One Model's Lessons from the 1993 Hokkaido Nansei-Oki and 1964 Alaska Tsunamis, (submitted to *Natural Hazards*).

Myers, E.P. and A.M. Baptista, 1998b. Finite Element Modeling of Potential Cascadia Subduction Zone Tsunamis, (submitted to *Science of Tsunami Hazards*).

Skamarack, W.C., 1989. Truncation Error Estimates for Refinement Criteria in Nested and Adaptive Models, *Monthly Weather Review*, 117(4), 872-886.

Turner, P.J. and A.M. Baptista, 1991. *ACE/gredit User's Manual: Software for Semi-Automatic Generation of Two-Dimensional Finite Element Grids*, Center for Coastal and Land-Margin Research.

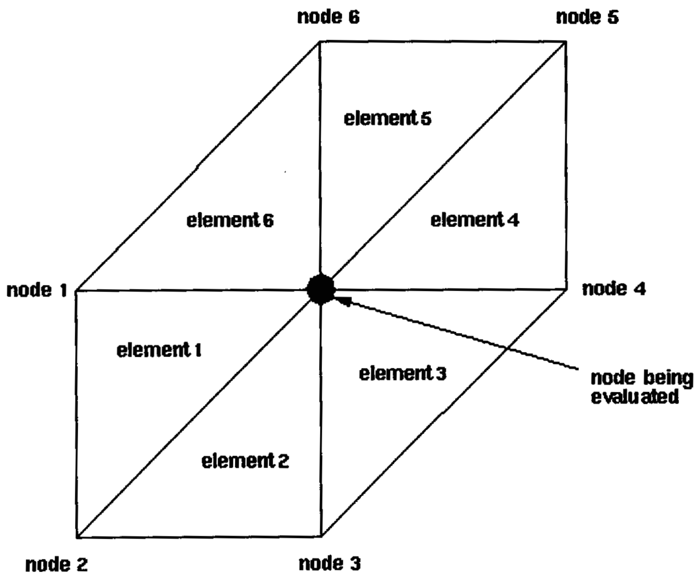

Figure 5.1 Grid configuration for truncation error analysis.

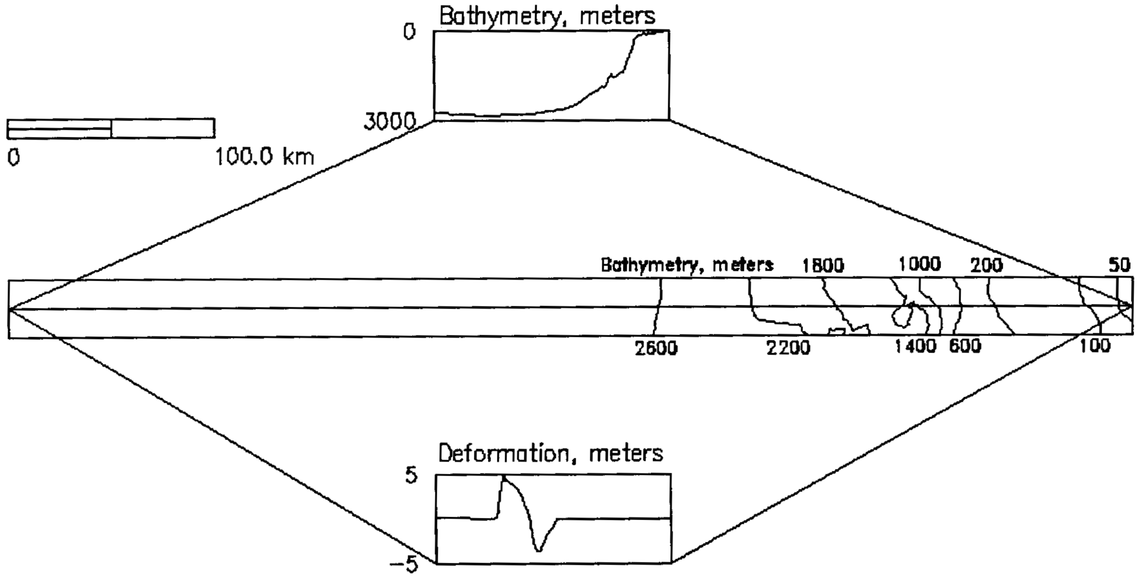

Figure 5.2 Bathymetry and ocean floor deformation for the channel test case.

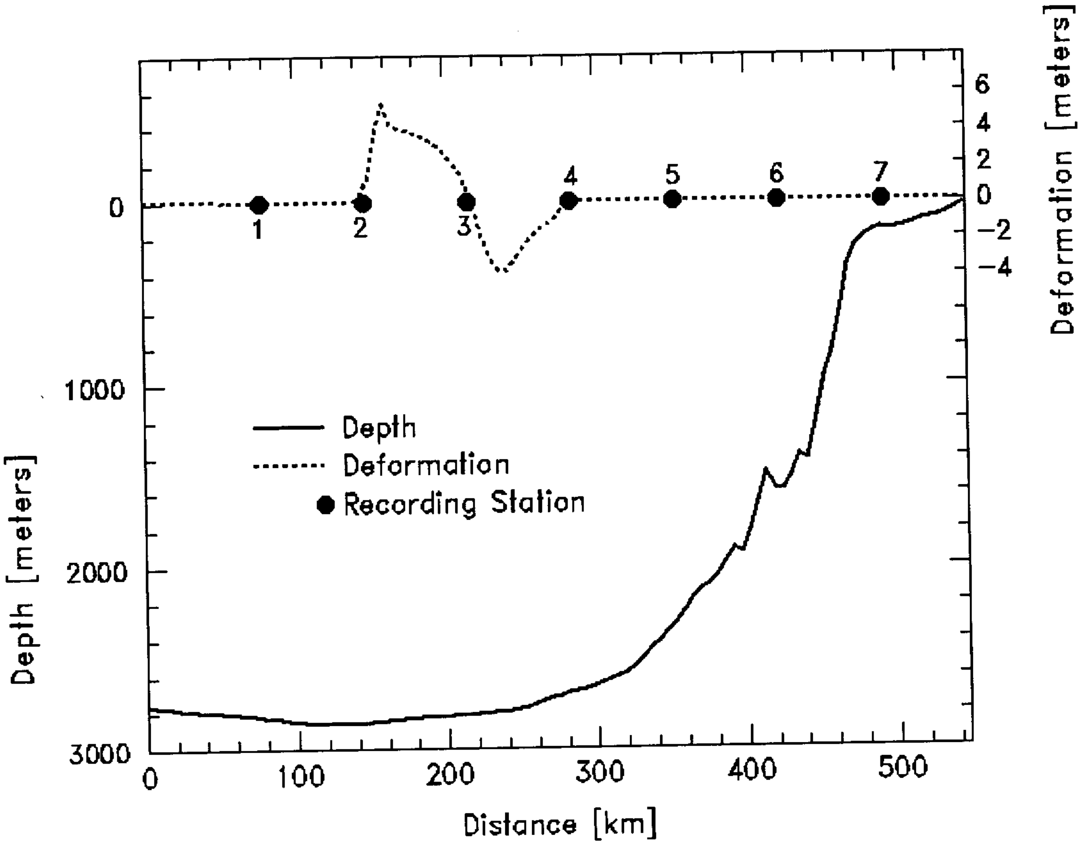

Figure 5.3 Placement of stations for recording results. Note the scale difference on the axes.

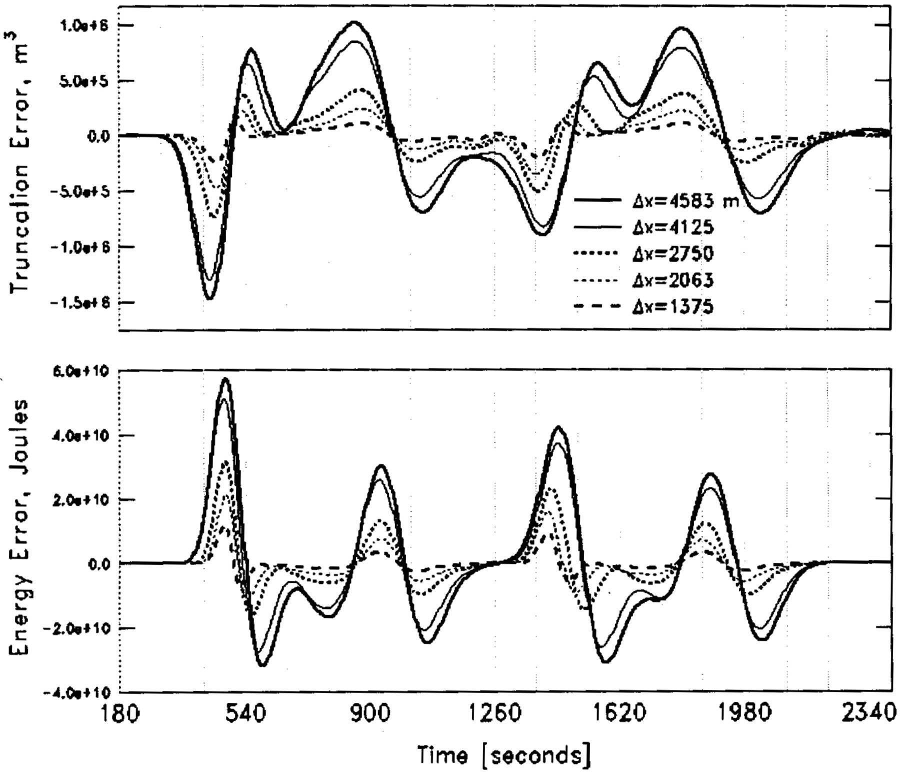

Figure 5.4a Truncation errors and energy errors as a function of grid spacing at station 1.

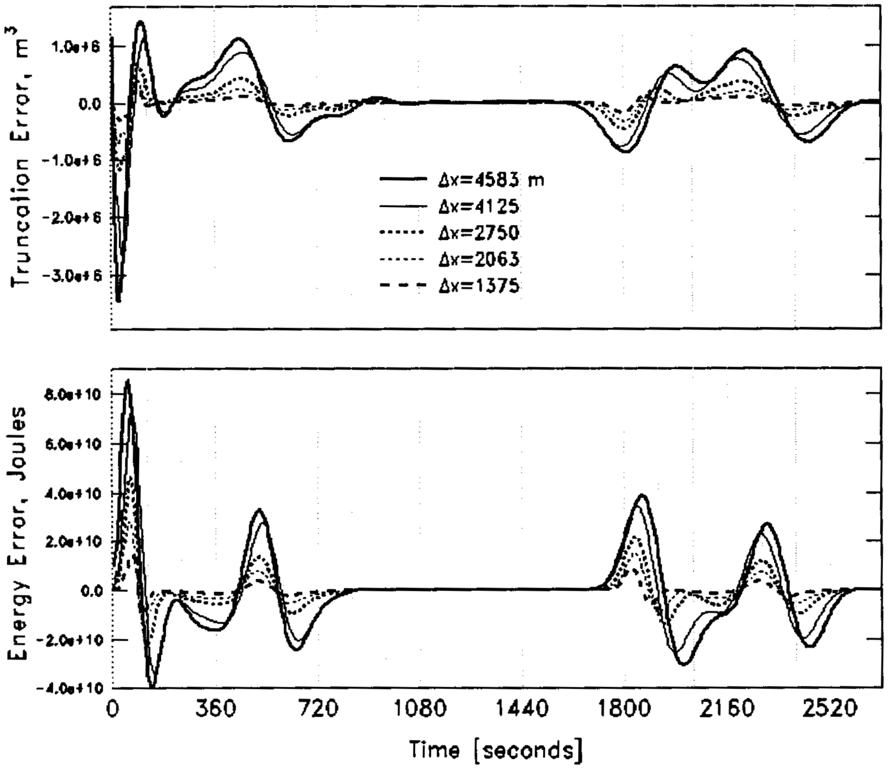

Figure 5.4b Truncation errors and energy errors as a function of grid spacing at station 2.

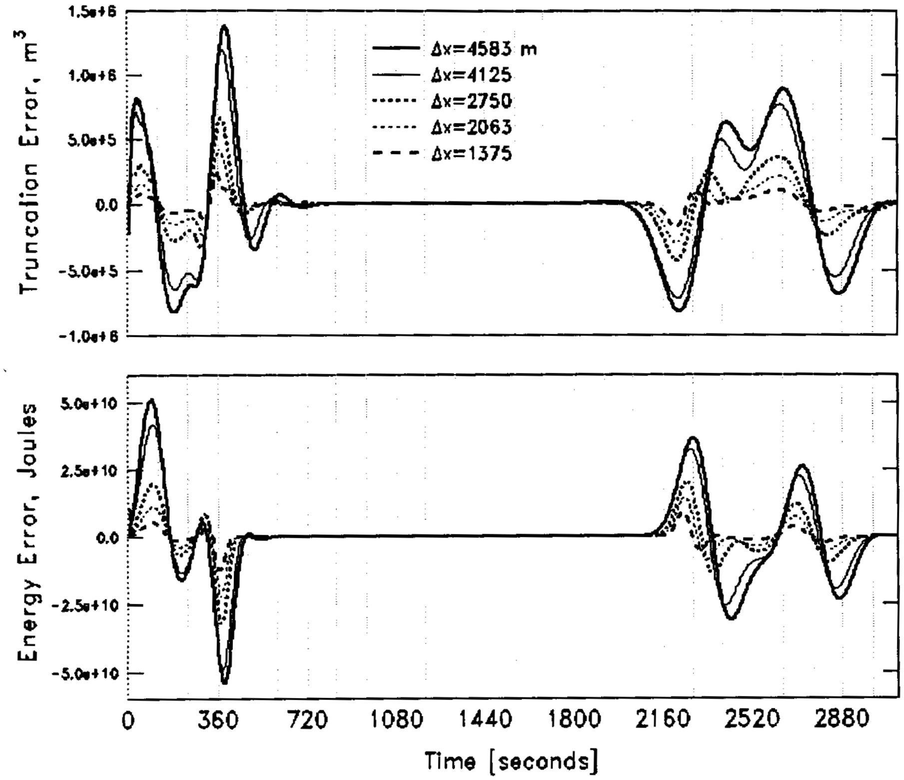

Figure 5.4c Truncation errors and energy errors as a function of grid spacing at station 3.

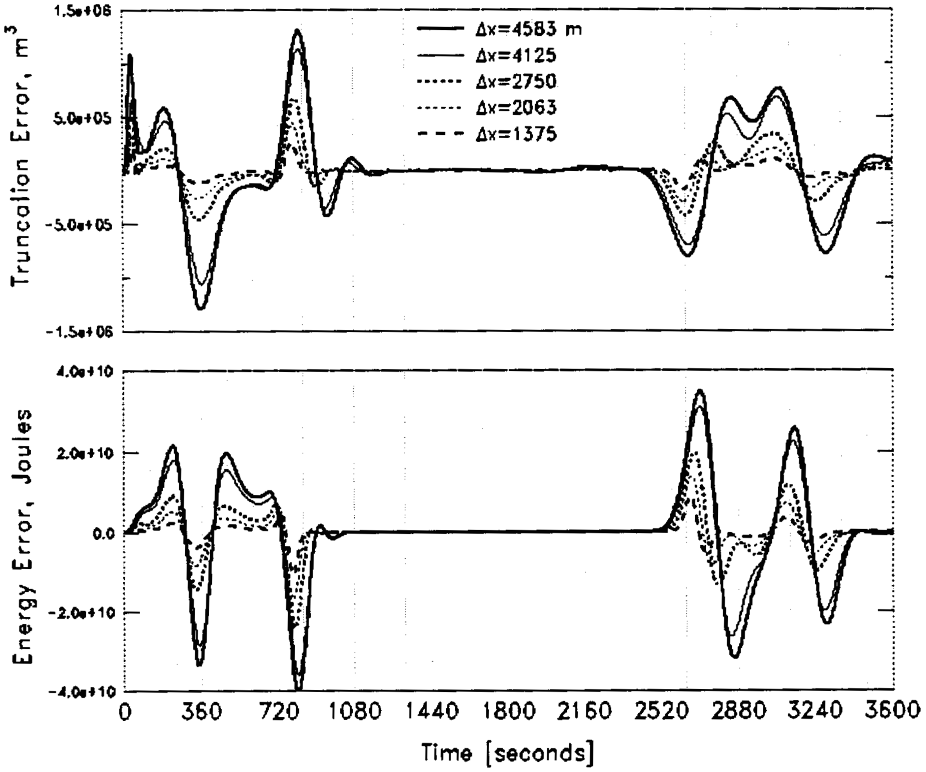

Figure 5.4d Truncation errors and energy errors as a function of grid spacing at station 4.

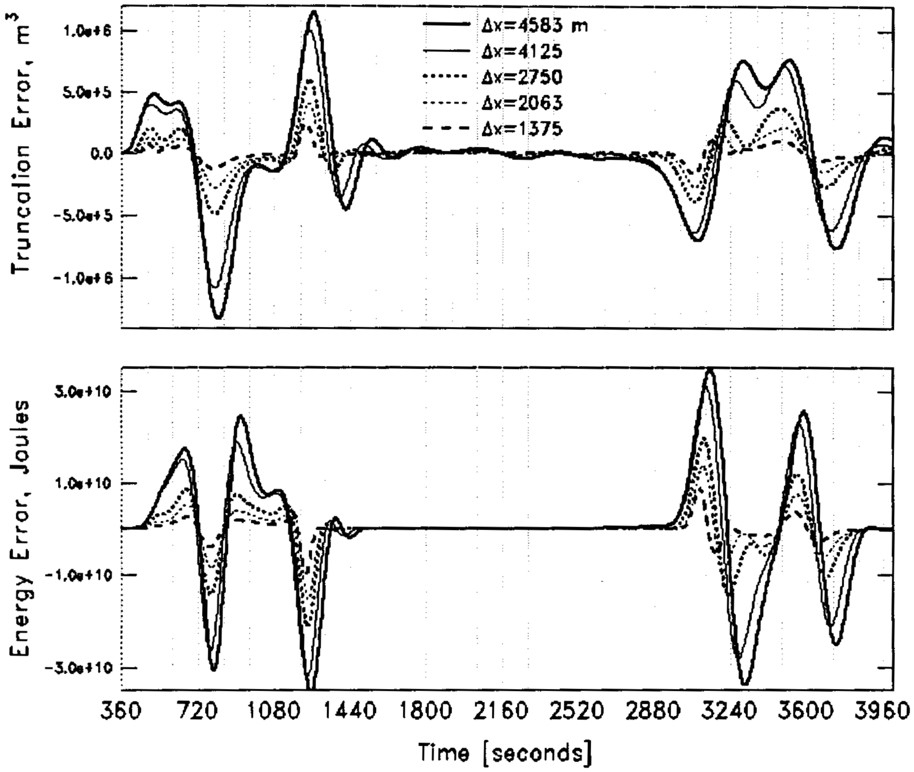

Figure 5.4e Truncation errors and energy errors as a function of grid spacing at station 5.

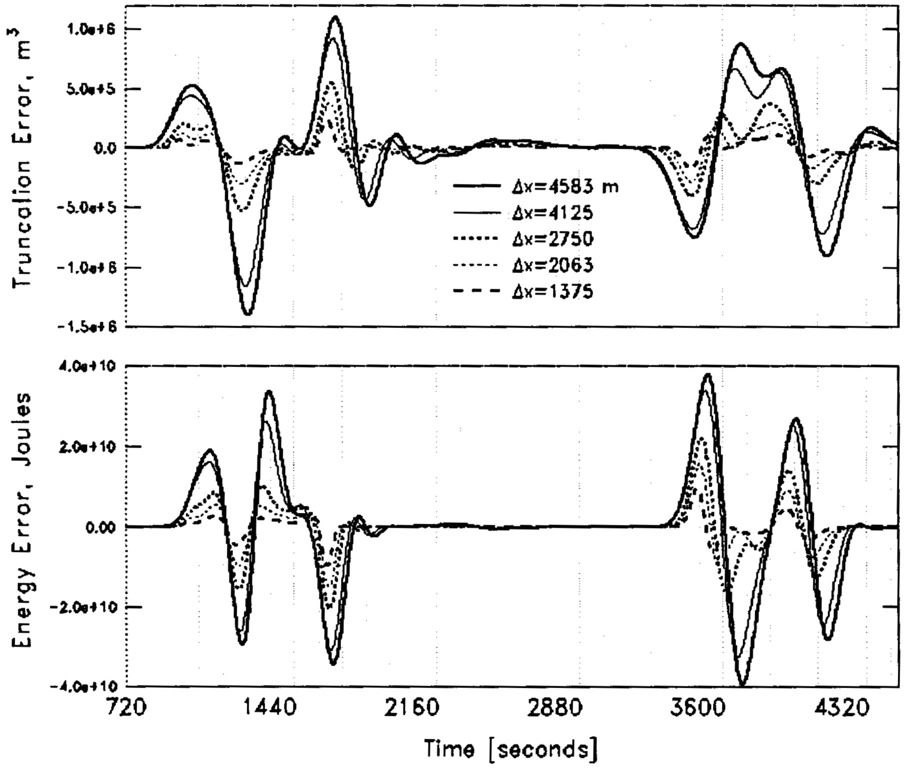

Figure 5.4f Truncation errors and energy errors as a function of grid spacing at station 6.

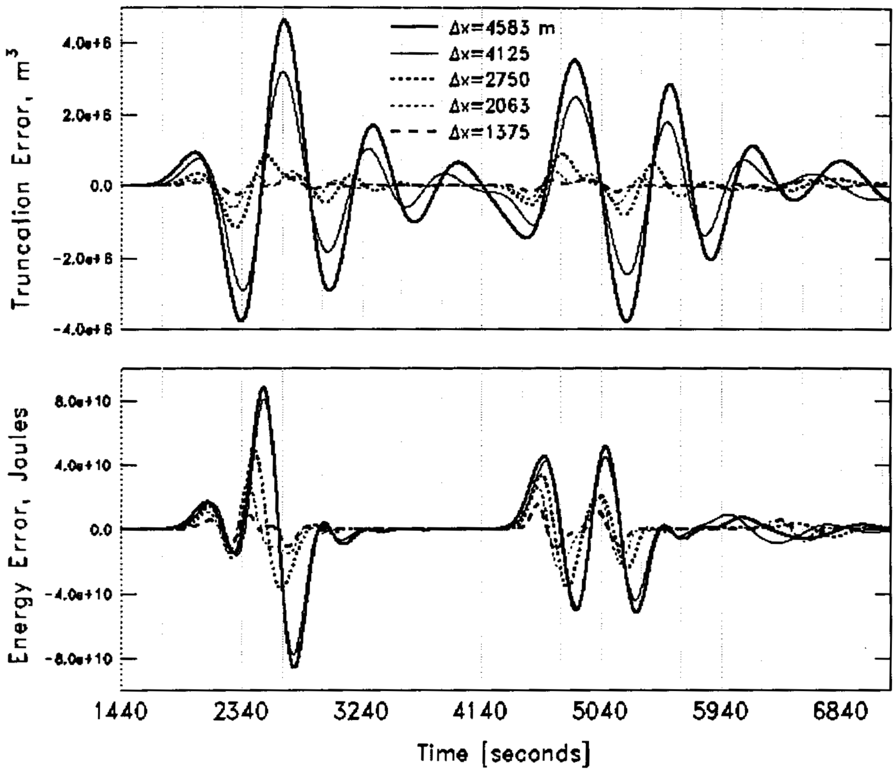

Figure 5.4g Truncation errors and energy errors as a function of grid spacing at station 7.

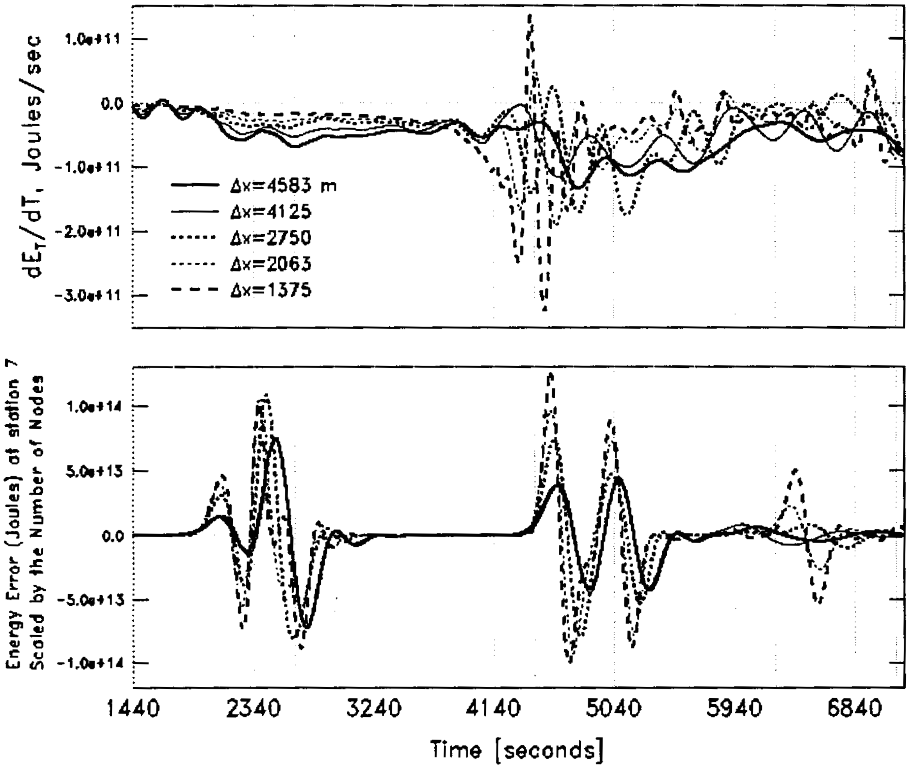

Figure 5.5 Rate of change in total energy for each Δx simulation and the scaled energy error at station 7.

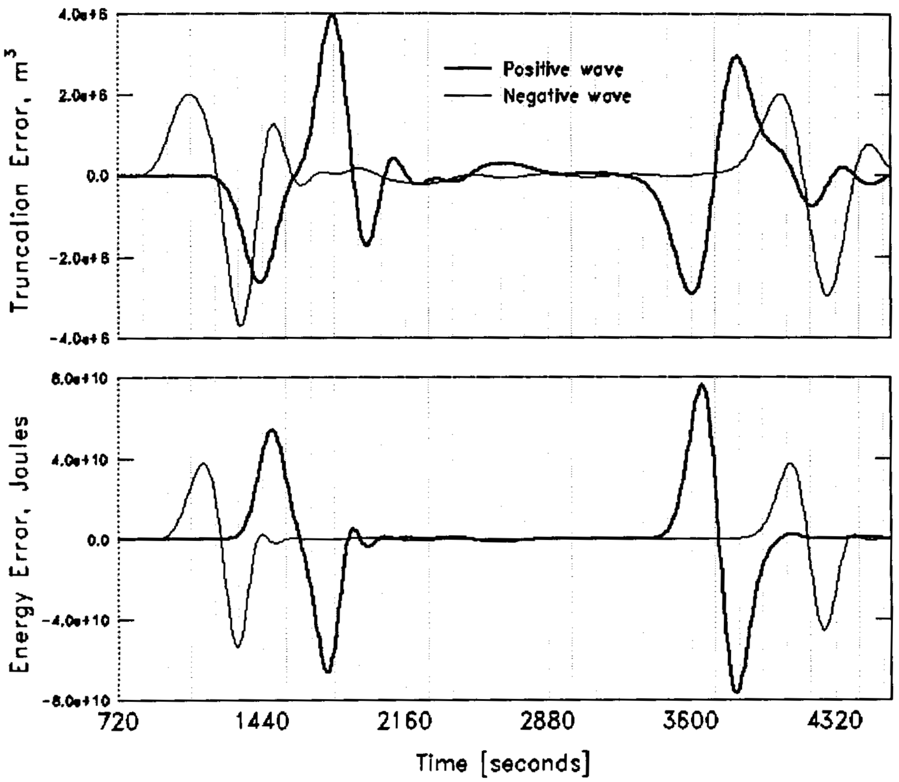

Figure 5.6 Relation between truncation errors and energy errors for positive and negative waves.

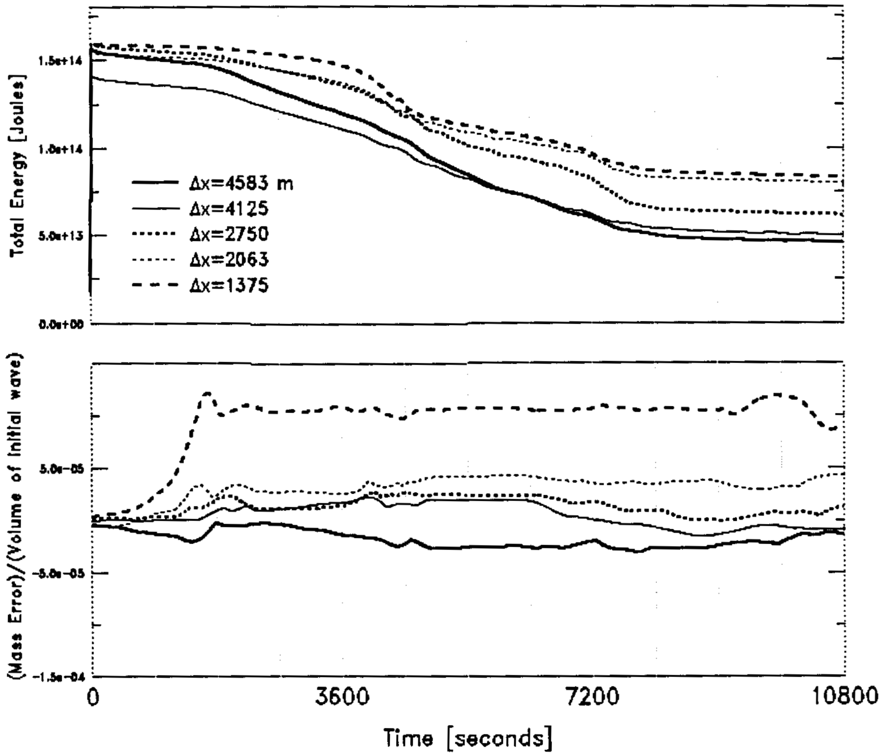

Figure 5.7 Global mass and energy preservation as a function of grid spacing.

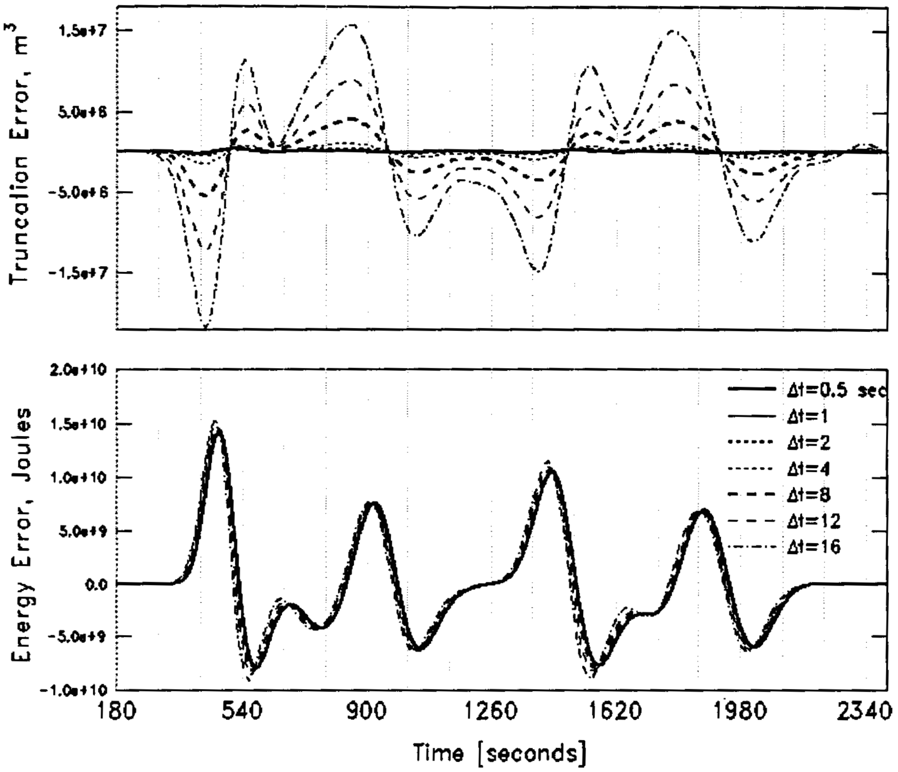

Figure 5.8a Truncation errors and energy errors as a function of the time step at station 1.

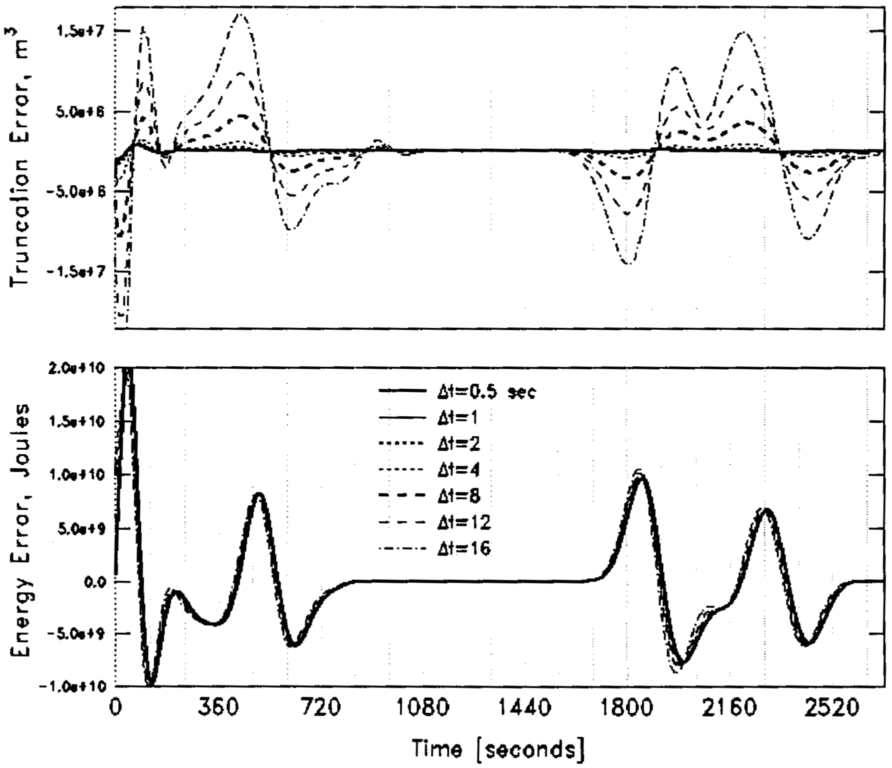

Figure 5.8b Truncation errors and energy errors as a function of the time step at station 2.

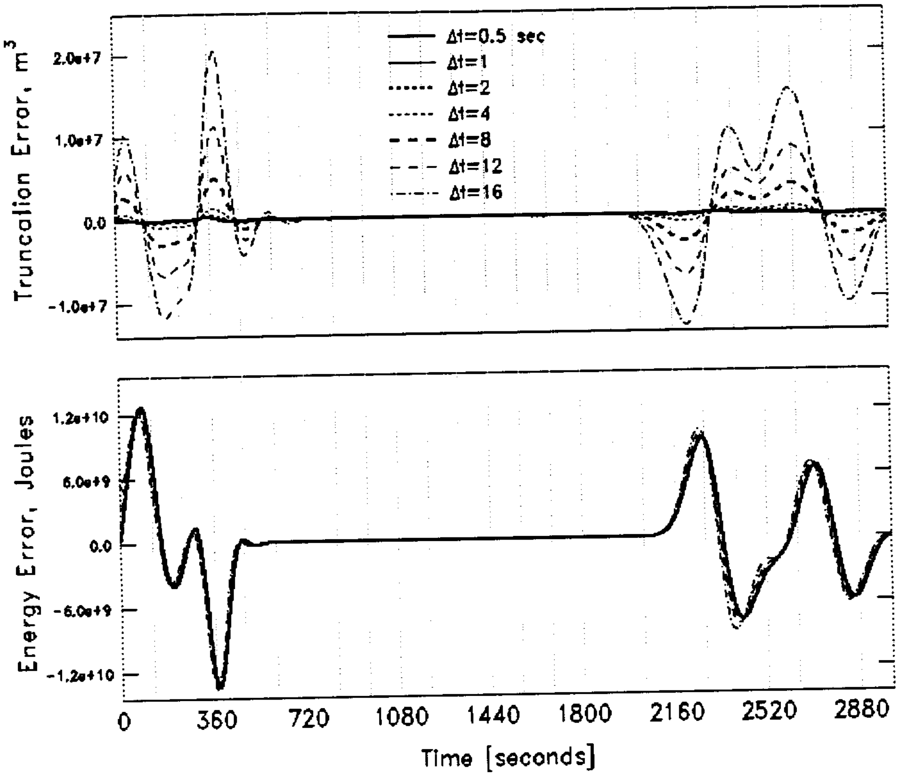

Figure 5.8c Truncation errors and energy errors as a function of the time step at station 3.

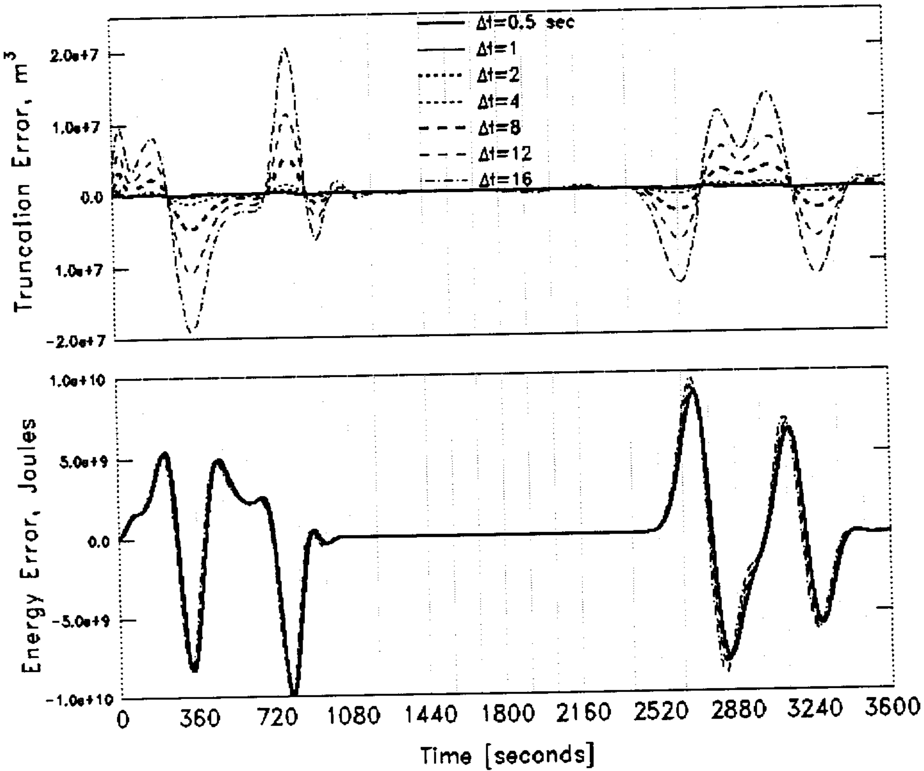

Figure 5.8d Truncation errors and energy errors as a function of the time step at station 4.

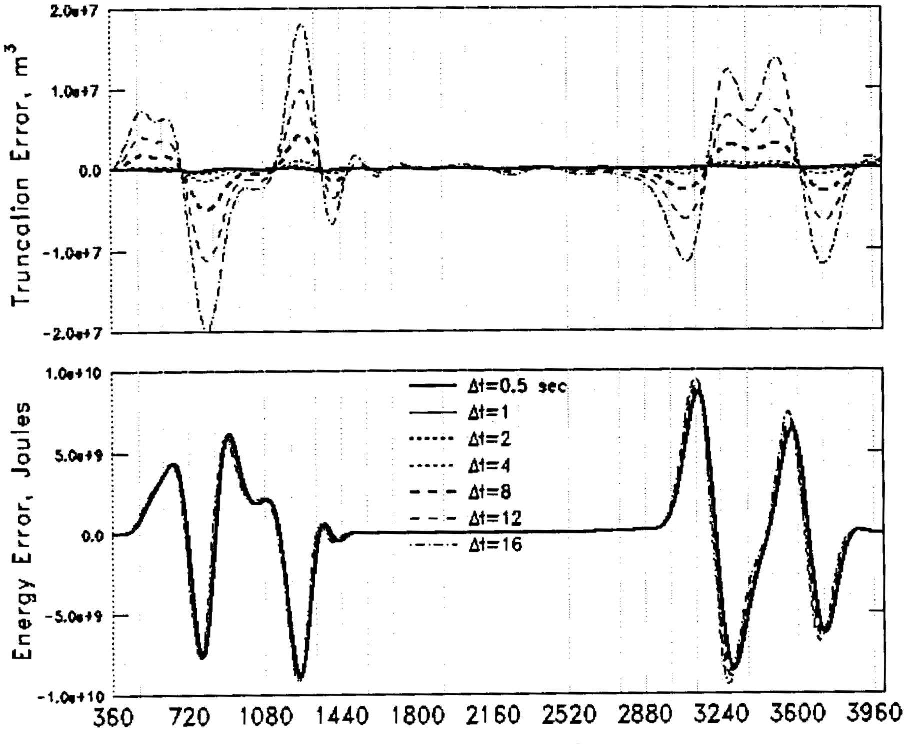

Figure 5.8e Truncation errors and energy errors as a function of the time step at station 5.

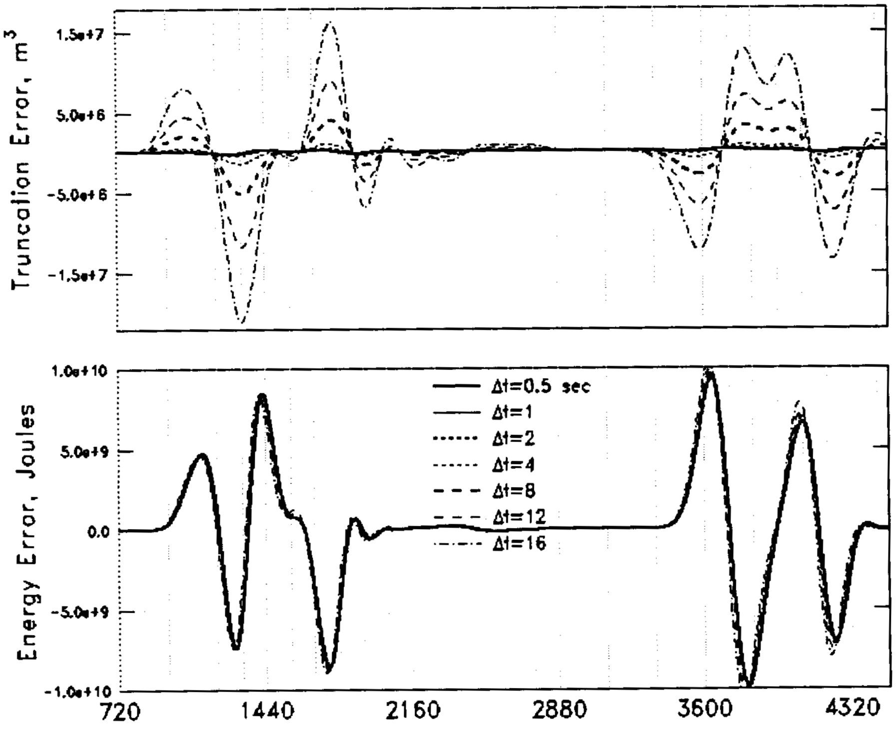

Figure 5.8f Truncation errors and energy errors as a function of the time step at station 6.

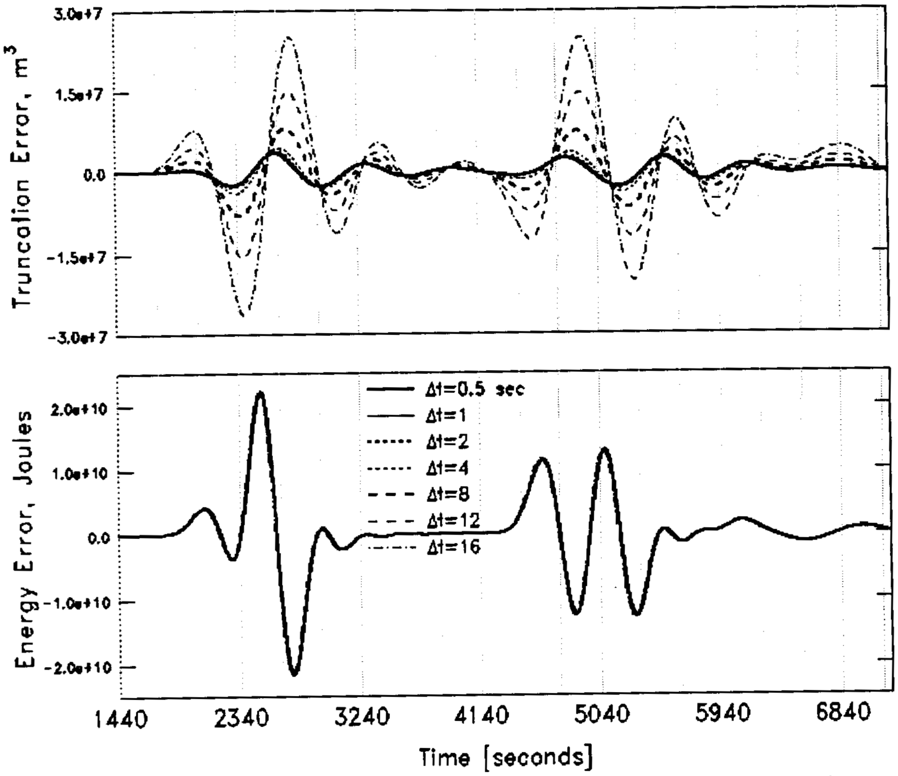

Figure 5.8g Truncation errors and energy errors as a function of the time step at station 7.

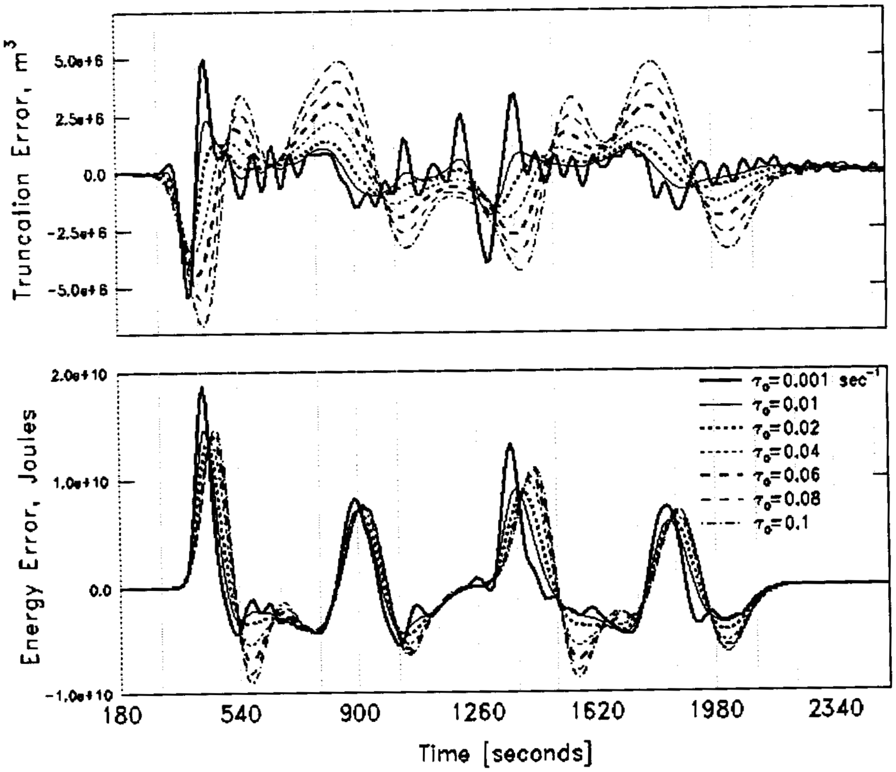

Figure 9a Truncation errors and energy errors as a function of the GWCE weighting factor at station 1.

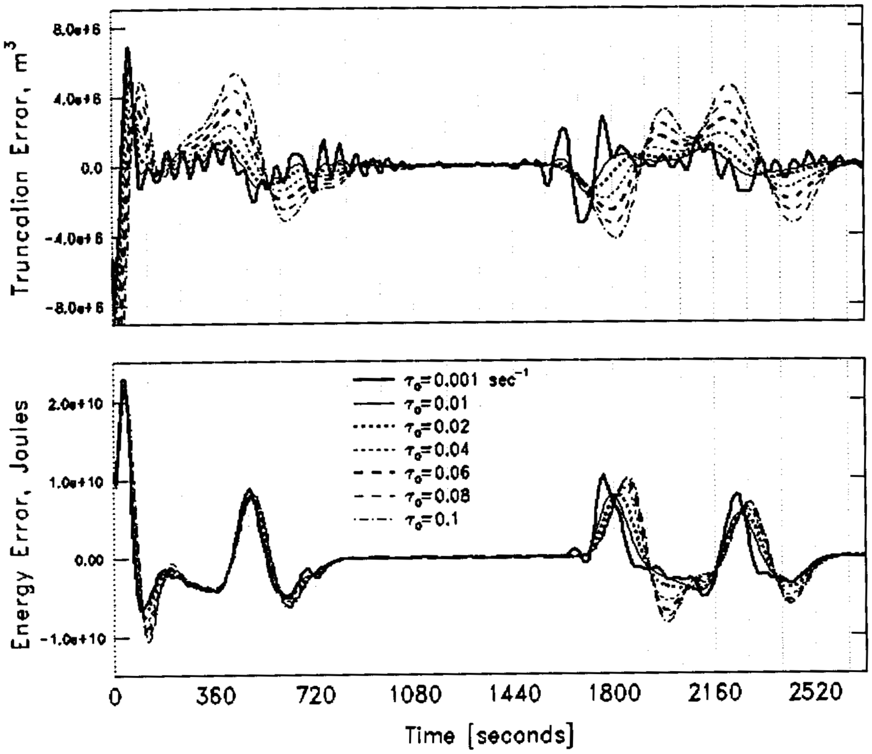

Figure 5.9b Truncation errors and energy errors as a function of the GWCE weighting factor at station 2.

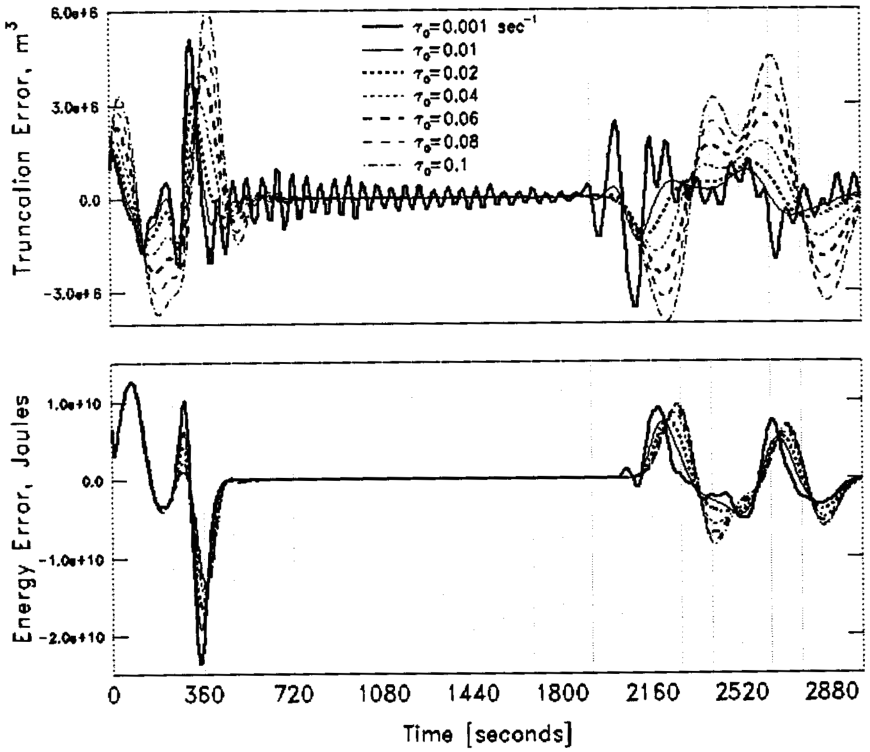

Figure 5.9c Truncation errors and energy errors as a function of the GWCE weighting factor at station 3.

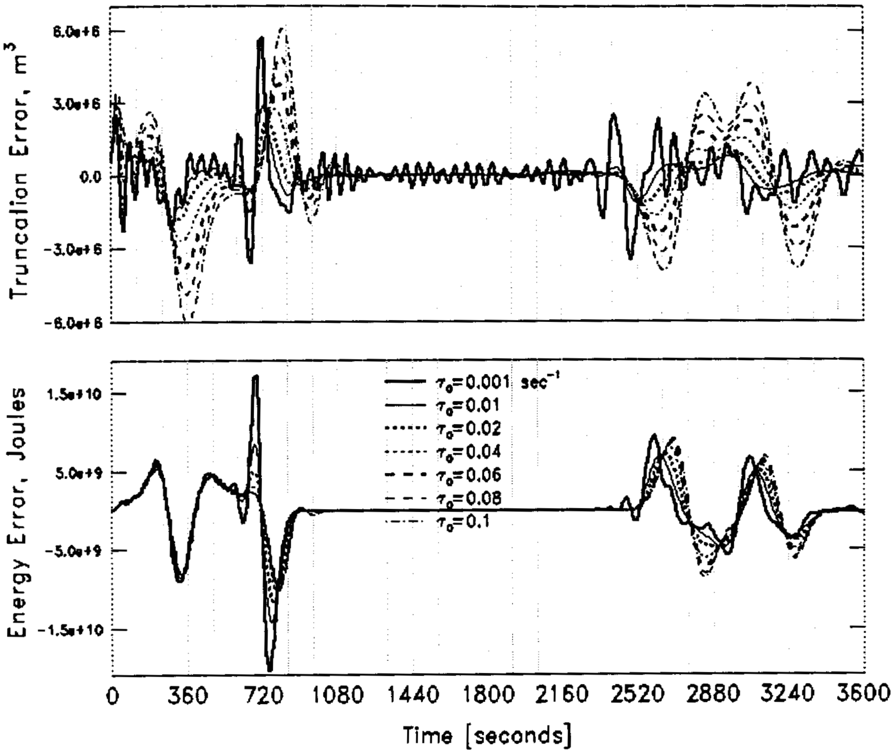

Figure 5.9d Truncation errors and energy errors as a function of the GWCE weighting factor at station 4.

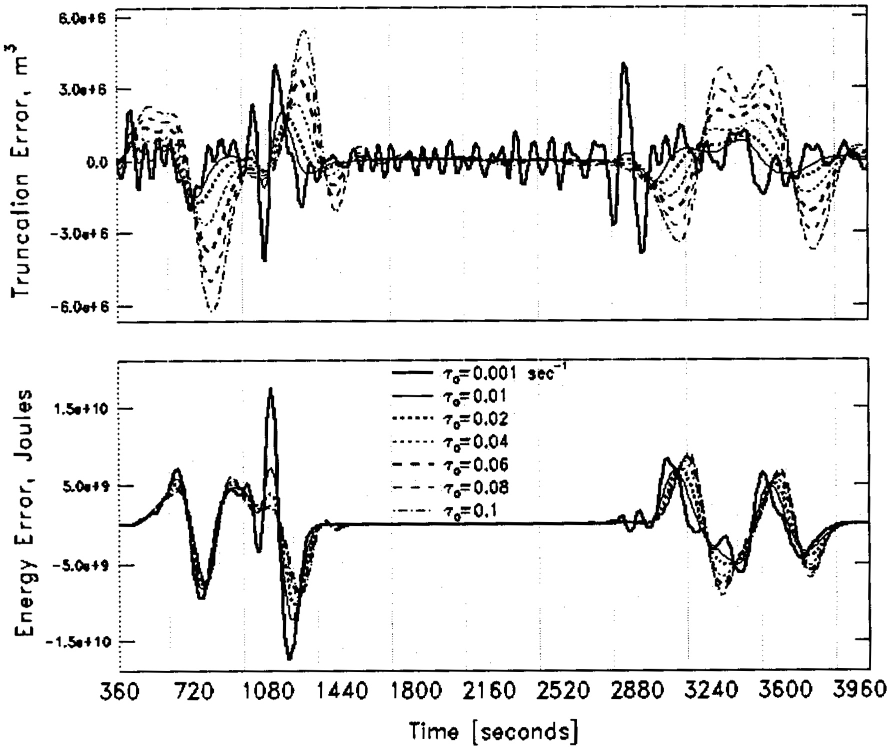

Figure 5.9e Truncation errors and energy errors as a function of the GWCE weighting factor at station 5.

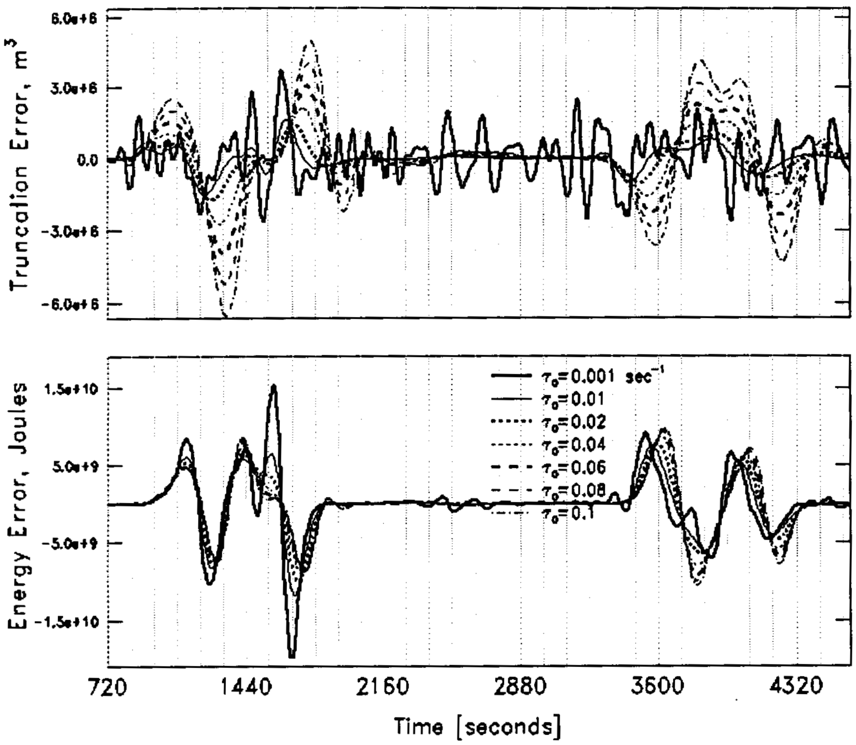

Figure 5.9f Truncation errors and energy errors as a function of the GWCE weighting factor at station 6.

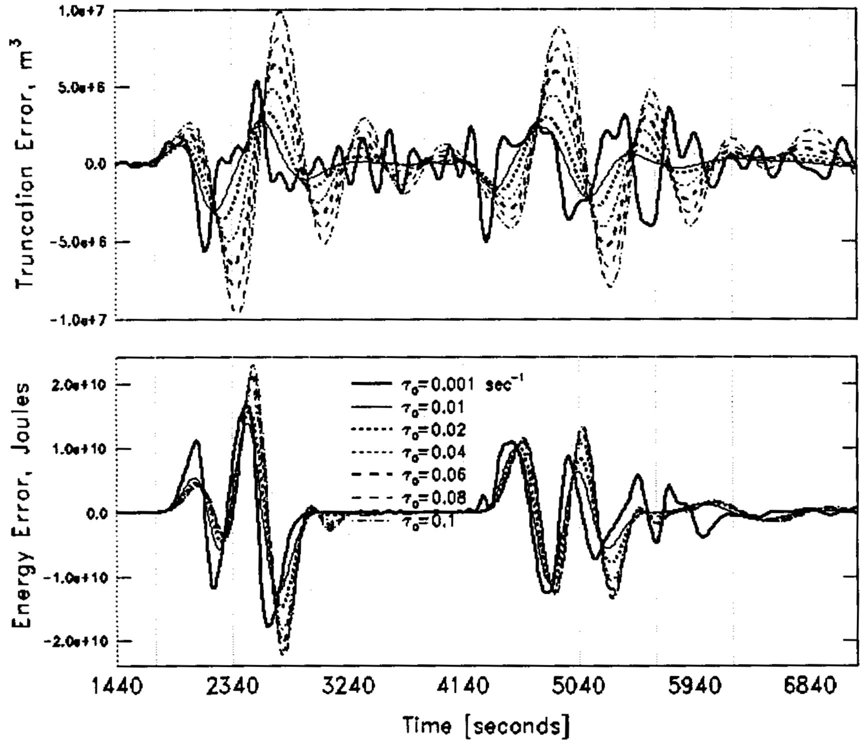

Figure 5.9g Truncation errors and energy errors as a function of the GWCE weighting factor at station 7.

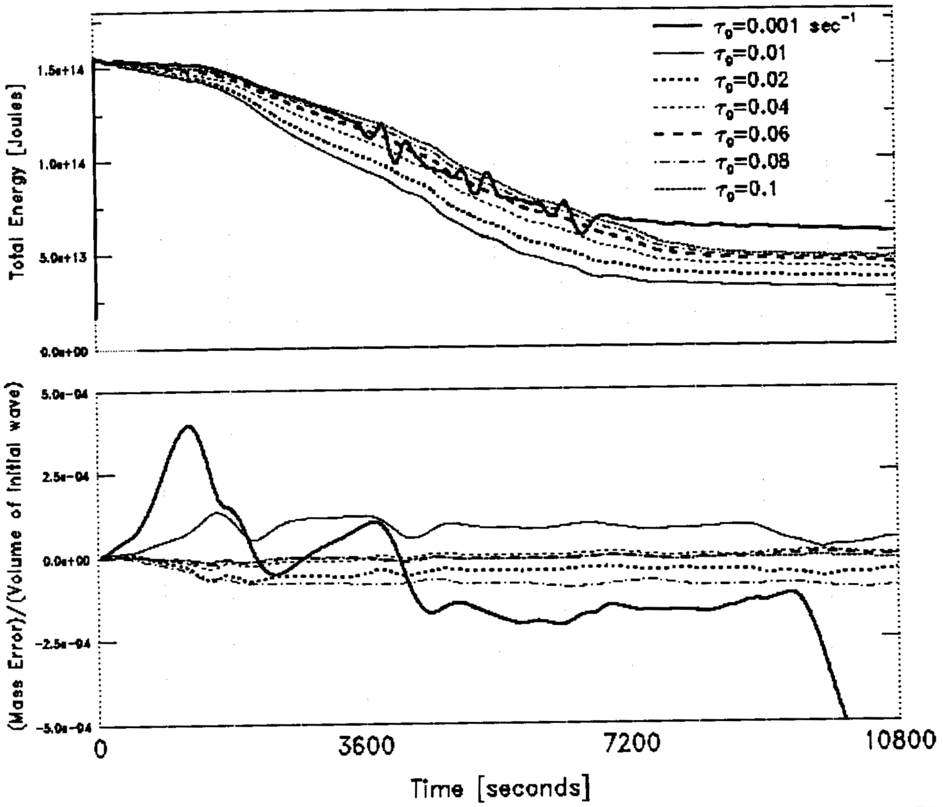

Figure 5.10 Global mass and energy preservation as a function of the GWCE weighting factor.

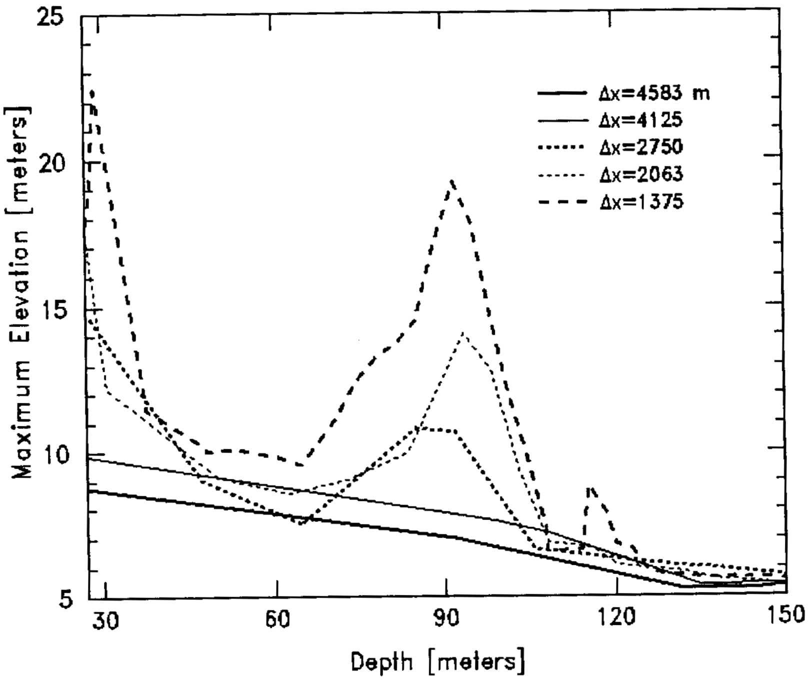

Figure 5.11 Maximum wave elevations in shallow waters as a function of Δx.

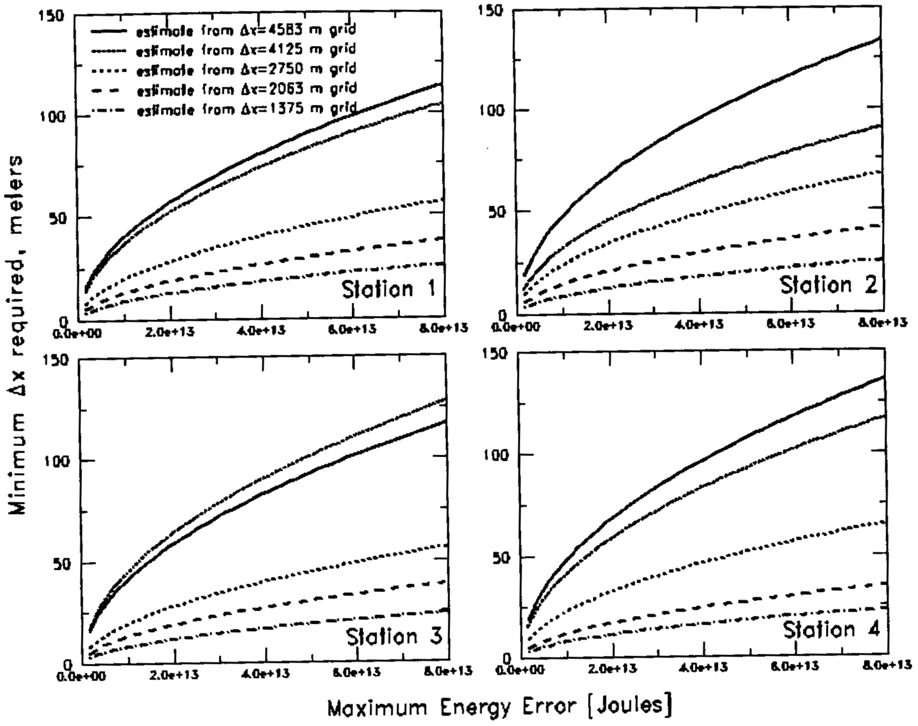

Figure 5.12a Δx required to keep nodal energy errors below a specified maximum level, stations 1-4.

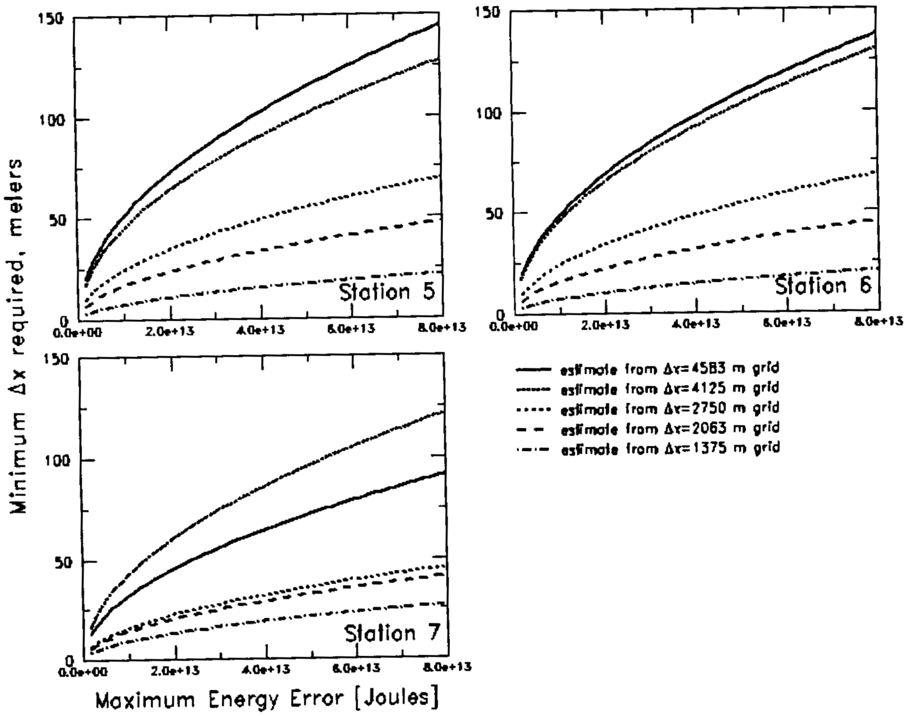

Figure 5.12b Δx required to keep nodal energy errors below a specified maximum level, stations 5-7.

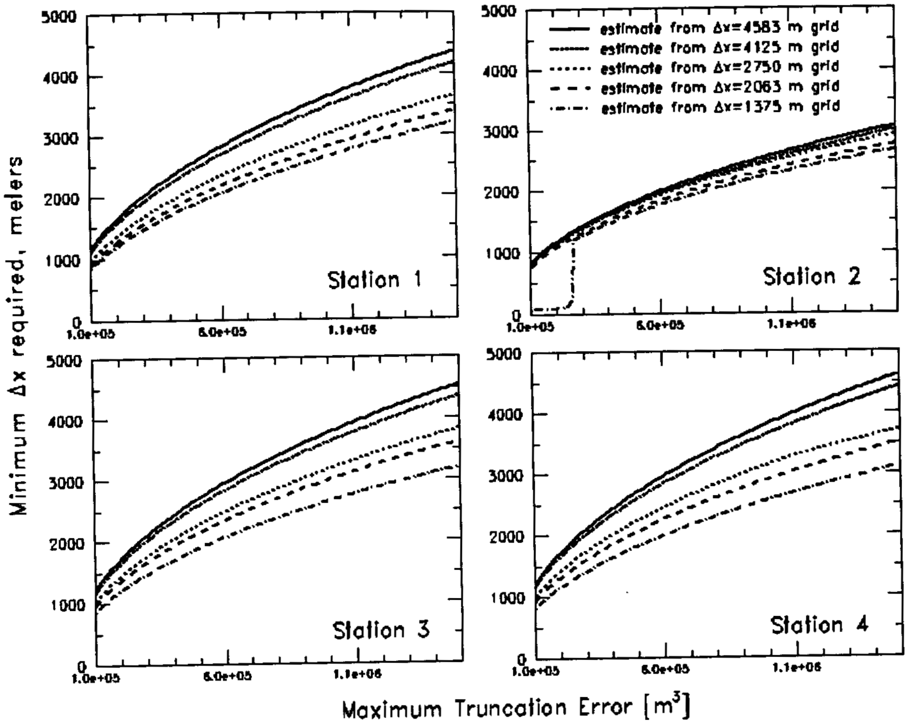

Figure 5.13a Δx required to keep truncation errors below a specified maximum level, stations 1-4.

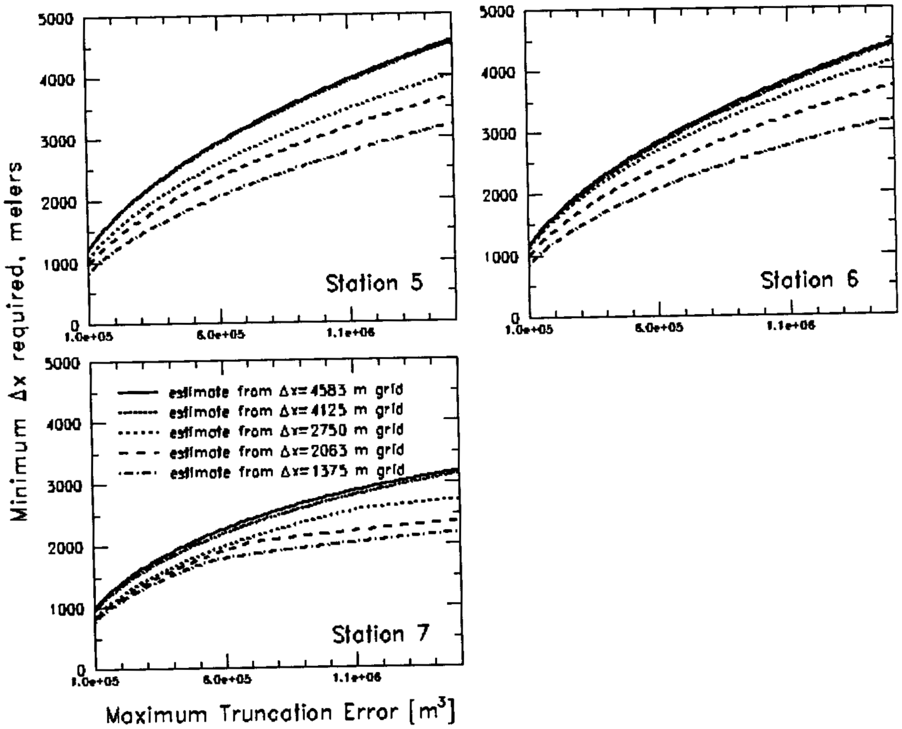

Figure 5.13b Δx required to keep truncation errors below a specified maximum level, stations 5-8.

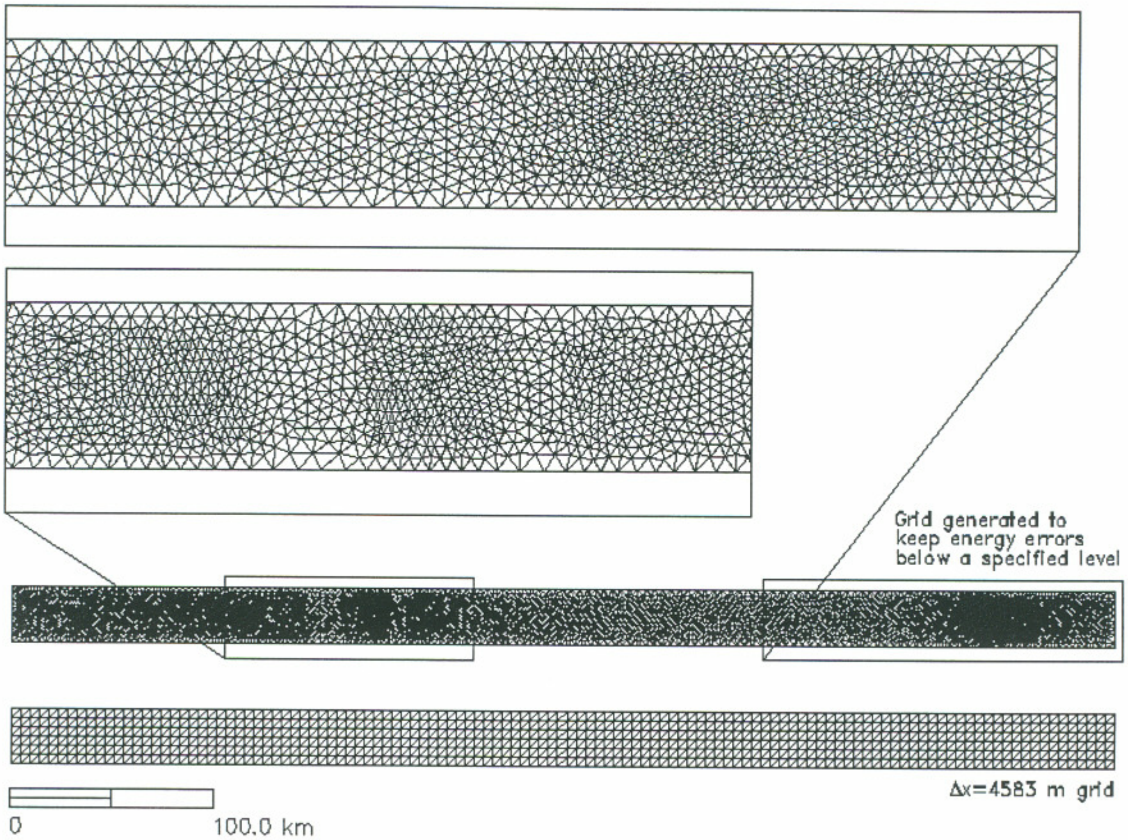

Figure 5.14 New grid generated using the energy errors from the Δx=4583 meter simulation.

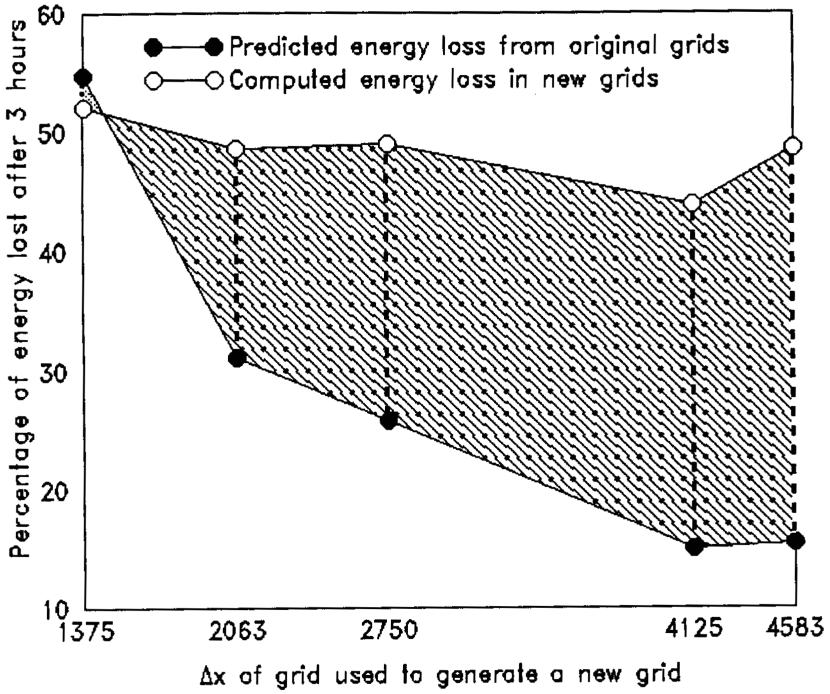

Figure 5.15 Predictions of energy loss derived from the old grid contrasted with observed energy losses on the generated grids.

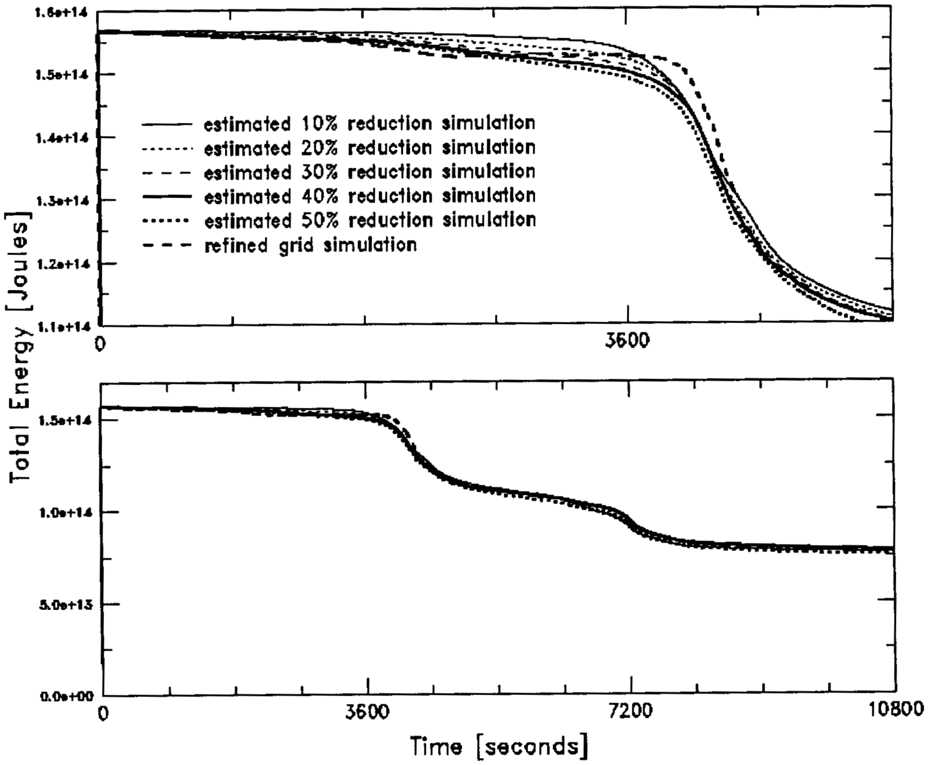

Figure 5.16 Global energy preservation on grids generated to lose a specified amount of energy.

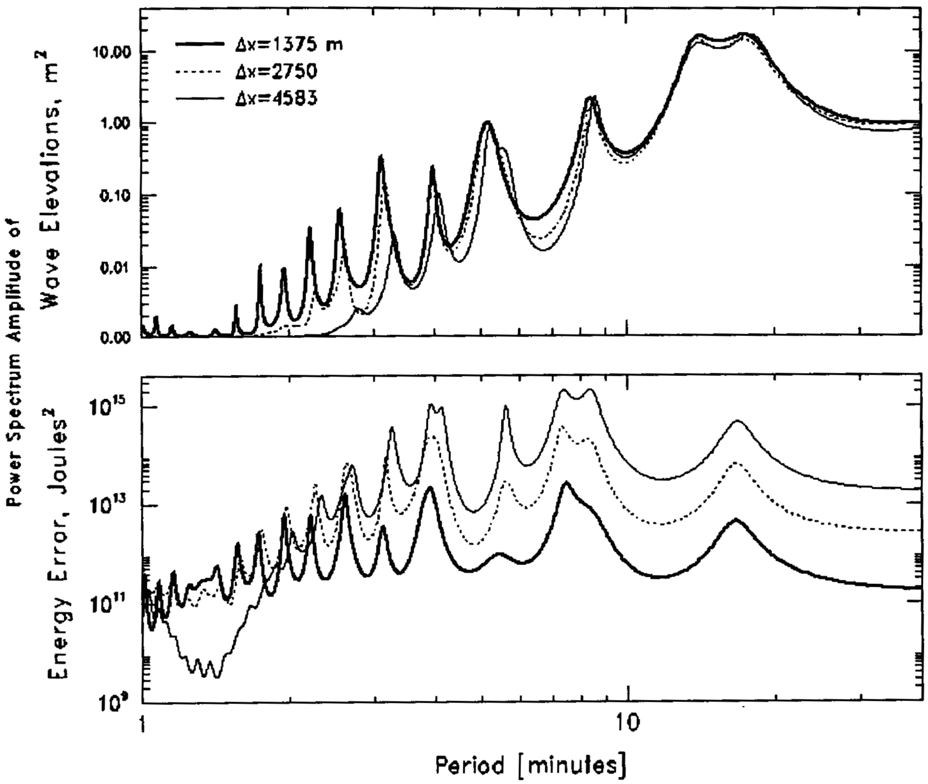

Figure 5.17a Power spectrum of wave elevations and energy errors at station 1.

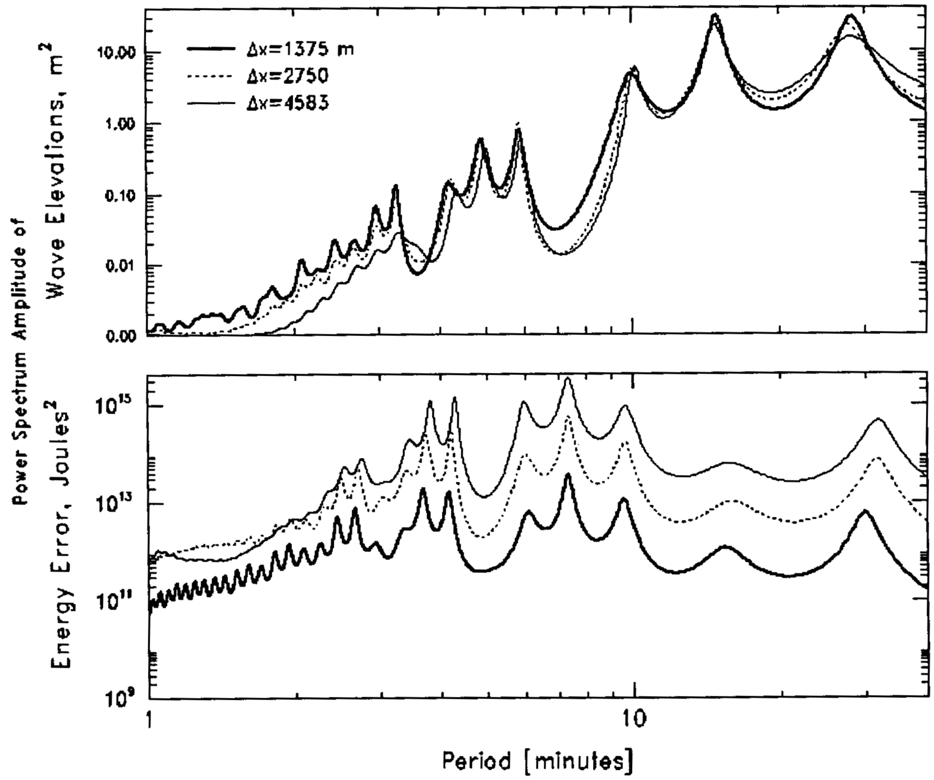

Figure 5.17b Power spectrum of wave elevations and energy errors at station 2.

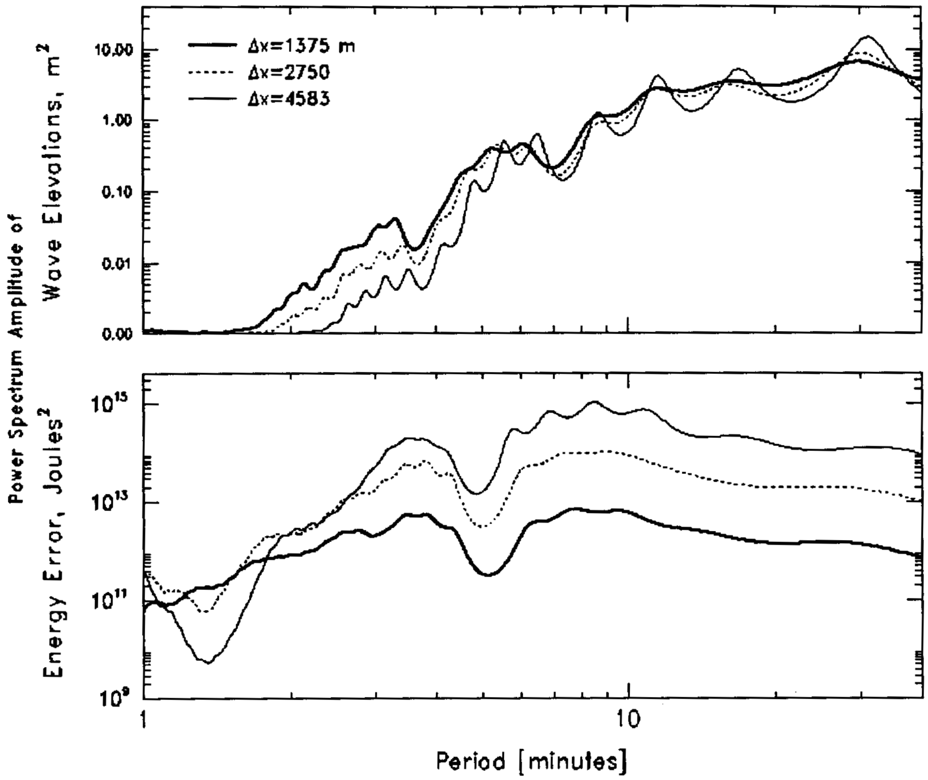

Figure 5.17c Power spectrum of wave elevations and energy errors at station 3.

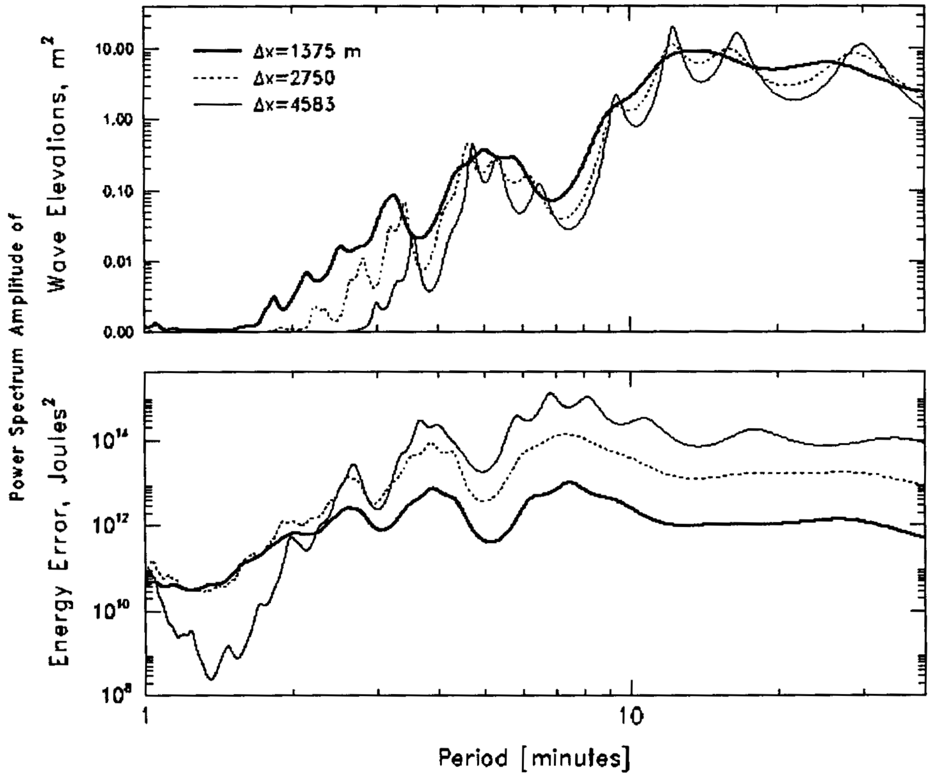

Figure 5.17d Power spectrum of wave elevations and energy errors at station 4.

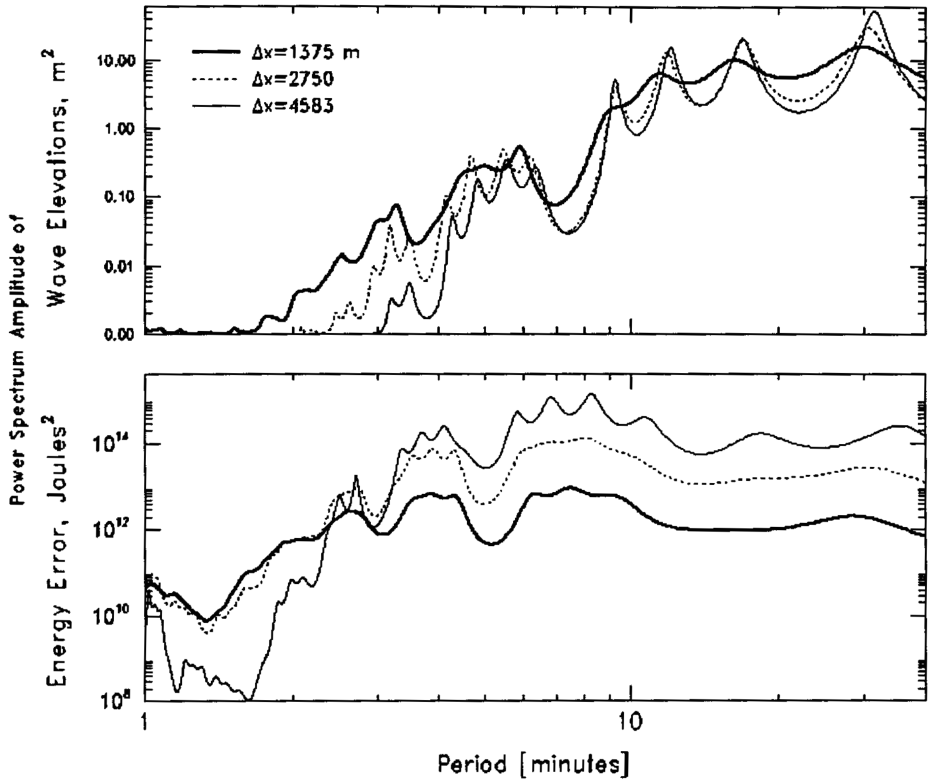

Figure 5.17e Power spectrum of wave elevations and energy errors at station 5.

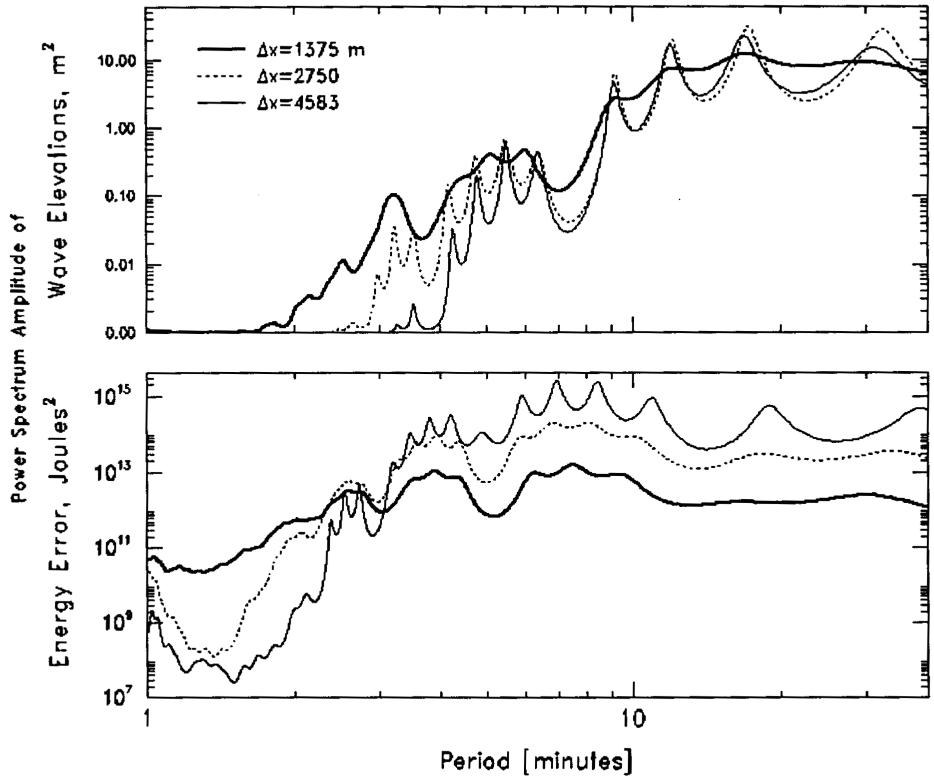

Figure 5.17f Power spectrum of wave elevations and energy errors at station 6.

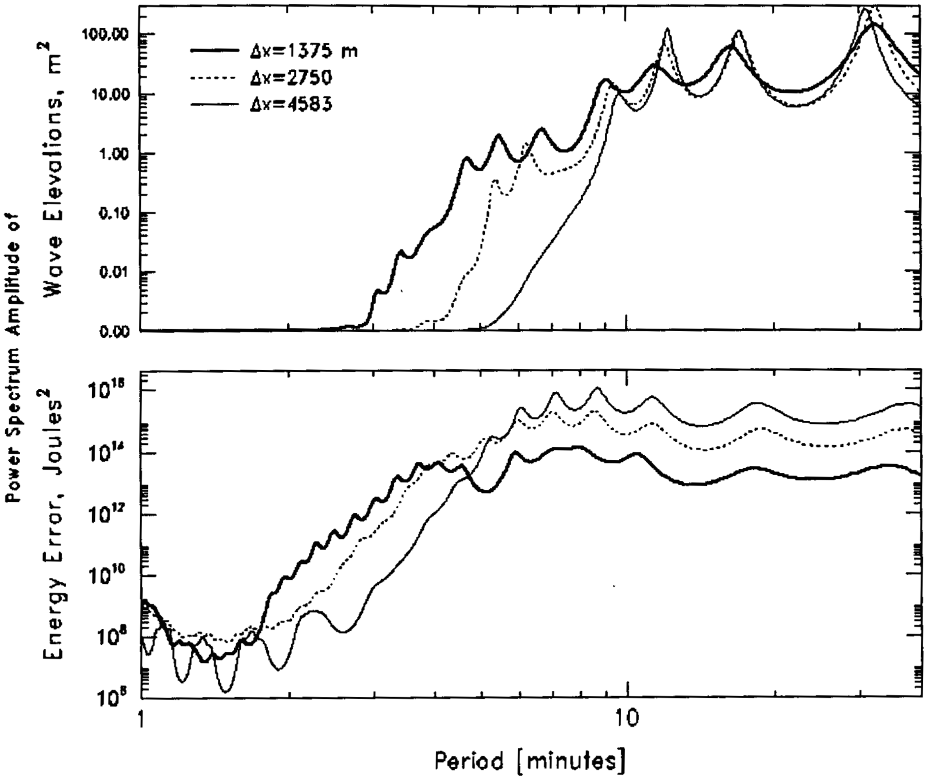

Figure 5.17g Power spectrum of wave elevations and energy errors at station 7.

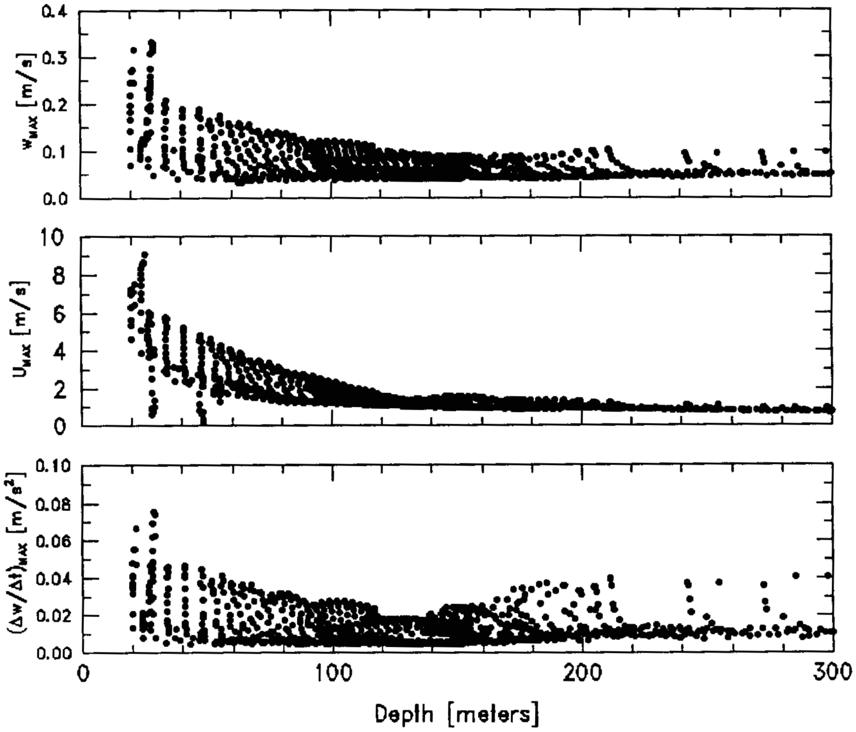

Figure 5.18 Maximum vertical velocity, maximum depth-averaged horizontal velocity, and maximum rate of change of the vertical velocity in shallow waters.

CHAPTER 6

Conclusions

6.1 Contributions

The ability to simulate the physics of regional tides and tsunamis through the use of barotropic numerical models was examined in this thesis. Tides were simulated in the eastern north Pacific Ocean, and selected events for tsunami modeling scenarios included the 1993 Hokkaido Nansei-Oki, 1964 Alaska, and potential Cascadia subduction zone events. Each of these modeling applications yielded insight on the physical representation of these events through a numerical model and how the numerical approach could be improved in representing such physics.

The inversion for tides in the Eastern North Pacific Ocean improved our understanding of tidal propagation in this region. A global tide modeling solution (Egbert et al., 1994) was used as an initial condition, from which changes could be computed through inversion techniques. The most significant changes between the regional inversion and the global tide model were observed in the K_1 tidal constituent, the amplitudes of which differed as much as 20 cm. Such differences most likely explain why a local modeling study in the Columbia River (Baptista et al., 1998), which was using the global tide modeling solution for boundary conditions, observed the largest errors in the K_1 constituent. Indeed, use of the regional inversion results as boundary conditions for this same study yielded smaller RMS errors. Amplitudes and phases for eight constituents were contrasted with various global modeling solutions at tide gauges in this region. Results showed that RMS errors were constrained below 5-10 cm at most open ocean locations for all models. However, the strength of the regional model derives from its improved representation of the physics as the waves approach shallow waters. In addition, the bathymetry is better depicted in the more refined grid of this model, thus permitting a more accurate portrayal of how the waves are altered by bottom slopes. Sensitivity tests with the inversion helped guide the final solution by providing insight as to an optimal selection of transfer functions, tide gauges, and numerical parameters used in the regional solution.

While it was shown that a regional model of tides could reproduce well the physics of tidal propagation, numerical models of tsunamis face more difficulty in providing such accurate results. The primary obstacle is the amount of uncertainty in the initial conditions, owing to the inability of verifying whether a proposed seismic source is correct or not. Two approaches of handling this problem have been proposed in this thesis. The first approach involves using new techniques in defining the parameters used by the deformation model. Rather than relying on ambiguous post-seismic estimations of the amount and direction of slip occurring between the two plates, slip vectors were derived based on more accurate measurements of plate motion Euler vectors and time intervals between earthquakes. The geometry of the subduction zone was determined from geodetic data, and modifications to the slip vectors were computed based on geothermal models. A three-dimensional dislocation model was then used to translate these newly derived parameters into a deformation along the ocean floor.

The Cascadia subduction zone was selected as the application for this approach to computing the deformation. Geologic evidence indicates that this subduction zone generates earthquakes every 200-600 years, the last of which occurred in the year 1700. Thus, evaluating the impact of tsunamis that are likely to be generated in the future is a vital tool for Cascadia coastal communities to use in hazard mitigation. Using the deformations computed as described above, potential tsunamis were simulated with a finite element hydrodynamic model. Simulations were made on two finite element grids, the results of which exemplified the importance of grid refinement in representing the higher frequencies generated by refraction and reflection of the waves. Numerical modeling of tsunamis over the past several years has often underpredicted the observations of wave heights along the shore, and the work presented here on grid refinement shows that it is one of the primary culprits. Results from the Cascadia tsunami simulations were analyzed in terms of wave elevations and water velocities off the northwest coast of the United States. Energy patterns were analyzed to reveal wave focusing mechanisms from bathymetric heterogeneities perpendicular to the wave direction. Wave elevations and velocities were provided along the entire coast as estimations of the energy of the waves as they reached the shoreline.

While the regional propagation of Cascadia tsunamis can provide many clues as to how locally-generated tsunamis would propagate through this system in future events, the physics at more local scales will ultimately provide the most useful information to communities at risk. Detailed representations of the communities of Seaside and Newport, Oregon were included in the finite element grid. Just as bathymetry is interpolated onto the main oceanic portion of the grid, topography in these communities was mapped on to the land extensions of the grid to permit inundation to occur in the numerical simulations. Because much of Newport is on relatively high ground above mean sea level, inundation was primarily limited to low-lying regions south of Yaquina Bay. Seaside, on the other hand, consists mostly of land that is low to mean sea level, thus allowing the tsunami waves to inundate most of the town. While the uncertainty in the seismic source and hydrodynamic model should be kept in mind when evaluating such results, the inundation patterns should also serve as a tool in determining the risks that these communities could face. Priest et al. (1995, 1997, 1998) has translated these results into inundation maps that communities along Oregon's coastline can use in making hazard mitigation decisions at the state and local levels of government.

The second approach to handling uncertainty in tsunami simulations is to evaluate the best way in which to minimize errors that are not associated with the seismic source. There has been a tendency in recent years for modelers to derive a source that, when used by a particular model, generates waves consistent with observations of a tsunami which has just occurred. In doing so, much of the focus has been directed towards the elusive definition of the source for each tsunami event. It is a moot point for now, considering that a myriad of different sources will ultimately be proposed for each tsunami, there will always be questions regarding landslides and the temporal nature of the deformation, and no verification of the source can be provided. It makes more sense to focus on the other components of the modeling process, the analysis of which can provide insight as to how well the physics of these waves is incorporated in the numerical models.

The impact of selected model parameters on the quality of tsunami simulations was investigated in this thesis. Physical parameterizations for friction, diffusion, and shoreline bathymetry were shown to play a significant role in the computed wave elevations and velocities at the coastline. Of these, friction is generally the most difficult to quantify in numerical models and attempts should be made to investigate this parameterization in more detail. Using as small a diffusion coefficient as possible should ensure that the solution isn't unnecessarily damped, and bathymetry should be optimally represented in the numerical grid. Another component of the physical representation of these events is the nonlinear interaction between tides and tsunamis. Tidal predictions have historically been linearly filtered out of tide gauge recordings of both the tide and the tsunami to yield a recording of just the tsunami wave. However, simulations of the 1964 Alaska tsunami with and without a tidal forcing indicated that significant nonlinearities are generated by the interaction of these two long waves. Neglecting such nonlinear interactions will yield false representations of the dynamics of such events, and linear filtering of data is likewise not an appropriate process. The linear superposition of the tides and tsunami waves also plays an important role in how well the model is able to replicate observations such as the extent of inundation. The impact of the tsunami will be strengthened or weakened depending on whether it arrives at the coastline during high or low water tides, respectively.

While these physical representations play a non-negligible role in the simulations, the model performance was shown to be most sensitive to the selection of certain numerical parameters. The time step affected the solutions in nearshore regions, most likely due to the dispersion of the waves at the coastline and to the sensitivity of the inundation algorithm to this parameter. The GWCE weighting factor also impacted the solutions globally, too small a value of which led to strong deviations from the continuity equation and too large a value of which could cause numerical instabilities. Finally, the amount of grid refinement was the primary factor influencing the numerical simulations. The simulations of the 1964 Alaska and 1993 Hokkaido Nansei-Oki tsunamis exhibited that the dispersion of the waves to higher frequencies was limited by the amount of grid refinement, both in shallow waters for near-field tsunamis and in deeper waters for far-field tsunamis. Such higher frequency representations appear to be needed, as evidenced by tide gauge recordings for both of these events.

The most important consequence of these numerical factors on the solution is the loss of energy throughout the length of the simulations. As mentioned, tsunami simulations have historically underpredicted the impact of tsunamis at the shoreline, and energy loss would certainly explain much of this. Selection of the grid spacing, time step, and GWCE weighting factor can potentially influence the numerical solution such that over 50% of the initial energy is inexplicably lost as the waves propagate for hours after the earthquake. To investigate this in more detail, an energy error was formulated and contrasted with truncation errors from the nonlinear GWCE. The influence of the above-mentioned numerical parameters was tested on the temporal and spatial nature of truncation and energy errors in a channel test case. Results showed that the energy error provided a more effective measurement of the quality of computed wave elevations and velocities from the numerical model. An algorithm was developed which would allow for solution of optimal numerical parameters that would procure minimal energy loss. While use of this algorithm provided improved results, energy loss as the waves reflected off vertical walls could not be avoided. This appears to indicate a limitation of long wave assumptions inherent in the shallow water equations.

6.2 Future Work

The tidal inversion results have been shown in preliminary tests to provide improved boundary conditions to more local modeling studies. The results should further be utilized in forecasts of tidal patterns in the CORIE project. While barotropic models of tides have proven to reduce RMS errors to within 1-10 cm at open ocean locations, there are options available for further minimizing such errors. One of these options is to use satellite altimetry data in the inversion. TOPEX/POSEIDON crossover points are more equally spaced across the ocean, and data at these points has been filtered through adequate quality control to be of propitious use to modeling efforts. Another available option is to commence using full or quasi three-dimensional models in the inversion. This will allow temperature and salinity transport to be incorporated, permitting baroclinic effects on the physics to be accounted for. Improved modeling of tides will become feasible as more quality data is incorporated, as the physics is better represented in the models, and as computer processing times decrease.

Numerical modeling of tsunamis, on the other hand, has a longer road ahead. Faced with the daunting task of overcoming the uncertainty in the seismic source, it seems like the best battle strategy to employ is the divide and conquer tactic: Divide the tsunami modeling process into at least two components - the seismic source definition and the hydrodynamic modeling of the tsunami propagation and inundation. Conquer each of these components by deriving solutions that independently minimize the errors in each. Compare these independent solutions to test for convergence. If there is no convergence, formulate new techniques for the 'conquer' step. Without such an algorithm, the dependencies between the source and the numerical model only proliferate prodigious degrees of freedom in defining a problem statement that cannot be verified.

The tools for constructing an effective divide and conquer algorithm have been presented in this thesis. For example, inversion techniques can potentially play an important role in the hydrodynamic modeling component of the algorithm. As the errors in the modeling are minimized and our understanding of the physics becomes more comprehensive, inversion for arbitrary shapes of the initial tsunami wave will converge upon more physically realistic initial conditions. Use of arbitrary shape functions rather than assumptions regarding the seismic source in the inversion would ensure independence from the deformation theory. This thesis has identified the primary factors affecting the quality of numerical simulations and provided solution strategies for minimizing the errors resulting from such factors. Using inversion theory in this manner could lead to a solution of the initial conditions based purely on the hydrodynamic model and wave observations. Another independent solution could be derived by optimizing computations of the deformation from seismic and geodetic data. Techniques have likewise been developed in this thesis for providing more efficient approaches to such calculations. By optimizing the deformation model independent of any knowledge of the tsunami observations or hydrodynamic model, our understanding of the plate movement during earthquakes will be improved. These independent solutions could then be compared with the hydrodynamic component solutions of the initial conditions. If the solutions appear to converge, the algorithm will have succeeded in reducing the number of degrees of freedom and in providing some form of verification for the problem.

This convergence upon proper solutions may take some time, in the midst of which the models need to be used as tools in mitigating hazards from future events. The tools developed, for example by this thesis, thus need to be concomitantly incorporated into models of potential tsunamis from active subduction zones. Such work is currently being performed for the states of Oregon, Washington, Alaska, Hawaii, and California (Bernard, 1998) in an effort to identify, model, and mitigate the hazards posed by future tsunamis. Better modeling techniques thus beget improved hazard mitigation, the convergence of both shall yield an invaluable understanding of the physics and the eventual impacts of these waves.

6.3 References

Baptista, A.M., M. Wilkin, P. Pearson, P. Turner, C. McCandlish, P. Barrett, S. Das, W. Sommerfield, M. Qi, N. Nangia, D. Jay, D. Long, C. Pu, J. Hunt, Z. Yang, E. Myers, J. Darland and A. Farrenkopf, 1998. Towards a Multi-Purpose Forecast System for the Columbia River Estuary, submitted to *Ocean Community Conference*, Marine Technology Society, Baltimore, MD.

Bernard, E.N., 1998. Program Aims to Reduce Impact of Tsunamis on Pacific States, *EOS Transactions*, 79(22), 258-263.

Egbert, G.D., A.F. Bennett and M.G.G. Foreman, 1994. TOPEX/POSEIDON Tides Estimated Using a Global Inverse Model, *Journal of Geophysical Research*, 99(C12), 24821-24852.

Priest, G.R., 1995. *Explanation of Mapping Methods and Use of the Tsunami Hazard Maps of the Oregon Coast*, O-95-67, State of Oregon Department of Geology and Mineral Industries.

Priest, G.R., E.P. Myers, A.M. Baptista, P. Fleuck, K. Wang, R.A. Kamphaus and Peterson, C.D., 1997. *Cascadia Subduction Zone Tsunamis: Hazard Mapping at Yaquina Bay, Oregon*, O-97-34, State of Oregon Department of Geology and Mineral Industries.

Priest, G.R., E.P. Myers, A.M. Baptista, R.A. Kamphaus, B.K. Fiedorowicz, C.D. Peterson and T.S. Horning, 1998. *Tsunami Hazard Map of the Seaside-Gearhart Area, Clatsop County, Oregon*, IMS-3, State of Oregon Department of Geology and Mineral Industries.

Vitae

The author was born in Pasadena, California on August 17th, 1970. He attended Washington University in St. Louis, where he received his B.Sc. in Civil Engineering in 1992. He then came to the Oregon Graduate Institute of Science and Technology and earned a M.Sc. in Environmental Science and Engineering in October of 1994. The M.Sc. thesis was entitled "Numerical Modeling of Tsunamis with Applications to the Sea of Japan and the Pacific Northwest". In 1997, he received the Director's Award from the Center for Coastal and Land-Margin Research.

Publications and Conferences:

Baptista, A.M., G.R. Priest, Y. Tanioka and E.P. Myers, 1993. A Post-Tsunami Survey of the 1993 Hokkaido Tsunami, *EOS Transactions*, 74(43), 349.

Baptista, A.M., E.P. Myers, M. Qi, B.C. Beck, G.R. Priest and C.D. Peterson, 1995. Tsunami Propagation and Inundation from Cascadia Subduction Zone Earthquakes: Tools and Approaches (abstract), *Proceedings, IAPSO XXI General Assembly*, 264.

Baptista, A.M., M. Wilkin, P. Pearson, P. Turner, C. McCandlish, P. Barrett, S. Das, W. Sommerfield, M. Qi, N. Nangia, D. Jay, D. Long, C. Pu, J. Hunt, Z. Yang, E. Myers, J. Darland and A. Farrenkopf, 1998. Towards a Multi-Purpose Forecast System for the Columbia River Estuary, submitted to *Ocean Community Conference*, Marine Technology Society, Baltimore, MD.

Myers, E.P., A.M. Baptista and Y. Wang, 1993. Nonlinear Inversion of Tsunami Waveforms, *EOS Transactions*, 74(43), 350.

Myers, E.P., 1994. *Numerical Modeling of Tsunamis with Applications to the Sea of Japan and the Pacific Northwest*, M.Sc. Thesis, Department of Environmental Science and Engineering, Oregon Graduate Institute of Science & Technology, Portland, OR.

Myers, E.P. and A.M. Baptista, 1995. Finite Element Modeling of the July 12, 1993 Hokkaido Nansei-Oki Tsunami, *Pure and Applied Geophysics*, 144(3/4), 769-801.

Myers, E.P. and A.M. Baptista, 1996. Finite Element Solutions of the Hokkaido Nansei-Oki Benchmark, Long-Wave Runup Models, World Scientific, Singapore.

Myers, E.P. and A.M. Baptista, 1998a. Inversion for Tides in the Eastern North Pacific Ocean, (submitted to *Advances in Water Resources*).

Myers, E.P. and A.M. Baptista, 1998b. Modeling of Past Tsunamis: One Model's Lessons from the 1993 Hokkaido Nansei-Oki and 1964 Alaska Tsunamis, (submitted to *Natural Hazards*).

Myers, E.P. and A.M. Baptista, 1998c. Numerical Considerations in Finite Element Simulations of Tsunamis, (submitted to *International Journal for Numerical Methods in Fluids*).

Myers, E.P. and A.M. Baptista, 1998d. Finite Element Modeling of Potential Cascadia Subduction Zone Tsunamis, (submitted to *Science of Tsunami Hazards*).

Priest, G.R., E.P. Myers, A.M. Baptista, P. Fleuck, K. Wang, R.A. Kamphaus and C.D. Peterson, 1997. *Cascadia Subduction Zone Tsunamis: Hazard Mapping at Yaquina Bay, Oregon*, O-97-34, State of Oregon Department of Geology and Mineral Industries.

Priest, G.R., E.P. Myers, A.M. Baptista, R.A. Kamphaus, B.K. Fiedorowicz, C.D. Peterson and T.S. Horning, 1998. *Tsunami Hazard Map of the Seaside-Gearhart Area*, Clatsop County, Oregon, IMS-3, State of Oregon Department of Geology and Mineral Industries.